Mechanistic Investigation of Cell Cryopreservation Aided by Raman Spectroscopy: Challenges and Solutions for hiPSC Technologies

A Dissertation
SUBMITTED TO THE FACULTY OF
UNIVERSITY OF MINNESOTA
BY

Rui Li

IN PARTIAL FULFILLMENT OF THE REQUIREMENTS
FOR THE DEGREE OF
DOCTOR OF PHILOSOPHY

Allison Hubel, Ph.D., Advisor

September 2021

Parts of this dissertation have been published previously:

Yu G, **Li R** and Hubel A. Chapter 14 – Raman Cryomicroscopic Imaging and Sample Holder for Spectroscopic Subzero Measurements. *Methods in Molecular Biology: Cryopreservation and Freeze-Drying Protocols.* Fourth edition. W.F. Wolkers and H. Oldenhof (Eds.). 2021. Springer Nature. 2180, 351-361.

Li R[†], Hornberger K[†], Duarte AR and Hubel A. Natural Deep Eutectic Systems for Improved Cryopreservation of Cells. *AIChE Journal.* 2021. 67, e17085.

Li R[†], Hornberger K, Dutton J and Hubel A. Cryopreservation of iPS cell aggregates in a DMSO-free solution – an optimization and comparative study. *Frontiers in Bioengineering and Biotechnology.* 2020. 8, 1-13.

Li R[†], Johnson R[†], Yu G, McKenna DH and Hubel A. Preservation of cell-based immunotherapies for clinical trials. *Cytotherapy*. 2019. 21, 943-957.

Yu G, **Li R** and Hubel A. Interfacial interactions of sucrose during cryopreservation detected by Raman spectroscopy. *Langmuir*. 2018. 35, 7388-7395.

Li R[†], Yu G[†], Azarin S and Hubel A. Freezing responses in DMSO-based cryopreservation of human iPS cells: aggregates vs. single cells. *Tissue Engineering: Part C*. 2018. 24, 289-299.

[†]These authors contributed equally.

Parts of this dissertation will be published in the future:

Li R, Walsh P, Truong V, Peterson A, Dutton JR and Hubel A. DMSO-free freezing of hiPSC-derived sensory neurons reveals stage-specific mechanisms for addressing cryopreservation challenges during cell manufacturing. (In preparation.)

Acknowledgements

Throughout the work and writing of this dissertation I have received a great deal of support and guidance from many groups and individuals. Firstly, I would like to thank my advisor, Prof. Allison Hubel. Thank you for introducing me to the world of scientific research and cryobiology, teaching me scholarly rigor, challenging me to think out of the box and lead creatively, and always encouraging, supporting me in my professional and personal growth. I would also like to thank my committee members, Drs. Samira Azarin, Brenda Ogle, and Wei Shen. Your continuous inspiration, generous contribution, and insightful feedback have fueled this work and sharpened my thinking.

Thanks are due to the funding sources that supported me personally as well as the projects included in this dissertation (National Institutes of Health awards R01EB023880 and R01HL154734, and National Science Foundation awards 1951443 and 1941543). Parts of this work involving Raman spectroscopy were carried out in the Characterization Facility, University of Minnesota, which received partial support from the National Science Foundation through the MRSEC program. I would like to thank Dr. Bing Luo, who has shown me the ropes in maintaining the intricate Raman microscope and addressing the unknown, surprising elements of Raman-based scientific discovery.

This work would not be possible without my past and present colleagues and their wonderful collaboration. I would like to thank Dr. James Dutton for his mentorship, guidance, and support through the scientific and professional journey (coauthored work

included in Chapters 5-7), as well as his former student, Caitlin Hill, who had trained me on stem cell culture and assisted with my experiments prior to this dissertation. I would like to thank Dr. Ashley Peterson for her expertise in statistics and contribution to this work (included in Chapter 7) and our group's statistical literacy. In addition, I would like to thank Patrick Walsh and Vincent Truong, who are former staff scientists in the Dutton Lab and now cofounders of Anatomic Incorporated, for always lending a helping hand and providing thought-provoking discussions as well as valuable distractions. A thank-you also goes out to the Stem Cell Institute for allowing us to use their Laboratory for Stem Cell Automation, to the Ogle Lab for allowing us to use their flow cytometer, and to the Bischof Lab for allowing us to borrow their -80 ˚C freezer and plate reader.

My former and present lab mates in the Hubel Lab have not only been the backbone of my work and growth but also made my five years of graduate school much more enjoyable. Thank you, Dr. Katie Pollock for welcoming me into Hubel Lab 5 years ago and leaving us with such a rich legacy. Thank you, Dr. Guanglin Yu for teaching me low-temperature Raman spectroscopy that eventually became the foundation of this dissertation (coauthored work included in Chapters 4 and 5) and being a wonderful friend. Thank you, Katie Hornberger for designing and performing the DSC experiments (included in Chapters 5 and 6), bouncing ideas with me through numerous brainstorming sessions, and for your partnership in and outside of the lab. Thank you as well to Dr. Chia-Hsing Pi, Ryan Stublaski, Rachel Johnson, Julianne Connors, Adam Joules, Tessa Burrows, and Troy Louwagie for your intellectual stimulation and friendship.

I had the honor and pleasure of mentoring several undergraduate students during my time in graduate school. A big thank you goes to my amazing team for their assistance in advancing this work towards process automation and technology dissemination: Madeline Wagner, Jordan Wallace, Kyle Knofczynski, Katelyn Fitzgerald, and Gretchen Koomjohn. Another thank you goes to my other undergraduate mentees, Hafsa Ibrahim, Po Tin Mak, Taylor Liao, Jacob Herbers, Colin Bain, and Cole Cullen, for allowing me the honor and joy of being part of your professional journey.

The mentorship I received in college has driven me to pursue a research career. A special thank you goes to Prof. Lydia Sohn at the University of California, Berkeley for believing in me and supporting me on my soul-searching journey, to Dr. Eric Jabart for teaching me integrity and resilience of being an experimentalist, to Dr. Olivia Scheideler for showing me the art of scientific collaboration and patiently guiding me through some of the stormiest times, and to Dr. Sewoon Han for being a wonderful role model and shaping me into the person I am today.

Last but not least, I would like to express my immense gratitude to my support network of family and friends. Thank you, grandpa (Tingyuan Li), grandma (Weifen Li), dad (Pu Li), mom (Yimei Zhang) for raising me to follow my own path and loving me all the way from the other side of the world. Thank you, Sophie Yu and John Shen for providing a home away from home and caring for me as my parental figures. Thank you, Julia Wolter Holmstrom, my dearest friend for filling even the hardest days with love and joy.

Dedication

This thesis is dedicated to Jiang “Xiao’er” Wu,

to those we lost,

whose passion for life

and kindness to all

motivated us to pursue this career in biomedical research.

Abstract

Human induced pluripotent stem cells (hiPSCs) possess the potential to differentiate into any cell of the human body for translational research towards drug discovery, disease modeling, cell therapy, and tissue engineering applications. hiPSCs and differentiated cells of certain lineages and maturity have been challenging to cryopreserve. Effective cryopreservation will enable off-the-shelf use of the hiPSC-derived personalized medicine platforms and therapeutic products. Systematic understanding of cryobiological mechanisms is a key to the effective design of cryopreservation methodology.

We hypothesize that the mechanism of cryopreservation challenge varies between different forms of the same cell type, particularly multicellular aggregates versus single cells of hiPSCs, as well between different developmental stages of the same tissue-specific lineage derived from hiPSCs; for example, neural crest cells versus immature versus mature sensory neurons. Using low-temperature Raman spectroscopy as a tool for label-free mechanistic discovery in molecular and cell cryobiology, this research demonstrates that multicellular aggregates of hiPSCs are significantly more sensitive to undercooling stresses due to their lower membrane fluidity than single cells. Similarly, undercooling sensitivity of different hiPSC-derived neuronal cell stages also inversely correlate with their respective membrane fluidity. However, a synergistic formulation of non-DMSO osmolyte-based cryoprotective agents (CPAs) can effectively reduce cell sensitivity to undercooling otherwise manifested by DMSO, by strengthening the hydrogen bonds with water and inhibiting intracellular ice. We find that hiPSC-derived

developmental stages with larger cell sizes require significantly slower cooling rates than those with smaller cell sizes to avoid intracellular ice and consequent cell damages upon fast cooling. The mechanisms of action of sucrose, glycerol, L-isoleucine, human serum albumin, and poloxamer 188 are respectively examined. Their thermophysical interaction with water, with each other, and biological interaction with cells act in concert to optimize pre-freeze cell stability, post-thaw survival and function, producing cells superior in quality and undercooling tolerability to those cryopreserved in DMSO-based alternative formulations.

Learning the mechanisms of cryoinjury in cell forms and cell types that are challenging to cryopreserve, as well as the mechanisms of cryoprotection by different CPAs under different cooling rates and nucleation temperatures, allows us to target identifiable problems with effective solutions. The outcome of this dissertation will bring empirical perspectives into designs of cryopreservation strategy for hiPSCs and hiPSC-derived neural crest cells, sensory neurons and present a potentially imitable approach for future cryobiological studies of other hiPSC-based cell technologies.

Table of Contents

List of Tables

List of Figures

List of Abbreviations and Symbols

1^{st}	first
2D	two-dimensional
3D	three-dimensional
7-AAD	7-amino-actinomycin D
AIC	area proportion (or fraction) of intracellular ice to cell
AO	acridine orange
AO/PI	20 mM AO and 10 µg/ml PI in PBS
B.hRM	BAMBanker hRM Cell Freezing Media
Ca^{2+}	calcium ion
CC	carbon-carbon covalent bond
CD3	cluster of differentiation 3
CH	carbon-hydrogen covalent bond
CO_2	carbon dioxide
CPA	cryoprotective agents
CRF	controlled-rate freezer
CS	carbon-sulfur covalent bond
CS10	Cryostor 10 Cell Freezing Medium
cyt C	cytochrome C
D5 crest	day-5 neural crest cell
D7 SN	day-7 fully differentiated, immature sensory neuron
D14 mSN	day-14 more mature, electrophysiological active sensory neuron

DE	differential evolution
DMEM/F12	Dulbecco's Modified Eagle Medium/Nutrient Mixture F-12
DMSO	dimethyl sulfoxide
DSC	differential scanning calorimetry
E8	TeSR-E8, Essential 8 medium
ECM	extracellular matrix
e.g.,	for example,
FBS	fetal bovine serum
FOXA2	Forkhead Box Protein A2
FSC	forward scattering channel
HAND1	Heart And Neural Crest Derivatives Expressed Protein 1
HBSS	Hank's Balanced Saline Solution with Ca^{2+}, Mg^{2+} and glucose
HCO_3^-	bicarbonate
HEPES	4-(2-hydroxyethyl)-1-piperazineethanesulfonic acid
hESC	human embryonic stem cell
hiPSC	human induced pluripotent stem cell
HSA	human serum albumin
i.e.,	in this case,
IIF	intracellular ice formation
KCl	potassium chloride
LN2	liquid nitrogen
MCO	multicomponent osmolyte

mFreSR	mFreSR Cryopreservation Medium for PSCs
Mg^{2+}	magnesium ion
MRI	magnetic resonance imaging
MSC	mesenchymal stromal cells
NADES	natural deep eutectic system, natural deep eutectic solvent
NANOG	Homeobox Protein NANOG
NESTIN	Neuroepithelial Stem Cell Protein
NMMIIA	nonmuscle myosin IIA
NMR	nuclear magnetic resonance
n.s.	no statistical significance
OCT4	Octamer-binding Transcription Factor 4
OH	oxygen-hydrogen covalent bond
P188	poloxamer 188
PAX6	Paired Box Protein 6
PBMC	peripheral blood mononuclear cell
PBS	phosphate buffered saline
PBS++	phosphate buffered saline with Ca^{2+} and Mg^{2+}
PDA	pyrene-decanoic acid
PI	propidium iodide
PRPH	peripherin (a cytoskeletal protein found in neurons of the peripheral nervous system)
PSF	point spread function

ROCKi	ROCK inhibitor, Y-27632
SE	standard error
seed	seeding, seeding temperature
SOX9	SRY-Box Transcription Factor 9
SOX10	SRY-Box Transcription Factor 10
SOX17	SRY-Box Transcription Factor 17
SSC	side scattering channel
STR	Short Tandem Repeat
T	Brachyury (a gene of the T-box family)
T:G	trehalose: glycerol, a NADES composed of trehalose and glycerol
TGI	trehalose, glycerol and isoleucine
TRA-1-60	T Cell Receptor Alpha Locus, Podocalyxin
TTX	tetrodotoxin
TUJ1	Neuron-specific class III beta-tubulin
(-)	minus, without
(+)	plus, with added
2x	twice, twice the final working concentration of
a	semimajor axis
b	semiminor axis
B	cooling rate, effective cooling rate during ice growth phase
CR	crossover (a parameter in DE algorithm configuration)
f	ellipticity, first flattening

ΔF	intensity differential compared to background fluorescence (F_0)
ΔH_m	enthalpy of melting
F	weight, mutation factor (a parameter in DE algorithm configuration)
F_0	background fluorescence
n	sample size
NP	population size (a parameter in DE algorithm configuration)
p	p-value
R^2	R squared value, coefficient of determination
T_g	glass transition temperature
T_{m1} or T_m	melting temperature defined as the onset of melting
T_{m2}	melting temperature defined as the peak of melting
T_{NUC}	nucleation temperature, ice nucleation temperature, seeding temperature

List of Units

˚C	Degree Celsius
˚C/min	Degree Celsius per minute (cooling rate)
cm^{-1}	inverse of centimeter (unit of wavenumber)
ex/em	excitation/emission
h	hour
J/g	joule per gram
mg	milligram
min	minute
ml	milliliter
mm	millimeter
mM	millimolar
mOsm/kg	milliosmoles per kilogram
mW	milliwatt
µg/ml	microgram per milliliter
µl	microliter
µm	micron, micrometer
µM	micromolar
nm	nanometer
s	second
% v./v.	percent volume/volume
% w./v.	percent weight/volume

Chapter 1

Introduction

1.1 Motivation

Possessing the potential to represent patient-specific disease models and differentiate into cells of all three germ layers[1,2], human induced pluripotent stem cells (hiPSCs) are the backbone of academic research and therapeutic endeavors in disease modeling[3,4], cell therapy[5], tissue engineering[6–8], and personalized medicine[9–11]. Since the discovery of induced pluripotent stem cells 15 years ago, *in vitro* culture of an abundance of new cell types and differentiation lineages has been enabled by advances in hiPSC research. As a result, there has been an expanding need for cryobiological wisdom to accelerate the translation and adaptation of prior cryopreservation methods to these rapidly emerging cell forms. Based on databases such as Grantome and ClinicalTrials.gov, there were over 1000 federal funded projects and over 200 clinical trials ongoing in 2020, nearly doubled since 2016. Equipped with translational knowledge and fit-for-purpose technologies, cryopreservation can enable efficient clinical cell manufacturing and accessible medicine to more patients worldwide.

The field of cryobiology has extensively studied the cell types at the front end of hiPSC-based manufacturing processes, including somatic starting materials such as peripheral blood mononuclear cells (PBMCs)[12–14] and fibroblasts[15,16]. While cryobiological research has touched on the cryopreservation of hiPSCs, the approaches have been limited to either vitrification[17], which is restricted by its technical difficulty and low scalability, or

slow freezing and apoptosis inhibitor-based rescue of singularized hiPSCs[18], which is adopted from methodologies developed for single cells like lymphocytes and not suitable for the multicellular nature of hiPSCs. In stem cell biology practices, hiPSC cryopreservation has been challenged by loss of viability, function or pluripotency[19–21]. Tracing down the hiPSC-based cell manufacturing workflow, utilization of cryopreservation has been reported in stem cell biology studies of hiPSC-derived cell types such as cardiomyocytes and endothelial cells[22,23]. However, there is a lack of cryobiological knowledge and scientific principles that would guide the formulation of cryopreservation media, parametric requirements for freezing and thawing, mechanisms of cryoinjury – whether and how they change from one cell type to another –in the context of the growing variety of cell types in this dynamic and complex realm of hiPSC-based manufacturing.

Summarizing these opportunities and challenges, this dissertation work will focus on dissecting mechanisms of action involved in the freezing of hiPSCs and its difficulties and developing a paradigm of effective non-DMSO cryoprotective agents and defined quality metrics. Using hiPSCs as a model cell type in this cryobiological frontier, we will learn of multicellular systems' unique sensitivities. Tracing cryobiology along a given differentiation lineage from hiPSCs, we will discover that a cell's freezing behavior and the source of its cryopreservation challenge change as it differentiates and matures, and how the similarities and differences it carries can inform future cryopreservation designs.

1.2 Hypothesis and Aims

This research proposes to understand the mechanisms of damages in hiPSC aggregates and differentiated cells during cryopreservation as well as the mechanisms of action of different cryoprotective agents (CPAs). We hypothesize that cell sensitivity to cooling rate and undercooling will differ by cell form and cell developmental stage, and that a synergistic combination of multiple non-DMSO CPAs will provide superior cryoprotection against freezing damages in cells compared to DMSO. The following aims will be used to test these two hypotheses.

Aim 1 – Mechanisms of freezing damage in hiPSCs and hiPSC-derived neuronal cells as elucidated by Raman spectroscopy and supported by cell-based fluorescence assays.

Aim 1.1 – Characterize damage in hiPSC single cells versus multicellular aggregates given different cooling rates.

In Chapter 4, large, small hiPSC aggregates and their single-cell counterparts will be frozen in a simple 10% DMSO solution with cooling rate varied between -1, -3 and -10 ˚C/min, where intracellular ice formation during freezing and post-thaw cell survival and function will be analyzed using low-temperature Raman spectroscopy, membrane exclusion assay, cell reattachment assay, apoptosis assay, and cytoskeleton imaging respectively.

Aim 1.2 – Characterize damage in hiPSC single cells versus multicellular aggregates given different ice nucleation temperatures (undercooling).

In Chapter 4, parallel to Aim 1.1, hiPSC aggregates and their single-cell counterparts will be frozen in the 10% DMSO solution subjected to varied degrees of undercooling by inducing ice nucleation at -4 or -8 ˚C, where intracellular ice formation during freezing and post-thaw cell survival and function will be analyzed using low-temperature Raman spectroscopy, membrane exclusion assay, cell reattachment assay, apoptosis assay, and cytoskeleton imaging respectively.

Aim 1.3 – Compare damage by suboptimal cooling rate in hiPSC-derived neuronal cells of different development stages.

In Chapter 7, day-5 neural crest cells, day-7 immature sensory neurons, and day-14 more mature sensory neurons will be frozen in the optimized solution from Aim 3.1 with cooling rate varied between -1, -3 and -5 ˚C/min, where intracellular ice formation, membrane partitioning, cell shrinkage, and cytochrome C release will be analyzed during freezing and compared across the three cell stages using low-temperature Raman spectroscopy.

Aim 1.4 – Compare damage by undercooling in hiPSC-derived neuronal cells of different development stages.

In Chapter 7, parallel to Aim 1.3, day-5 neural crest cells, day-7 immature sensory neurons, and day-14 more mature sensory neurons will be frozen in the optimized solution from Aim 3.1 with ice nucleation induced at -4 or -8 ˚C, where intracellular ice formation, membrane partitioning, cellular integrity, and cytochrome C release will be analyzed during freezing and compared across the three cell stages using low-temperature Raman spectroscopy.

Aim 2 – Mechanisms of cryoprotection by CPA-CPA, CPA-water and CPA-cell interactions as unveiled by Raman and assisted by other analytical chemistry

techniques.

Aim 2.1 – Analyze interfacial interactions of sucrose during freezing.

In Chapter 5, based on Jurkat cells as a simplified cell model, under constant cooling rate and nucleation temperature (CRF parameters), the molecular concentration of sucrose in the nonfrozen solution, the spatial distribution of sucrose at its interface with extracellular ice and with cell, and the correlation between intracellular ice formation and extracellular sucrose distribution will be analyzed during freezing using low-temperature Raman spectroscopy.

Aim 2.2 – Examine interactions of NADES with water and NADES with cells.

Also in Chapter 5, based on Jurkat cells, under constant CRF parameters, the morphology of ice crystals and the strength of hydrogen bond in dilute trehalose-glycerol NADES will be analyzed during freezing and compared with that in individual trehalose and glycerol solutions using low-temperature Raman spectroscopy; the suppression and depression of ice crystallization in dilute NADES of varying concentrations will be analyzed using differential scanning calorimetry (DSC) and compared with a non-NADES solution containing trehalose and glycerol; cell recovery immediately post-thaw and persistence over time in culture will be quantified using membrane exclusion assay and compared to the non-NADES solution and a simple DMSO solution.

Aim 2.3 – Investigate the nature of cryoprotection by isoleucine and albumin.

In Chapters 5 and 6, based on Jurkat cells representing simpler cell forms and hiPSC aggregates representing multicellular systems, under constant CRF parameters, changes in the morphology of ice crystals, the suppression and depression of overall ice formation, and post-thaw cell survival upon the addition, subtraction, or removal of isoleucine and albumin will be analyzed

using a combination of low-temperature Raman spectroscopy, DSC, membrane exclusion and reattachment assays respectively.

Aim 2.4 – Explore the effect of poloxamer 188 on water crystallization and cell adhesion.

In Chapters 5 and 6, based on hiPSC aggregates representing multicellular systems, changes in the morphology of ice crystals, the suppression and depression of overall ice formation, post-CPA exposure cell survival, and post-thaw cell adhesion upon the presence or absence of poloxamer 188 (P188) will be analyzed using a combination of low-temperature Raman spectroscopy, DSC, and cell reattachment assay respectively.

Aim 3 – Translational development of a new DMSO-free method to cryopreserve hiPSC aggregates.

Aim 3.1 – Optimize a multicomponent non-DMSO CPA solution using the DE algorithm.

In Chapter 6, under constant CRF parameters, a CPA formulation composed of sucrose, glycerol, L-isoleucine, human serum albumin and P188 will be optimized for the highest post-thaw reattachment of hiPSC aggregates using a differential evolution (DE) algorithm in a 1296-point parameter space. Post-thaw survival, phenotypic and chromosomal stability of the optimally cryopreserved hiPSCs will be examined upon freeze-thaw stress amplification cycles.

Aim 3.2 – Benchmark against standard DMSO solutions on undercooling sensitivity.

In Chapter 6, under a constant cooling rate but varied degrees of undercooling by ice nucleation induced at -4 or -12˚C, hiPSC aggregates cryopreserved in the optimized non-DMSO formulation from Aim 3.1 will be benchmarked against a group of 4 different commonly used DMSO-based

CPA solutions, in terms of post-thaw reattachment and their change in response to undercooling.

Aim 3.3 – Establish requirements for basal buffer components.

In Chapter 6, under ambient environment, hiPSC aggregates will be collected in a basal buffer upon the presence, exclusion or replacement of each key component. After introducing the optimized non-DMSO CPAs from Aim 3.1 and incubating for 1 hour, cell reattachment will be measured with or without freeze-thaw and compared between the basal buffer variants.

Aim 3.4 – Test the cryopreservation method optimized for hiPSCs on hiPSC-derived neuronal cells.

In Chapter 7, day-5 neural crest cells, day-7 immature sensory neurons, and day-14 more mature sensory neurons will be frozen in the optimized non-DMSO CPA solution from Aim 3.1 using the best-case cooling rate and nucleation temperature from Aim 1.4, where the post-thaw recovery, reattachment and function of each cell stage will be benchmarked against a DMSO-based gold standard solution and examined in comparison with a fresh cell control.

In addressing these specific aims, we will understand why hiPSC aggregates are more difficult to freeze than single cells, what factors influence the bankability of differentiating cells, how non-DMSO CPAs like sucrose, glycerol, L-isoleucine and poloxamer 188 act in concert to protect cells against cryopreservation stresses, and whether our DMSO-free method improves post-thaw cell survival and function from the DMSO-based standards. The outcome of this dissertation will bring empirical perspectives into subsequent designs of the cells' cryopreservation strategy and present a

potentially imitable approach for future cryobiological studies of other hiPSC-derived cellular technologies.

Chapter 2

Background

2.1 Human induced pluripotent stem cells

2.1.1 Pluripotent stem cells

Induced pluripotent stem cells (iPSCs) were discovered for the first time in 2006 by Takahashi and Yamanaka[24], reprogrammed from mouse somatic fibroblasts using a cocktail of four factors, Oct3/4, Sox2, c-Myc and Klf4. Exhibiting the properties of embryonic stem cells (ESCs) yet not requiring the harvest of an embryo, hiPSCs are much more readily obtainable and widened the possibilities of stem cell-based biological research and therapeutic development[25]. Consequently, the field of stem cell biology exploded with new hiPSC clones of different species, different somatic tissue origins or different reprogramming methods, as well as ever improving protocols differentiating hiPSCs into specific tissue lineages and functional cell types.

Human induced pluripotent stem cells (hiPSCs) have been spotlighted in this field for their ability to represent the genomic profile of particular patients or patient populations and generate an *in vitro* model of the disease accelerating drug discovery and enabling personalized medicine. It also has the potential to differentiate into any cell type of the human body and serve as a "factory" of off-the-shelf cell products. Examples include sensory neurons for pain management research[26], retinal pigment epithelium for macular degeneration repair[27], and natural killer cells for cancer immunotherapy[28].

2.1.2 Cell culture modalities

hiPSCs are conventionally maintained and expanded in the form of 2D adherent cultures, where they adhere onto a fibroblast feeder cell monolayer or an ECM-coated surface and grow as compact colonies made of tens to thousands of cells. A chemically defined formulation named E8 was developed by the Thomson group in 2011 for the culture of hiPSCs and has since been one of the most widely used pluripotent stem cell media[29]. Subculture of adherent hiPSCs requires dissociating the cells from the ECM into 2D multicellular aggregates (or clusters), most commonly using non-enzymatic chelating agents such as ethylenediaminetetraacetic acid (EDTA) that sequesters the calcium and magnesium ions[30]. The cell-cell adhesion between hiPSCs is partially preserved, whereas the cell-ECM adhesion is disrupted and reestablished per passage in this culture modality.

Alternative to 2D adherent culture, 3D suspension culture of hiPSCs has recently gained popularity due to its scalability demanded by preclinical and clinical cell productions[31] and its suitability for subsequent generation of organoids[32] and differentiated cell spheroids[33]. Cells form 3D spherical aggregates with diameters ranging from 30 to 300 μm, where an aggregate larger than 300 μm would suffer oxygen depletion and apoptosis at its center, and that an ideal aggregate size may be determined to maximize the directed differentiation efficiency[34]. Subculture of 3D suspension hiPSCs is typically achieved by breaking up larger aggregates into smaller aggregates via gentle shear flow, where cell-ECM dissociation is not relevant. hiPSCs from 3D suspension culture may also be replated into 2D adherent cultures on an ECM-coated surface for downstream

applications.

2.1.3 Non-cryopreservation stresses and abnormality

Like other types of stem cells and progenitor cells (e.g., mesenchymal stromal cells, MSCs), hiPSCs are prone to spontaneous differentiation in culture due to, for example, suboptimal colony size and density, overgrowth, insufficient growth factors (e.g., mis-formulated or expired media), and excessive stress during passaging[35]. Interventions such as hypoxia (i.e., ≤ 5% instead of 21% O_2)[36] and hypothermia (i.e., 35 instead of 37˚C)[37] have been used in culture to reduce the occurrence of spontaneous differentiation. While hiPSCs possess the potential to self-renew indefinitely, the phenotype and karyotype of hiPSCs in reality can drift within several passages. Trisomy 21 is a common chromosomal abnormality found in hiPSCs and amplified by prolonged hiPSC cultures, as a result of apoptosis-inducing cell stresses (e.g., suboptimal cryopreservation) that have given selective advantage to the survival and proliferation of this subpopulation overexpressing anti-apoptotic genes[38].

In 2D and 3D hiPSC aggregates, neighboring cells are adhered to each other via E-cadherin. E-cadherin-mediated cell-cell adhesion is pivotal for the self-renewal and pluripotency of these pluripotent stem cells. Loss of this cell-cell adhesion can lead to ROCK activation-mediated apoptosis and spontaneous differentiation, and ROCK inhibitors are required to prevent apoptosis of singularized hiPSCs[39,40]. Therefore, for hiPSCs and other multicellular systems that rely on cell-cell adhesion for survival and

function, preservation of the cell-cell contact is critical in their manipulation including cryopreservation.

2.1.4 Existing post-thaw cell metrics

In order to quantify the outcome of cryopreserved cells, a variety of post-thaw metrics have been used in literature. The most common metric is post-thaw cell viability, defined as the percent population of viable cells post-thaw among total cell population post-thaw, where viable cells are determined by the exclusion of a charged dye Trypan Blue[41]. The calculation of post-thaw viability neglects to account for any cell loss by lysis, as it is based on the counting of visible, morphologically intact cells. Despite its popularity, the use of Trypan Blue is not appropriate for cryopreserved cells, frequently underestimating or overestimating the viable cell count, due to high background noise and arbitrary thresholding[42].

Post-thaw cell recovery is a modified version of post-thaw cell viability. It is defined as the percent population of viable cells post-thaw divided by viable cells pre-freeze[43]. Accounting for cell lysis, it is more conservative in estimating the survival of cells through cryopreservation. The combination of acridine orange (AO) and propidium iodide (PI) is an improved alternative to Trypan Blue, where green and red fluorescence provides a binary distinction between viable and non-viable cells. However, based on membrane exclusion alone, neither methods account for other mechanisms of freezing damage that do not result in increased permeability of the plasma membrane to the

molecular dye of interest[44].

Post-thaw cell apoptosis can be quantified using a fluorescent caspase antibody like FAM FLICA combined with a membrane exclusion dye like 7-AAD[45]. The live (double-negative), early apoptotic (FLICA-positive), late apoptotic (double-positive) and necrotic (7-AAD-positive) subpopulations are distinguished using flow cytometry. In addition, other characteristic markers specific to the cell type of interest or a metabolic dye like esterase-based Calcein AM may be used to identify live cells.

Post-thaw cell reattachment has gained utility in recent years to quantify the survival of cryopreserved adherent cells like MSCs[46]. After thawing, cells are washed by centrifugation and inoculated into 2D adherent culture. Upon undisturbed incubation at 37 ˚C for several hours until cell adhesion is established (e.g., 4 hours for MSCs), the culture is washed to remove non-adherent cells, stained using a metabolic viability dye like Calcein AM, and measured for fluorescence intensity using a microplate reader. A control curve may be established to correlate the fluorescence intensity with an exact cell count. Alternatively, a positive control group may be used, where fresh cells of equivalent quantity are collected and inoculated back into 2D adherent culture. This metric captures the preservation of viable, functionally adherent cells and potential freezing damage of subcellular components like the cytoskeleton.

2.2 Existing hiPSC cryopreservation methods and problems

Currently, the cryopreservation of hiPSCs involve either direct vitrification of the 2D adherent culture or slow freezing of dissociated single cells and aggregates.

2.2.1 Vitrification

Vitrification is a freezing modality commonly used to preserve organs[47], oocytes and embryos[48] in a glass-like state, avoiding crystallization altogether, and achieved by rapid cooling up to -100,000 ˚C/min. Despite high post-thaw survival of vitrified cells up to 100%, vitrification is technically challenging and prone to failure during cryogenic storage and warming[49]. To our knowledge, there has been one report of the vitrification of hiPSCs. Cells are inoculated onto a so-called TWIST substrate inside a specialized multi-chamber culture vessel, and the 2D adherent culture is vitrified by injection of liquid nitrogen into the chamber adjoining the culture chamber by the TWIST substrate[17]. This TWIST method enables the single-containment culture, cryopreservation, and re-culture of hiPSCs without dissociation. However, similar to other vitrification methods, the vitrification of hiPSCs lack scalability, limiting its utility in translational settings.

2.2.2 Slow freezing - passive freezing

Alternative to vitrification, slow freezing is a modality that utilizes cooling rates typically between -0.5 and -50 ˚C/min and lower concentrations of CPA aimed to achieve crystallization of extracellular water and partial glass transition of cells and nonfrozen solution between ice. Background on CPA formulation used for hiPSC cryopreservation will be introduced in section 2.4. Slow freezing of hiPSCs in literature is achieved by

primarily passive freezing[50] rather than controlled rate freezing. Cryogenic vials of dissociated hiPSCs are placed in an insulative secondary container or passive freezing device like CoolCell (Biocision) or Mr. Frosty (ThermoFisher Scientific) and cooled inside a -80˚C mechanical freezer overnight before being transferred into cryogenic storage. Compared to controlled rate freezing, passive freezing subject cells to cooling rates that change over time, spontaneous ice nucleation, and environmental fluctuations inside the freezer, likely suffering poor and highly irreproducible post-thaw cell outcome.

2.2.3 Single cell freezing and apoptosis inhibitor

While there has been a report of ESC aggregates cryopreserved by passive freezing[51], fewer than 30% of the cell population was found viable and adherent in the post-thaw culture. This method had yet to demonstrate superior post-thaw cell survival. More studies cryopreserved ESCs and hiPSCs in the form of single cells and inoculated the post-thaw cultures using ROCK inhibitor Y-27632 to counteract cell-cell dissociation-induced apoptosis[51–53]. The cryopreservation of hiPSCs as single cells is compatible with downstream differentiation protocols that require singularized hiPSCs as the starting material. However, masking underlying damages with apoptosis inhibitor is not a long-term solution for the advancement of multicellular system cryopreservation, where an effective method that not only enables high post-thaw cell survival but also preserve the natural multicellular form and function will be necessary.

2.3 Controlled rate freezing

As mentioned in section 2.2, controlled rate freezing is a slow freezing method with higher controllability and reproducibility than passive freezing, and better usability and scalability than vitrification. Cooling rate and ice nucleation temperature are two main parameters controlled by this method and contributing to cryoprotection of cells[54].

2.3.1 Cooling rate

It has been postulated that cooling rate acts to balance the dehydration of cells and the inhibition of intracellular ice formation[55,56]. As temperature decreases during cooling, ice crystals form and grow in the extracellular space, removing water from nonfrozen solution and increasing the extracellular solute concentration in the nonfrozen space between ice. While slow cooling rates promote exosmosis and dehydrate the cell potentially beyond its minimum tolerable cell volume causing subcellular and membrane damage, slow cooling rates prevent ice formation in the highly dehydrated cytoplasm. On the other hand, while fast cooling rates may not allow sufficient time for exosmosis resulting in intracellular ice formation, they reduce the extent of cellular dehydration and related stresses.

It has also been demonstrated that cells of different sizes respond to the effect of cooling rate differently[57]. Larger cells have lower surface-to-volume ratio and thus less efficient exosmosis during freezing. Compared to smaller cells, they require a slower maximum cooling rate in order to avoid intracellular ice. While the correlation between post-thaw cell survival and cooling rate would resemble an inverted “U” shape, due to the balance

between cell dehydration and intracellular ice inhibition, the correlation between cell size and optimal cooling rate would likely shift this inverted "U" curve towards slower cooling rates for larger cells and faster cooling rates for smaller cells.

2.3.2 Undercooling

The effect of different ice nucleation temperatures have been examined in literature given a certain cooling rate. The nucleation of ice crystals is a stochastic event that is distributed across a range of temperatures. Undercooling, also known as supercooling, is the process of decreasing sample temperature below its freezing point without solidification. The lower the ice nucleation temperature, the greater the degree of undercooling. It has been postulated in literature that as cell membrane permeability to water decreases with temperature, the efficiency of exosmosis also decreases, and as a result, the likelihood of intracellular ice increases[54]. Therefore, it is desirable to minimize undercooling and prevent intracellular ice by maximizing the temperature of ice nucleation allowed by the sample's thermophysical property.

Two main categories of methods to control ice nucleation temperature include seeding of a sample and addition of a nucleating agent. Seeding here refers to seeding (or induced nucleation) of ice crystals and is to be distinguished from seeding (or inoculation) of cell culture. Methods of seeding include (a) electromagnetic perturbations[58], which has yet to be applied to cell cryopreservation, (b) mechanical perturbation (e.g., shaking and hitting of a cryogenic vial), which is difficult to standardize and scale, (c) rapid withdrawal of

heat via programmed temperature ramp of a controlled-rate freezer, which is most widely used in industrial-scale cell cryopreservation, and (d) direct contact by a chilled object, which is commonly used in oocyte slow freezing[54]. Nucleating agents include (a) silver and mercuric iodide[59,60], (b) diamond, gold and other metal nanoparticles[61], (c) bacteria[62] and microbial-derived proteins (e.g., Snowmax)[63], (d) mineral beads (i.e., IceStart, Asymptote)[19,64], and (e) crystalline cholesterol[65–67], in descending order of cytotoxicity concerns and ascending order of current utility in cell cryopreservation.

2.4 Cryoprotective agents

2.4.1 DMSO

Dimethyl sulfoxide (DMSO), a byproduct of paper making, was originally used as a solvent in the mid 1800s and is still widely used to dissolve a variety of polar and nonpolar compounds including proteins in cell biology laboratories. The use of DMSO in cell cryopreservation was first reported in the 1950s[68] and has since been the gold standard[69]. As an organic solvent with colligative properties, DMSO suppresses and depresses ice formation in aqueous solutions. With relatively low molecular weight, DMSO is a cell-penetrating CPA that can inhibit intracellular ice formation given the appropriate cooling rate and ice nucleation temperature. Cryoprotection may be improved upon combination with non-penetrating CPAs such as trehalose[70].

On the other hand, DMSO also exhibits cytotoxicity and causes safety concerns around its infusion as part of cell therapies. Studies have demonstrated that exposing mammalian

cells to DMSO can reduce cell proliferation[71], induce apoptosis by disintegrating the mitochondrial and plasma membrane[72], alter gene expression on a RNA and microRNA level, and cause genomic changes by disrupting DNA methylation mechanisms[46,73]. Preclinical and clinical investigations have reported toxic effects of DMSO in animals and human patients, including decreased cell respiration and subsequent cell death within minutes of contact[74] and adverse events ranging from nausea, vomiting, fever, to hypertension, anaphylaxis, and seizure[75–77].

2.4.2 Non-DMSO osmolytes

To minimize the cytotoxicity of DMSO, alternative CPAs have been developed, reducing the concentration of DMSO used or replacing DMSO altogether. These non-DMSO CPAs include anti-freeze peptides and glycopeptides (AFPs) inspired by animals like the arctic fish[78,79], osmolytes inspired by trees that naturally survive frozen winters[80,81], and synthetic polymers such as polyvinyl alcohol[82] and ficoll[51,83]. Examples of non-DMSO osmolytes found effective in the cryopreservation of mammalian cells include sugars like sucrose, trehalose, sugar alcohols like glycerol, and amino acids like L-isoleucine and creatine. While the use of AFPs have been limited to research applications, yet to be proven safe for infusion as an excipient of cell-based therapies, osmolytes are Generally Recognized as Safe (GRAS) and readily suitable for use in clinical manufacturing and cryopreservation. In contrast to the cryoprotective mechanism of DMSO that dehydrates cells and spatially decouple water from the surface of subcellular macromolecules, non-DMSO osmolytes incorporate into the hydrogen bond network of water and globally alter

the properties of the intermolecular system[84], inhibiting ice formation while preserving cell integrity. Statistical modeling of these CPAs recently found an interactive effect between sucrose and glycerol and between glycerol and isoleucine, only at a particular concentration, that correlated with superior post-thaw cell survival, whereas the interaction between sucrose and a different sugar alcohol, mannitol, inversely correlated with post-thaw cell survival[85,86].

2.4.3 Optimization by differential evolution algorithm

Given the diversity of non-DMSO CPAs and limited understanding of their complex mechanisms of action, formulating an effective CPA cocktail currently requires screening to identify the appropriate molecules for each cell type and their cytotoxicity limit, as well as subsequent optimization to determine the best concentration of each molecule in this molecular combination. Existing methods of optimization include (a) high-throughput carpet bombing, which tests all possible scenarios of the parameter space and is most resource intensive, (b) trial and error, which lacks systematic transfer of learning and is most inefficient, (c) design of experiment (DOE) and its variant methods, which assume a unimodal effect of each parameter without interaction between parameters and are not suitable for complex, interactive parameter spaces, and (d) differential evolution (DE) algorithm, which do not build upon these assumptions but stochastic direct search iterated through each generation of experimentation and has been proven not only efficient but accurate at locating the parametric optimum in recent cryobiological studies[87,88].

2.5 Raman spectroscopy

Much of the text and figures in this section have previously appeared in the publication below, included here with copyright permission from Springer Nature.

Yu G, **Li R** and Hubel A. Chapter 14 – Raman Cryomicroscopic Imaging and Sample Holder for Spectroscopic Subzero Measurements. *Methods in Molecular Biology: Cryopreservation and Freeze-Drying Protocols.* Fourth edition. W.F. Wolkers and H. Oldenhof (Eds.). 2021. Springer Nature. 2180, 351-361.

Current theories of cell freezing damage were developed in the 1960s. Darkening of the cell observed by conventional cryomicroscopy at a low temperature has been associated with formation of ice crystals inside the cell, which leads to cell death[89]. The fundamental knowledge of the mechanism of cell freezing damage has not changed in the intervening more than 50 years; however, the tools available to interrogate cell freezing responses have evolved greatly. A previous study in our lab has utilized low-temperature Raman spectroscopy to verify the presence of ice inside a frozen cell and illustrate the partitioning of dimethyl sulfoxide (DMSO) across the cell membrane at a low temperature for the first time[90]. The high spatial resolution of Raman microscopy also allows us to investigate the freezing damage imposed to subcellular structures such as mitochondria[91], granting us a better understanding of the mechanism of cell damage during freezing.

Raman scattering is based on the interaction between a monochromatic light with molecular vibrations. It was first discovered by C.V. Raman in liquids in 1928[92], and two

years later Raman won the Nobel Prize in Physics for his outstanding contributions. During Raman scattering, molecules are excited to the short-lived higher energy levels through direct absorption of a photon from the incident monochromatic light. The excited molecules can further scatter a photon and return to the stable energy levels. Elastic Raman scattering refers to the situation in which the energy of scattered photons is different from that of absorbed photons. Raman spectra plots the intensity of the scattered light as a function of its frequency difference to the incident light, and Raman imaging generates false-color images of component distribution by acquiring and interrogating Raman spectra at every pixel of the image. In reality, Raman scattering is a rare phenomenon with an extremely low probability of occurrence. As a result, many advanced techniques are being developed to enhance Raman signal intensity, such as surface enhanced Raman spectroscopy (SERS), Resonance Raman spectroscopy and simulated Raman spectroscopy (SRS)[93].

Raman spectroscopy has been widely used for characterizing biological materials, as Raman spectra and images provide plentiful information of the material[94]. Furthermore, Raman bioanalysis is non-invasive and non-destructive to the sample and requires little effort of sample preparation[95]. A review of applications of Raman spectroscopy in single cell analysis has been published by Huser and colleagues[96], and examples of common applications include identification of cells[97], drug-cell interaction[98], and discrimination between healthy and unhealthy cells[99]. Recently, Raman spectroscopy is emerging as a powerful technique for characterizing the freezing responses of cells cryopreserved in

various cryoprotectants[80], defining morphology and size of ice crystals formed in different freezing solutions[70,85,100], as well as analyzing phase compositions of complex frozen samples[101,102]. In this dissertation, we will demonstrate the manner by which low-temperature Raman spectroscopy can be employed to analyze multicellular aggregates as well as single cells during freezing and to reveal the mechanisms of damage in cells and mechanisms of action of CPAs.

Chapter 3

Methods

3.1 Materials and equipment

Table 1 lists all materials described in the following methods section, along with associated abbreviations and manufacturer information. All products are from the United States unless otherwise indicated.

Table 1. Materials

Chapter(s)	Material	Details	Abbreviation	Manufacturer/ location
4	Accutase			Innovative Cell Technologies/ San Diego, CA
4	Camptothecin			AdipoGen Life Sciences/ San Diego, CA
4	Essential 8 medium		Essential 8, E8	ThermoFisher Scientific/ Waltham, MA
4	FAM-FLICA Poly Caspase Assay Kit			Immunochemistry Technologies/ Bloomington, MN
4	Hoechst 33342			Invitrogen - ThermoFisher Scientific/ Waltham, MA
4	Matrigel	hESC-qualified, LDEV-free		Corning/ Corning, NY
4	Rhodamine phalloidin	R415		Invitrogen - ThermoFisher Scientific/ Waltham, MA
4, 5	Via-Probe	7-aminoactinomycin D	7-AAD	BD Biosciences - BD/ East Rutherford, NJ
4, 5, 6	ReLeSR			STEMCELL Technologies/ Vancouver, Canada
4, 5, 6, 7	Acridine orange		AO	MilliporeSigma/ Burlington, MA

4, 5, 6, 7	Calcein AM	C1430		Invitrogen - ThermoFisher Scientific/ Waltham, MA
4, 5, 6, 7	Costar 6-well Clear TC-treated Multiple Well Plate		6-well plate	Corning/ Corning, NY
4, 5, 6, 7	Dimethyl sulfoxide		DMSO	ThermoFisher Scientific/ Waltham, MA or MilliporeSigma/ Burlington, MA
4, 5, 6, 7	Nunc CryoTubes			ThermoFisher Scientific/ Waltham, MA
4, 5, 6, 7	Propidium iodide		PI	MilliporeSigma/ Burlington, MA
4, 5, 6, 7	TeSR-E8 medium		TeSR-E8, E8	STEMCELL Technologies/ Vancouver, Canada
4, 6	Anti-Oct-4 antibody	MAB4401	OCT4	MilliporeSigma/ Burlington, MA
4, 6	BD Accuri C6 flow cytometer			BD Biosciences - BD/ East Rutherford, NJ
4, 6, 7	Alexa Fluor 488-conjugated donkey anti-mouse IgG	A-21202		Invitrogen - ThermoFisher Scientific/ Waltham, MA
4, 6, 7	Alexa Fluor 555-conjugated donkey anti-goat IgG	A-21432		Invitrogen - ThermoFisher Scientific/ Waltham, MA
4, 6, 7	Bovine serum albumin	Prometheus Protein Biology Products, 25-529		Genesee Scientific/ San Diego, CA
4, 6, 7	DAPI			ThermoFisher Scientific/ Waltham, MA
4, 6, 7	MycoAlert PLUS detection kit	LT07-701		Lonza/ Walkersville, MD

4, 6, 7	Paraformaldehyde			ThermoFisher Scientific/ Waltham, MA
4, 6, 7	Triton X-100	X100-100mL		MilliporeSigma/ Burlington, MA
4, 6, 7	Tween-20	P7949-100mL		MilliporeSigma/ Burlington, MA
4, 7	Accumax			Innovative Cell Technologies/ San Diego, CA
5	Fetal bovine serum	Qualified	FBS	Gibco - ThermoFisher Scientific/ Waltham, MA
5	FTA Sample Collection Kit			ATCC/ Manassas, VA
5	High-glucose RPMI-1640	30-2001	RPMI	ATCC/ Manassas, VA
5	Human anti-CD3	PE-Cy7		BioLegend/ San Diego, CA
5	Jurkat cells	Clone E6-1	Jurkat	ATCC/ Manassas, VA
5	Vybrant FAM Poly Caspases Assay Kit			Invitrogen - ThermoFisher Scientific/ Waltham, MA
5, 6	Aluminum pan	hermetically sealed lid		DSC Consumables/ Austin, MN
5, 6	Normosol-R			Hospira/ Lake Forest, IL
5, 6, 7	Corning 96-well Flat Clear Bottom Black Polystyrene TC-treated Microplate		96-well plate	Corning/ Corning, NY
5, 6, 7	Glycerol	USP grade	G, Gly	Humco/ Texarkana, TX
5, 6, 7	Hank's Balanced Saline Solution with Ca2+, Mg2+ and glucose		HBSS	Lonza/ Walkersville, MD
5, 6, 7	Human serum albumin	Albutein	A, HSA	Grifols/ Los Angeles, CA
5, 6, 7	L-isoleucine	ACS reagent or	I, isoleucine	MilliporeSigma/ Burlington,

		PharmaGrade		MA
5, 6, 7	MEM non-essential amino acids	100x	NEAA	MilliporeSigma/ Burlington, MA
5, 6, 7	Poloxamer 188	USP grade	P, P188	Spectrum Chemical/ Gardena, CA
5, 6, 7	Sodium bicarbonate		HCO_3^-	MilliporeSigma/ Burlington, MA
5, 6, 7	Sucrose	ACS reagent or PharmaGrade	S	MilliporeSigma/ Burlington, MA
5, 6, 7	Vitronectin	recombinant human	VTN	Peprotech/ Cranbury, NJ
6	BAMBanker hRM Cell Freezing Media		B.hRM	LYMPHOTEC Inc./ Japan
6	HAND1 monoclonal antibody (OTI1G10)	MA5-25494	HAND1	Invitrogen - ThermoFisher Scientific/ Waltham, MA
6	Human Brachyury antibody	MAB20851	Brachyury	R&D Systems - Bio-Techne/ Minneapolis, MN
6	Human HNF-3 beta /FoxA2 antibody	AF2400	FOXA2	R&D Systems - Bio-Techne/ Minneapolis, MN
6	Human Nanog antibody	AF1997	NANOG	R&D Systems - Bio-Techne/ Minneapolis, MN
6	Human SOX17 antibody	AF1924	SOX17	R&D Systems - Bio-Techne/ Minneapolis, MN
6	Pax6 antibody		PAX6	DSHB
6	STEMdiff trilineage differentiation kit			STEMCELL Technologies/ Vancouver, Canada
6	Trehalose	ACS reagent or PharmaGrade	T	MilliporeSigma/ Burlington, MA

6	Type T thermocouple	FEP insulation and jacket		McMaster-Carr/ Elmhurst, IL
6	Anti-human Nestin antibody	60091		STEMCELL Technologies/ Vancouver, Canada
6, 7	Alexa Fluor 647 donkey anti-rabbit IgG	A-31573		Invitrogen - ThermoFisher Scientific/ Waltham, MA
6, 7	Cryostor 10 Cell Freezing Medium		CS10	BioLife Solutions/ Bothell, WA
6, 7	mFreSR Cryopreservation Medium		mFreSR	STEMCELL Technologies/ Vancouver, Canada
6, 7	Versene			ThermoFisher Scientific/ Waltham, MA
7	Anti-SOX9 antibody	AB5535	SOX9	MilliporeSigma/ Burlington, MA
7	Anti-Tubulin antibody	MAB1637	TUJ1	MilliporeSigma/ Burlington, MA
7	Calbryte 520 AM	20651		AAT Bioquest/ Sunnyvale, CA
7	Costar 6-well Clear TC-treated Multiple Well Plate		12-well plate	Corning/ Corning, NY
7	DMEM/F12 media		DMEM/F12	Gibco - ThermoFisher Scientific/ Waltham, MA
7	Human SOX10 antibody	AF2864	SOX10	R&D Systems - Bio-Techne/ Minneapolis, MN
7	Membrane Fluidity Kit	ab189819		Abcam/ Cambridge, United Kingdom
7	Potassium chloride	P5405	KCl	MilliporeSigma/ Burlington, MA
7	PowerLoad Concentrate	P10020		ThermoFisher Scientific/ Waltham, MA
7	Rabbit polyclonal	NB300137	PRPN	Novus Biologicals/ Littleton,

	anti-Peripherin antibody			CO
7	Senso-DM	7007		Anatomic Incorporated/ Minneapolis, MN
7	Senso-MM	7008		Anatomic Incorporated/ Minneapolis, MN
7	Tetrodotoxin	00061	TTX	Biotium/ Fremont, CA
7	Veratridine	2918		Tocris - Bio-Techne/ Minneapolis, MN

Table 2 lists all equipment described in the following methods section, along with manufacturer information and physical location where the equipment was used. All products are from the United States unless otherwise indicated.

Table 2. Equipment

Chapter(s)	**Equipment**	**Details**	**Location used**	**Manufacturer/ location**
4, 5, 6	Microplate reader	Synergy HT	Bischof Lab	BioTek/ Winooski, VT
4, 5, 6, 7	100x air objective	NA 0.90	CharFac	Nikon Instruments, Melville, NY
4, 5, 6, 7	37˚C water bath		Hubel Lab	
4, 5, 6, 7	Controlled-rate freezer	Kryo 560-16	Hubel Lab	Planer/ Middlesex, United Kingdom
4, 5, 6, 7	Cryogun		Hubel Lab	Brymill/ Ellington, CT
4, 5, 6, 7	CryoPod Carrier		Hubel Lab	BioCision - Brooks Life Sciences/ Chelmsford, MA
4, 5, 6, 7	Four-stage Peltier	TEC4-97-49-17-7-05	Hubel Lab	Thermonamic/ Nanchang, Jiangxi, China
4, 5, 6, 7	Hemocytometer	Bright-Line	Hubel Lab	Hausser Scientific/ Horsham, PA
4, 5, 6, 7	Optical power meter		Hubel Lab	Thorlabs/ Newton, NJ
4, 5, 6, 7	Series 800 temperature controller		Hubel Lab	Alpha Omega Instruments/ Houston, TX

4, 5, 6, 7	ThawSTAR		Hubel Lab	BioCision - Brooks Life Sciences/ Chelmsford, MA
4, 5, 6, 7	WITec Confocal Raman Microscope	Alpha 300R	CharFac	WITec/ Ulm, Germany
5	BD FACSCanto Clinical Flow Cytometry System		UFCR	BD Biosciences - BD/ East Rutherford, NJ
5	OSMETTE osmometer		Hubel Lab	Precisions Systems/ Natick, MA
5, 6	Aluminum pan		Hubel Lab	DSC Consumables/ Austin, MN
5, 6	TA Differential Scanning Calorimeter Q1000		CEMS Polymer Characterization Facility	TA Instruments/ New Castle, DE
6	-80˚C mechanical freezer		Hubel Lab	So-Low Environmental/ Cincinnati, OH
6	CoolCell		Hubel Lab	BioCision - Brooks Life Sciences/ Chelmsford, MA
6	DI-245 USB Thermocouple Data Acquisition system		Hubel Lab	DATAQ Instruments/ Akron, Ohio
6	pH meter	Φ 300 Series	Hubel Lab	Beckman Coulter/ Brea, CA
6, 7	10x air objective	NA 0.25	Dutton Lab	Leica Microsystems/ Buffalo Grove, IL
6, 7	Cytation 1 cell imaging multi-mode reader		Dutton Lab	BioTek/ Winooski, VT
6, 7	DFC365FX camera		Dutton Lab	Leica Microsystems/ Buffalo Grove, IL
6, 7	Leica DMI6000B microscope		Dutton Lab	Leica Microsystems/ Buffalo Grove, IL
6, 7	Microplate reader	Synergy HTX	Hubel Lab	BioTek/ Winooski, VT

Table 3 lists all software described in the following methods section, along with

developer information and physical location where the software was used. All products are from the United States unless otherwise indicated.

Table 3. Software

Chapter(s)	Software	Details	Location used	Developer/ location
4, 5, 6, 7	Gen5 Software		Dutton Lab	BioTek/ Winooski, VT
4, 5, 6, 7	WITec Control		CharFac	WITec/ Ulm, Germany
4, 5, 6, 7	WITec Project FOUR		Hubel Lab	WITec/ Ulm, Germany
4, 6, 7	FIJI	versions 2.0.0 through 2.1.0	Hubel Lab	National Institutes of Health/ Bethesda, MD
5, 6	TA Universal Analysis Software		Hubel Lab	TA Instruments/ New Castle, DE
6, 7	MATLAB	versions 2015b through 2020b	Hubel Lab	MathWorks/ Natick, MA
7	GeoDa		Hubel Lab	University of Chicago/ Chicago, IL

3.2 Cell culture

3.2.1 Induced pluripotent stem cell culture

Two human induced pluripotent stem cell (hiPSC) lines, respectively DF-19-9-11[1] and UMN PCBC16iPS[103], were used in different projects of this dissertation. The cells were cultured as 2D adherent colonies on Matrigel (hESC-qualified, LDEV-free, Corning) or recombinant human vitronectin (Peprotech) in TeSR-E8 medium (STEMCELL Technologies) or Essential 8 medium (ThermoFisher Scientific) in a 37 ˚C incubator at 5% CO_2. Cultures were kept below 75% confluence. Cells were passaged every 4 days as multicellular aggregates using enzyme-free dissociation reagent ReLeSR (STEMCELL Technologies) or Versene (ThermoFisher Scientific) at a split ratio of 1:16. Cultures were

routinely tested for mycoplasma using the MycoAlert PLUS detection kit (Lonza, LT07-701) and karyotyped using G-banding at a 400-band resolution.

3.2.2 Jurkat cell culture

Jurkat cells (ATCC, TIB-1522) were cultured in high-glucose RPMI-1640 (Gibco) supplemented with 10% fetal bovine serum (Qualified, Gibco). The cell concentration was maintained between 1×10^5 and 3×10^6 cells/ml. The passage number was maintained between 8 and 25. Cell line identification was done by Short Tandem Repeat (STR) through ATCC using the FTA Sample Collection Kit (ATCC).

3.2.3 Sensory neuron differentiation

hiPSCs were differentiated into sensory neurons using a commercially available kit (Senso-DM, Anatomic Incorporated, 7007) and further matured (Senso-MM, Anatomic Incorporated, 7008) per the manufacturer's instructions. Briefly, hiPSCs were passaged as 3 to 10-cell aggregates using Versene at a split ratio of 1:20 onto Matrix 1. 24 hours later, cultures were exposed to the first of a series of Senso-DM formulations, with subsequent formulations applied daily for one week total. The differentiated cells were dissociated and replated onto Matrix 3 and allowed to mature in Senso-MM media for another 7 days with half media exchange every two days. Three different stages of neuronal cells were selected for this investigation on the cryobiological change along this hiPSC-derived lineage. They were respectively the intermediate SOX9-, SOX10-positive, TUJ1-negative neural crest cells obtained on day 5 of this protocol, the fully

differentiated but immature TUJ1-, PRPH-positive sensory neurons obtained on day 7, and the electrophysiologically active and more mature sensory neurons.

3.3 Immunocytochemistry

The immunocytochemistry methods described below share the same procedures of fixation, permeabilization, blocking, primary and secondary antibody staining. Cultures were fixed in 3.7% paraformaldehyde (Fisher Scientific) for 10 minutes, permeabilized in 0.2% Triton X-100 (MilliporeSigma, X100-100mL) for 10 minutes, and incubated overnight at 4 ˚C with primary antibodies diluted in a blocking buffer containing 1% bovine serum albumin (Prometheus Protein Biology Products, 25-529) and 0.1% Tween-20 (MilliporeSigma, P7949-100mL). The cultures were subsequently washed twice with the blocking buffer and incubated for 2 hours with secondary antibodies. DAPI (1:1000, ThermoFisher Scientific) or Hoechst 33342 (1:1000, Invitrogen) was added for 30 minutes before washing twice in DPBS. Negative controls included unstained cultures and positively stained cultures known not to express the antigens of interest. Stained cultures were imaged using a Leica DMI6000B microscope and a DFC365FX camera.

3.3.1 Phenotyping of fresh and cryopreserved hiPSCs

Co-expression of two transcription factors were used to characterize hiPSC cultures for their pluripotency, whether fresh or cryopreserved and thawed. Primary antibodies used include OCT4 (1:250, Millipore, MAB4401) and NANOG (1:100, R&D Systems, AF1997). Secondary antibodies used include Alexa Fluor 488-conjugated donkey anti-

mouse IgG (1:1000, Invitrogen A-21202) and Alexa Fluor 555-conjugated donkey anti-goat IgG (1:1000, Invitrogen, A-21432). Quantification of the total population stained with DAPI and of population proportion co-expressing OCT4 and NANOG was performed using FIJI via automatic binary thresholding and boundary recognition.

3.3.2 Actin filament staining of fresh and cryopreserved hiPSCs

Spatial distribution of f-actin filaments were used to characterize the cytoskeletal health versus damage of hiPSC cultures, whether fresh or cryopreserved and thawed. TRITC-conjugated primary antibody, rhodamine phalloidin (1:1000, R415, Invitrogen). In addition, Hoechst 33342 was used in place of DAPI to counterstain the cultures and detect chromatin condensation.

3.3.3 Phenotyping of fresh and cryopreserved neural crest cells

Co-expression of two neural crest transcription factors and absence of a terminal neuron marker were used to characterize neural crest cells for their progenitor state in the developmental path, whether fresh or cryopreserved and thawed. Primary antibodies used included SOX9 (1:1000, MilliporeSigma, AB5535), SOX10 (1:100, R&D Systems, AF2864), and TUJ1 (1:500, MilliporeSigma, MAB1637). Secondary antibodies used included Alexa Fluor 488-conjugated donkey anti-mouse IgG (1:1000, Invitrogen A-21202), Alexa Fluor 555-conjugated donkey anti-goat IgG (1:1000, Invitrogen, A-21432), and Alexa Fluor 647 donkey anti-rabbit IgG (1:1000, Invitrogen, A-31573). Quantification of the total population stained with DAPI and of population proportion co-

expressing SOX9 and SOX10 but not TUJ1 was performed using FIJI via automatic binary thresholding and boundary recognition.

3.3.4 Phenotyping of fresh and cryopreserved sensory neurons

Co-expression of a neuron-specific marker and a peripheral nervous system marker were used to characterize sensory neurons for their terminally differentiated state in the developmental path, whether fresh or cryopreserved and thawed. Primary antibodies used included TUJ1 (1:500, MilliporeSigma, MAB1637) and PRPH (1:1000, Novus Biologicals, NB300137). Secondary antibodies used included Alexa Fluor 488 donkey anti-mouse (1:1000, Invitrogen A-21202), Alexa Fluor 647 donkey anti-rabbit (1:1000, Invitrogen, A-31573). Quantification of the total population stained with DAPI was performed using FIJI via automatic binary thresholding and particle analysis.
Visual confirmation was used to threshold positively co-stained cells from negatively stained cells and quantify the population proportion co-expressing TUJ1 and PRPH.

3.3.5 Calcium imaging of electrophysiological active sensory neurons

Electrophysiologically active sensory neurons were obtained by treating day-7 sensory neurons, either freshly differentiated or cryopreserved and thawed, in the maturation media for another 7 days. Live cultures were loaded with 2.5 μM Calbryte 520 AM (AAT Bioquest, 20651) and PowerLoad Concentrate (1:100, ThermoFisher, P10020) for 1 hour before imaging. Fluorescent videos of the stained cultures were acquired using a Leica DMI6000B microscope, a DFC365FX camera, and a 10x air objective (NA 0.25, Leica

Microsystems) for a duration of 185 seconds at 4 frames per second. Varying drug solutions were added to the cultures within the first 10 seconds of each video. The drugs included veratridine (Tocris, 2918) at a final concentration of 1 μM containing 0.1% DMSO in DPBS, 30 mM potassium chloride (KCl, Millipore Sigma, P5405) containing 0.1% DMSO, 0.1% DMSO as negative control, and 1 μM tetrodotoxin (TTX, Biotium, 00061) intended to block voltage-gated sodium channels.

The image analysis was automated using FIJI (see Appendix 1 for the FIJI macro). Specifically, individual somata were detected by local maxima-based image segmentation and binary threshold. Mean intensity was measured over time inside each soma. The intensity profiles were graphed, in terms of $\Delta F/F_0$, where ΔF is the intensity differential compared to background fluorescence (F_0) of the given sample, and responding cells quantified using MATLAB (see Appendix 2 for the MATLAB script). Responders were mathematically defined by the maximum of the first derivative of its fluorescent intensity over time above a constant threshold that was determined by that of the background fluorescence over time.

3.4 Cryoprotective agent formulation

DMSO-free (or non-DMSO) cryoprotective agents (CPA) in this dissertation included sucrose (Sigma-Aldrich), trehalose (Sigma-Aldrich), glycerol (Humco), L-isoleucine (Sigma-Aldrich), human serum albumin (Albutein, Grifols), and poloxamer 188 (P188, Spectrum Chemical). Additives included MEM non-essential amino acids (NEAA,

Sigma-Aldrich) and sodium bicarbonate (Sigma-Aldrich). Basal buffers included phosphate-buffered saline with Ca^{2+}, Mg^{2+} (PBS++), Hank's Balanced Saline Solution with Ca^{2+}, Mg^{2+} and glucose (HBSS, Lonza), and Normosol-R (Hospira). The final working concentrations of the DMSO-free CPA molecules were varied to optimize the effectiveness of the CPA formulation. DMSO (Sigma-Aldrich) was used as the control CPA at a concentration between 7.5% and 10%, and either Normosol-R or HBSS were used as its basal buffer. The DMSO-free compositions discussed in this dissertation are covered by issued Patent #10,314,302 and patent application #16/383,165, owned by Regents of the University of Minnesota. Each of the multicomponent aqueous solutions was prepared by mixing the respective solid and liquid components directly using a vortex mixer or a magnetic stirrer at room temperature until a clear liquid was formed.

Natural deep eutectic system (NADES) versions of some of the DMSO-free solutions were prepared by firstly mixing trehalose and glycerol at a molar ratio of 1:30 to form NADES using a magnetic stir rod in a water bath at 70 ˚C on top of a magnetic stirring hot plate until a clear viscous liquid was formed. To obtain dilute NADES-based CPA solutions, NADES were subsequently diluted in Normosol-R and supplemented with isoleucine at varying concentrations.

Several commercially available products of CPA solution were used in a subsequent benchmark experiment. These ready-made CPA formulations included BAMBanker hRM Cell Freezing Media (B.hRM, LYMPHOTEC Inc.), Cryostor 10 Cell Freezing

Medium (CS10, BioLife Solutions), and mFreSR Cryopreservation Medium for PSCs (mFreSR, STEMCELL Technologies). No modifications or dilutions were made.

3.5 Pre-freeze cell preparation

3.5.1 Preparing hiPSCs for freezing

hiPSCs were cultured to a 65-75% confluence on the day of freezing. Freezing studies were performed using small aggregates (3-50 cells). After dissociation, the cell aggregates were collected using the basal buffer. The aggregate size was controlled by the timing of dissociation and the amount of gentle pipetting. The freezing solutions were prepared at twice the final working concentration (2x) and added dropwise to the suspension of aggregates at a 1:1 ratio. The mixture was incubated at room temperature for 30 min to 1 h before freezing to allow sufficient internalization of cell-penetrating CPAs.

For the benchmark study with commercial ready-made solutions, dissociated hiPSC aggregates were directly resuspended in the respective solution following the manufacturer's instructions. In the case of B.hRM, pre-freeze incubation was not recommended and, therefore, omitted in the cell preparation procedures.

3.5.2 Preparing Jurkat cells for freezing

Cells were cultured to 3×10^6 cells/ml on the day of cryopreservation. After centrifugation, cells were resuspended in Normosol-R to 1.2×10^7 cells/ml. The CPA

solutions were prepared at twice (2x) the final working concentration and added stepwise to the cell suspension at 1:1 volume ratio, so that the cell freezing concentration was 6×10^6 cells/ml. The mixture was incubated at room temperature for 1 h before freezing to allow sufficient internalization of cell-penetrating CPAs.

3.5.3 Preparing neural crest cells and sensory neurons for freezing

Neural crest cells fully differentiated but immature sensory neurons, and mature, electrophysiologically active sensory neurons were dissociated with Accumax (Innovative Cell Technologies) for 10, 45 or 90 minutes respectively at room temperature on day 5, 7 or 14 of the hiPSC-to-sensory neuron differentiation protocol. Accumax was inactivated using 37 ˚C DMEM/F12 media (Gibco). The dissociated cells were centrifuged and resuspended in a basal buffer containing P188. A twice concentrated (2x) CPA solution optimized for hiPSC cryopreservation was added at equal volume. The mixture was incubated at room temperature for 1 hour before freezing to allow sufficient internalization of cell-penetrating CPAs.

For the benchmark study with CS10, dissociated neural crest cells and sensory neurons were resuspended respectively in CS10 without dilution following the manufacturer's instructions. Pre-freeze incubation of varying duration between 0 and 1 h was tested to assess the cytotoxicity of this DMSO-based solution on the neuronal cells.

3.6 Freezing and thawing

3.6.1 Controlled rate freezing

Cell suspensions of interest were dispensed in cryogenic vials (Nunc CryoTubes, ThermoFisher Scientific) at 1 ml per vial. Vials of cells were frozen using either controlled rate freezing or passive freezing. For controlled rate freezing, cells were frozen in a controlled-rate freezer (Kryo 10 or Kryo 560-16, Planer) following the steps listed below.

1. Starting temperature 20 ˚C;
2. -10 ˚C/min to intended nucleation temperature (T_{NUC});
3. Hold at T_{NUC} for 15 minutes to equilibrate sample and chamber temperatures;
4. Induce ice nucleation manually by briefly spraying liquid nitrogen onto vials using a Cryogun (Brymill) for accurate control of the nucleation temperature;
5. B ˚C/min (cooling rate) to -60 ˚C;
6. -10 ˚C/min to -100 ˚C.

Alternatively, manual induction of ice nucleation as shown in step 4 above can be replaced by automated induction of ice nucleation using the following steps.

a) -50 ˚C/min to -45 ˚C;
b) +15 ˚C/min to -12.4 ˚C;
c) +2.16 ˚C/min to -7.4 ˚C.

Sample temperature was logged using the built-in thermocouple of the controlled-rate freezer, which was inserted via a bored, fitted cap into a “dummy” vial replicating the content of the experimental samples. After freezing was complete, the vials were transferred in a CryoPod Carrier (BioCision) and stored in the liquid phase of liquid

nitrogen (LN2).

3.6.2 Passive freezing

For passive freezing, cells were frozen in an insulated freezing container CoolCell (Biocision) inside a -80 ˚C mechanical freezer. In the case of BAMBanker hRM Cell Freezing Media, vials of cells were placed on a non-insulative tube rack and directly exposed to the air inside the -80 ˚C freezer. Cells were kept in the -80 ˚C freezer for a duration between 4 and 24 hours. Sample temperature was logged using a DI-245 USB Thermocouple Data Acquisition system (DATAQ) and a type T thermocouple that was inserted via a holed, fitted cap into a "dummy" vial containing a replicate sample. After freezing was complete, vials were transferred in the CryoPod Carrier and stored in the liquid phase of LN2.

3.6.3 Thawing

Frozen vials of cells were thawed in a 37 ˚C water bath for exactly 2 min 30 s using a continuous, swirling motion. Alternatively, an automated thawing device (ThawSTAR, Biocision) was used following the manufacturer's instructions. Thawed cells were immediately used for downstream experiments as follows.

3.7 Post-thaw cell counting

3.7.1 Dissociating cell aggregates for cell counting

For hiPSC frozen and thawed in the form of multicellular aggregates, one replica of each

sample was sacrificed for post-thaw cell counting. Cells were singularized by mixing the cell suspension and Accumax at 1:1 volume ratio and incubating for 10 minutes at room temperature. Single cell suspension was ensured by gentle pipetting.

3.7.2 Counting single cells using hemocytometer

Dissociated cells were stained for viability based on membrane integrity by mixing the single cell suspension 1:1 with a solution containing 20 mM acridine orange (Sigma-Aldrich) and 10 µg/ml propidium iodide (Sigma-Aldrich) in PBS (AO/PI). Live cells (stained green by AO) and dead cells (stained red by PI) were counted using a hemocytometer (Hausser Scientific) and a Zeiss Axioskop 50 fluorescent microscope.

3.7.3 Calculating post-thaw viability and post-thaw recovery

Post-thaw viability was calculated by the ratio of live cell count and total cell count after thawing.

$$\text{post-thaw viability} = \frac{\text{post-thaw live cell count}}{\text{post-thaw live cell count} + \text{post-thaw dead cell count}} \times 100\%$$

Post-thaw recovery required cell counting prior to cryopreservation by preparing a fresh cell control per experiment representative of the sample cell population before CPA introduction and cryopreservation. Live cell counts in the fresh cell samples were obtained using AO/PI and hemocytometer as described above. Post-thaw recovery was calculated by the ratio of live cell count after thawing and live cell count before freezing.

$$\text{post-thaw recovery} = \frac{\text{post-thaw live cell count}}{\text{pre-freeze live cell count}} \times 100\%$$

3.7.4 High-throughput quantification of live cells using microplate reader

Alternative to manual, direct cell counting, the following procedure was used to quantify post-thaw recovery at higher throughput. Pre-warmed cell growth media was added dropwise to the thawed cell suspension at 1:6 dilution ratio. After gentle mixing and centrifugation, cells were resuspended in 1 ml pre-warmed phenol red-free media per sample and distributed at 50 µl/well using multi-channel pipettes and reservoirs into a 96-well clear-bottom black microplate (Corning). Cells were then stained for viability (i.e., esterase activity) by adding 50 µl/well of calcein AM (1:1000, Invitrogen) and incubating for 30 min at 37 ˚C. Fluorescence intensity of the stained cells was measured using a BioTek Synergy HT or HTX microplate reader using a 485/20 nm excitation filter, a 528/20 nm emission filter and the top probes with sensitivity of 35. The fluorescence measurement (y) of each well was correlated to a cell count (x) via a pre-established control curve. Fresh Jurkat cells were resuspended in media and distributed into a 96-well plate at varying concentrations via serial dilution to establish the correlation between live cell count per well and fluorescence measurement.

$$y = 0.0831x^2 + 193.35x \ (R^2 = 0.999)$$

The calculated live cell count of thawed cell samples was divided by anticipated fresh live cell count equivalent to the cell freezing concentration of 6×10^6 cells/ml to produce the post-thaw cell recovery rate.

3.8 Post-thaw cell reattachment

For the adherent cells of interest, including hiPSCs, neural crest cells, and sensory neurons, post-thaw cell reattachment was used to quantify the integrity of cell adhesion, a fundamental cell function of the cryopreserved cells.

3.8.1 Reattachment of cryopreserved hiPSCs

After thawing, TeSR-E8 or Essential 8 was added dropwise to the cell suspension at 1:6 dilution ratio and gently mixed to obtain a homogenous suspension of hiPSC aggregates. The cells were then seeded onto a freshly coated 6-well plate and cultured undisturbed for 24 hours. Subsequently, the post-thaw culture and the post-passage control culture were washed with PBS++ and stained for esterase activity using calcein AM. Fluorescence intensity of the stained cells were measured using a Synergy HT or HTX microplate reader with an ex/em 485/528 nm filter set. Post-thaw reattachment was calculated by the ratio of fluorescence measurement of cryopreserved sample to that of the control. In some experiments, in place of a fresh cell control, cells cryopreserved in 7.5% DMSO and seeded into post-thaw culture at 1:6 split ratio was used as the denominator in the calculation of post-thaw reattachment.

3.8.2 Reattachment of cryopreserved neural crest cells and sensory neurons

After thawing, pre-warmed DMEM/F12 was added dropwise to the cell suspension at 1:10 dilution ratio and gently mixed to remove cell-penetrating CPA molecules from the cytoplasm. The cells were then centrifuged, resuspended in the respective cell growth media, seeded onto a freshly coated 12-well plate, and cultured undisturbed for 24 hours.

Subsequently, the post-thaw culture and the post-passage control culture were washed with PBS++ and stained for esterase activity using calcein AM. Fluorescence intensity of the stained cells were measured using a Synergy HT or HTX microplate reader with an ex/em 485/528 nm filter set. Post-thaw reattachment was calculated by the ratio of fluorescence measurement of cryopreserved sample to that of the control.

3.9 Post-thaw cell growth

3.9.1 Growth of post-thaw Jurkat cell culture

After thawing, pre-warmed Jurkat cell growth media (10% FBS in high-glucose RPMI-1640) was added dropwise to the thawed cell suspension at 1:6 dilution ratio. After gentle mixing and centrifugation, Jurkat cells were resuspended in the growth media and seeded into post-thaw culture at 5×10^5 cells/ml. At 0, 24, 48, 72 h post-thaw, the cultures were each sampled to measure the live cell count based on membrane integrity using AO/PI and a hemocytometer.

3.9.2 Growth of post-thaw hiPSC culture

After thawing, suspension of hiPSC aggregates was diluted using TeSR-E8 at a 1:6 split ratio as described above. Fresh hiPSC aggregates of equivalent quantity were passaged at the same split ratio as the control. Growth in the cultures were monitored label-free by imaging daily using a Cytation 1 cell imaging multi-mode reader (BioTek) with a 4x objective (NA 0.13, Olympus) in the bright-field and scan mode using default focusing method. Images were automatically analyzed by the Gen5 Software (BioTek) using

boundary recognition and thresholding to measure the confluence. Confluence was sampled at 24-, 48-, 72-, and 96-hour post-thaw or post-passage respectively.

3.10 Post-thaw cell apoptosis

3.10.1 Apoptosis assay of Jurkat cells

Apoptosis of cryopreserved Jurkat cells was assessed immediately post-thaw. Cells were thawed as described above and then stained for poly caspase activation following the manufacturer's instructions (Vybrant FAM Poly Caspases Assay Kit, Invitrogen). In brief, cells were incubated with the FLICA reagent in the dark for 60 minutes at 37 ˚C and 5% CO_2. They were then washed twice with the apoptosis wash buffer, stained for CD3 (Human Anti-CD3, PE-Cy7, BioLegend), and incubated in the dark at room temperature for 15 minutes. After a final wash step, cells were stained with a membrane integrity-based viability dye for 10 minutes (Via-Probe, 7-AAD, BD Biosciences). Samples were analyzed using a BD FACSCanto (BD Biosciences).

Proportions of viable, early and late apoptotic, and necrotic Jurkat cells were determined. Viable, healthy cells stained negative for both caspases and 7-AAD. Necrotic cells stained negative for caspases but positive for 7-AAD. Cells in early apoptosis stained positive for caspases but negative for 7-AAD, while cells in late apoptosis stained positive for both caspases and 7-AAD.

The gating strategy identified Jurkat cells using forward scattering channel (FSC) and

side scattering channel (SSC) to eliminate debris. A gate was applied to FSC-W and FSC-H to select only single cells. CD3+ cells were identified from this plot and gated using isotype control (BioLegend) to select only CD3+ cells. FLICA was plotted against 7-AAD to divide CD3+ cells into viable, necrotic, early apoptotic, and late apoptotic sub-populations.

3.10.2 Apoptosis assay of hiPSCs

Apoptosis of cryopreserved hiPSCs was assessed immediately post-thaw. hiPSCs freshly dissociated from culture were served as control. Cell aggregates were singularized using Accumax as described above and stained for poly caspase activation using FLICA FAM-VAD-FMK antibody (Immunochemistry Technologies) and for loss of membrane integrity using 7-AAD, that were resulted from either cryopreservation or cell dissociation. Apoptosis was actively induced using camptothecin (Adipogen) and cell death was induced by incubating cells at 60 ˚C for 15 minutes and 4 ˚C for 5 minutes to serve as gating controls. Samples were analyzed using BD Accuri C6 flow cytometer (BD Biosciences). Early apoptotic cells were defined as positive for FLICA and negative for 7-AAD staining, late apoptotic cells as positive for both FLICA and 7-AAD, necrotic cells as negative for FLICA and positive for 7-AAD, and live cells as negative for both FLICA and 7-AAD.

3.11 Post-thaw cell function

3.11.1 Trilineage differentiation of cryopreserved hiPSCs

On day 4 after seeding, the post-thaw hiPSC culture was differentiated into cells representing all three germ layers using a STEMdiff trilineage differentiation kit (STEMCELL Technologies) over 7 days. The endodermal cells were detected with anti-FOXA2 and anti-SOX17 antibodies (R&D Systems), the mesoderm with anti-Brachyury (T, R&D Systems) and anti-HAND1 (Invitrogen) antibodies, the ectoderm with anti-PAX6 (DSHB) and anti-NESTIN (STEMCELL Technologies) antibodies, and all counterstained with DAPI. Fluorescent secondary antibodies (Invitrogen) were utilized to detect primary antibody binding and imaged using the Cytation 1 cell imaging multi-mode reader with a 20x objective (NA 0.45, Olympus).

3.11.2 Continued differentiation of cryopreserved neural crest cells

24 hours after seeding, the post-thaw culture of day-5 neural crest cells was treated sequentially with the day-6 and day-7 Senso-DM sensory neuron induction media for 24 hours each. Immunocytochemistry was subsequently performed to measure the cell population proportion co-expressing TUJ1 and PRPH, and cell morphology was assessed to observe neurite outgrowth. Fresh neural crest cells were passaged and treated in a similar fashion as control.

3.11.3 Maturation of cryopreserved sensory neurons

24 hours after seeding, the post-thaw culture of day-7 sensory neurons was treated with the Senso-MM sensory neuron maturation media for 7 days. Electrophysiological response to the aforementioned drug molecules (i.e., DMSO, KCl, veratridine, TTX) was

measured using calcium imaging, and the responder proportion and response waveform were evaluated in comparison to the day-14 sensory neurons prepared from fresh day-7 cells.

3.12 Differential evolution algorithm

A DE algorithm with the basic mutation strategy (DE/rand/1/bin)[104–106] was used to rapidly optimize the composition of the DMSO-free CPA solution for hiPSCs based on the functional metric of post-thaw reattachment. Briefly, the DE algorithm utilizes stochastic direct search to randomly generate an initial group (Generation 0) of sample parameters (i.e., concentrations of DMSO-free CPA molecules) from the population spanning the entire parameter space. Generation 0 samples were tested experimentally, and their post-thaw reattachment rates were used by the algorithm to output the next group (Generation 1) of CPA concentrations that were mutated versions of Generation 0 to be tested. Cumulatively the best members after each generation were stored as an emergent population. The algorithm-driven optimization was completed, and convergence was achieved when the emergent population of the latest generation was the same as that of the previous generation. Parameter space of the DE algorithm was determined by the cytotoxicity limit and was discretized into 5 intervals between 20 mM and 120 mM for sucrose, 2.5% v./v. and 5% v./v. for glycerol, 0 mM and 37.5 mM for isoleucine, and 0% and 2.5% for albumin. Cytotoxicity was defined as decrease in cell reattachment in the hiPSC culture measured using calcein AM 24 hours after 1-hour exposure to the respective molecules compared to fresh cell control.

3.13 Raman spectroscopy

3.13.1 Instrumental configuration

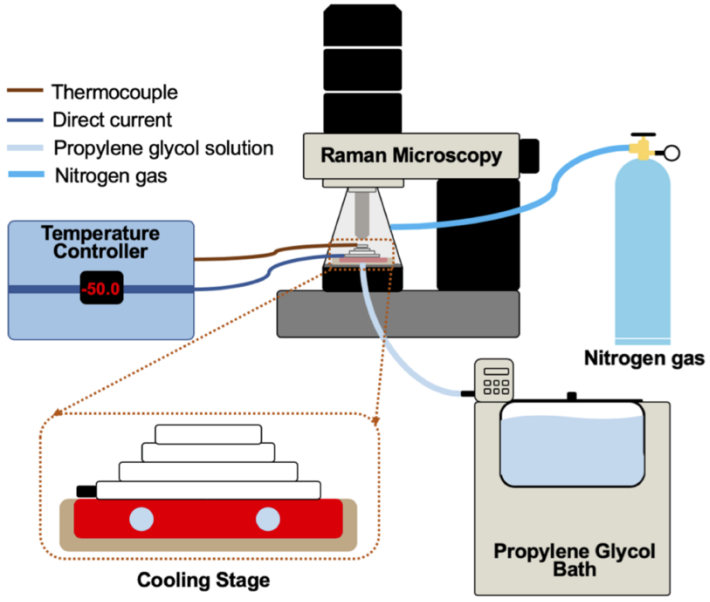

Figure 1. Sketch of the instrumental setup of low-temperature Raman spectroscopy with a zoomed-in view of the cooling stage.

As illustrated in Figure 1, a Peltier stage (Thermonamic Electronics) and a series 800 temperature controller (Alpha Omega Instruments) were used to freeze samples of cells of interest in the CPA solution of interest or samples of the CPA solution alone for low-temperature confocal Raman microscopy[107]. Cooling rate of -1, -3, -5 or -10 ˚C/min was used for cells and -10 ˚C/min for solution alone, and ice nucleation was induced at -4 or -8 ˚C by briefly touching a LN2-chilled needle, unless otherwise noted. Final temperature was stabilized at -50 ˚C, where Raman data were collected. Raman spectroscopic measurements were made using the WITec Confocal Raman Microscope Alpha 300R

with UHTS spectrometer and DV401 CCD detector with 600/mm grating. A 532 nm Nd:YAG laser was used as the excitation source. A 100x air objective (NA 0.90, Nikon Instruments) was used to focus the laser. Laser power at the objective was measured at 10 mW using an optical power meter (Thorlabs). Spatial resolution of the microscope was measured by WITec (unpublished) at 305 nm in lateral direction and 790 nm axial. More details can be found in the published protocol[108].

3.13.2 Data acquisition and rendering

Full spectra at a given point of interest was acquired using the Single Spectrum mode on the WITec Control software, with an integration time of 0.5 s and denoised by averaging over 100 collections. Hyperspectral data within a given region of interest was acquired using the Image Scan mode, with the scan dimensions defined by a resolution of 333 nm/pixel and an integration time of 0.2 s used to scan each pixel. The Raman image (or heat map) of each substance of interest was rendered by integrating the area under the peak of Raman spectra pixel-by-pixel. Correlation between different wavenumbers and different chemical bond vibrations within substances of interest was based on literature and used to select the position of the peak and the width of the bandpass filter used in image rendering. Image intensity was proportional to the number of photons generated from the Raman scattering as a result of the chemical bond vibration and, therefore, proportional to the content of the substance of interest within the pixel space.

3.13.3 Spatial deconvolution of Raman images

The rendered Raman heat maps were spatially deconvolved using the theoretical point spread function (PSF) based on the instrumental setup. 2D PSF was generated using the ImageJ macro, Diffraction PSF 3D. Spatial deconvolution was performed using the ImageJ macro, Iterative Deconvolve 3D.

3.14 Raman hyperspectral data analysis

3.14.1 Cell boundary and integrity

Spatial distribution of amide I signal (1660 cm^{-1}), or cellular hydrogen bond signal (115 cm^{-1}), was used to delineate the area of the cell or cell aggregate. Thresholding was used to create a binary mask of the cell(s) via WITec Project FOUR or FIJI. Cellular integrity on a protein level was quantified by calculating the Moran's I value of amide I signals in GeoDa, where spatial dispersion versus autocorrelation was determined between -1 and 1 using a spatial weight matrix based on 8 nearest neighbors.

3.14.2 Intracellular ice formation

Spatial distribution of OH stretching signal (3125 cm^{-1}), or ice hydrogen bond signal (215 cm^{-1}), was used to delineate the area of the crystalline ice. Thresholding was used to create a binary mask of the ice crystals in WITec Project FOUR or FIJI. Binary masks of cell(s) and ice were multiplied to create the binary mask of intracellular ice. The area proportion of intracellular ice to cell (AIC) was used as the metric to quantify intracellular ice formation.

3.14.3 Cytochrome C release

Heme vibration signal (1127 cm^{-1}) was used to analyze the distribution of cytochrome C. Spatial autocorrelation of the heme vibration signal was calculated using Moran's I and an 8 nearest-neighbor weight matrix in GeoDa. Autocorrelation values of individual cells within a large cell population of healthy and apoptotic cells were used to define the quantitative threshold of cytochrome C release and mitochondrial apoptosis in the cryopreserved cell(s).

3.14.4 Membrane partitioning of solutes

CC stretching signal (840 cm^{-1}) was used to analyze the distribution of non-DMSO CPA molecules. Symmetric CS stretching (687 cm^{-1}) was used to analyze the distribution of DMSO. Line profile of the CPA distribution was obtained by tracing segmented lines along the midline of the nonfrozen CPA channels from outside the cell on one side, through the center of the cells, to the nonfrozen channel on the other side of the cell using FIJI. The binary mask of cell was used to distinguish intracellular pixels containing the CPA molecules from extracellular pixels containing the CPA molecules. Membrane partitioning ratio of CPA was calculated by the ratio of mean Raman image intensity of extracellular CPA to intracellular CPA. It was used to characterize the extent of internalization of DMSO versus non-DMSO CPAs by different cell types as well as the extent of membrane damage in cells subjected to different cooling rates or ice nucleation temperatures.

3.15 Differential scanning calorimetry

Differential scanning calorimetry (DSC) was performed on a TA Differential Scanning Calorimeter Q1000. Approximately 5 mg of each sample CPA solution was encapsulated in an aluminum pan (DSC Consumables) with a hermetically sealed lid. Samples were frozen and thawed using the following protocol: (1) start at 20 ˚C, (2) cool to -140 or -150 ˚C at -10 ˚C/min, (3) hold for 3 min at -140 or -150 ˚C, and (4) warm to 20 or 40 ˚C at +10 ˚C/min. An empty pan was used as a reference.

TA Universal Analysis Software was used to determine the thermophysical behavior of the CPA solutions. The endothermic peak for each sample was used to calculate the enthalpy of melting and melting temperature. Enthalpy of melting was defined as the area under the endothermic peak, and melting temperature was defined as the onset of melting of the endothermic peak. Glass transition temperature and softening temperature, both second-order phase transitions, were determined by plotting the first derivative of heat flow over time against temperature. Two local maxima were found for each CPA solution except for DMSO, representing the glass transition and softening temperatures[109] respectively in ascending order.

3.16 Osmolality

Osmolality of solutions was prepared at room temperature at 50 µl unit volume and measured based on freezing point depression using an OSMETTE osmometer (Precisions Systems). All measurements were repeated in independent triplicate. A dilution curve

showed a linear relationship between the dilution ratio of NADES in water and the measurement of osmolality and was used to extrapolate the osmolality of solutions that were out of range of the osmometer.

3.17 pH

pH of solutions and extracellular supernatant was measured at room temperature using a pH meter (Beckman, Φ 300 Series) that was calibrated routinely. Sample volume was kept constant at 1 ml. Measurements were taken in independent triplicate.

3.18 Membrane fluidity

iPSC cultures were dissociated with Versene for 8 minutes or 20 minutes to obtain a suspension of multicellular aggregates or single cells. Neural crest cells, immature and mature sensory neurons were dissociated with Accumax for 10, 45 or 90 minutes respectively at room temperature on day 5, 7 or 14. Dissociated cells were washed once and stained with a fluorescent pyrene-decanoic acid (PDA) probe (Membrane Fluidity Kit, Abcam, ab189819) at room temperature for exactly 20 minutes before washing twice and quantification per the manufacturer's instructions. Phenol red-free DMEM/F12 was used as the suspension media to minimize extrinsic variability between samples. Relative membrane fluidity was measured by the PDA excimer-to-monomer ratio using a Synergy HTX microplate reader with excitation at 360 nm and emission at 400 nm and 460 nm.

3.19 Cell diameter

Neural crest cells, immature and mature sensory neurons were dissociated with Accumax for 10, 45 or 90 minutes respectively at room temperature on day 5, 7 or 14. Dissociated cells were washed once, resuspended in DMEM/F12, stained using AO/PI and imaged in a hemocytometer using a Zeiss Axioskop 50 fluorescent microscope. Fluorescent images of AO-positive, PI-negative live cells were processed in FIJI, where the cell area was measured using automatic thresholding and particle analysis functions. Cell diameter estimate was calculated from the cell area as below.

$$Diameter = 2 \times \sqrt{\frac{Area}{\pi}}$$

3.20 Statistical analysis

Independent biological replicates were used with sample size specified per dataset. Power analysis was performed to ensure sufficient sample size with a power of 0.95. Sample size of 1 was used in the DE algorithm-driven experiments to optimize the DMSO-free CPA formulation with high efficiency. Error bars represented either standard error or 95% confidence intervals as noted in later text. Two-tailed Student's *t*-tests were performed for two-sample comparisons, unless otherwise noted. Fisher's exact test performed for two-sample comparisons of samples with binomial distribution. ANOVA with Bonferroni correction was performed for comparisons of multiple samples, with the exception of Kruskal-Wallis ANOVA performed for sample populations with non-normal distribution. Levene's Test was used to verify the assumption for homogeneity of variance for the two or more samples. The null hypothesis was defined as no statistical

difference between the parameters (e.g., means) for any pair of groups or between the experimental group and control group. The null hypothesis was rejected, and differences were considered statistically significant for a *p*-value less than 0.05.

Chapter 4

Mechanism of Damage in DMSO-Based Cryopreservation of hiPSC Multicellular Aggregates Compared to Single Cells

Much of the text and figures in this chapter have previously appeared in the publication below, included here with copyright permission from Mary Ann Liebert.

Li R[†], Yu G[†], Azarin S and Hubel A. Freezing responses in DMSO-based cryopreservation of human iPS cells: aggregates vs. single cells. *Tissue Engineering: Part C*. 2018. 24, 289-299.

4.1 Introduction

Human induced pluripotent stem cells (hiPSCs) are multicellular aggregates that can be reprogrammed from a variety of somatic cells and have the potential to be differentiated into all three germ-layers[1,2], attracting much interests in tissue engineering[6–8], disease modeling[3,4], and personalized medicine[9,10]. For both clinical and scientific purposes, effective cryopreservation of hiPSCs is required for transportation, storage of frozen hiPSCs and other downstream uses. However, cryopreserved hiPSCs are vulnerable to the loss of viability, function or pluripotency[19–21]. hiPSCs can be frozen either as aggregates or single cells depending upon the application.

Cryopreservation of hiPSCs typically involves two different methods: conventional slow cooling and vitrification. Briefly, vitrification uses high concentrations of cryoprotective agents combined with high cooling rates to avoid the formation of ice during freezing.

Conventional slow cooling in this particular application implies using a solution using 10% dimethyl sulfoxide (DMSO) and a cooling rate of -1 ˚C/min. High rates of post-thaw recovery are observed (~100%) by vitrification, but the method faces limitations of poor scalability and high risk for contamination[110]. Slow-cooling studies have attempted to find suitable freezing parameters for the cells[41,111–114].

ROCK inhibitor (ROCKi) Y-27632 has been used to enhance the survival of dissociated hiPSCs (i.e., single cells)[53,115,116]. The disruption of nonmuscle myosin IIA (NMMIIA) and actin as a result of ROCK inhibition has been shown to increase survival and pluripotency of single hiPSCs[117,118]. However, the addition of ROCKi can have contradictory effects in the case of hiPSC aggregates. The downregulation of NMMIIA has been shown to impair cell adhesion, cell-cell junction, self-renewal and pluripotency of hiPSC aggregates[119,120]. In order to exclude the confounding effect of ROCKi and capture native cell response to freezing, we hereby studied the cryopreservation of hiPSCs without the use of ROCKi.

Despite attempts to improve cryopreservation of multicellular aggregates, the mechanisms of damage for different freezing conditions are poorly understood. As with single cells, extensive intracellular ice formation (IIF) has been proven to be damaging[121]; exposure to high solute concentration at low temperatures can cause the "solute effect" in cells, and the addition, removal of cryoprotective agents can result in osmotic stress.[19] However, freezing responses of cell aggregates are more complex than

single cells. For example, propagation of IIF in cell aggregates via gap junctions has been observed experimentally in a variety of cell types[122–124].

Recently, Raman spectroscopy has become a powerful tool for understanding cell responses to the freezing environment[80,90,125–127]. The magnitude and spatial distribution of specific chemical signals (liquid water, ice, cryoprotective agent, hydrohalite) and biological signals (cytochrome c) have been measured for single cells during freezing[127,128]. However, to the best of our knowledge, there has been no Raman spectroscopy study of cell aggregates. In this study, Raman spectroscopy was used to observe both hiPSC single cells and aggregates frozen at three cooling rates and two seeding temperatures. The seeding temperature is the temperature at which ice forms in the extracellular solution (Figure 2A).

In parallel, hiPSCs as single cells or aggregates were frozen using a programmable controlled-rate freezer (CRF) with the same cooling rates and seeding temperatures as Raman spectroscopy. Cell recovery, attachment, apoptosis, and cytoskeletal organization were examined after rapid thawing in 37 ˚C water bath. This chapter deepens our understanding of behaviors of single cells and aggregates frozen at various conditions and promotes the development of improved cryopreservation protocols for hiPSCs.

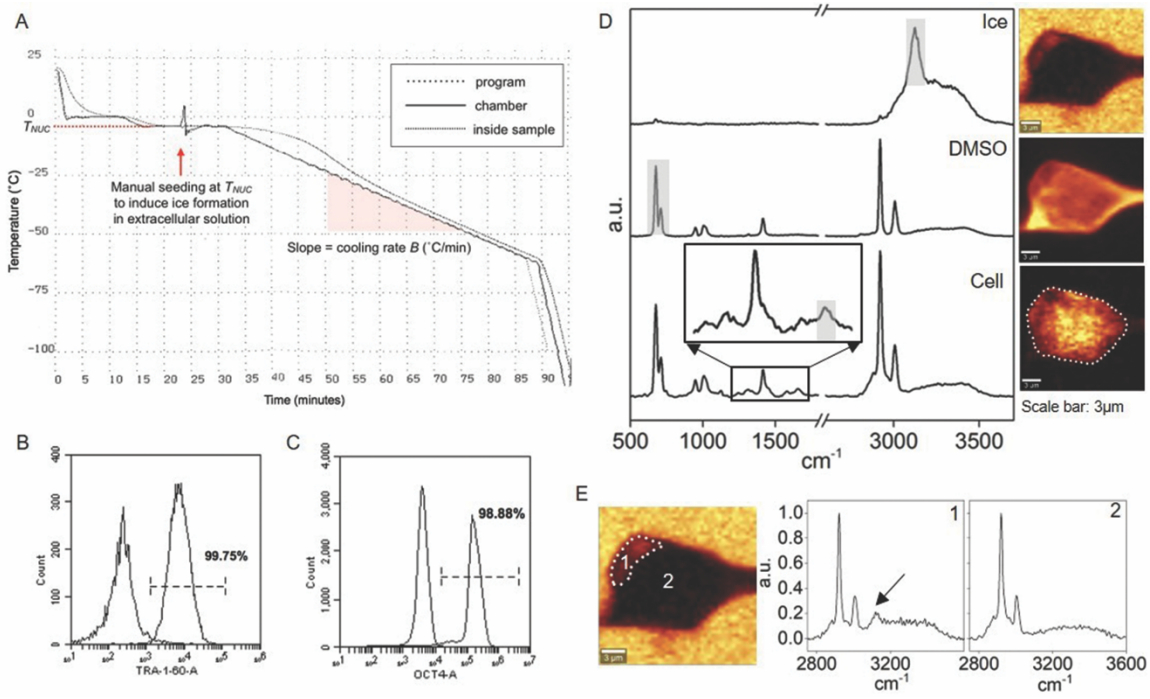

Figure 2. Illustration of CRF, flow cytometry and Raman methodology. (**A**) A CRF cooling curve showing cooling rate of-1 ˚C/min and seeding temperature at -4 ˚C. (**B**) Flow cytometry overlaid histograms of anti-TRA-1-60 and its isotype control, showing 99.75% TRA-1-60 positive cells. (**C**) Flow cytometry overlaid histograms of anti-OCT4 and its isotype control, showing 98.88% OCT4 positive cells. (**D**) Raman spectra of ice, DMSO and single hiPSCs cryopreserved in 10% DMSO. Raman images of ice, DMSO and amide I are rendered based on the specific Raman signal indicated on the spectra. (**E**) Raman image of ice showing cell section with IIF (1) and without IIF (2) with corresponding Raman spectra. The arrow indicates the Raman signal of ice. [Panels D and E are based on Guanglin Yu's work.]

4.2 Methods

hiPSCs used in this chapter were from cell line DF-19-9-11 and cultured as described in section 3.2.1. Cells were >95% positive (Figure 2B and C) for hiPSC pluripotency surface marker TRA-1-60 and transcription factor OCT4.

Aggregates and single cells were dissociated from culture as described in section 3.5.1.

Aggregate size was controlled by the amount of gentle pipetting. Large aggregates consisted of 100 or more cells, whereas small aggregates consisted of 3 to 10 cells. Membrane fluidity of hiPSC in the form of small aggregates versus single cells was measured as described in section 3.18. 10% DMSO in PBS++ was formulated as the CPA solution of interest. Cells in CPA solution were incubated at room temperature for 30 minutes before freezing. Controlled rate freezing was performed as described in section 3.6.1 with varying cooling rates, B, of -1, -3, or -10 ˚C/min and ice nucleation manually induced at varying temperatures, T_{NUC}, of -4 or -8 ˚C.

From immediately post-thaw to 4 days post-thaw, a series of assays were performed to characterize the survival and function and examine potential mechanism of damage in the cryopreserved hiPSCs for each freezing condition (i.e., cooling rate and ice nucleation or seeding temperature), following a progression in both time and depth of analysis. After thawing as described in section 3.6.3, post-thaw recovery was measured as described in sections 3.7.1 through 3.7.3. Post-thaw reattachment was selected as the cell functional metric and measured as described in section 3.8.1. Post-thaw apoptosis was analyzed as described in section 3.10.2. Cytoskeletal organization and chromatin condensation in the post-thaw culture were monitored for 24 hours, sampled and measured by immunocytochemistry as described in section 3.3.2 every 4 hours. Growth of post-thaw culture was also measured daily for 4 days as described in section 3.9.2. A fresh cell control was used for each set of post-thaw cell assays.

Low-temperature Raman spectroscopy was set up as described in section 3.13.1. Raman images of hiPSC, DMSO, and ice (Figure 2D) were rendered respectively per freezing condition as described in section 3.13.2, where image size was fixed at 15 μm by 15 μm for samples of single cells and varied for samples of multicellular aggregates depending on the actual size of the aggregates. The Raman signals for this study did not overlap with each other; as a result, multivariate data analysis was not required. Cells were delineated as described in section 3.14.1, and intracellular ice formation (IIF) was determined as described in section 3.14.2. Raman spectra of cell sections with IIF showed presence of OH stretch peak, while Raman spectra of cell sections without IIF showed absence of OH stretch peak (Figure 2E).

In this chapter, data was represented as mean plus/minus standard error. Two-tailed student t-tests were performed for two-sample comparisons and one-way ANOVA tests with Tukey HSD were performed for simultaneous three-sample comparisons to obtain *p*-values with a significance level set at 0.05. Three independent biological replicates were used.

4.3 Results

4.3.1 High IIF found with high cooling rate and low seeding temperature

IIF can be influenced by many freezing parameters, including cell type, cell-cell interaction, cooling rate, seeding temperature, and solution composition.[129] In order to investigate the effects of cooling rates and seeding temperatures on the IIF of

cryopreserved hiPSCs, single cells and aggregates in 10% DMSO solution were frozen at a constant cooling rate of -1, -3, or-10 ˚C/min with seeding temperature of -4 or -8 ˚C.

Typical Raman images rendered on the signal associated with ice and amide I were shown for both single cells and aggregates cryopreserved at three different cooling rates grouped by seeding temperatures (Figure 3A, B, E and F). In order to characterize the proportion of IIF, the ratio of cross-sectional area of IIF to the cross-sectional area of single cells or aggregates (AIC) was calculated. The effect of cooling rates on AIC was examined for a given seeding temperature. For single cells, there is no statistical difference of AIC between cells cryopreserved at -1 and -3 ˚C/min, however cells cryopreserved at -10 ˚C/min showed statistically greater AIC for both seeding temperatures (Figure 3C). Similar conclusions on the effect of cooling rate on AIC can be drawn for aggregates (Figure 3G).

The effects of seeding temperature on AIC were also investigated. There was no statistical difference in AIC between single cells seeded at -4 ˚C and -8 ˚C for all three cooling rates. For aggregates, greater AIC was observed at a seeding temperature of -8 ˚C than -4 ˚C for a cooling rate of -1 and -3 ˚C/min (Figure 3D). Aggregates cryopreserved at -10 ˚C/min showed no difference in AIC between the two seeding temperatures (Figure 3H).

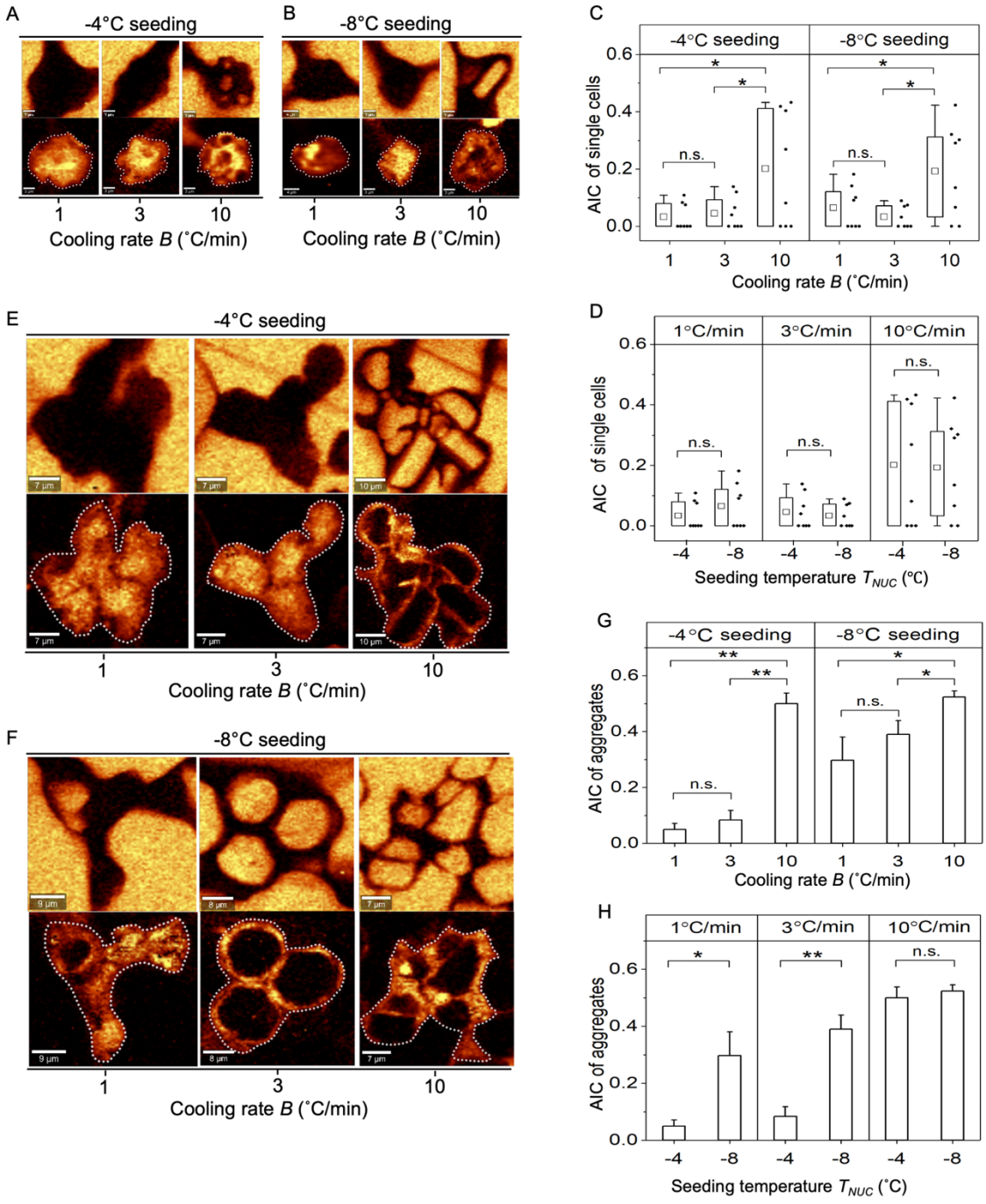

Figure 3. Intracellular ice formation in frozen hiPSC single cells versus aggregates. (**A**) Raman images of ice and amide I of single cells at seeding temperature of -4 ˚C. (**B**) Raman images of ice and amide I of single cells at seeding temperature of -8 ˚C. AIC of single cells grouped by (**C**) seeding temperature (n=8, ∗: p<0.05) and by (**D**) cooling rate (n=8, ∗: p>0.05). Ends of the whiskers represent the minimum and maximum of the data. The bottom and top of the box are the first and third quartiles and the square inside

the box is the average. (**E**) Raman images of ice and amide I of aggregates at seeding temperature of -4 ˚C. (**F**) Raman images of ice and amide I of aggregates at seeding temperature of -8 ˚C. (**G**) AIC of aggregates grouped by seeding temperature (SE, n=5, ∗: p<0.05, ∗∗: p<0.01). (**H**) AIC of aggregates grouped by cooling rates (SE, n=5, ∗: p<0.05, ∗∗: p<0.01). [This figure is based on Guanglin Yu's work.]

4.3.2 DMSO distribution more variable in multicellular aggregates

Single cells and aggregates frozen without a significant amount of IIF were used to study whether the distribution of DMSO varied in aggregates[127]. Raman images of DMSO in cells frozen at -1 ˚C/min seeded at -4 ˚C were shown as examples (Figure 4A and B). For single cells, a diagonal line was drawn across the image and the normalized DMSO concentration (DMSO peak intensity at each pixel to the maximum DMSO peak intensity of the line) was calculated (Figure 4A). Standard deviation of normalized DMSO concentration (SD) was calculated to represent the variation of DMSO concentration across the cell. It was noteworthy that 1 μm from the cell membrane inward to the cell was not considered for the calculation because of partitioning of DMSO by the cell membrane (calculation within gray shading). For aggregates, two diagonal lines were drawn across the image and the DMSO concentration along those lines as well as its variation were quantified (Figure 4B). It was found that SD was significantly greater in aggregates than single cells frozen at -1 or -3 ˚C/min (Figure 4C).

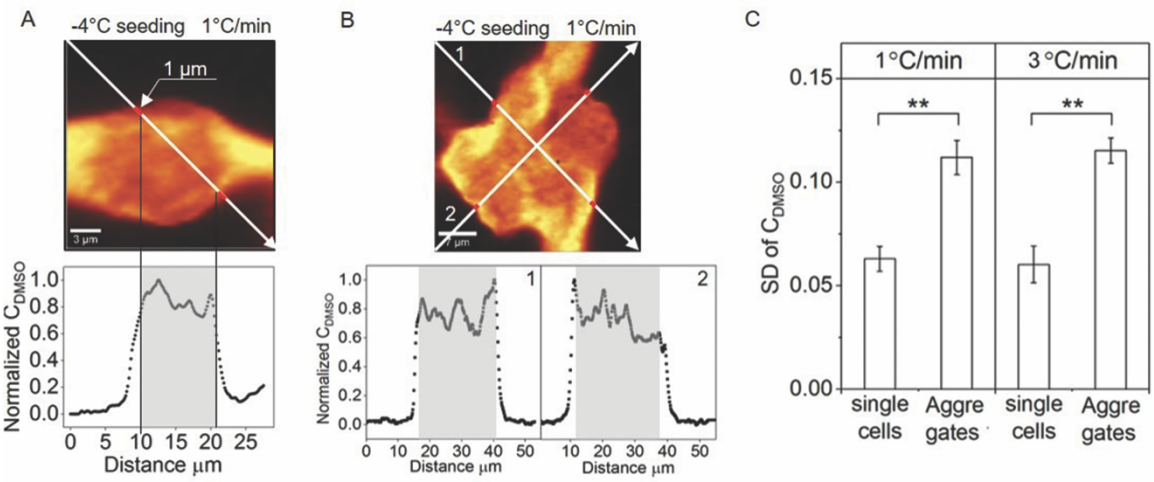

Figure 4. Heterogeneity of intracellular DMSO distribution. (**A**) Raman image of DMSO in the single hiPSCs cryopreserved at -1 ˚C/min with a seeding temperature of -4 ˚C. (Scale bar: 3 µm.) The white arrow goes through different regions of the image and represents the location where peak intensity of DMSO is obtained. Normalized DMSO concentration (peak intensity of DMSO at each data point along the arrow divided by maximum peak intensity of DMSO) is plotted as a function of horizontal distance of the arrow from its start point. Gray shading indicates the region used for calculation of standard deviation of normalized DMSO concentration. (**B**) Raman image of DMSO of aggregates cryopreserved at -1 ˚C/min with seeding temperature of -4 ˚C. (Scale bar: 7 µm.) Normalized DMSO is plotted as a function of horizontal distance of the arrow from its start point for both arrows. (**C**) Standard deviation of normalized DMSO concentration for single cells and aggregates cryopreserved at -1 and -3 ˚C with seeding temperature of -4 ˚C (SE, n=8 for single cells, n=5 for aggregates, **: p<0.01). [This figure is based on Guanglin Yu's work.]

4.3.3 Freezing damages of hiPSC aggregates reflected in poor reattachment

Post-thaw recovery and attachment rates were examined for both hiPSC as single cells and aggregates cryopreserved using CRF with the same set of cooling rates -1, -3, -10 ˚C/min and seeding temperatures -4, -8 ˚C. Post-thaw recovery was measured in terms of membrane integrity. Post-thaw attachment was normalized to the post-passage attachment of fresh, nonfrozen aggregates, so a post-thaw attachment rate close to 1 indicates attachment ability of cryopreserved cells comparable to what was observed of

fresh cells. Of all freezing conditions tested, the combined cooling rate of -1 ˚C/min and seeding temperature of -4 ˚C had the highest mean post-thaw recovery at 97.93% and highest mean post-thaw attachment rate at 0.9851.

The effect of different cooling rates was examined for each seeding temperature. For single cells, membrane integrity for both -1 and -3 ˚C/min were significantly higher than -10 ˚C/min regardless of the seeding temperature (Figure 5A). All of the single cell conditions tested had few to no cells attached to the culture substrate post-thaw (Figure 5C), consistent with previous studies[130–132]. For aggregates, little difference in the membrane integrity was observed for the range of cooling rates studied (Figure 5B). However, aggregates cryopreserved at -1 ˚C/min attached to the surface post-thaw at greater rates than either -3 or -10 ˚C/min for a seeding temperature of -4 ˚C (Figure 5D). The effect of different seeding temperatures was examined for each cooling rate. For cells frozen at -1 and -3 ˚C/min, membrane integrity (of both single cells and aggregates, Figure 5E, F) and cell attachment (of aggregates, Figure 5H) for seeding temperature of -4 ˚C were significantly higher than -8 ˚C; for those frozen at -10 ˚C/min, little difference in membrane integrity or cell attachment was observed for the seeding temperatures studied (Figure 5E-H).

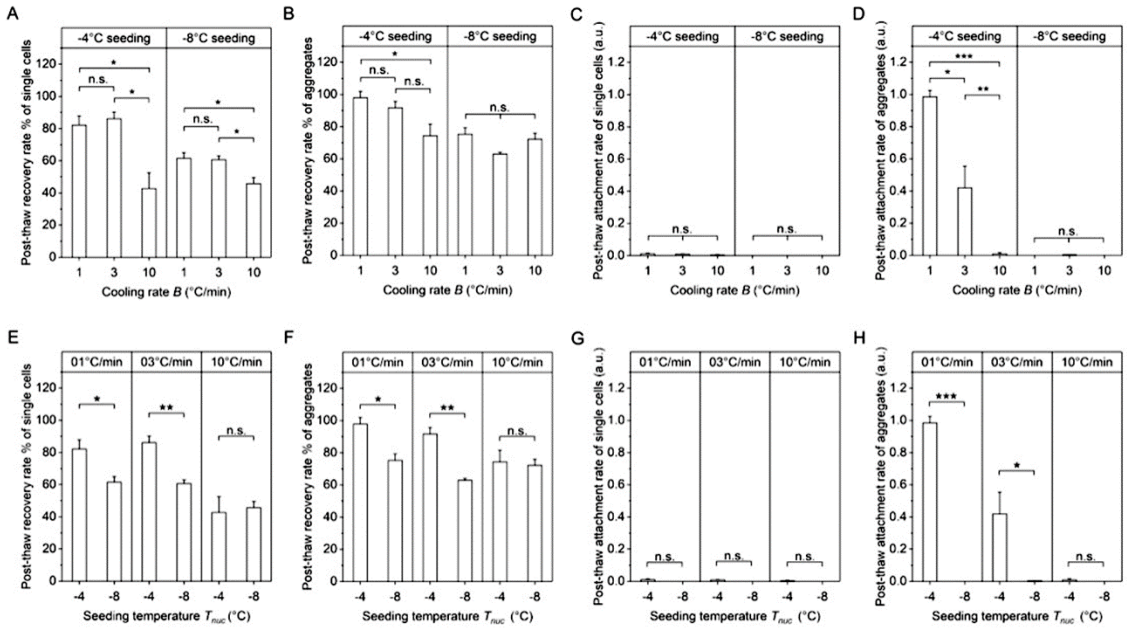

Figure 5. (**A**) Post-thaw recovery rate of single cells against the cooling rate grouped by seeding temperature. (**B**) Post-thaw recovery rate of aggregates against the cooling rate grouped by seeding temperature. (**C**) Post-thaw attachment rate of single cells against the cooling rate grouped by seeding temperature. (**D**) Post-thaw attachment rate of aggregates against the cooling rate grouped by seeding temperature. (**E**) Post-thaw recovery rate of single cells against the seeding temperature grouped by cooling rate. (**F**) Post-thaw recovery rate of aggregates against the seeding temperature grouped by cooling rate. (**G**) Post-thaw attachment rate of single cells against the seeding temperature grouped by cooling rate. (**H**) Post-thaw attachment rate of aggregates against the seeding temperature grouped by cooling rate. (SE, n=3, n.s.: $p \geq 0.05$, *: $p<0.05$, **: $p<0.01$, ***: $p<0.001$).

4.3.4 Apoptosis and onset of proliferation varied in post-thaw cultures

In many different cell types, post-thaw apoptosis can result in significant cell losses[133,134]. As a result, we investigated both post-thaw apoptosis and proliferation. The proportions of apoptotic and necrotic subpopulations were measured (Figure 6A) for all cryopreserved cell aggregate samples immediately post-thaw as well as a fresh cell aggregate control immediately after dissociation from culture, by detecting caspase activation and membrane integrity. All samples, including the post-passage control, had

large proportions of cells expressing apoptosis markers (64 to 78% of total cell population, Figure 6B). The ratio of early to late apoptotic subpopulations was also calculated. Freezing at higher cooling rates resulted in 2 to 3-fold less predominantly early apoptosis and more late apoptosis (Figure 6B). No obvious difference in apoptotic subpopulations was observed between the different seeding temperatures at each cooling rate.

Post-thaw apoptosis was further monitored via chromatin condensation in attached colonies for up to 24 hours post-thaw. Condensed chromatin was not visible at 4 hours post-passage but was visible until 8 hours post-thaw for the aggregates frozen at -1 ˚C/min seeded at -4 ˚C, up to 24 hours post-thaw for the aggregates frozen at -3 ˚C/min seeded at -4 ˚C (Figure 6C). In addition, sister chromatids were also clearly visible starting at 8 hours post-passage, 8 hours post-thaw for the aggregates frozen at -1 ˚C/min seeded at -4 ˚C, but not observed for the aggregates frozen at -3 ˚C/min seeded at -4 ˚C. As shown by the growth curves in Figure 6D, the aggregates frozen at -3 ˚C/min seeded at -4 ˚C proliferated greatly between 24 and 48 hours post-thaw, surpassing the culture of aggregates frozen at -1 ˚C/min seeded at -4 ˚C; the culture of aggregates frozen at -3 ˚C/min seeded at -8 ˚C proliferated and became detectable starting at 48 hours post-thaw; all the rest of the sample conditions, single cells and aggregates, did not show detectable amount of attached cells throughout the 4-day period.

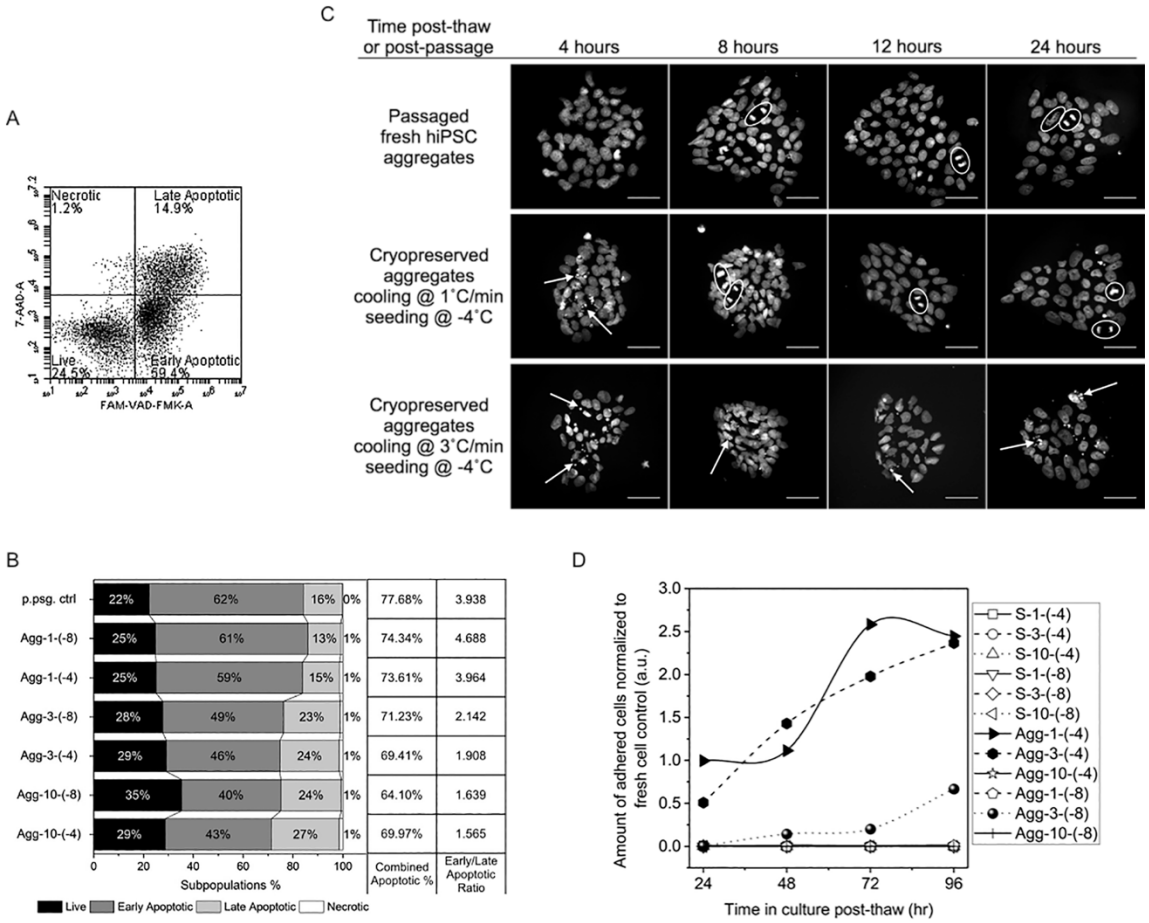

Figure 6. Post-thaw apoptosis and proliferation. (**A**) An example of the flow cytometry density plot of FAM-VAD-FMK against 7-AAD, with four quadrants defining live, early apoptotic, late apoptotic and necrotic cell subpopulations respectively. (**B**) Left: 100% stacked column graph of cell subpopulation proportions against fresh post-passage control or the freezing condition in abbreviated forms of "Aggregates-cooling rate (˚C/min)-seeding temperature (˚C)". Right: combined apoptotic population proportion and ratio of early-to-late apoptotic population proportions calculated from the subpopulation proportions on the left. (**C**) Attached colonies in culture 4, 8, 12, 24 hours post-passage or post-thaw, stained with Hoechst 33342. White arrows point at condensed chromatin. White circles highlight formed, aligned or separated sister chromatids. (Scale bar: 50 μm.) (**D**) Modified Bezier curves of cell growth up to 4 days post-thaw. Sample conditions are shown in abbreviated forms of "Single cells (or aggregates)-cooling rate (˚C/min)-seeding temperature (˚C)".

4.4 Discussion

4.4.1 Multicellular aggregates more sensitive to undercooling than single cells

AIC values of single cells and aggregates cryopreserved at -10 ˚C/min were significantly greater than those at -1 and -3 ˚C/min, consistent with earlier studies that fast cooling rates resulted in greater IIF[135] and greater value of AIC led to lower cell survival[127]. Two different types of ice crystals were observed in this study: 1) small ice crystals mixed with cytoplasm and 2) large pure ice crystals (Figure 7A). Type-1 ice crystals were intracellular as observed in a previous study[127]; type-2 ice crystals could be either intracellular or intercellular, where future study is needed to determine their location relative to the cell membrane. However, because the size of some type-2 ice crystals was clearly greater than that of an individual cell, they were most likely intercellular. Only high cooling rate (-10 ˚C/min) resulted in type-2 ice crystals in cryopreserved single cells. Undercooling occurs when the temperature at which ice forms or seeding temperature drops below the melting temperature of the system. The lower the seeding temperature, the greater the undercooling. The relative insensitivity of hiPSC single cells to undercooling is similar to that observed with peripheral lymphocytes[136], but differs from hepatocytes[137], erythrocytes[138] and hiPSC aggregates. In contrast, high cooling rates (-10 ˚C/min) and low seeding temperature (-8 ˚C) resulted in type-2 ice crystals in aggregates. This suggests that aggregates are more sensitive to undercooling than single cells. As the seeding temperature decreased from -4 ˚C to -8 ˚C, the cooling rate threshold for IIF in aggregates also decreased from -10 ˚C/min to -1 ˚C/min, which is consistent with an early study, where the higher the degree of undercooling, the lower the cooling rate at which IIF is observed[138].

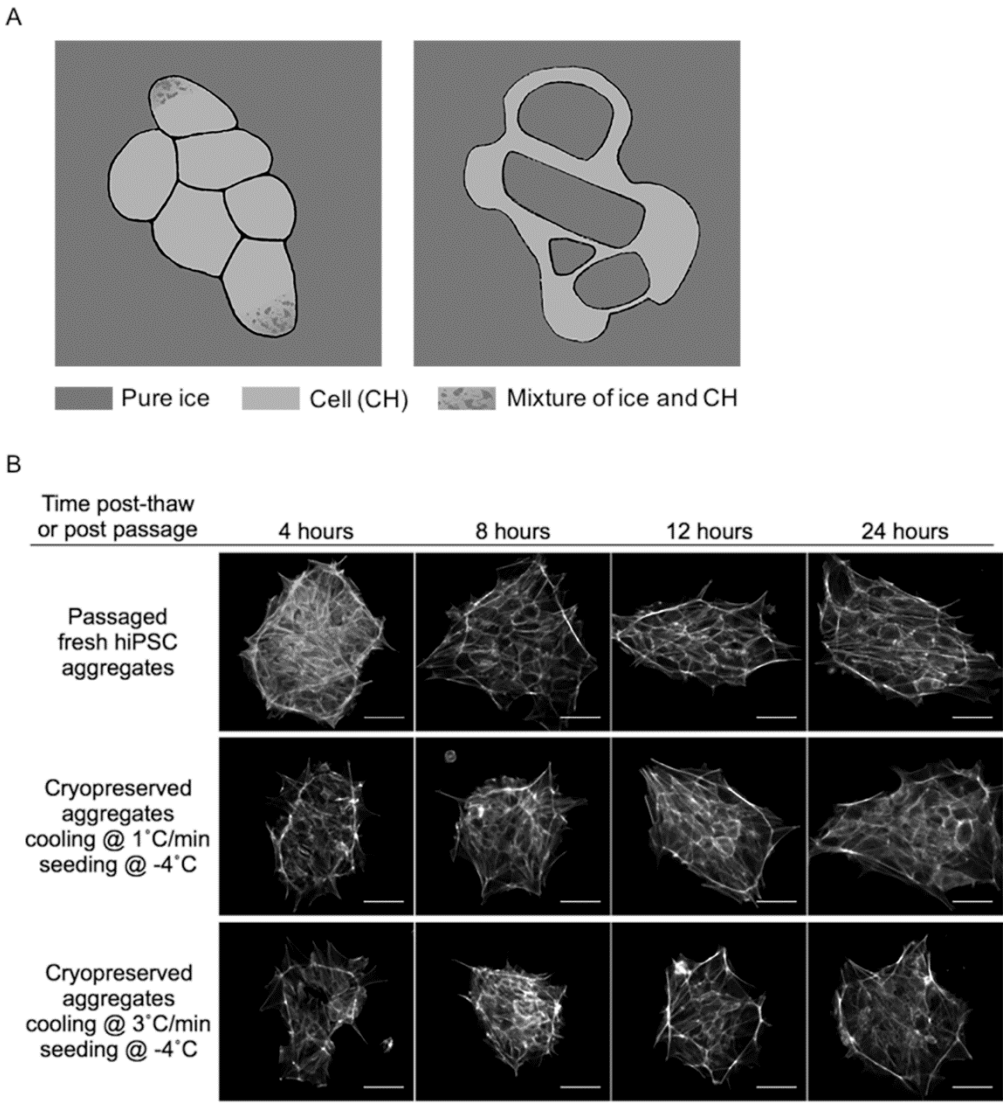

Figure 7. Intracellular ice crystal categorization and f-actin organization. (**A**) Sketches of frozen cell aggregates showing two types of ice crystals. (**B**) Attached colonies in culture 4, 8, 12, 24 hours post-passage or post-thaw, stained for f-actin. The honeycomb-like pattern became clearly visible around 8 hours post-passage and around 12 hours post-thaw for the aggregates cryopreserved at -1 ˚C/min with seeding at -4 ˚C and for those cryopreserved at -3 ˚C/min with seeding at -4 ˚C. All other freezing conditions tested were not assessed here due to failed post-thaw cell attachment. (Scale bar: 50 μm.) [Panel A is based on Guanglin Yu's work.]

A lower seeding temperature results in a greater difference in chemical potential across

the cell membrane[139]. It has been hypothesized that a new equilibrium can be reached by dehydration of cells or solidification of water inside the cell. Several effects could influence the probability of IIF at lower seeding temperatures, including water permeability of cell membrane. Compared to single cells, aggregates have a more complex cytoskeletal structure (Figure 7B), which can interact with the plasma membrane, compacting the aggregates[140], therefore decreasing membrane water permeability[141]. In addition, membrane fluidity was found to be significantly lower in aggregates (i.e., 1.39 ± 0.01 a.u., 95% confidence interval) than in single cells (i.e., 1.52 ± 0.01 a.u., 95% confidence interval). Membrane permeability of water should be proportional to the membrane fluidity[142]. Kinetic energy and molecular motion decrease with undercooling, and upon ice nucleation in the extracellular space, a more rigid plasma membrane may not allow water molecules to transport quickly enough from the intracellular space following the sudden increase in the transmembrane concentration differential and avoid intracellular ice formation. The higher sensitivity to undercooling of aggregates than single cells is likely a result of their decreased membrane fluidity and water permeability.

Propagation of ice crystals from cell-to cell has been observed in non-hiPSC aggregates.[122,124,143,144] In this study, small ice crystals mixed with cytoplasm were confined within the cell where ice was initially formed, and there was no evidence that these small ice crystals propagated from one cell to the next.

4.4.2 DMSO distribution more heterogeneous in aggregates than single cells

Variation of DMSO concentration across aggregates was significantly greater than that across single cells frozen at cooling rates of -1, -3 ˚C/min with a seeding temperature of -4 ˚C. These differences could result from greater disturbance to transport by more complex membrane-cytoskeletal structure[140] of multicellular systems. Previous studies have measured DMSO transport in tissues using MRI[145] and demonstrated variations in the concentration with time and location, but no previous studies have had the spatial resolution to look at the distribution of cryoprotective agents in a multicellular system on a cell-by-cell basis. Raman spectroscopy served as an ideal tool to investigate the distribution of cryoprotective agent cell-by-cell for both single cells and multicellular aggregates in this study.

4.4.3 Membrane integrity decoupled from post-thaw function of adherent cells

For single cells, similar to what was reported in literature[111–114], slow cooling rates (-1, -3 ˚C/min) allowed significantly better preservation of membrane integrity than higher cooling rate (-10 ˚C/min) regardless of the seeding temperature. This outcome was consistent with the observation that AIC increased with the increasing cooling rate.

For aggregates, however, slow cooling rates (-1, -3 ˚C/min) combined with high seeding temperature (-4 ˚C) had little effect on the membrane integrity but resulted in significantly better cell attachment than higher cooling rate (-10 ˚C/min) or low seeding temperature (-8 ˚C). The clear advantage of seeding temperature -4 ˚C compared to -8 ˚C

suggests that the range of seeding temperatures of -7 to -12 ˚C being used in literature[110] is suboptimal, and that seeding temperature should be considered as a critical parameter when designing cryopreservation protocol for hiPSCs. Cell attachment of the aggregates correlated with AIC. The two freezing conditions that successfully attached post-thaw both had little intracellular ice, while those freezing conditions that formed large pure ice crystals all failed to attach post-thaw. Similar to the results observed with hMSCs[43], membrane integrity of hiPSC aggregates did not always correlate with cell attachment. All conditions tested using aggregates had reasonable levels of post-thaw membrane integrity, but only two of these conditions had detectable cell attachment post-thaw. It is not clear the specific mechanism for the impaired attachment observed in this study. Previous studies have found that freezing can result in damage to the cytoskeleton[15] or exposure to DMSO can result in damage to DNA and proteins [57,146] that does not alter membrane integrity. This suggested that the two metrics, post-thaw recovery rate and post-thaw attachment rate, could be decoupled. The conventional approach of optimizing hiPSC cryopreservation based on only post-thaw membrane integrity may be insufficient. Functional metrics like post-thaw attachment should be incorporated into screening of cryoprotective agents and tuning of freezing protocols.

4.4.4 Predominantly late apoptosis and late onset of proliferation linked to poor post-thaw reattachment

Post-thaw apoptosis can influence the persistence of cells with time post-thaw. Significant cell losses can be experienced with time post-thaw resulting from

apoptosis[133]. High levels of post-thaw apoptosis were observed in this investigation and apoptosis dominated necrosis. This result is similar to that observed in renal cells and hESCs[133,147]. However, unlike hematopoietic stem cells[148,149] and lymphocytes[150], no association between the caspase activation (early apoptosis) and post-thaw function (cell attachment) was found in cryopreserved hiPSC aggregates. Different freezing conditions resulted in similar levels of caspase activation. Similar level of caspase activation was also observed in passaged fresh hiPSC aggregates, suggesting that the high caspase activation was primarily induced by cell dissociation, rather than cryopreservation[131]. The presence of condensed chromatin (late apoptosis) and absence of mitotic chromosomes (proliferation) up to 24 hours post-thaw correlated with low cell attachment measured at 24 hours post-thaw.

F-actin cytoskeleton has been evaluated by previous studies in ROCKi-conditioned adherent single cells[151]. In this study, f-actin cytoskeletal organization was monitored in attached colonies of ROCKi-free culture (Figure 7B). The colonies underwent remodeling and reestablishing of f-actin organization both post-thaw in the cryopreserved samples and post-passage in the fresh sample, where f-actin fibers progressed to localize near the cell-cell interfaces and the edge of the colony, forming a honeycomb-like pattern. Impaired f-actin organization was seen in the cryopreserved cells up to 8 hours post-thaw compared to fresh cells, which could be explained by actin depolymerization due to osmotic stress during freeze-thaw[15]. The dense f-actin at the edge of the colony was identified in a recent study as a contractile actin fence that reinforces colony

structure and pluripotency[140], supporting that the f-actin organization plays an important role in post-thaw survival and growth of these multicellular aggregates.

4.4.5 Aggregate size-dependent post-thaw survival and further complexity in cryopreservation of multicellular systems

Data thus far has been acquired using small aggregates of 3 to 50 cells. A recent study found that the survival of cryopreserved aggregates depended on the size of aggregates, preferring those around 109 μm in diameter to larger sizes[152]. Following the publication, we explored the cryopreservation of larger hiPSC aggregates (> 100-cell) and whether their survival would be affected by variations in the cooling rate. In cryobiological studies of single cells, it has been postulated that larger cells require slower cooling rates to avoid lethal intracellular ice and consequent cell death due to their lower surface-to-volume ratio[57]. Interestingly, we found that the optimal cooling rate of the larger aggregates favored a faster cooling rate (i.e., -3 ˚C/min) whereas the smaller aggregates required a slower cooling rate (i.e., -1 ˚C/min) to avoid significant loss of viable adherent cells (Figure 8), opposing the trend observed in the single cell-based literature.

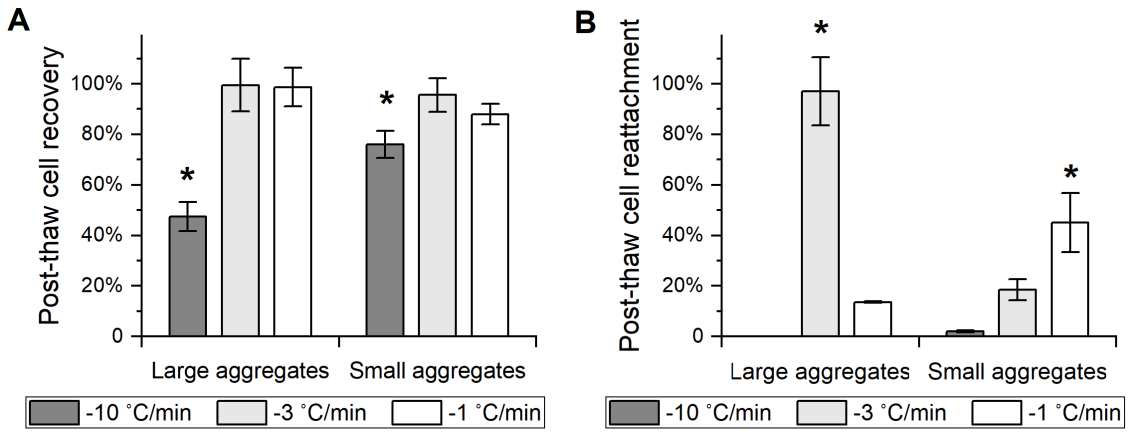

Figure 8. Post-thaw survival of hiPSC aggregates of different aggregate sizes in terms of (**A**) post-thaw cell recovery based on membrane integrity and (**B**) post-thaw cell reattachment based on viable, adherent cell count in 24 h post-thaw culture, showing drastically lower sensitivity of the membrane integrity assay to freezing damages caused by suboptimal cooling rates, -3 ˚C/min as the best cooling rate for the large aggregates and -1 ˚C/min as the best cooling rate for the small aggregates with statistical significance.

Combined with other findings in this chapter, it is clear that hiPSCs as a multicellular system respond to freezing in a complex fashion, and the successful establishment of post-thaw culture depends on various critical factors. Further studies will need to not only continue exploring additional factors to optimize the freezing protocol for hiPSCs but investigate the biological pathways connecting the factors and the observed cryopreservation outcomes to provide targets for future development of cryoprotective agents.

4.5 Conclusion

Inadequate preservation methods of human induced pluripotent stem cells (hiPSCs) have impeded efficient reestablishment of cell culture after freeze-thaw. In this chapter, we examined the roles of cooling rate, seeding temperature and the difference between cell

aggregates (3-50 cells) and single cells in controlled rate freezing of hiPSCs. Intracellular ice formation (IIF), post-thaw membrane integrity, cell attachment, apoptosis and cytoskeleton organization were evaluated to understand the different freezing responses between hiPSC single cells and aggregates, among cooling rates of -1, -3, -10 ˚C/min, and between seeding temperatures of -4, -8 ˚C. Raman spectroscopy images of ice showed that lower seeding temperature (-8 ˚C) did not affect IIF in single cells but significantly increased IIF in aggregates, suggesting higher sensitivity of aggregates to undercooling. In absence of IIF, Raman images showed greater variation of DMSO concentration across aggregates than single cells, suggesting cryoprotective agent transport limitations in aggregates. Ability of cryopreserved aggregates to attach to culture substrates did not correlate with membrane integrity for the wide range of freezing parameters, indicating inadequacy of using only membrane integrity-based optimization metrics. Lower cooling rates (-1, -3 ˚C/min) combined with higher seeding temperature (-4 ˚C) were better at preventing IIF and preserving cell function than higher cooling rate (-10 ˚C/min) or lower seeding temperature (-8 ˚C), proving the seeding temperature range of -7 to -12 ˚C from literature to be suboptimal. Unique f-actin cytoskeletal organization into a honeycomb-like pattern was observed in post-passage and post-thaw colonies and correlated with successful reestablishment of cell culture.

Chapter 5

Non-DMSO Cryoprotective Agents Synergistically Strengthen Hydrogen Bonds and Alter Solidification Behaviors of Water

Much of the text and figures in this chapter have previously appeared in the publications below, included here with copyright permission from John Wiley & Sons, American Chemical Society and Frontiers.

Yu G, **Li R** and Hubel A. Interfacial interactions of sucrose during cryopreservation detected by Raman spectroscopy. *Langmuir*. 2018. 35, 7388-7395.

Li R†, Hornberger K†, Duarte AR and Hubel A. Natural Deep Eutectic Systems for Improved Cryopreservation of Cells. *AIChE Journal.* 2021. 67, e17085.

Li R†, Hornberger K, Dutton J and Hubel A. Cryopreservation of iPS cell aggregates in a DMSO-free solution – an optimization and comparative study. *Frontiers in Bioengineering and Biotechnology.* 2020. 8, 1-13.

5.1 Introduction

Cryopreservation is the technology used to stabilize cells at cryogenic temperatures for a variety of research and clinical applications. The majority of mammalian cells are cryopreserved with dimethyl sulfoxide (DMSO) using slow cooling rates. Unfortunately, there are cells that respond poorly to this conventional method of freezing[153,154], and DMSO itself is associated with dangerous adverse effects when infused into the human body[155]. As a result, non-DMSO cryoprotective agents (CPA) such as sugars have been commonly utilized in the cryopreservation of various mammalian cell types to replace the use of DMSO[156–158]. In addition, we have recently demonstrated that sugars in

combination with sugar alcohols and amino acids are effective in preserving cells[46,80]. This chapter dissects the cryoprotective mechanisms of action of these non-DMSO CPAs in terms of the interaction of sugar with water and with cells, the interaction between sugar and sugar alcohol as well as their interaction with water and with cells, and the interaction of a complete multicomponent CPA solution with water, so as to build the scientific foundation for future DMSO-free cryopreservation designs.

5.1.1 Sucrose

Numerous studies have been performed to understand the mechanisms of protective properties of sucrose, most of which aimed at the interactions between sucrose and water, proteins and membranes. In dilute aqueous solutions, the destructuring effect of sucrose on the water tetrahedral hydrogen bond network has been observed in both experimental studies and molecular dynamics simulations[159,160]. In sucrose/water mixture at concentrations over 30%, it was found that all the water molecules were involved in hydrogen bonds with sucrose[161], and that the hydrogen bonds formed between sucrose and water significantly slowed down the water dynamics[162]. In these studies, the interactions between sucrose and water were examined based on a limited range of solute concentrations; however, the change of solute composition induced by the formation and growth of ice crystals in the real situation of cryopreservation might be substantial. As a result, it will be beneficial to explore the interactions between sucrose and water in a frozen sucrose solution.

The interactions between sucrose and macromolecules including proteins and membranes have been extensively examined, with several hypotheses being proposed to explain the protective properties of sucrose, including the water-replacement hypothesis[163–167] and the vitrification hypothesis[168]. Various techniques including infrared spectroscopy[166,167,169], nuclear magnetic resonance[170], differential scanning calorimeter[168] and molecular modeling[171] have been employed to provide supporting evidence for these hypotheses. However, there have been no studies to visualize the interactions between sucrose and cell membrane at a low temperature directly.

Interactions between cell and extracellular ice and their influence on cell survival have been systematically studied by the encapsulation and partitioning of cells in growing ice crystals[172–176]. It has been shown that interactions between cell and solidifying interface can produce a beneficial local environment to protect cells from damage[177]. However, information regarding the solute concentration at the interface between cell and extracellular ice was still lacking except for a few simulation studies[177,178]. It is still unclear how the cells interfere with the local solute transport ahead of the interface. Detailed knowledge of the distribution and concentration of sucrose relative to the cryopreserved cell is essential for understanding the interactions between the nonfrozen sucrose solution and cell, interactions between extracellular ice and cell, and dehydration induced cell damage.

Recently, Raman spectroscopy has been emerging as a powerful imaging tool to

investigate the freezing responses of various types of cells cryopreserved in different CPAs[70,80,90,91,101,102,107,179]. The high spatial resolution of Raman spectroscopy allowed us to visualize the distribution of extracellular and intracellular ice, CPAs and biological signals for single cells during freezing[91]. The morphology and size of ice crystals formed in different combinations of CPAs have also been successfully captured by Raman imaging[80,100]. Raman spectroscopy is sensitive to the structure of hydrogen bond network, making it a suitable tool to examine the effects of CPAs on the water hydrogen bond network at a low temperature[160]. In the first part of this chapter work, Raman spectroscopy was utilized to study the interactions between sucrose and water during freezing and to explore the biophysical environment at interfaces between cell and nonfrozen sucrose solution, between cell and extracellular ice, and between nonfrozen sucrose solution and ice. This work will enhance our understanding of the behaviors of sucrose solution at a low temperature and the mechanisms of its protective effects on cell.

5.1.2 Sugar-sugar alcohol natural deep eutectic systems

Natural deep eutectic systems or natural deep eutectic solvents (NADES) are solutions composed of primary metabolites including sugars, sugar alcohols, and amino acids at specific molar ratios that influence the freezing behavior of water[180]. Intermolecular hydrogen bonding between the NADES components and water results in strong depression of the melting point of the solution. Organisms that routinely survive below freezing temperatures, such as wood frogs, earthworms, and tardigrades, protect themselves naturally from freezing damage by synthesizing metabolites that likely form

NADES, resulting in melting point depression within the organism, reduced ice crystal formation and protection from osmotic stress[181,182].

NADES are emerging as alternative nontoxic solutions for a variety of applications, most commonly used as drug carriers or nontoxic extraction media to replace organic solvents[183]. NADES have been recently explored as potential CPAs (CPAs) for the preservation of mouse fibroblast cells[184] and lactobacillus[185]. Cells are commonly cryopreserved in 5-10% dimethyl sulfoxide (DMSO)[186], which is cytotoxic and unsuitable for cells intended to be administered to patients as cell therapies[187]. Thus, there is great interest in the development of non-DMSO CPAs for the cryopreservation of cells. Pure NADES typically have high viscosities, making them unsuitable for cell preservation, but previous studies have shown that NADES can be added to water to decrease their viscosity [184,188–191]. In particular, a NADES composed of trehalose and glycerol (T:G) has been shown to successfully preserve mouse fibroblast cells when added to water (10% w./v. T:G)[184].

In our previous studies, we used naturally occurring metabolites to develop an optimized multicomponent osmolyte (MCO) solution for the cryopreservation of Jurkat cells, an immortalized cell line used as a T lymphocyte model, via a differential evolution algorithm-driven optimization process. The optimized MCO solution composed of trehalose, glycerol, and isoleucine (TGI) resulted in 84% post-thaw recovery of Jurkat cells[86].

In the second part of this chapter, we study Jurkat cell cryopreservation using T:G NADES diluted in Normosol-R and supplemented with isoleucine to explore the capability of NADES as a CPA and the benefit of isoleucine as an additional CPA. Freezing behavior is characterized for all the dilute NADES solutions experimented in this study in comparison with the preexisting MCO solution and a standard DMSO solution. Differential Scanning Calorimetry (DSC) is used to define the thermophysical properties of the various CPA solutions. Raman spectroscopy is used to characterize the effect of T:G NADES on hydrogen bonding as well as the microscopic behavior of water at low temperatures. Cells are also frozen in NADES, MCO and DMSO solutions using a controlled rate freezing method, and post-thaw apoptosis and proliferation are used to quantify the freezing responses of the cells.

5.1.3 Multicomponent non-DMSO CPA solution

The last part of this chapter focuses on the effect of a multicomponent non-DMSO CPA solution derived from the cell-based studies described in Chapter 6, herein providing mechanistic insights to the practical benefits observed in later context. The CPA components include sucrose, glycerol, L-isoleucine, human serum albumin (HSA), and poloxamer 188 (P188), all of which are nontoxic and FDA-approved for infusion. Low-temperature Raman spectroscopy is used to analyze the freezing behavior of water in solution with an optimized versus deviated formulation of these five types of CPAs. This comparison investigates particularly the effect of subtle difference in the concentration of

individual CPAs on the cryoprotective effect of the complete CPA solution. Differential scanning calorimetry (DSC) is used to analyze the thermophysical behaviors of the optimized and deviated CPA solutions, as well as their variant forms each with one component of interest removed. This controlled experiment, in combination with other low-temperature Raman spectroscopy results in this chapter, examines the mechanism of action of the non-DMSO CPAs, individually and in concert, and the significance of their cryoprotective property.

5.2 Methods

Jurkat cells (ATCC, TIB-1522) were used as a cell model to aid the cell-based investigation of sucrose and dilute T:G NADES. They were cultured as described in section 3.2.2. No cells but the aqueous solutions alone were used in investigation of the complete multicomponent CPA formulation. Aqueous solutions of sucrose at varying concentrations, of T:G NADES at varying dilution ratios supplemented with varying concentrations of isoleucine, and of sucrose, glycerol, isoleucine, HSA and P188 at varying compositions were respectively formulated for the following experiments as described in section 3.4. The multicomponent non-DMSO CPA solutions discussed in this article are covered by issued Patent #10,314,302 and patent application #16/383,165, owned by Regents of the University of Minnesota.

To confirm the formation of NADES, mixtures of trehalose and glycerol at a molar ratio of 1:10 and 1:30 were imaged using a Zeiss TIRF imaging system in its phase contrast

configuration with a 20x air objective (Plan-Apochromat, NA 0.8, Zeiss) and a Zeiss AxioCam MRm 12-bit monochrome camera. Microscope slides containing 2-3 drops of each solution were observed under the microscope. The sample space was surveyed to verify the absence of sugar crystals or obtain the microscopic images of identified sugar crystals. Fibrous debris and dust particles in the samples were excluded based on their morphology. Osmolality of the dilute NADES was measured as described in section 3.16. A dilution curve was created to validate a linear relationship between the dilution ratio of NADES in water and the measurement of osmolality and was used to extrapolate the osmolality of solutions that were out of range of the osmometer.

Low-temperature Raman spectroscopy was set up as described in section 3.13.1. Independent experiments were performed with final sample temperature stabilized respectively at 20 ˚C, -10 ˚C and -50 ˚C to collect Raman data. For freezing experiments, ice nucleation was induced manually at a constant temperature of -6 ˚C. Samples containing cells were cooled at a constant rate of -1 ˚C/min, whereas samples containing aqueous solutions alone were cooled at a constant rate of -10 ˚C/min. When the samples stabilized at each target temperature, Raman images of cell (1660 cm^{-1}), ice (3125 cm^{-1}), sucrose (850 cm^{-1}), and DMSO (695 cm^{-1}) were rendered, and Raman spectra at various points of interest were acquired as described in section 3.13.2. Raman images were spatially deconvolved as described in section 3.13.3. Differential scanning calorimetry (DSC) was performed, and DSC results were analyzed as described in section 3.15. Samples were run in independent triplicate.

Jurkat cells were frozen in vials at a concentration of 6×10^6 cells/ml upon 1 h incubation at room temperature. Controlled rate freezing was performed as described in section 3.6.1 with a constant cooling rate of -1 ˚C/min and a constant ice nucleation temperature of -8 ˚C. After 24 h storage in the vapor phase of liquid nitrogen, post-thaw recovery was quantified for 6 independent biological replicates as described in section 3.7. Post-thaw cell growth was monitored daily for 3 days in independent biological replicates as described in section 3.9. Post-thaw cell apoptosis was measured as described in section 3.10.

In this chapter, data was represented as mean plus/minus standard error. Two-tailed student *t*-tests were performed for two-sample comparisons, and one-way ANOVA tests with Bonferroni correction were performed for comparisons between multiple sample groups to obtain *p*-values with a significance level set at 0.05. One-sample hypothesis testing was performed using a T distribution on the DSC measurements, post-thaw cell recovery rates and proportions of post-thaw apoptosis subpopulations, and 95% confidence intervals were calculated. Null hypothesis was defined as no statistically significant difference between any pair of samples. *p*-value less than 0.05 was used to reject the null hypothesis and determine the statistical significance. Power analysis was performed for the experiments in this study to ensure sufficient sample size with a power of 0.95.

5.3 Results

5.3.1 Sucrose aqueous solution between ice concentrated beyond solubility limit

In order to characterize the behaviors of a nonfrozen sucrose solution at a low temperature, 730 mM sucrose solution was seeded at -6 ˚C and cooled at -1 ˚C/min to -10 ˚C or -50 ˚C. Raman images rendered on the signals associated with ice and the sucrose were generated (Figure 9A). Spectra were averaged over the area of nonfrozen sucrose solution (excluding the influence of ice) for both temperatures and further normalized to the CH_2 stretching peak at 2936 cm^{-1} of the spectra at -50 ˚C[192] (Figure 9B). The stronger intensity of CH_2 stretching peak at -50 ˚C compared to that at -10 ˚C indicates a substantial increase of sucrose concentration as the temperature decreased. In order to determine the concentration of nonfrozen sucrose solution at a low temperature, Raman spectra of sucrose solutions with concentration ranging from 2920 mM to 4380 mM were collected. A calibration curve was developed based on the ratio of peak intensity at 2936 cm^{-1} to the peak intensity at 3420 cm^{-1} (Figure 9C and D). The concentration of sucrose in the nonfrozen solution at -10 ˚C was estimated to be 3650 mM. The concentration at -50 ˚C exceeded the range of the calibration curve, greatly higher than 4380 mM (i.e., the solubility limit achieved at room temperature), and no extrapolation was used to estimate the exact concentration (Figure 9D).

Raman spectra could also be used to characterize the hydrogen bond network of the nonfrozen solution. The broad OH stretching peak from 3100 cm^{-1} to 3800 cm^{-1} has been decomposed into symmetric OH stretching centered at 3230 cm^{-1} (corresponding to

tetrahedral hydrogen bond of water molecules) and asymmetric OH stretching centered at 3420 cm^{-1} (corresponding to a partially developed hydrogen bond of water molecules) for dilute sugar solutions[160,193]. However, in this work, the high concentration of nonfrozen sucrose solution no longer qualified as dilute sugar solution, and the OH stretching from sucrose also contribute to the broad OH stretching peak, so the method of decomposing OH stretching peak into symmetric and asymmetric OH stretching of water was not performed. However, it could still be observed that peak intensity at 3420 cm^{-1} slightly decreased from -10 ˚C to -50 ˚C in Figure 9B, and the whole OH stretching peak shifted to a lower wavenumber as the temperature decreased.

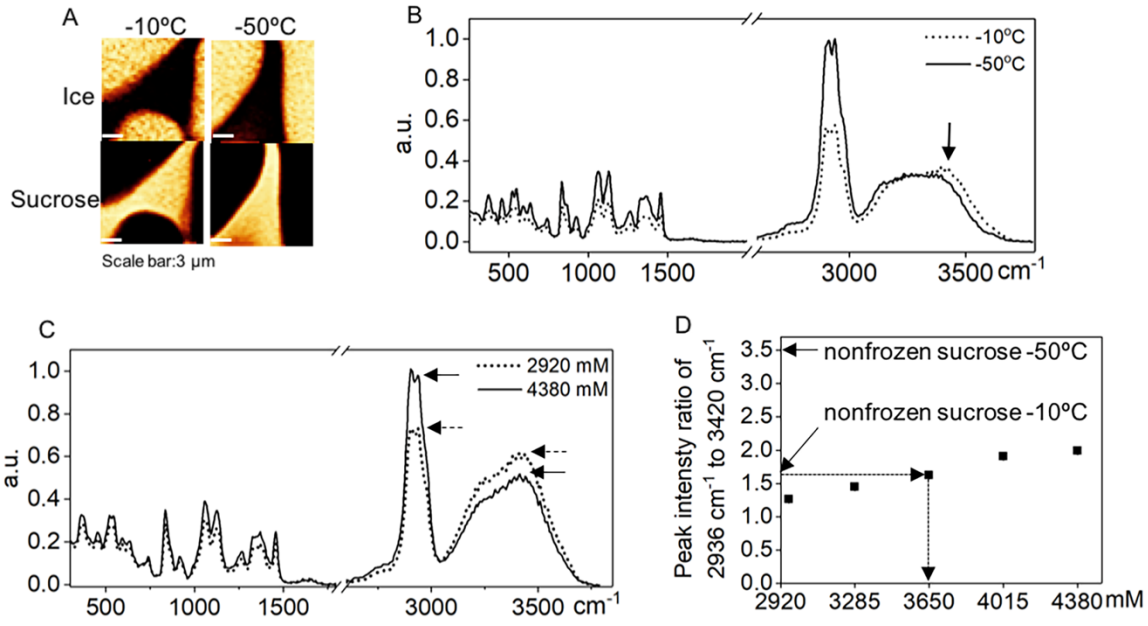

Figure 9. Raman analysis of sucrose concentration in nonfrozen solution. (**A**) Raman images of ice and nonfrozen sucrose solution at -10 ˚C and -50 ˚C for 730 mM sucrose solution. (**B**) Raman spectra averaged over the nonfrozen sucrose solution area at -10 ˚C and -50 ˚C. (**C**) Raman spectra of 2920 mM and 4380 mM sucrose solution. (**D**) Peak intensity ratio of 2936 cm^{-1} to 3420 cm^{-1} for a range of sucrose concentration. This ratio for Raman spectra averaged over nonfrozen sucrose solution at -10 ˚C and -50 ˚C were 1.6 and 3.5 respectively. [Experiments for this figure were performed by Guanglin Yu.]

Complex solutions, such as sucrose and water, freeze over a range of temperatures and the high spatial resolution of the Raman microscopy enabled us to closely investigate the nonfrozen solution between two adjacent ice crystals. Across the gap filled with nonfrozen solution (Figure 10A), a red arrow was drawn from one ice crystal through the nonfrozen sucrose solution to the other ice crystal. Normalized sucrose concentration and ice intensity were plotted (Figure 10B). At the interface of ice crystal and nonfrozen sucrose solution, the concentration of sucrose gradually increased away from the ice, while the ice density gradually decreased into the sucrose solution. The gradual nature of the changes in sucrose concentration and ice density at the interface was consistent with results shown by other interfacial studies. Across this channel of sucrose solution, the distribution of sucrose was relatively uniform in the non-interfacial region. The plateau of sucrose across the narrow channel of nonfrozen solution was unlike the accumulation of solutes at the interface during dynamic freezing process[194]. The high lateral and spectral (chemical) resolution of confocal Raman spectroscopy allowed us to observe the sucrose-ice interface on the submicron level. On the other hand, its lower axial and temporal resolution limited our ability to study the interface on the third dimension or capture transient states of the interface during freezing. The analysis here illustrates the interface in a relatively steady state, where images were taken roughly one hour after seeding and 30 minutes after reaching -50 ˚C.

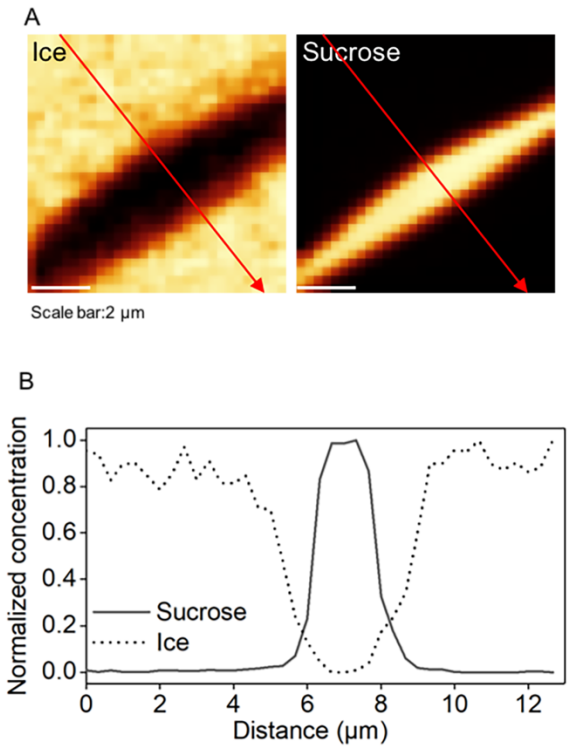

Figure 10. Raman analysis of sucrose-ice interface. (**A**) Raman images of sucrose and ice at -50 ˚C for 730 mM sucrose solution. (**B**) Normalized sucrose concentration and ice intensity along the red arrow. [Experiments for this figure were performed by Guanglin Yu.]

5.3.2 Nonfrozen sucrose solution of submicron thickness in and around cell membrane

It is generally accepted that sugars such as sucrose and trehalose are not cell-penetrating, although several techniques have been proposed to load sugars into cells to improve cell survival[195–197]. However, studies that explore the precise distribution of sucrose relative to the cryopreserved cells are limited. To remedy this gap, Jurkat cells were cryopreserved in 730 mM sucrose solution at -1 ˚C/min to -50 ˚C, and Raman images were rendered on the signals associated with sucrose, as well as of the ice and cell (amide I) (Figure 11A). Raman images of sucrose demonstrated that sucrose was predominantly distributed outside the cell. The cell membrane was either in close proximity to the

extracellular ice or connecting with a nonfrozen sucrose solution between adjacent ice crystals. It is noteworthy that sucrose was present at the interface between cell membrane and extracellular ice and formed a thin layer of nonfrozen solution surrounding the cell, which, to the best of our knowledge, has never been observed before.

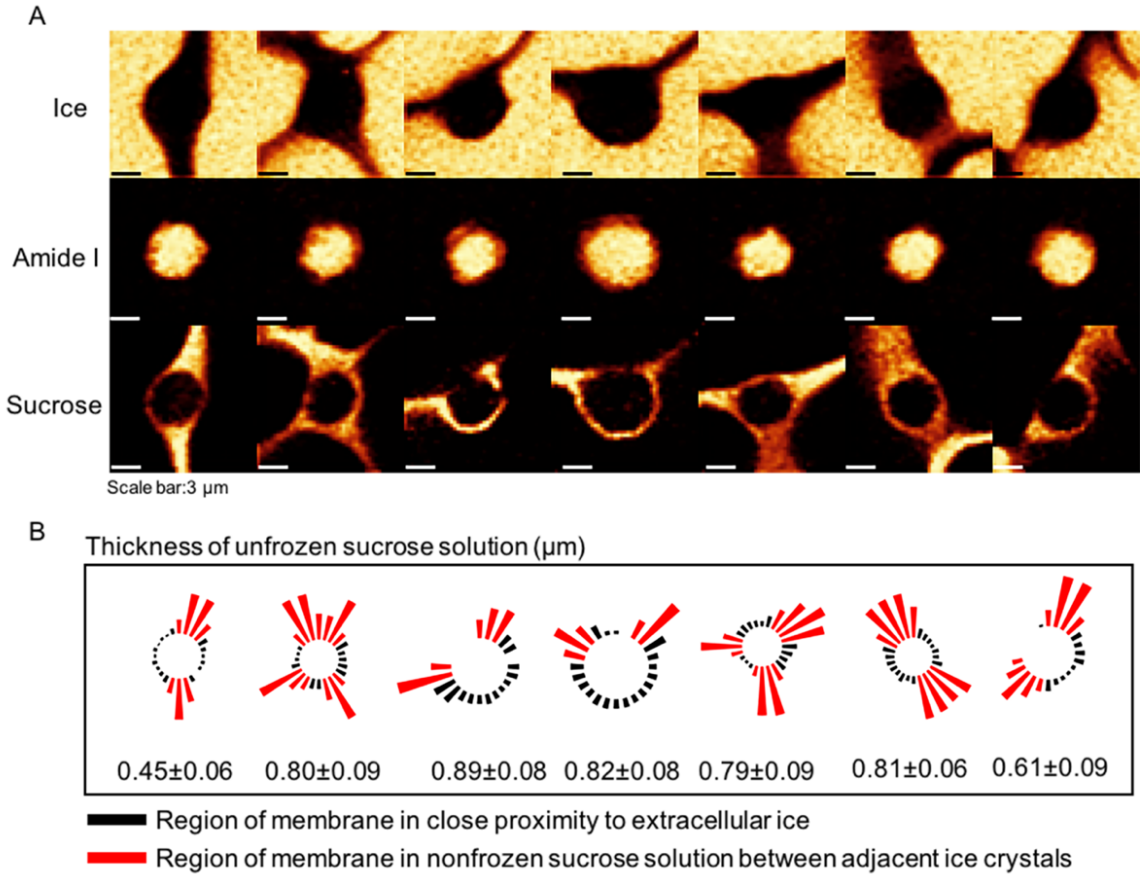

Figure 11. Raman analysis of spatial separation between Jurkat cells and ice. (**A**) Raman images of ice, cell (amide I) and sucrose for Jurkat cells cryopreserved in 730 mM sucrose solution. (**B**) The thickness of the nonfrozen sucrose solution around the cell. For the regions where solution thickness is not indicated, the thickness is less than the spatial resolution of the microscope (~300 nm). [Experiments for this figure were performed by Guanglin Yu.]

The thickness of the layer of sucrose solution between the cell membrane and the extracellular ice was calculated, and the average thickness was in the range of 0.4-0.9 μm

(Figure 11B). Distances between the cell membrane and extracellular ice that were below the lateral spatial resolution of the confocal Raman microscope could not be resolved. Raman images of ice showed little intracellular ice formation (IIF) in the cryopreserved cells, and Raman images of cells showed that the cells maintained their normal circular morphology.

Cells were trapped between adjacent ice crystals whose geometric proximity to the cell was not uniform. The next phase of investigation involved quantifying the variation in the sucrose concentration in a gap between a cell and the ice phase. Raman images of ice, cell (amide I) and sucrose were shown for the cell used for analysis (Figure 12A). The normalized sucrose concentration was obtained along the white arrow passing through the interface (Figure 12B). The sucrose concentration at the interface between cell and extracellular ice was lower than that in bulk nonfrozen solution (Figure 12C). It was also noteworthy that the ice front was curved when close to the cell (Figure 12A).

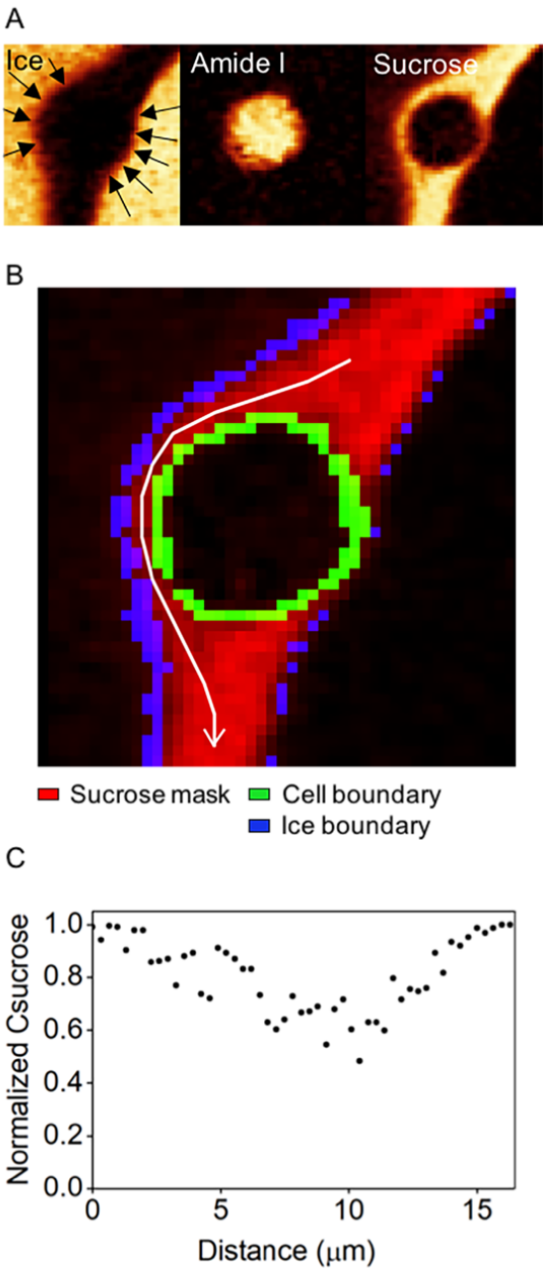

Figure 12. Raman analysis of heterogeneity of sucrose distribution around a cell. (**A**) Raman image of ice, cell (amide I) and sucrose for the cell used for analysis. (**B**) Binary image showing the location of white arrow used to illustrate sucrose concentration. (**C**) Normalized sucrose concentration obtained along the white arrow in (B). [Experiments for this figure were performed by Guanglin Yu.]

In order to further examine the interactions between cell and sucrose solution, a cell

engulfed in ice was analyzed (Figure 13A). Binary masks were created from Raman images of sucrose and amide I to indicate the location and area of sucrose solution and cell, and the overlay of the two binary masks was observed (Figure 13B). Averaged Raman spectra over the sucrose mask in Figure 13B showed both peaks of sucrose (box 1) and amide I (box 2), substantiating the overlap between sucrose solution and cell (Figure 13C). Raman spectra averaged over the cell area (excluded the overlapping area of cell and sucrose) showed much lower OH stretching peak than that of cell in DPBS at room temperature, indicating dehydration of the cells cryopreserved in sucrose solution (Figure 13D).

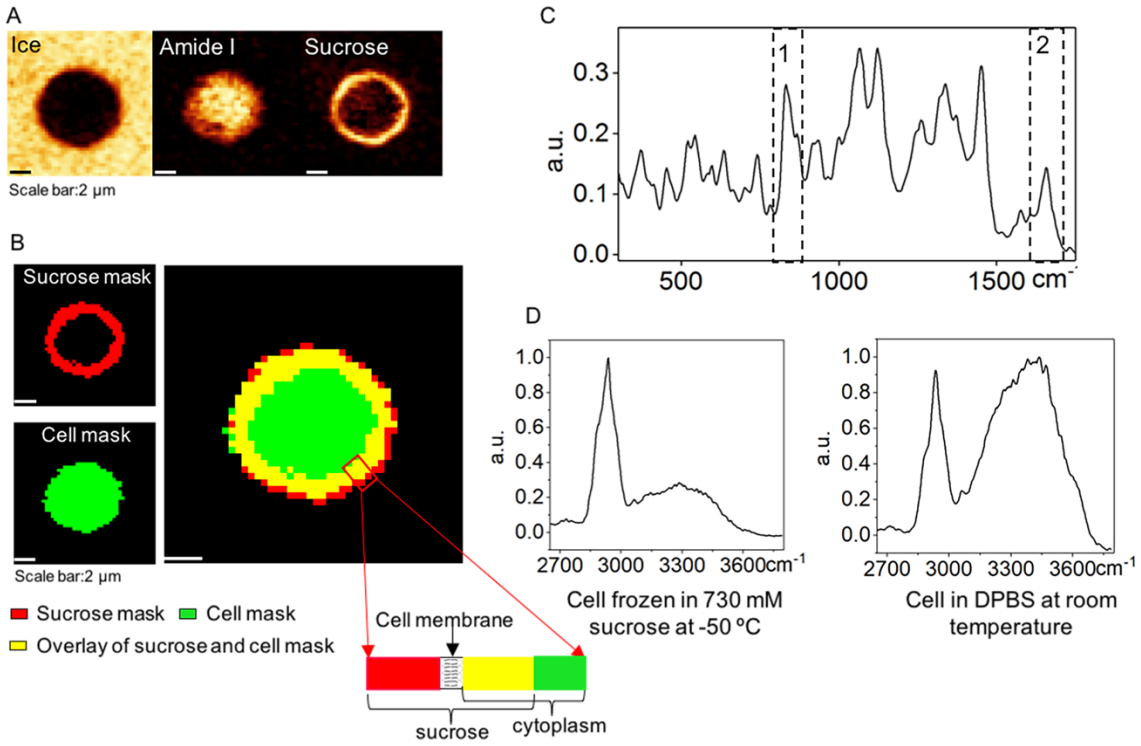

Figure 13. Raman analysis of spatial overlap between sucrose and cell. (**A**) Raman image of ice, cell (amide I) and sucrose for a Jurkat cell cryopreserved in 730 mM sucrose. (**B**) Binary masks of location and area of unfrozen sucrose solution and cell, and corresponding overlay of the two masks. Rectangle area showing the location of cell membrane relative to the sucrose solution. (**C**) Raman spectra averaged over the sucrose mask. Box 1 indicates Raman signal of sucrose and box 2 indicates Raman signal of amide I. (**D**) Raman spectra of a cell cryopreserved in 730 mM sucrose solution at -50 ˚C and in DPBS at room temperature. [Experiments for this figure were performed by Guanglin Yu.]

Furthermore, the partitioning of sucrose across the cell membrane was quantified by correlating intracellular and extracellular sucrose concentration for a Jurkat cell frozen in a 730 mM sucrose solution. A red arrow was drawn in the Raman image of sucrose, and normalized sucrose concentration was calculated (Figure 14A). The intracellular sucrose concentration was less than 10% of the extracellular sucrose concentration. The same method was employed on another Jurkat cell frozen in a 934 mM sucrose solution,

showing that the intracellular and the extracellular sucrose concentrations were comparable. This implies the breakdown of cell membrane (Figure 14B), which is consistent with the fact that Jurkat cells frozen in 934 mM sucrose exhibited poor post thaw recovery (data not shown). There was little IIF in both cells, based on the Raman images of ice. The partitioning of 10% DMSO across the cell membrane was also examined. It was found that the intracellular DMSO concentration was lower than the extracellular DMSO concentration (Figure 14C). Unlike sucrose, the gap between extracellular ice and the cell cryopreserved in DMSO solution was beyond the resolution limit of the Raman microscopy.

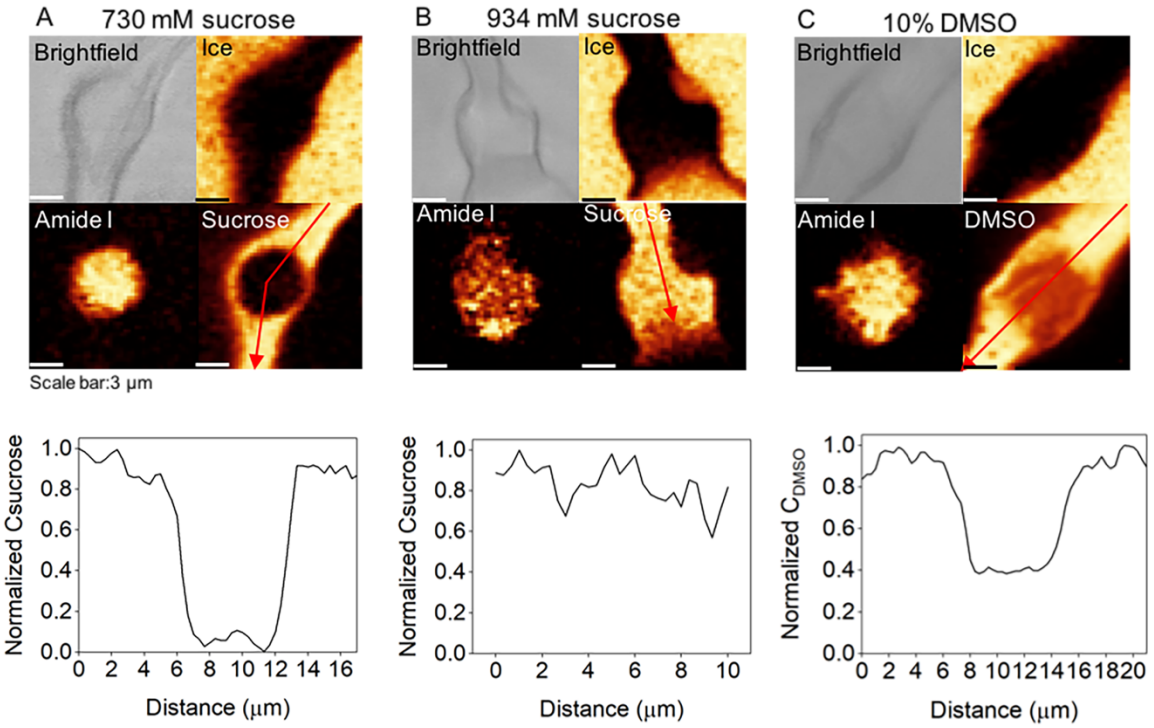

Figure 14. Membrane partitioning of sucrose. (**A**) Brightfield image and Raman image of ice, cell (amide I) and sucrose for a cell cryopreserved in 730 mM sucrose solution. Normalized sucrose concentration was obtained across the red arrow. (**B**) Brightfield image and Raman image of ice, cell (amide I) and sucrose for a cell cryopreserved in 934 mM sucrose solution. Normalized sucrose concentration was obtained across the red arrow. (**C**) Brightfield image and Raman image of ice, cell (amide I) and DMSO for a cell

cryopreserved in 10% DMSO solution. Normalized DMSO concentration was obtained across the red arrow. Representative images of one cell were selected from eight different cells and shown here for each condition. [Experiments for this figure were performed by Guanglin Yu.]

During freezing, cells respond to the change of composition of a nonfrozen solution by an efflux of water[56,198,199]. Cells cryopreserved in a 730 mM sucrose solution were significantly dehydrated, as demonstrated by the Raman spectra; however, the cell membrane was still intact. Raman spectroscopy also enables us to determine loss of membrane integrity during freezing, which could not be detected by conventional microscopy without a fluorescent tag. The freezing of cells in 934 mM sucrose solution demonstrated such a loss in membrane integrity, and corresponding post thaw recoveries were poor.

5.3.3 Formation of NADES confirmed by light microscopy

The T:G NADES was prepared at a molar ratio of 1:30[184], which resulted in the formation of a clear viscous liquid after continuous mixing at 70 ˚C (Figure 15A). Phase contrast microscopic imaging at room temperature showed that no trehalose crystals were formed in the T:G 1:30 NADES, while sugar crystals were easily found in the mixture of trehalose and glycerol at a molar ratio of 1:10, as exemplified in Figure 15B.

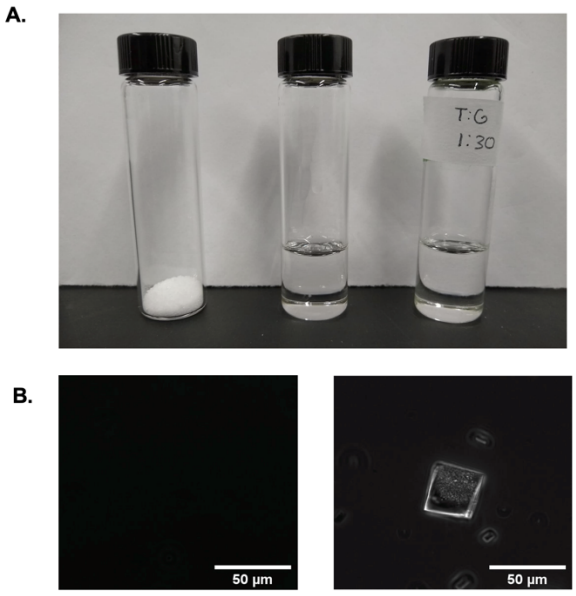

Figure 15. Visual confirmation of NADES formation. (**A**) From left to right: trehalose, glycerol, and T:G 1:30. (**B**) Confocal microscope image of T:G 1:30 shows no undissolved crystals (left) while trehalose and glycerol at a molar ratio of 1:10 shows undissolved crystal (right). [Experiments for this figure were performed by Kathlyn Hornberger and Adam Joules.]

5.3.4 T:G NADES distinct from trehalose and glycerol alone in interaction with water

To demonstrate the effect of NADES formation on the freezing behaviors of water, aqueous solutions containing only trehalose, only glycerol or T:G NADES of equivalent concentrations of trehalose and glycerol were frozen and analyzed using low-temperature Raman spectroscopy. Both ice crystal morphology and hydrogen bonding were characterized.

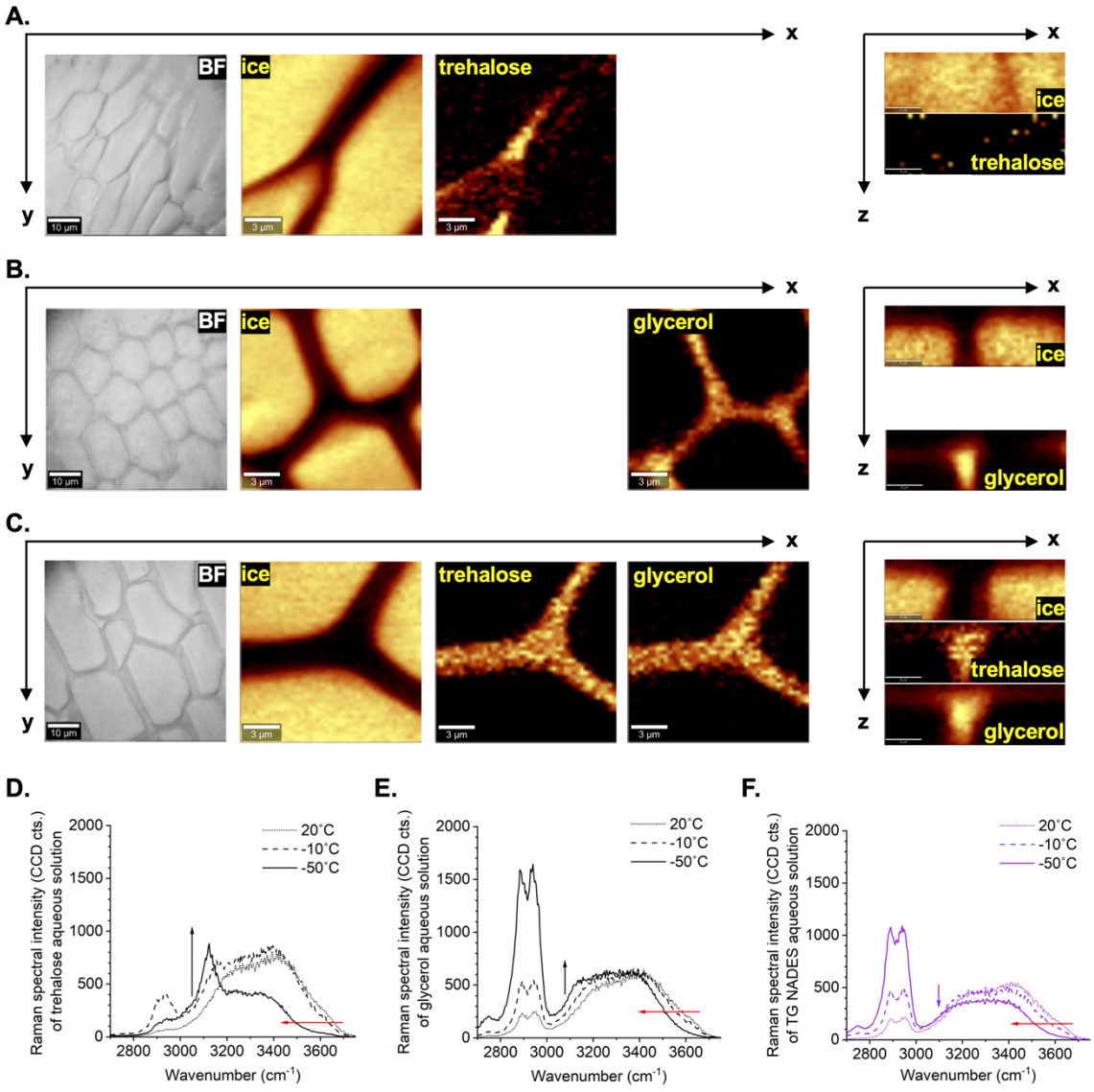

Figure 16. Ice crystal morphology and nonfrozen hydrogen bond network. (**A**-**C**) Brightfield images (scale bar: 10 µm) and Raman spectral heat maps (scale bar: 5 µm) of ice, trehalose and glycerol acquired in both lateral and axial planes at -50 ˚C for (**A**) 1.1% w./v. trehalose in Normosol-R, (**B**) 8.9% w./v. glycerol in Normosol-R and (**C**) 10% w./v. T:G NADES in Normosol-R, showing difference in ice morphology and width of the nonfrozen channel between ice crystals, the quantified results of which are given in Table 4. (**D**-**F**) Overlaid Raman spectra independently acquired at 20 ˚C, -10 ˚C and -50 ˚C from (**D**) 1.1% w./v. trehalose in Normosol-R, (**E**) 8.9% w./v. glycerol in Normosol-R and (**F**) 10% w./v. T:G NADES in Normosol-R, showing difference in shift of the OH stretching band (solid arrows) in response to temperature decrease.

As shown by the brightfield images in Figure 16A-C, ice morphology was different among the three solutions of interest. Ice crystals were fitted to ellipses, and ellipticity was defined by the first flattening:

$$f = \frac{(a - b)}{a}$$

f: ellipticity (or first flattening); a: semimajor axis; b: semiminor axis.

As quantified from Raman heat maps in Figure 16 (Table 4), the ellipticity of ice crystals that formed in 10% T:G NADES solution at -50 ˚C was significantly lower than that in the solution composed of trehalose alone but significantly higher than that in the solution composed of glycerol alone. However, the distance between adjacent ice crystals in the NADES solution was significantly greater than that in the trehalose or glycerol solution.

Table 4. Quantified morphology of ice crystals in Raman heat maps[a]

CPA solutions	**Ellipticity of ice crystals**	**Distance between adjacent ice crystals (μm)**
1.1% w./v. trehalose	0.617 ± 0.096	0.956 ± 0.504
8.9% w./v. glycerol	0.212 ± 0.071	1.607 ± 0.288
10% w./v. T:G	0.436 ± 0.073*,†	2.328 ± 0.417*,†

[a]CPA: cryoprotective agents; T:G: NADES composed of trehalose and glycerol at 1:30 molar ratio and equivalent concentrations to the single component solution. 95% confidence intervals each calculated from a sample size greater than 8 using a T distribution. *: $p < 0.05$ compared to the trehalose solution using ANOVA with Bonferroni correction; †: $p < 0.05$ compared to the glycerol solution using ANOVA with Bonferroni correction.

To characterize hydrogen bonding during freezing, the trehalose, glycerol and T:G NADES solutions were also cooled to different final temperatures using a constant

cooling rate. Raman spectra were acquired in the middle of a nonfrozen region. All three compositions of interest remained in solution as temperature decreased (no precipitation was observed). As shown in Figure 16D-F, a red shift of the broad OH stretching band was observed in all samples as temperature decreased, indicating lower-energy vibration of the chemical bonds and therefore, a strengthened hydrogen bond network. For the sample containing only trehalose, the OH stretching peak of ice was clearly visible at -50 ˚C in the Raman spectra at the visually based middle of the nonfrozen region, indicating that the space between adjacent ice crystals was less than 333 nm (the spatial resolution of the Raman microscope) apart (Figure 16D). In comparison, the sample containing only glycerol was found with an upshift of the ice region of the broad OH stretching band (Figure 16E), whereas the NADES sample was found with a downshift of the entire OH stretching band (Figure 16F) as temperature decreased. This result suggests suppression of ice formation by NADES in comparison to its two components separately.

5.3.5 Thermophysical property of dilute NADES unaffected by addition of isoleucine

The thermophysical properties of varying NADES compositions, a multicomponent osmolyte (MCO) solution containing trehalose, glycerol and isoleucine (TGI), and a DMSO solution were measured using DSC. Melting temperature, enthalpy of melting, glass transition temperature, and softening temperature were calculated and are listed in Table 5.

Table 5. DSC measurements of melting temperatures, enthalpy of melting, glass transition and softening temperatures for NADES, MCO and DMSO solutions[a]

CPA solutions		T_m (˚C)	ΔH_m (J/g)	T_g (˚C)	T_s (˚C)
NADES solutions	5% T:G	-5.407 ± 1.709	248.867 ± 17.497	-88.823 ± 1.322	-64.047 ± 3.384
	10% T:G	-8.660 ± 0.197*	201.133 ± 5.601*	-93.917 ± 0.291*	-65.813 ± 4.143
	15% T:G	-10.347 ± 1.963*	199.633 ± 28.799*	-95.353 ± 0.619*	-66.253 ± 2.758
	5% T:G + 10.75 mM isoleucine	-5.820 ± 0.323	249.167 ± 10.231	-89.700 ± 1.193	-63.983 ± 3.253
	5% T:G + 21.5 mM isoleucine	-5.527 ± 1.491	249.767 ± 12.740	-87.597 ± 0.436	-63.707 ± 0.274
	5% T:G + 43 mM isoleucine	-5.367 ± 0.188	250.333 ± 16.807	-86.463 ± 0.911*	-63.243 ± 3.098
TGI (MCO)		-7.853 ± 0.438†	206.600 ± 2.370†	-91.490 ± 2.035	-63.220 ± 1.334
10% DMSO		-10.270 ± 0.422†	188.467 ± 11.578†	-121.150 ± 0.675†	(N/A)

[a]DSC: differential scanning calorimetry; NADES: natural deep eutectic system; TGI or MCO: a multicomponent osmolyte solution containing trehalose, glycerol and isoleucine; DMSO: dimethyl sulfoxide; CPA: cryoprotective agents; T:G: NADES composed of trehalose and glycerol at 1:30 molar ratio; T_m: melting temperature; ΔH_m: enthalpy of melting; T_g: glass transition temperature; T_s: softening temperature. 95% confidence interval calculated from 3 independent replicates for each sample using a T distribution. *: $p < 0.05$ in two-sample comparison with 5% T:G. †: $p < 0.05$ in two-sample comparison with 5% T:G + 21.5 mM isoleucine.

T:G NADES diluted in Normosol-R showed lower melting temperature and enthalpy of

melting as the percentage of NADES increased (Figure 17A, $p < 0.05$). Lower melting temperature indicates depressed ice crystallization, and lower enthalpy of melting indicates a reduced amount of ice crystal formation. Based on recent unpublished work by Adam Joules et al., deepness of dilute T:G NADES was estimated using equation

$$\text{Deepness} = T_m\_\text{trehalose alone} + T_m\_\text{glycerol alone} - T_m\_\text{T:G}$$

and found to be statistically equal to 0 for 5% – 20% T:G and greater than 1 for 30% and higher concentrations. This result indicated that working concentrations of T:G NADES in the present study were too dilute to exhibit deep eutectic behavior (i.e., having an effect of depressing ice crystallization no greater than the combined effect of their individual trehalose and glycerol components).

As 5% T:G was determined to be the optimal dilution for post-thaw survival of Jurkat cells, the thermophysical properties of 5% T:G supplemented with different concentrations of isoleucine were determined. DSC results of 5% T:G with varying amounts of isoleucine showed no significant change in melting temperature or enthalpy of melting (Figure 17B), indicating that adding isoleucine did not significantly depress or suppress ice formation. Figure 17C compares the melting profiles of the optimized NADES (i.e., 5% T:G supplemented with 21.5 mM isoleucine), MCO, and 10% DMSO solutions. The optimized NADES solution has the highest melting temperature and enthalpy of melting, while 10% DMSO has the lowest.

The glass transition, consisting of glass transition temperature and softening temperature,

was also measured for each solution. The glass transition is defined as the transition of a cooling material from a viscoelastic to a glassy state, and softening temperature is when the warming material becomes viscoelastic, collapsing under its own weight[109,200,201]. As the percentage of NADES increased, the glass transition ($p < 0.05$) and softening ($p > 0.05$) temperatures decreased (Figure 17D). Comparing the three isoleucine-containing solutions shows that the addition of isoleucine gradually increased the glass transition and softening temperatures (Figure 17E). This increase in glass transition temperature increases the stability of the solution in cryogenic storage, while transient warming above this temperature could damage the cells. Both glass transition peaks were identified for all the tested solutions except for 10% DMSO (Figure 17F).

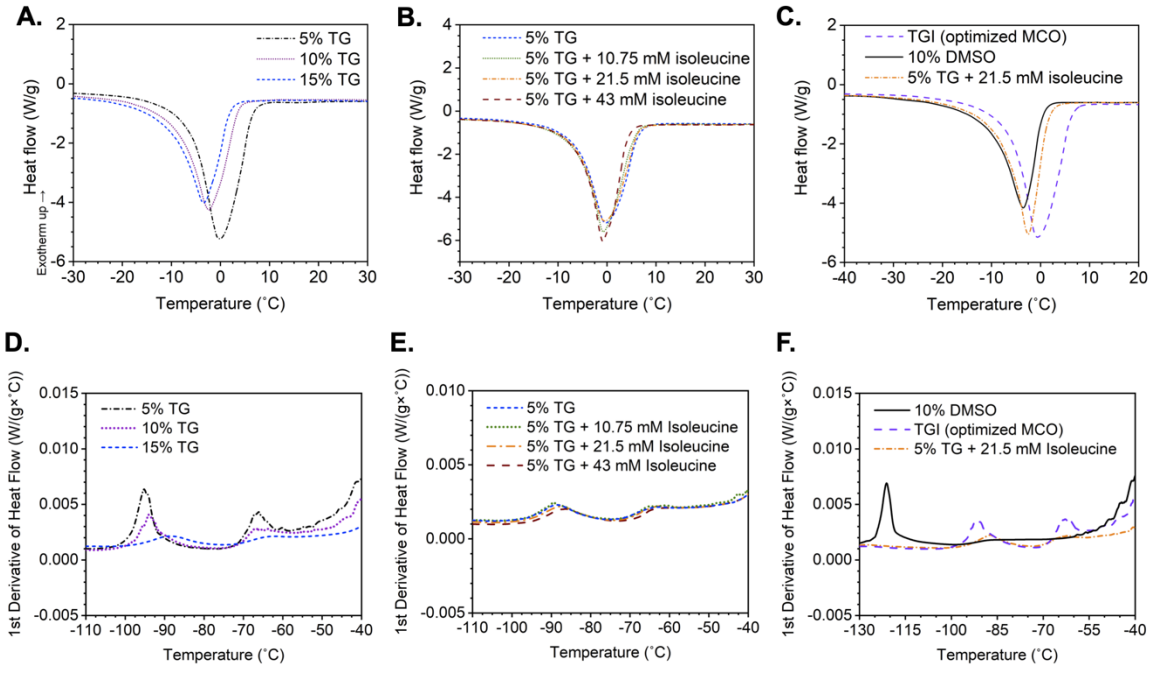

Figure 17. DSC melting profiles (**A**-**C**) and glass transitions (**D**-**F**) of (**A**, **D**) 5, 10, and 15% (w/v) T:G in Normosol-R, (**B**, **E**) 5% T:G with increasing concentration of isoleucine, and (**C**, **F**) 5% T:G with 21.5 mM isoleucine (optimized NADES), TGI (optimized MCO), and 10% DMSO (control). [Experiments for this figure were performed by Kathlyn Hornberger.]

5.3.6 More concentrated NADES aqueous solution measured higher in osmolality

Cryopreservation solutions are typically hypertonic, and the cells must respond to the changes in osmolarity (or osmolality) in their environment both at introduction of the CPA solution pre-freeze and removal of the solution post-thaw. In order to characterize the solutions, the osmolality of the T:G NADES and MCO were measured and are shown in Table 6. A higher percentage of NADES resulted in higher osmolality, and the TGI MCO had comparable osmolality to the 10% T:G NADES. Significant cell losses were not observed for a single step introduction of the NADES solutions for NADES compositions < 20% (data not shown).

Table 6. Osmolality measurements of increasing NADES concentration (%w/v) in Normosol-R and MCO[a]

CPA Solution	Osmolality (mOsm/kg)
5% T:G	640 ± 10
10% T:G	1350 ± 60
15% T:G	1710 ± 10*
TGI (MCO)	1340 ± 10

[a]NADES: natural deep eutectic system; MCO or TGI: a multicomponent osmolyte solution containing trehalose, glycerol and isoleucine; CPA: cryoprotective agent; T:G: NADES composed of trehalose and glycerol at 1:30 molar ratio. 95% confidence interval calculated from 3 independent replicates for each sample using a T distribution. *Estimated osmolality extrapolated using a dilution curve (Figure 18).

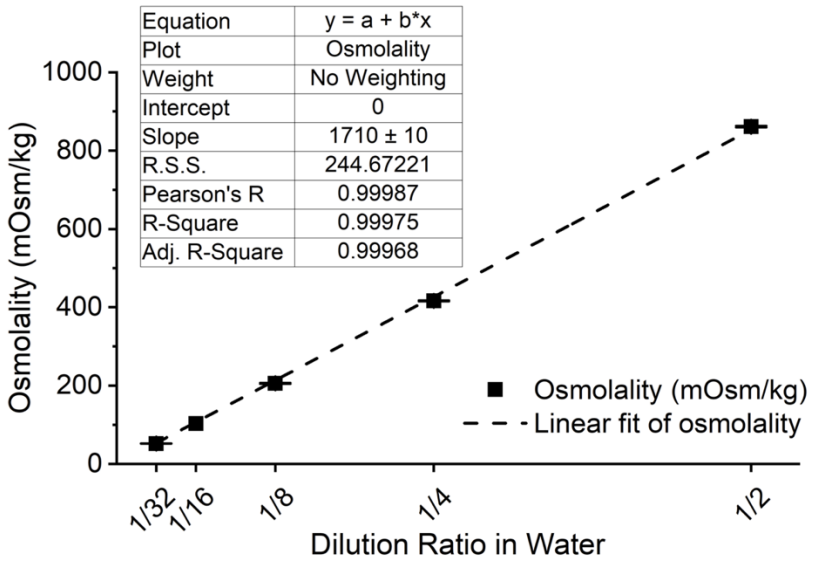

Figure 18. Dilution curve showing linear regression of osmolality measurements with a dilution ratio of 15% T:G NADES in water. Curve fitting was performed using OriginLab with no weighting and intercept of 0. R-square values close to 1 determined that over 99.9% of the variance in the measured osmolality was predictable from the dilution ratio of the NADES in water. As 15% T:G NADES undiluted by water fell out of range for the freezing point depression osmometer, this dilution curve was used to extrapolate and estimate its osmolality (i.e., slope) by a 95% confidence interval using a T distribution.

5.3.7 Post-thaw recovery insensitive to compositional variation of dilute NADES

Jurkat cells were frozen using a controlled-rate freezer at a cooling rate of -1 ˚C/min as determined previously[105]. Post-thaw recovery was measured for samples of Jurkat cells cryopreserved in NADES, MCO and DMSO solutions immediately after thawing, based on cell esterase activity determined using calcein AM. Cell loss due to lysis as well as intact, dead cells were accounted for. As shown in Table 7, there was no statistically significant difference among the post-thaw recovery rates for all conditions of interest. Despite the varying thermophysical properties displayed by the different solutions, their different effect on ice formation did not result in significantly different post-thaw

recovery of the Jurkat cells. This suggests that CPA components in each solution may not only act upon altering the freezing behavior of water but interact with cells stabilizing them, and immediate post-thaw recovery may not be reflective of the complete cell response to cryopreservation or the longer-term manifestation of freezing damage.

Table 7. Post-thaw recovery of Jurkat cells cryopreserved in NADES, MCO and DMSO solutions[a]

CPA solutions	Post-thaw recovery (%)	CPA solutions	Post-thaw recovery (%)
5% T:G	75.8 ± 6.3	5% T:G + 10.75 mM isoleucine	86.1 ± 16.7
10% T:G	77.2 ± 5.5	5% T:G + 21.5 mM isoleucine	76.0 ± 13.0
15% T:G	81.9 ± 6.4	5% T:G + 43 mM isoleucine	78.7 ± 15.8
TGI (MCO)	79.8 ± 5.7	10% DMSO	82.2 ± 13.9

[a]NADES: natural deep eutectic system; TGI or MCO: a multicomponent osmolyte solution containing trehalose, glycerol and isoleucine; DMSO: dimethyl sulfoxide; CPA: cryoprotective agents; T:G: NADES composed of trehalose and glycerol at 1:30 molar ratio. Data represented as mean +/- 95% confidence interval. $n = 6$. No significant difference was found between any pair of sample groups ($p > 0.05$).

5.3.8 Low-concentration NADES combined with mid-range isoleucine yielded most persistent post-thaw cell culture

Cryopreserved samples of Jurkat cells in NADES, MCO and DMSO solutions were thawed and immediately stained. While viability can determine cell loss that occurred during freezing and thawing, cell losses over time post-thaw can also be significant. Therefore, post-thaw apoptosis was quantified in order to determine the extent of those losses (Table 8). For each of the solution compositions tested, the sample had minimal cells in late apoptosis or necrosis (<3%). Cells frozen in a high percentage of T:G (10%,

15%) experienced a high percentage of early apoptosis (>40%), while cells frozen in 5% T:G had less than 10% early apoptosis. Adding 10.75 mM isoleucine to 5% T:G resulted in the highest fraction of healthy, viable cells, outperforming all other NADES, MCO, and 10% DMSO. In general, as the percentage of T:G or isoleucine concentration increased, the percentage of healthy, viable cells decreased.

Table 8. Post-thaw apoptosis of Jurkat cells cryopreserved in NADES, MCO and DMSO solutions[a]

CPA solutions		Live (%)	**Early apoptotic (%)**	Late apoptotic (%)	Necrotic (%)
NADES solutions	5% T:G	89.97 ± 0.29	9.03 ± 0.39	0.34 ± 0.17	0.65 ± 0.48
	10% T:G	52.37 ± 2.01	46.40 ± 2.15	0.58 ± 0.15	0.68 ± 0.73
	15% T:G	47.07 ± 7.52	50.83 ± 8.61	1.29 ± 0.16	0.80 ± 0.89
	5% T:G+10.75 mM isoleucine	94.97 ± 0.52	4.45 ± 0.33	0.22 ± 0.087	0.37 ± 0.18
	5% T:G+21.5 mM isoleucine	88.70 ± 0.25	10.43 ± 0.14	0.42 ± 0.20	0.42 ± 0.11
	5% T:G+43 mM isoleucine	80.80 ± 0.90	18.03 ± 0.76	0.62 ± 0.38	0.50 ± 0.13
TGI (MCO)		90.30 ± 1.14	8.91 ± 1.29	0.36 ± 0.029	0.42 ± 0.19
10% DMSO		92.87 ± 0.14	5.90 ± 3.19	0.27 ± 0.12	0.32 ± 0.28

[a]NADES: natural deep eutectic system; TGI or MCO: a multicomponent osmolyte solution containing trehalose, glycerol and isoleucine; DMSO: dimethyl sulfoxide; CPA: cryoprotective agents; T:G: NADES composed of trehalose and glycerol at 1:30 molar ratio. 95% confidence interval calculated from 3 independent replicates for each sample using a T distribution. Fresh Jurkat cells in culture were 99.1% live, 0.29% early apoptotic, 0.03% late apoptotic, and 0.56% necrotic.

Post-thaw function of the cells was determined by measuring cell growth in normal culture conditions over a 72-hour period. Among the different T:G concentrations tested,

cells frozen in 5% T:G showed the highest proliferation as well as total cell number ($p < 0.05$) at the end of a 3-day culture period (Figure 19A and D) compared to 10% and 15% T:G. Both 10% and 15% T:G samples displayed cell loss in the initial 24 hours post-thaw that was consistent with post-thaw early apoptosis measurements (Table 8). Among the 5% T:G solutions supplemented with amino acids, 5% T:G with 21.5 mM isoleucine showed optimal cell growth (highest proliferation with statistical significance, $p < 0.05$, and highest mean of final cell number, $p > 0.05$) in post-thaw culture compared to lower or higher amount of isoleucine (Figure 19B and E). Interestingly, the solution with the lowest immediate post-thaw apoptosis and highest percentage of healthy cells (5% T:G with 10.75 mM isoleucine) displayed the lowest cell proliferation ($p < 0.05$) in the initial 24 hours after thawing and ultimately lower than optimal cell yield by 72 hours. The proliferation of 5% T:G with 21.5 mM exceeded that of all other NADES solutions and was comparable to DMSO ($p > 0.05$) throughout the entire 72-hour culture period (Figure 19C and F). Cell concentration of the optimal NADES and 10% DMSO grew to 2.14×10^6 and 2.19×10^6 cells/ml, respectively, compared to 1.36×10^6 cells/ml for the MCO at the end of 72 hours in culture.

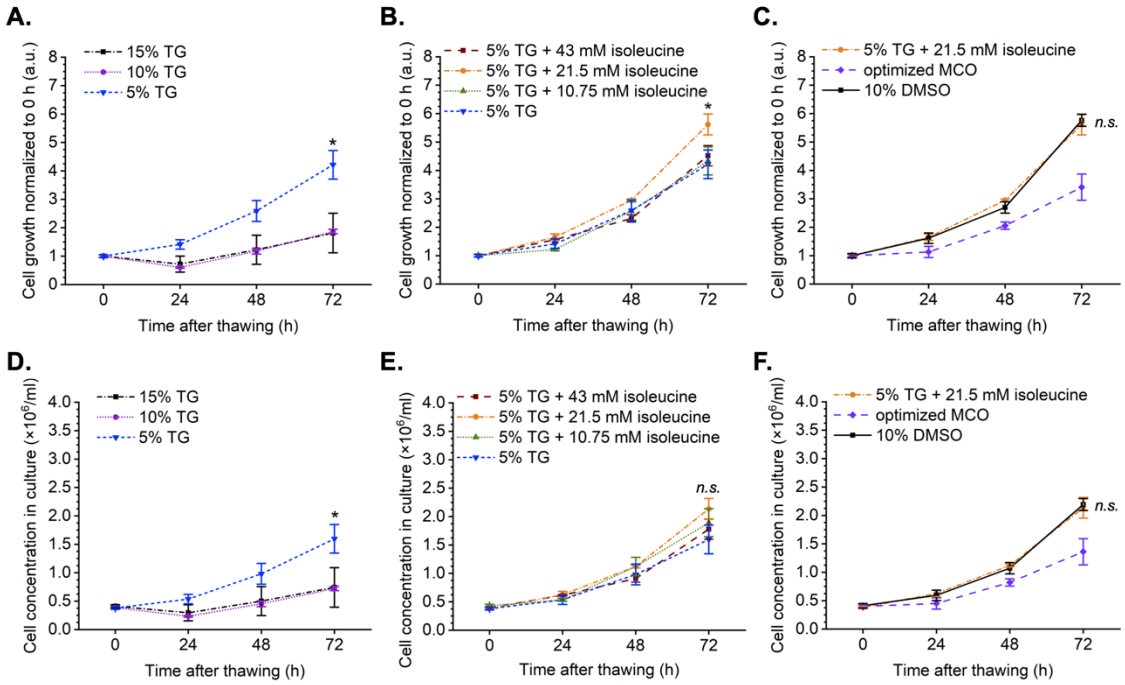

Figure 19. Cell growth in post-thaw culture of Jurkat cells cryopreserved in various NADES, MCO and DMSO solutions. **(A-C)** Growth curves visualized in the form of growth rate, with all measurements normalized to 0h of each sample, emphasizing on the cell proliferation. **(D-F)** Growth curves visualized in the form of absolute cell concentration at each point of post-thaw culture encompassing both the cell proliferation and the small differences in post-thaw cell recovery. (A, D) showing the effect of increasing concentration of T:G on post-thaw cell growth. *: $p < 0.05$ in comparison between three sample groups using ANOVA with Bonferroni correction at 72 hours. (B, E) showing the effect of increasing concentration of isoleucine in 5% T:G on post-thaw cell growth. *: $p < 0.05$; n.s.: $p > 0.05$ in comparison between four sample groups using ANOVA with Bonferroni correction at 72 hours. (C, F) showing the effect of 5% T:G + 21.5 mM isoleucine (optimized NADES) versus TGI (optimized MCO) versus 10% DMSO on post-thaw cell growth. n.s.: $p > 0.05$ in two-sample comparisons between the optimized NADES and 10% DMSO at 0, 24, 48 and 72 hours.

5.3.9 Ice morphology distinct between subtly varied multicomponent CPA solutions

As described later in Chapter 6, differences in CPA composition can have a profound effect on post-thaw cell survival, and higher levels of CPA did not always result in increased post-thaw cell survival. Two different non-DMSO solutions that appeared in

the DE algorithm were tested and compared for their effect on the freezing responses of hiPSCs. Solution A was the optimized CPA solution containing level-2 sucrose, level-5 glycerol, level-1 isoleucine, and level-4 albumin. Solution B was deviated from Solution A and contained level-3 sucrose, level-4 glycerol, level-2 isoleucine, and level-5 albumin, which differed from the optimum by only one concentration level per CPA variable (i.e., 20 mM, 0.5% v./v., 7.5 mM and 0.5%).

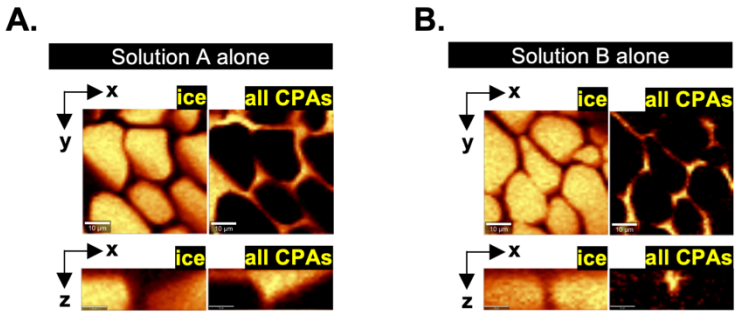

Figure 20. Raman heat maps representative of freezing behaviors in (**A**) optimized non-DMSO vs. (**B**) deviated non-DMSO solutions showing ice crystals separated by nonfrozen channels of the respective cryoprotective agent (CPA) solution at -50 ˚C shown in lateral plane (scale bar: 10 µm) and axial plane (scale bar: 3 µm).

Raman spectroscopy was used to characterize the freezing behavior of Solutions A and B. Effective cryopreservation of cells typically arises from the ability of CPA to control the freezing behavior of water, preventing the types of ice crystal formation that disrupt membrane integrity in suspended cells. When frozen alone without cells, Solution A formed ice crystals with a unique morphological characteristic not observed in Solution B: distinctly shown in both the lateral and axial Raman heat maps, each ice crystal in Solution A had a softened solid-liquid interface on one side and a regular, abrupt interface on the other side (Figure 20). As a result, although the total amount of ice

formation quantified by area fraction was similar between Solutions A and B, the distance between adjacent ice crystals was significantly greater in Solution A than Solution B (Table 9). As frozen cells are typically located in the space between adjacent ice crystals, the greater distance between ice could reduce the likelihood of intracellular ice formation and therefore cellular damage[127].

Table 9. Comparison of freezing responses in Solutions A, B and C under optimal freezing conditions[a]

Conditions and measurements	**Solution A (optimized non-DMSO)**	**Solution B (deviated non-DMSO)**
Cooling rate	-1 ˚C/min	-1 ˚C/min
Ice nucleation temperature	-4 ˚C	-4 ˚C
Area fraction of ice in frozen solution, n=5	76.0 % ± 7.93 %	80.3 % ± 4.28 %[n.s.]
Distance between adjacent ice crystals (μm), n=20	2.16 ± 0.667	0.670 ± 0.400*

[a]95% confidence intervals calculated from samples of size shown for each metric. ANOVA with Bonferroni correction used to determine statistical significance compared to Solution A. n.s.: p>0.05; *: p<0.05.

DSC was used to characterize the melting temperature, enthalpy of melting and glass transition temperature of different CPA compositions (Table 10). Lower enthalpy of melting suggests a lower amount of ice formed during freezing. There was no statistically significant difference in melting temperature, enthalpy of melting or glass transition temperature between Solutions A and B. These DSC findings suggest that the difference in post-thaw cell survival between Solutions A and B likely resulted from interactions

between components of the solution and different structures in the cell (membrane and proteins) rather than changes in the freezing behavior of water.

Table 10. Melting temperatures, enthalpy of melting and glass transition temperatures for non-DMSO solutions measured by DSC[a]

CPA solution	T_{m1} (˚C)	T_{m2} (˚C)	ΔH_m (J/g)	T_g (˚C)
A (optimized non-DMSO)	-6.727 ± 0.712	-2.047 ± 0.0940	205.87 ± 21.49	-89.150 ± 1.631
B (deviated non-DMSO)	-6.623 ± 0.826	-1.903 ± 0.225	210.97 ± 27.53	-88.637 ± 4.875

[a]CPA: cryoprotective agent; DSC: differential scanning calorimetry; T_{m1}: melting temperature defined as the onset of melting; T_{m2}: melting temperature defined as the peak of melting; ΔH_m: enthalpy of melting; T_g: glass transition temperature; A: Solution A; B: Solution B. Measurements shown as 95% confidence intervals. No statistical significance was found in the two-sample *t*-test (p<0.05) comparing Solutions A and B.

5.4 Discussion

5.4.1 Hydrogen bond between sucrose and water strengthened with lower temperature

The shorter OH stretching peak at 3420 cm^{-1} at the lower temperature indicates fewer "free" water molecules and strengthened intermolecular hydrogen bond between sucrose and water[159,202,203], which is consistent with the substantially increased sucrose concentration at -50 ˚C measured in this investigation. Previous studies suggested that sucrose molecules in concentrated solutions form chains via their hydroxyl groups and create a polymer-like structure with cavities[161]. As a result, nonfrozen water molecules could be constrained or trapped in the highly viscous sucrose glass, and the dynamics of the water molecules was halted[162,204]. The shift of wide OH stretching peak to lower

wavenumber also indicates an enhanced hydrogen bond network of the nonfrozen solution as lower OH stretching frequency is associated with stronger hydrogen bond[205,206]. However, it could not be discerned whether this shift resulted from an increased sucrose concentration or decreased temperature itself, or a combination of both, and will require further investigation.

5.4.2 Cells subject to heterogeneous chemical environment during freezing

The interactions between solidifying interface and biological cells have been investigated by both experimental and simulation studies[172,175–177,194,207–209]. The engulfment or entrapment of the cells between ice crystals in sugar solution have been studied before. It was previously suggested that molecular level interactions between the cell and sugar were important[172]. However, without accurate knowledge of the solute concentration, the effects of solute concentration and solidifying interface on the biological cells could not be precisely estimated. Concentration of solute at a concave solidifying interface was theorized by Dantzig and Rappaz to be higher than that at a planar interface for the same freezing conditions[210]. However, the results in this study showed that sucrose concentration at the concave interface between the cell and the extracellular ice was lower than that of bulk nonfrozen solution. This suggests that cells are exposed to a heterogeneous chemical environment during freezing. The most likely cause of this outcome was the outflow of water from the cell, thereby diluting the concentration of sucrose in the nonfrozen solution[199]. The timing of the exosmosis from the cell is unclear (during freezing, during the hold period, or both), but it is likely that the lower

concentration of sucrose in the narrow region of cell-extracellular ice interface and higher concentration in the bulk solution may reflect the inability of the water to quickly diffuse out of the narrow region and into the bulk regions at the low temperatures.

5.4.3 Sucrose protects cells against membrane phospholipid fusion and ice damage

Although sucrose is normally not cell-permeant, Raman imaging of the sucrose and cell (amide I) showed that sucrose was not completely excluded from the cell. The overlap of Raman image of sucrose with that of amide I suggests that sucrose was adjacent to the cell membrane and was potentially integrated into the cell membrane, an evidence supporting the interactions between sugars and cell membrane during freezing that have been postulated by others[163]. As the typical thickness of cell membrane is more than one order of magnitude below the spatial resolution of the microscope, the spectral composition of cell membrane could not be resolved from that of the cytoplasm, making it difficult to determine definitively the relationship between sucrose and the cell membrane. The presence of the nonfrozen solution between cell and extracellular ice resulted in the growth of ice around rather than into the cell, which is consistent with simulation studies of cell/particle capture in binary solidification[211,212]. The presence of a thin layer of nonfrozen sucrose solution also increased the distance between the cell membrane and the ice phase, which, in turn, reduced the potential for IIF[91].

5.4.4 NADES protects cells against intracellular ice and dehydration

This study investigated the capability of NADES as a nontoxic, alternative CPA to

DMSO for the cryopreservation of Jurkat cells. Existing literature of NADES[184,188–191] has contributed its unique properties to the establishment of hydrogen bonding between its molecular components as well as with water, which has been observed using nuclear magnetic resonance (NMR) methods. Strengthened hydrogen bonding has been associated with cryoprotective properties of CPAs in recent studies[184,213]. Here, low-temperature Raman spectroscopy interrogated the role of hydrogen bonding in NADES for cryopreservation applications from both microscopic and spectroscopic perspectives. Controlling ice formation has been a focus of cryopreservation research. While literature has presented mathematical and empirical evidence connecting different extents of hydrogen bonding to different water lattice structures and ice modifications[214–216], our Raman studies[85,213] including this one show that morphology of ice crystals can be a macroscopic reflection of the molecular interactions between water molecules and solutes. In addition, low-temperature Raman spectroscopy-based analysis of molecular vibrations in NADES expands upon the capabilities of NMR-based methods in literature of NADES by investigating the hydrogen bonding in frozen samples.

Both lower ellipticity[85] and greater distance between adjacent ice crystals[213,217] have been correlated to better cryoprotective outcome of a given CPA solution. Presence of CPA molecules can alter the solidification pattern of water and consequently allow ice to propagate around (rather than through) cells if they are present[174,218]. Similar to the instances presented in Figure 16, changing ice crystal growth from a typical unidirectional elongation to relatively uniform growth in various directions would result

in a rounder appearance of the ice crystals. Ellipticity of ice crystals is inversely a measurement of the strength of this influence of the CPAs. Proximity of the ice phase to cells has been associated with intracellular ice formation and consequently freezing damages in cells[127]. The more separated are the ice crystals, the less proximate the cells in the nonfrozen region would be to the ice phase. As a result of these studies, we understand that factors in the microscopic structures of ice crystals, in turn, affect the extent of cell damage by ice crystal formation that can manifest as post-thaw cell survival versus death.

Based on the quantitative analysis of Raman heat maps described in this study, T:G NADES had a relatively neutral effect on ice morphology resulting in ellipticity of ice crystals lower than trehalose alone and higher than glycerol alone. However, the T:G NADES resulted in significantly wider channels of nonfrozen solution between ice crystals than both trehalose and glycerol alone. As cells are located in the nonfrozen channels, wider channels will decrease the likelihood of lethal intracellular ice formation due to close proximity to extracellular ice[217]. This effect on the nonfrozen channels will likely contribute to the cryoprotective benefits of NADES-based solutions.

Red shift of OH stretching band of Raman spectra during freezing indicates that hydrogen bonds between trehalose, glycerol and water, all of which contain O-H covalent bonds, were strengthened in the nonfrozen regions surrounding ice crystals. This effect was observed in solutions of both T:G NADES and its individual components. In

contrast, the downshift of OH stretching band from -10 ˚C to -50 ˚C was observed only in the NADES solution. This downshift cannot be explained by the different molecular composition of NADES than its individual components, as the greater abundance of solutes containing O-H bonds would, on the contrary, result in an upshift of OH stretching band. In combination with the lower CH stretching band (~2800-3000 cm^{-1}) in NADES sample, this likely suggests that NADES formation resulted in lower concentration of trehalose and glycerol solution and therefore greater water content in its nonfrozen solution, which can then explain its wider nonfrozen channels in the macroscopic observation of Raman and expose cells to lower osmotic stress during freezing. Further studies will investigate methodologies of spectral deconvolution, measure definitively the CPA concentration and water content respectively in these nonfrozen regions and explore the subject of water retention in greater depth.

Thermophysical behavior of the CPA solutions were determined using DSC. Higher concentrations of NADES had lower melting temperatures and enthalpies of melting, which indicates less ice crystal formation[184,185,219]. However, higher NADES concentration has higher osmolality, and higher osmotic stress can lead to greater cell loss. For suboptimal conditions (i.e., 10-15% T:G), evidence of early apoptosis was found in both post-thaw growth and caspase activation. In contrast, using a lower concentration of T:G resulted in improved preservation of healthy cells (<10% of cells in early apoptosis).

In this study, optimized NADES and MCO solutions were compared via the proliferation of Jurkat cells cryopreserved in the respective solutions, which was a functional assay. It should be noted that the molar ratio of trehalose and glycerol in the MCO do not form a NADES. Despite containing the same molecules (trehalose, glycerol and isoleucine), the optimized NADES solution outperforms the optimized MCO solution, resulting in faster cell growth in the post-thaw culture. As temperature decreases during freezing, CPA molecules concentrate in the nonfrozen solution. A possible interpretation of our Raman spectral results, that the NADES retains more water in the nonfrozen solution than trehalose or glycerol alone, can translate to reduced cell dehydration and may decrease anti-proliferative signaling[220] and encourage proliferation. With these same components, NADES present a novel formulation strategy to enhance the capability of these CPAs. As a result, NADES can be a powerful tool to advance the non-DMSO cryopreservation of valuable cell types for both scientific and clinical purposes.

5.4.5 Sweet spot of interaction between isoleucine and cell for best post-thaw survival

Conventional wisdom indicates that CPAs work by controlling the freezing of water to reduce ice crystal formation and protect the cells from mechanical damage[221]. In this study, however, solutions with more favorable thermophysical properties (lower melting temperature, lower enthalpy of melting) did not result in improved post-thaw cell recovery and proliferation. Although immediate post-thaw recovery showed no significant differences between the MCO and varying NADES, post-thaw proliferation showed that 5% T:G with 21.5 mM isoleucine had the highest growth rate over 72 hours

compared to the MCO and all other NADES, with a comparable growth curve to 10% DMSO. These results suggest that reducing ice formation is not the only factor that contributes to cryoprotection of cells. In addition to controlling the freezing of water, biological interactions between CPA molecules and cells likely play a major role in the success of cryopreservation. Sugars have been shown to interact with and stabilize the cell membrane during freezing[213], glycerol penetrates the cell and can stabilize proteins[222], and isoleucine interacts with sugars and may help to keep them from precipitating out of solution[223].

In the development of alternatives to DMSO-based cryopreservation, post-thaw apoptosis is a critical concern for lymphocytes[133,149,224,225] and was included in the post-thaw analysis. The role of caspase activation in post-thaw apoptosis has been well-established in the literature. In particular, caspase-3 has been found to be activated post-thaw in T cells frozen in DMSO and likely contributes to cell death[149,224]. When supplemented with a small amount of isoleucine (10.75 mM), the live cell fraction increased, but larger amounts of isoleucine increased the percentage of cells in early apoptosis. This suggests that there is a "sweet spot" for the optimal concentration of isoleucine in T:G NADES. The importance of optimizing each component of a CPA is consistent with findings in our previous studies of MCO solutions[226,227]. While post-thaw caspase activation is a direct indicator of apoptosis immediately post-thaw, cell stress could manifest later, as seen in the discrepancy between immediate post-thaw apoptosis and cell growth over 72 hours. This highlights the importance of direct measurement of cell survival at the

functional time point of interest.

Similarly, while DSC results showed that isoleucine did not significantly contribute to the ice inhibition effects of the multicomponent CPA cocktail overall, DE algorithm results in Chapter 6 will show that post-thaw cell survival could be increased significantly (e.g., from 48.3% to 100%) by 7.5mM isoleucine. This again is likely a "sweet spot" between the stabilizing[228,229] and destabilizing[230] effects of a hydrophobic amino acid on protein molecules in the cells.

5.4.6 Poloxamer 188 altered freezing behavior of water at the solid-liquid interface

Most notably, we were able to use low-temperature Raman spectroscopy and DSC to characterize a novel additive for hiPSC cryopreservation, P188. In a synergistic combination with sucrose, glycerol, isoleucine and HSA, P188 was found here to not only inhibit ice formation significantly but also soften the solid-liquid interface of ice and increase the distance between adjacent ice crystals. It is important to understand that these cryoprotective effects of the non-DMSO CPA cocktail could be capitalized only with the optimized composition. Deviation from the optimum could result in significantly less desirable outcomes in cryopreservation as shown in Chapter 6. When a deviated non-DMSO solution is used to cryopreserve cells, formation of intracellular ice is changed, and cells are significantly less likely to survive post-thaw. One potential explanation for this difference is that the optimal non-DMSO CPA composition results in enhanced stabilization of the cell membrane and thereby confers greater resistance to intracellular

ice formation.

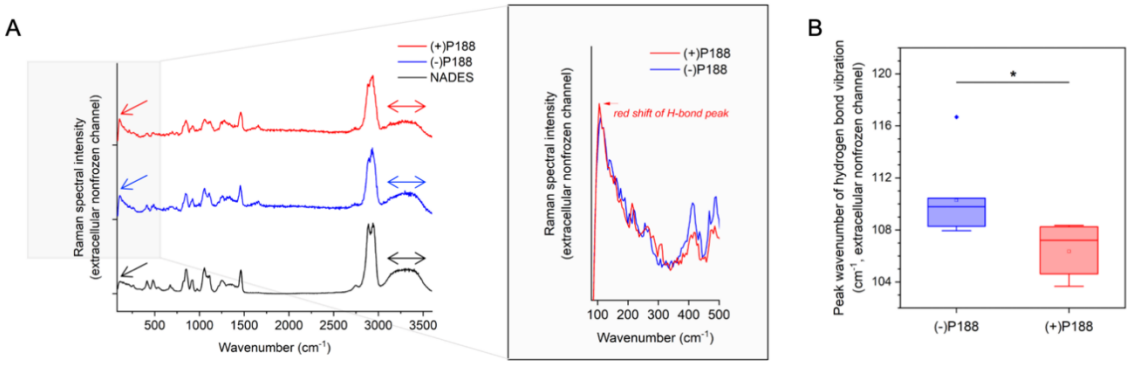

Figure 21. (**A**) Raman spectra acquired from the extracellular nonfrozen region of varying sample conditions at -50 ˚C showing the multicomponent non-DMSO solution with different waveforms in hydrogen bond (below 250 cm^{-1}, single-headed arrow) and OH stretching (3000-3600 cm^{-1}, double-headed arrow) vibrations and that (**B**) the addition of P188 significantly decreased the vibrational energy of the hydrogen bond network (as quantified based on A).

While it has been speculated that the nonfrozen regions of highly concentrated multicomponent CPAs may form NADES-like molecular interaction[86,184], preliminary experimentation using Raman spectroscopy (Figure 21) revealed a different waveform in the intermolecular hydrogen bond vibration and in the broader OH stretching band than T:G NADES. However, it was also found that the synergistic formulation of these CPAs resulted in a stronger hydrogen bond network in the extracellular space by a significant red shift of the hydrogen bond vibration, from 111 cm^{-1} to 106 cm^{-1} compared to when the synergy was disrupted by the removal of P188 ($p < 0.05$), which likely prevented extracellular ice from propagating into the cells. Supporting a prior hypothesis[127], these changes in ice crystal formation outside the cells in turn suppress ice formation inside the cells. Currently, DSC and NMR are being explored by other students in our group to define the formation of NADES and expand our understanding of the molecular

interactions within an optimal multicomponent non-DMSO CPA formulation.

5.5 Conclusion

This chapter capitalized on the label-free high-resolution technique of low-temperature Raman spectroscopy to characterize the freezing behaviors of aqueous CPA solutions and postulate the mechanisms of action of four major classes of non-DMSO CPA molecules – sugar, sugar alcohol, amino acid, and poloxamer. Mechanisms of cryoprotection for non-DMSO CPAs differ from that of DMSO, which is an organic solvent. Spatial overlap between nonfrozen sucrose solution and a cryopreserved cell was visually observed for the first time, suggesting that protective properties of sucrose might originate from its direct interaction with the cell. NADES was found to suppress both ice formation and dehydration of the nonfrozen region. Supplementing NADES with optimized amount of isoleucine does not affect the solution's thermophysical properties but significantly improves cell survival and proliferation in the days after thawing, which suggests that both physical interaction between NADES and water and biological interaction between isoleucine and cells play a role in successful cryopreservation. Hydrogen bonds of the water lattice in the nonfrozen regions are found strengthened by synergistic combinations of different CPA molecules at a particular ratio such as the optimized multicomponent solution from Chapter 6. It is also the first time that a softened solid-liquid interface was visualized and reported in slow freezing. In perfect concert with one another, P188 and the other non-DMSO CPAs were observed to alter the water solidification pattern during freezing and provide cryoprotection for cells by the means of widened nonfrozen

channels and a strengthened hydrogen bond network. Hopefully, future advancement in Raman spectroscopy modality will allow faster data acquisition at higher spatial resolution, and that in non-interfering molecular probes will enable more in-depth analyses with higher chemical specificity and sensitivity. Nonetheless, the results of this chapter demonstrated Raman spectroscopy as a powerful tool to enable mechanistic discovery in cryobiology through a window into the otherwise inaccessible frozen state.

Chapter 6

Optimized Formulation of Non-DMSO Cryoprotective Agents Mitigate Non-Cryopreservation and Cryopreservation Stresses in hiPSCs

Much of the text and figures in this chapter have previously appeared in the publication below, included here with copyright permission from Frontiers.

Li R[†], Hornberger K, Dutton J and Hubel A. Cryopreservation of iPS cell aggregates in a DMSO-free solution – an optimization and comparative study. *Frontiers in Bioengineering and Biotechnology.* 2020. 8, 1-13.

6.1 Introduction

Human induced pluripotent stem cells (hiPSCs) are an important cell source for cell therapy and regenerative medicine[4,231]. With the potential to differentiate into all cell types, high-efficiency banking of hiPSCs is critical for downstream clinical and commercial production of cells and tissues for human therapeutic applications. Effective, consistent methods of hiPSC cryopreservation reduce cost and time associated with production of regenerative medicine and enable development of a manufacturing paradigm for these products.

Current methods of preservation of hiPSCs are not suitable for current and emerging applications. Specifically, conventional methods use dimethyl sulfoxide (DMSO) as a cryoprotective agent (CPA)[52,107,116]. DMSO increases the mRNA level of the de novo

DNA methyltransferase DNMT3A in mouse embryoid bodies, accompanied by hyper- or hypo-methylation of many genetic loci[153] making it unsuitable for use with reprogrammed cells. Furthermore, DMSO is cytotoxic, and it is common practice for cells to be frozen immediately upon introduction of DMSO-containing CPA solutions. After thawing, the cells are typically washed or diluted quickly as well to minimize their exposure to DMSO. These are pain points associated with the use of DMSO in hiPSC-based cell production processes regardless of the type of application.

Non-DMSO CPAs have the potential to alleviate the aforementioned pain points and improve the utility, effectiveness and efficiency of hiPSC cryopreservation. We have demonstrated in previous studies that combinations of sugar, sugar alcohols and amino acids can be used to preserve human mesenchymal stem cells and T lymphocytes[80,85,86,105]. When used to cryopreserve cells *in vitro*, they have been shown to act in concert with each other and amino acids to protect and stabilize cells[80,85]. This study uses a cocktail of non-DMSO CPAs including sucrose, glycerol, L-isoleucine, human serum albumin (HSA) and poloxamer 188 (P188), which are nontoxic and FDA-approved for infusion.

In this chapter, a DMSO-free CPA formulation is optimized using a DE algorithm. The optimized non-DMSO solution is compared to alternative non-DMSO solutions, with subtly deviated CPA concentrations or one molecular component removed, to explore the mechanism of action of the complete formulation as well as that of individual CPAs.

Requirements of basal buffer composition are defined in terms of pH buffer, energy conservation, cell-cell contact stabilization, and osmotic balance. The optimized DMSO-free method is also benchmarked against a variety of standard DMSO-based methods under varying freezing conditions. Undercooling damage in the hiPSC aggregates are revealed using low-temperature Raman spectroscopy and a variety of post-thaw cell-based assays. Effect of different CPA solutions on the cells' undercooling sensitivity is evaluated.

6.2 Methods

hiPSCs used in this chapter were from cell line UMN PCBC16iPS and cultured as described in section 3.2.1. Passage numbers used in the following experiments were between 59 and 71. Cell culture of the latest passage used for karyotyping arose from cells previously cryopreserved and was the result of 3 freeze-thaw cycles with 3 passages in between via the optimized DMSO-free cryopreservation method described in this investigation.

Final working concentrations of non-DMSO CPA molecules – sucrose, glycerol, isoleucine and albumin – were varied to optimize the cryopreservation of hiPSC aggregates. A basal buffer composed of P188 at a non-micelle forming concentration, supplemented with NEAA and HBSS was constant for all non-DMSO freezing solutions studied. DMSO was used as a control at an optimized concentration of 7.5%, and HBSS was used as its basal buffer. The non-DMSO compositions discussed in this article are

covered by issued Patent #10,314,302 and patent application #16/383,165, owned by Regents of the University of Minnesota. The solutions used in this article can be acquired directly from the authors for replication of the studies.

Parameter space of the DE algorithm was determined by the cytotoxicity limit and was discretized into 5 intervals between 20 mM and 120 mM for sucrose, 2.5% v./v. and 5% v./v. for glycerol, 0 mM and 37.5 mM for isoleucine, and 0% and 2.5% for albumin. Cytotoxicity was defined as decrease in cell reattachment in the hiPSC culture measured using calcein AM 24 hours after 1-hour exposure to the respective molecules compared to fresh cell control.

Small (3 to 50-cell) aggregates were dissociated as described in section 3.5.1. After dissociation, the cell aggregates were collected using the basal buffer of interest. The freezing solutions were prepared at twice (2x) the final working concentration and added dropwise to the suspension of aggregates at a 1:1 ratio. The mixture was incubated at room temperature for 30 min to 1 h before freezing. Working cell concentration for cryopreservation was defined based on surface area of the 2D cell culture as shown in Table 11 (e.g., all cells produced from 1 well of a 6-well cell culture plate were frozen in 1 ml of 1x cryopreservation solution.). Exact cell concentration was measured as described in sections 3.7.1 and 3.7.2. The working cell concentration from samples used for cryopreservation in this study was between 1.46 and 1.89 million cells per ml (95% confidence interval).

Table 11. Working cell concentration for hiPSC cryopreservation[a]

Cultureware	**Growth surface area**	**Number of cells**	Step 1. Cell collection		Step 2. CPA introduction		**Number of cryogenic vials**
			Volume of basal buffer	**2x cell concen-tration**	**Volume of 2x CPA solution**	**Final cell concen-tration**	
6-well plate	9.5 cm^2	1.5×10^6/well	500 µl/well	3×10^6/ml	500 µl/well	1.5×10^6/ml	1/well
T25 flask	25 cm^2	4×10^6	1.3 ml		1.3 ml		2
T75 flask	75 cm^2	1.2×10^7	3.9 ml		3.9 ml		7
T175 flask	175 cm^2	2.8×10^7	9.2 ml		9.2 ml		18

[a]Numerical values in this table are estimates of the respective parameters; CPA: cryoprotective agent.

Controlled rate freezing was performed, and sample temperature was logged as described in section 3.6.1 using a constant cooling rate of -1 ˚C/min and ice nucleation manually induced at varying temperatures of -4 or -12 ˚C. Alternative to controlled rate freezing, passive freezing was performed, and sample temperature was logged as described in section 3.6.2.

After cryogenic storage for a minimum of 24 hours and thawing as described in section 3.6.3, a series of assays were performed to characterize the survival and function of the cryopreserved hiPSCs. Post-thaw reattachment was selected as the metric of optimization driving the DE algorithm and measured as described in section 3.8.1. The split ratio at thawing was 1:1, and the reattachment rate was normalized to a DMSO control in the DE

algorithm experiments, where the split ratio was 1:6, and the reattachment rate was normalized to a fresh cell control otherwise. Post-thaw cell growth was monitored daily for 4 days as described in section 3.9.2. On day 4 after thawing, immunocytochemistry was performed as described in section 3.3.1, and the post-thaw culture was dissociated into single cells, stained with anti-TRA-1-60 antibody and its isotype control (Invitrogen) and measured using a BD Accuri C6 flow cytometer (BD Biosciences). Also on day 4, trilineage differentiation and immunocytochemistry of the resulting cultures were performed as described in section 3.11.1.

Low-temperature Raman spectroscopy was set up as described in section 3.13.1. Cooling rate of -1 ˚C/min was used for cells and -10 ˚C/min for solution alone, and ice nucleation was induced at -4 ˚C unless otherwise noted. When final temperature was stabilized at -50 ˚C, Raman images of different substances were rendered as described in section 3.13.2 (illustrative example given in Figure 22A, characteristic wavenumber assignments given in Table 12) and spatially deconvolved as described in section 3.13.3. hiPSC aggregates were delineated as described in section 3.14.1. Intracellular ice formation was quantified as described in section 3.14.2. DSC was performed to determine the thermophysical behavior of the CPA solutions, and DSC results were analyzed as described in section 3.15 and shown in Figure 22B. Samples were run in independent triplicate.

Table 12. Raman spectral peak assignments[a]

Substance	**Wavenumber (cm^{-1})**	**Assignments**[125,232–235]
Proteins, lipids (cell)	1620-1700	amide I and C=C stretching
Ice	3087-3162	OH stretching
Glycerol	460-510	CCO rocking
P188	1267-1303	CH_2 twisting
Sucrose, glycerol, isoleucine, P188 (heat map labeled as "CPA")	815-885	CC stretching
DMSO	648-698	symmetric CS stretching

[a]P188: poloxamer 188; CPA: cryoprotective agent; DMSO: dimethyl sulfoxide; C=C, OH, etc. refer to chemical bonds.

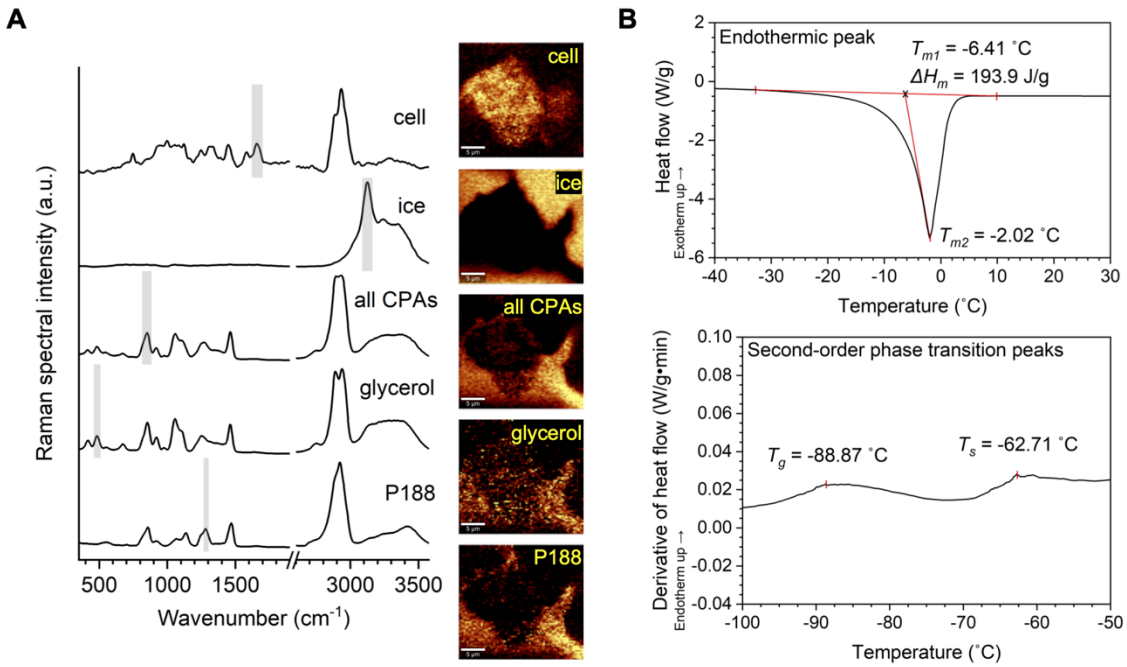

Figure 22. Illustration of Raman and DSC methodology. (**A**) Raman spectra of a hiPSC aggregate, ice, all CPAs combined, glycerol and P188, as well as Raman heat maps rendered from the spectra based on the characteristic Raman signal shown by the shaded region respectively. (**B**) Top: DSC thermogram showing endothermic peak (melting). The melting temperature was defined as the onset of melting (T_{m1}) for evaluation of thermophysical properties and the peak of melting (T_{m2}) for the interpretation of undercooling. Enthalpy of melting (ΔH_m) was defined as the area under the curve of the endothermic peak. Bottom: First derivative of SC thermogram showing second-order phase transitions. Glass transition temperature (T_g) and softening temperature (T_s) were visualized by deriving heat flow with respect to time and defining T_g and T_s as two local maxima along the derivative curve. [Panel B is based on Kathlyn Hornberger's work.]

In this chapter, data was represented as mean plus/minus standard error. Sample size of 1 was used in the DE algorithm-driven experiments to optimize the non-DMSO CPA formulation with high efficiency. Power analysis was performed for the remaining experiments to ensure sufficient sample size with a power of 0.95. One-sample hypothesis testing was performed on measurements for each sample, where 95% confidence intervals were shown. Two-tailed Student's *t*-tests were performed for two-sample comparisons, with the exception of a Fisher's exact test performed for two-sample comparisons of samples with binomial distribution. ANOVA with Bonferroni

correction was performed for comparisons of multiple samples. Levene's Test was used to verify the assumption for homogeneity of variance for the two or more samples. Null hypothesis was defined as no statistical difference between any pairs of samples or between sample and control. *p*-value less than 0.05 was used to make the decision of rejecting the null hypothesis and determining the significant difference.

6.3 Results

6.3.1 DE algorithm accelerated optimization of a complex CPA parameter space

Optimizing the non-DMSO freezing solution in this study involved using the DE algorithm to identify the composition of CPA variables (sucrose, glycerol, isoleucine and albumin) associated with the highest post-thaw cell survival. A single cooling rate (-1 ˚C/min) and a single ice nucleation temperature (-4 ˚C) were used in this investigation based on preliminary studies that screened different cooling rates as previously described[107] with different compositions. The DE algorithm was used with a population size (*NP,* i.e., the number of unique solutions output per generation) of 10, with mutation factor (*F* or weight, i.e., amplification of the differential variance) of 0.85 and crossover (*CR*) of 1. Quantified outcome of a functional assay – post-thaw cell reattachment measured by calcein AM-stained, adherent, live cells in culture 24 hours after thawing – was used as the metric of optimization.

The mean post-thaw cell reattachment increased with every generation, and the number of non-DMSO freezing solutions better than the 7.5% DMSO control increased

gradually, until both plateaued between Generations 6 and 7 (Figure 23A). Therefore, the DE algorithm converged to the global maximum after 8 generations, or 8 sets of 10-sample experiments. The topology of this parameter space was non-linear and NOT unimodal (Figure 23B). It was complex with closely spaced contour lines within the region containing the optimum, which was level-2 sucrose, level-5 glycerol, level-1 isoleucine and level-4 albumin (Figure 23C).

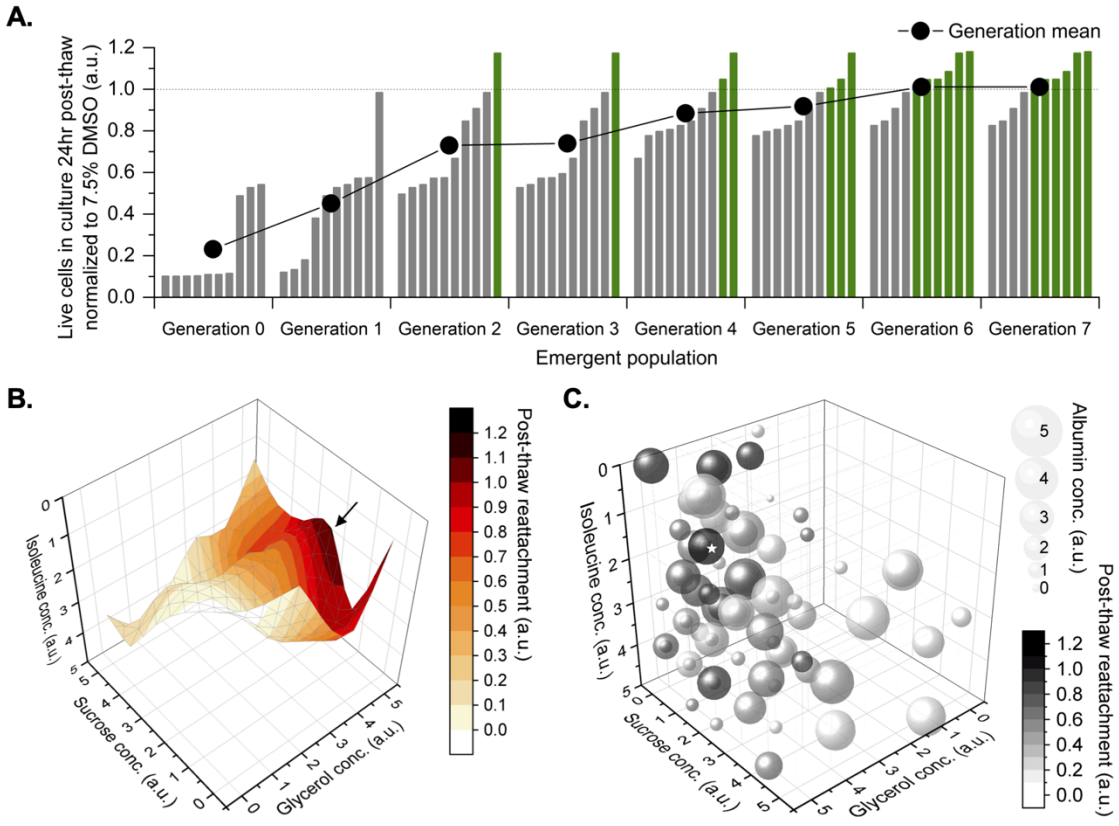

Figure 23. Results of differential evolution (DE) algorithm-driven optimization. Sample size of 1 for accelerated optimization. (**A**) Emergent population of formulations of freezing solution improving then stabilizing in terms of their post-thaw reattachment normalized to a 7.5% dimethyl sulfoxide (DMSO) solution, at the end of which, 6 DMSO-free solutions were better than the DMSO control. (**B**) Topology of parameter space that the DE algorithm navigated through during optimization, shown in 4 of 5 dimensions. An optimum (→) was located towards medium concentration of sucrose, high concentration of glycerol and low concentration of isoleucine. (**C**) Bubble chart of all formulations tested by the DE algorithm, shown in

all 5 dimensions. Bubble size correlated to albumin concentration. Grayscale intensity correlated to post-thaw cell reattachment. The optimum (★) located at level-2 sucrose, level-5 glycerol, level-1 isoleucine, level-4 albumin.

6.3.2 High post-thaw survival and function withstood stress amplification cycles

To evaluate the suitability of this optimized non-DMSO method for cell banking purposes, cells were characterized after freezing, thawing and one passage of post-thaw culture for three freeze-thaw cycles amplifying any phenotypic instability that could result from cryopreservation. The hiPSC aggregates cryopreserved using this method consistently yielded post-thaw culture with efficiency comparable to fresh cells passaged and better than cells cryopreserved in DMSO. Specifically, 24 hours after plating at a split ratio of 1:6 (3 independent experiments of 6 biological replicates), reattachment measured for cells cryopreserved using the optimized non-DMSO solution was similar to fresh cells (p>0.05) and 52-95% (95% confidence interval) higher than cells cryopreserved using DMSO. On day 4 post-thaw, the cells cryopreserved using the optimized non-DMSO formulation exhibited high expression of NANOG, OCT4 and TRA-1-60 (Figure 24A) and demonstrated the ability to differentiate into representative cell types of all three germ layers (Figure 24B), illustrating that the cells retained their pluripotent phenotype and differentiation potential. In addition, samples of hiPSC aggregates were karyotyped after freezing, thawing and three passages of post-thaw culture for three freeze-thaw cycles amplifying any chromosomal instability that could result from cryopreservation. G-banding found a normal male karyotype with no clonal numerical or structural chromosomal abnormality in all 16 metaphase cells available for

analysis (Figure 24C).

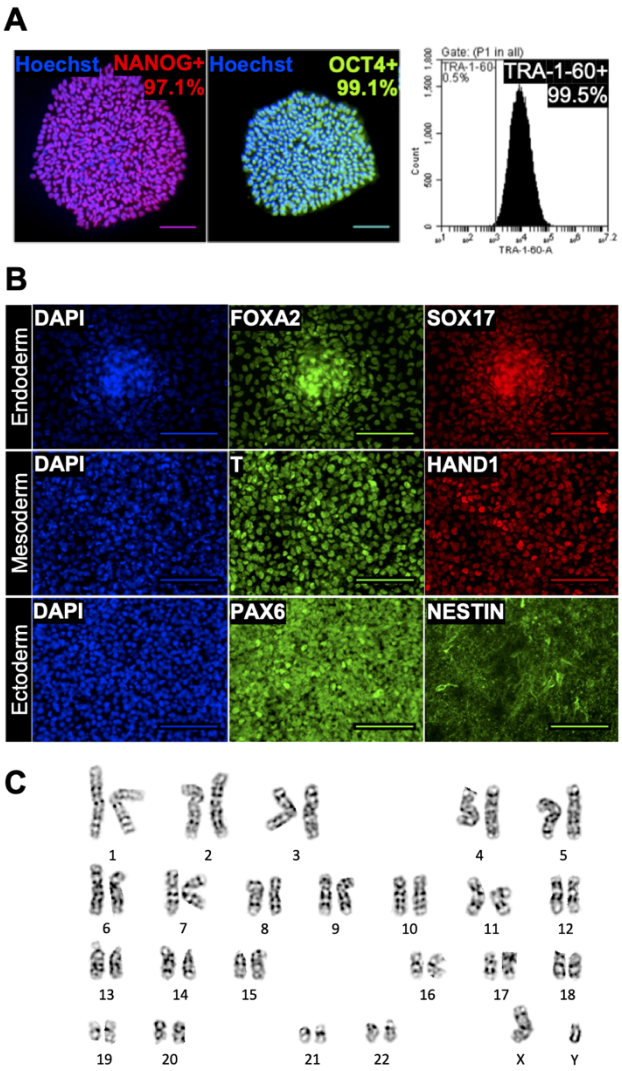

Figure 24. Phenotype and karyotype of hiPSCs cryopreserved using the optimized non-DMSO solution. Monochromatic images with pseudo-coloring matching the real color of respective fluorescent dye. (**A**) Quantitative fluorescent microscopy (counterstained with nuclear dye Hoechst 33342, blue) and forward versus side scatter-gated flow cytometry of cryopreserved hiPSCs showing high expression of transcription factors NANOG (red), OCT4 (green) and pluripotency surface marker TRA-1-60. Scale bar: 100 µm. (**B**) Immunocytochemistry images showing trilineage differentiation of cryopreserved hiPSCs into three germ layers and expression of endodermal markers, FOXA2 and SOX17, mesodermal markers, T and HAND1, and ectodermal markers, PAX6 and NESTIN. Scale bar: 100 µm. (**C**) A representative image of normal male karyotype without numerical or structural chromosomal abnormality from the 16 metaphase cells available for analysis.

6.3.3 Drastic increase in freezing damage and cell loss due to CPA deviation

As described above in section 6.3.1, differences in CPA composition can have a profound effect on post-thaw cell survival, and higher levels of CPA did not always result in increased post-thaw cell survival. Two different non-DMSO solutions that appeared in the DE algorithm were tested and compared for their effect on the freezing responses of hiPSCs. Solution A was the optimized CPA solution containing level-2 sucrose, level-5 glycerol, level-1 isoleucine, and level-4 albumin. Solution B contained level-3 sucrose, level-4 glycerol, level-2 isoleucine, and level-5 albumin, which differed from the optimum by only one concentration level per CPA variable (i.e., 20 mM, 0.5% v./v., 7.5 mM and 0.5%). Solution A resulted in post-thaw cell reattachment of approximately 100% when compared to fresh cells post-passage, whereas Solution B resulted in significantly lower post-thaw cell reattachment and cell losses of over 50% at 24 hours after thawing (Table 13).

As discussed in Chapter 5, when frozen alone without cells, Solution A formed ice crystals with a unique softened solid-liquid interface as well as greater distance of nonfrozen region between one another, which was not observed in Solution B. Raman spectroscopy was also used to characterize the freezing response of hiPSC aggregates in the two solutions of interest. Freezing of hiPSCs in Solution A resulted in the formation of little to no intracellular ice, whereas freezing of hiPSCs in Solution B resulted in significantly more intracellular ice (Table 13). None of the cells (0/12 cells) frozen in Solution A exhibited intracellular ice formation, whereas 6 out of 12 cells contained

intracellular ice when frozen in Solution B. As represented by Figure 25E, the ice crystals found inside the cell aggregates frozen in Solution B were near or in direct contact with extracellular ice, suggesting that the intracellular ice was nucleated by extracellular ice on the other side of the plasma membrane. The fraction of cells exhibiting intracellular ice was consistent with the post-thaw cell reattachment rates of the two solutions. The Raman heat maps also permitted quantification of CPAs partitioning across the cell membrane, an indicator of membrane integrity. As expected, sucrose was non-penetrating and located outside of the hiPSCs, and glycerol penetrated the plasma membrane of the cells in Solution A, indicating normal membrane permeability (Figure 25D). However, higher concentration of sucrose and glycerol was found inside the cells in Solution B, which is consistent with a loss of membrane integrity (Figure 25E).

Table 13. Comparison of freezing responses in Solutions A, B and C under optimal freezing conditions[a]

Conditions and measurements		Solution A (optimized non-DMSO)	Solution B (non-optimized non-DMSO)	Solution C (optimized DMSO)
Cooling rate		-1 ˚C/min	-1 ˚C/min	-1 ˚C/min
Ice nucleation temperature		-4 ˚C	-4 ˚C	-4 ˚C
Post-thaw cell reattachment rate, n=18		104 % ± 5.73 %	48.7 % ± 9.85 %*	58.4 % ± 6.58 %*
Quantitative analysis of Raman heat maps represented by Figure 25	Area fraction of ice in frozen solution, n=5	76.0 % ± 7.93 %	80.3 % ± 4.28 %$^{n.s.}$	68.6 % ± 10.4 %$^{n.s.}$
	Distance between adjacent ice crystals (μm), n=20	2.16 ± 0.667	0.670 ± 0.400*	1.85 ± 0.952$^{n.s.}$
	Area fraction of intracellular ice in frozen cell aggregate, n≥3	2.76 % ± 1.58 %	25.7 % ± 23.9 %*	16.6 % ± 9.05 %*
	Proportion of cells that had intracellular ice, n=12	0/12	6/12*	5/12*

[a]DMSO: dimethyl sulfoxide. 95% confidence intervals calculated from samples of size shown for each metric. ANOVA with Bonferroni correction used to determine statistical significance compared to Solution A. n.s.: $p>0.05$; *: $p<0.05$.

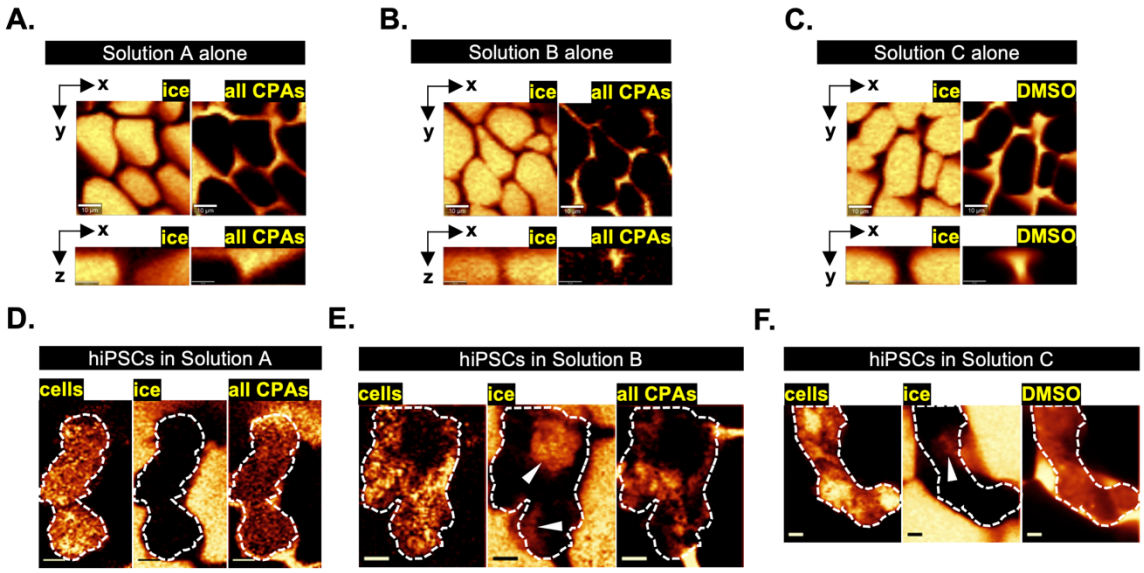

Figure 25. Raman heat maps representative of extracellular and intracellular ice formation in optimized DMSO-free (Solution A) vs. non-optimized DMSO-free (Solution B) vs. optimized DMSO (Solution C). (**A**-**C**) Raman heat maps of ice crystals separated by nonfrozen channels of the respective cryoprotective agent (CPA) solution at -50 ˚C shown in lateral plane (scale bar: 10 µm) and axial plane (scale bar: 3 µm). (**D**-**F**) Raman heat maps of ice formation and CPA distribution in cell aggregate frozen in the respective solution at -50 ˚C (scale bar: 5 µm), with the cell aggregate outlined (white dash) and intracellular ice marked (white arrowhead).

6.3.4 Superior intracellular ice inhibition by optimized non-DMSO than DMSO

Low-temperature Raman spectroscopy was used to characterize the freezing behavior of Solutions A, the optimized non-DMSO composition, and Solution C, a 7.5% DMSO solution commonly used to cryopreserve hiPSCs[20]. Compared to the unique morphology of ice that formed in Solution A, the ice crystals formed in Solution C had typical, abrupt solid-liquid interfaces (Figure 25C). The total amount of ice measured in a given field of view for each solution (Figure 25A and C) was not different ($p > 0.05$, Table 13). In addition, the distance between adjacent ice crystals was similar between the two solutions ($p > 0.05$, Table 13). DSC was used to compare the thermophysical behavior of Solutions

A and C. As shown in Table 13, Solution C had a statistically significantly lower melting temperature than Solution A (with or without P188). However, the total amount of ice measured by the enthalpy of melting was not different ($p > 0.05$) between Solutions A and C, which was consistent with Raman measurements described above. Despite its higher melting temperature, Solution A resulted in significantly better post-thaw cell survival when it was used to cryopreserve the hiPSC aggregates, whereas the lower melting temperature of Solution C, a typically desirable property of CPAs, was not sufficient to result in high levels of post-thaw cell survival. Solution C also exhibited glass transition temperature significantly lower than Solution A.

Raman spectroscopy was also used to characterize the freezing responses of hiPSC aggregates in the two solutions. While Solution A resulted in little to no intracellular ice, Solution C resulted in significantly more intracellular ice (Table 13). While none of the cells (0/12) frozen in Solution A contained intracellular ice, 5 out of 12 cells frozen in Solution C were found with intracellular ice crystals. This was consistent with the percent cell loss measured by post-thaw cell reattachment, suggesting that similar to Solution B, intracellular ice formation likely damaged the cells during freezing when Solution C was used and resulted in cell death or impaired cell adhesion after thawing.

As shown in Figure 25F, similar to cells frozen in Solution A, those frozen in Solution C showed normal permeability of the plasma membrane (i.e., normal partitioning of non-DMSO CPAs or DMSO inside and outside the cell aggregates), suggesting intact

membrane integrity. However, Raman heat maps rendered from signals of proteins and lipids showed high variance in the distribution of protein and lipid content in the cells frozen in Solution C. A considerable number of pixels were saturated in these Raman signals of interest, suggesting aggregation of cellular materials such as organelles and cytoskeleton, while other parts of the cells contained dark regions with very low Raman signals, suggesting loss of cellular integrity. This outcome was not observed in the cells frozen in Solution A.

6.3.5 Undercooling sensitivity mitigated by the optimal non-DMSO formulation

In a previous study[107], we demonstrated that hiPSCs in DMSO were sensitive to undercooling (the difference between the melting temperature and the temperature at which ice forms or ice nucleation temperature). Based on the DSC measurements of the peak of melting (T_{m2}) shown in Table 10, the extent of undercooling was similar ($p > 0.05$) between Solutions A and B when ice nucleation was induced at the same temperature in the respective samples. The extent of undercooling was approximately 2 ˚C when ice nucleation was induced at -4 ˚C and increased to 10 ˚C when ice nucleation was induced at -12 ˚C. The sensitivity of hiPSC aggregates frozen in the optimized versus deviated non-DMSO formulations of interest to undercooling was compared. As shown in Figure 26A, decreasing ice nucleation temperature from -4 to -12 ˚C did not affect the post-thaw reattachment of cells cryopreserved in Solution A. In contrast, high sensitivity to undercooling was observed when the formulation was shifted away from the optimum. Cells cryopreserved in Solution B showed significantly lower post-thaw cell survival

with decreasing ice nucleation temperature. For hiPSCs cryopreserved in Solution A, the cell growth rates measured over a 3-day period after seeding were very similar among fresh cells and frozen cells nucleated at -4 or -12 ˚C (Figure 26B). This outcome indicated that both the post-thaw reattachment and the growth rate of the cells cryopreserved in Solution A were similar for the different ice nucleation temperatures tested.

Cell sensitivity to undercooling was also compared between the optimized non-DMSO and DMSO formulations. When ice nucleation was induced at -12 ˚C, both solutions were subject to 8 ˚C greater undercooling than when ice nucleation was induced at -4 ˚C. Based on measurements of peak of melting shown in Table 14, for a given ice nucleation temperature, the extent of undercooling was always 0.48 ˚C greater in Solution A than in Solution C ($p < 0.05$). In spite of this slight advantage of Solution C, hiPSC aggregates in Solution C were sensitive to undercooling, whereas those in Solution A were not. Consistent with the results from a recent study that used DMSO to cryopreserve a different cell line of hiPSCs[107], post-thaw reattachment of the cells cryopreserved in Solution C dropped significantly with lower ice nucleation temperature (Figure 26A). When ice nucleation occurred at -12 ˚C, post-thaw cell reattachment was 9.53-10.4% (95% confidence interval) in Solution C, while no cell loss was observed in Solution A for the same ice nucleation temperature.

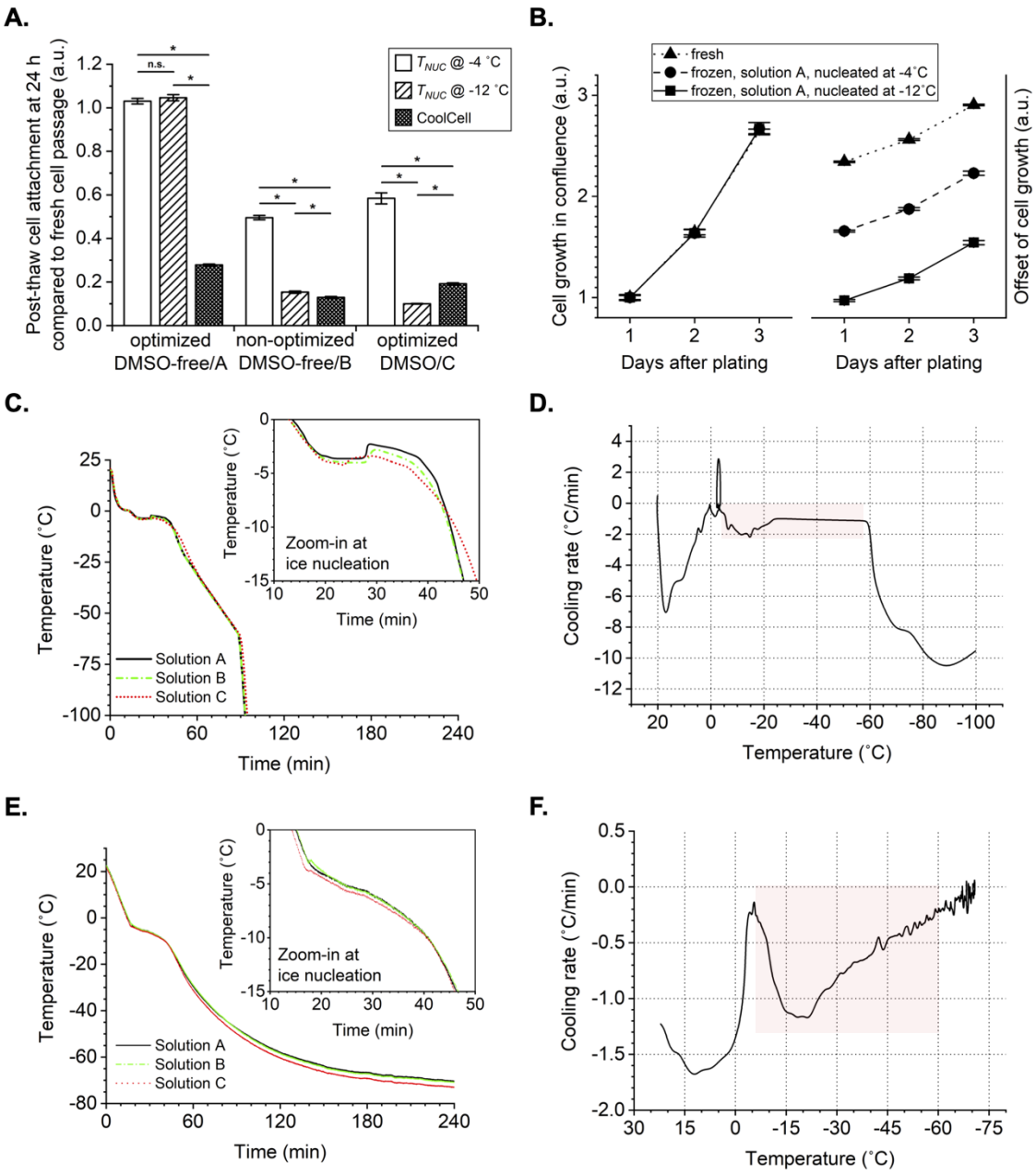

Figure 26. Effect of ice nucleation temperature (undercooling) on post-thaw cell survival in conditions of different cryoprotective agent (CPA) solutions. Error bars of standard error. (**A**) Cell reattachment measured by calcein AM staining 24 hours after thawing at 1:6 split ratio, showing greater cell sensitivity to the freezing condition when using the non-optimized dimethyl sulfoxide (DMSO)-free or optimized DMSO solution than the optimized DMSO-free solution. ANOVA with Bonferroni correction performed for comparison. n.s.: $p>0.05$; *: $p<0.05$. Sample size of 18 (3 independent experiments of 6) biological replicates. (**B**) Cell growth in terms of culture confluence monitored for 3 days after thawing or passaging

at 1:6 split ratio, showing normal growth rate of cryopreserved cells not affected by the ice nucleation temperature (T_{NUC}). Sample size of 6 biological replicates. (**C**) Sample internal temperature recorded over the course of controlled rate freezing with ice nucleation induced manually at -4 ˚C. (**D**) 1st derivative of (C) plotted against the corresponding sample internal temperature. Shaded region (pink): ice growth phase where effective cooling rate ranged roughly between -0.3 and -2.1 ˚C. (**E**) Sample internal temperature recorded over the course of passive freezing in CoolCell with spontaneous ice nucleation. (**F**) 1st derivative of (E) plotted against the corresponding sample internal temperature. Shaded region (pink): ice growth phase where effective cooling rate ranged between -0.2 and -1.2 ˚C.

It was also noteworthy that, passive freezing of hiPSC aggregates using insulated containers such as a CoolCell in -80 ˚C mechanical freezer resulted in significant cell loss regardless of CPA composition (Figure 26A). The increase in temperature associated with the release of latent heat (Figure 26E) suggests that nucleation occurred approximately between -3 ˚C and -4 ˚C for all solutions tested. Therefore, there was no evidence of excessive undercooling that would lead to cell loss in the CoolCell. The temperature-time profiles (Figure 26C and E) and the corresponding cooling rate experienced by the samples (Figures 26D and F) indicate that lower cooling rates were observed using the CoolCell than using the controlled-rate freezer, which can explain the cell loss.

6.3.6 Benchmark study with commercial hiPSC CPA solutions

Within the nucleation temperature range of -4 and -12 ˚C, earlier sections of this chapter showed that the optimized non-DMSO CPA formulation was able to maintain consistently high post-thaw viability and function of hiPSC aggregates, whereas the simple DMSO solution with an optimized concentration of 7.5% in HBSS could not. The

superior ability of the non-DMSO CPA solution to reduce multicellular aggregates' sensitivity to undercooling was subsequently validated in comparison with a group of DMSO-based solutions that are commercially available and have been used to cryopreserve hiPSCs in clinical manufacturing, which included mFreSR, CS10, and B.hRM. All of the three commercial benchmark solutions experienced significantly lower post-thaw cell survival with greater undercooling (Figure 27), emphasizing the commonality of hiPSC multicellular aggregates' vulnerability to undercooling stresses in a variety of DMSO-based solutions as well as the uniqueness of the optimized multicomponent non-DMSO CPA solution's ability to mitigate these stresses.

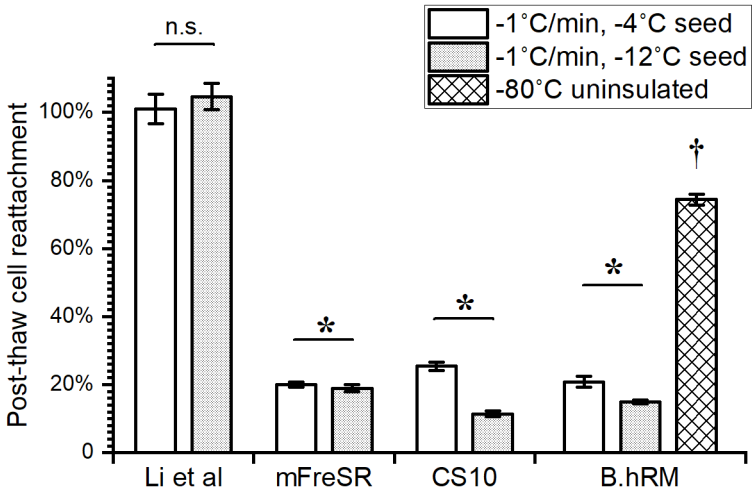

Figure 27. Effect of ice nucleation temperature (undercooling) on post-thaw cell reattachment normalized to fresh cell passaging, comparing the optimized non-DMSO solution (Li et al) developed in this chapter with three different commercial DMSO-based CPA products frozen using a CRF, as well as one additional condition of B.hRM solution frozen using a -80˚C mechanical freezer without insulative secondary containment following the manufacturer's recommendation. Data represented as mean +/- 95% confidence interval. *: $p < 0.05$ in two-sample comparison between -4 and -12 ˚C nucleation; †: $p < 0.05$ in ANOVA comparison with all the other sample groups.

One may note that another sample condition (i.e., -80˚C uninsulated passive freezing)

was also included in Figure 27, a freezing modality particularly prescribed for B.hRM by its manufacturer. Post-thaw cell reattachment resulted from this condition (i.e., 74.4% +/- 1.6%) was second to the optimized non-DMSO solution with controlled rate freezing (i.e., 100% +/- 4.3%) and significantly higher than the two controlled rate freezing conditions in B.hRM ($p < 0.05$). It is likely that the defined cooling rate of -1˚C/min was suboptimal for the molecular formulation and cryoprotective mechanisms of B.hRM.

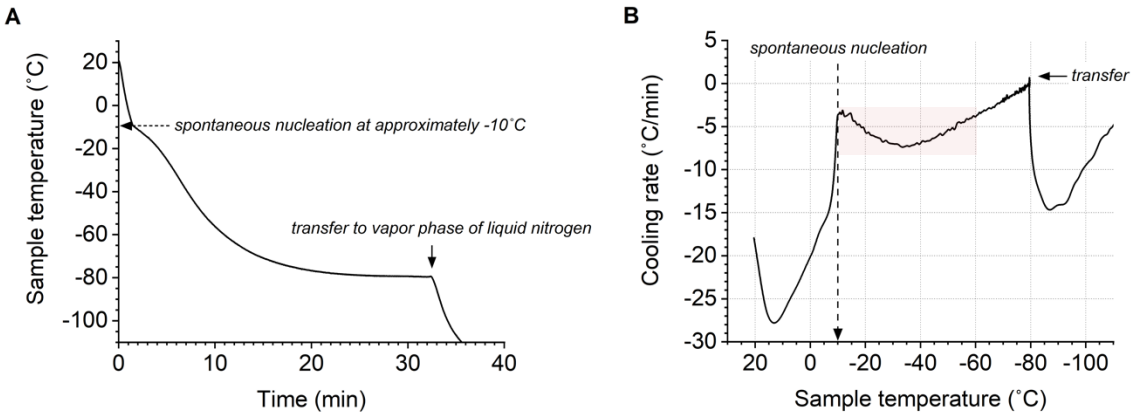

Figure 28. Temperature log inside a dummy vial of 1 ml B.hRM frozen using a -80˚C mechanical freezer without insulative secondary containment corresponding to the additional condition in Figure 27. (**A**) Sample internal temperature over time. (**B**) 1st derivative of (A) plotted against the corresponding sample internal temperature. Shaded region (pink): ice growth phase where effective cooling rate ranged roughly between -3 and -8 ˚C.

Internal temperature of the B.hRM sample was monitored over the course of its freezing in the -80˚C freezer without insulative secondary containment (Figure 28) as described in section 3.6.2. The effective cooling rate ranged between -3.0 and -7.4 ˚C/min, overall higher than the stable cooling rate of -1 ˚C/min achieved in the controlled rate freezing profiles shown in Figure 28C and D. Based on Chapter 4, small hiPSC aggregates

experience significant cell loss with cooling rates of -3 ˚C/min and higher. Consistently, hiPSC aggregates frozen in the optimized non-DMSO solution using this rapid freezing method was found to suffer near complete loss of viable, adherent cells after thawing (data not shown). The CPA composition of B.hRM is likely optimized for fast cooling rates, containing intracellular ice inhibitors, whereas the multicomponent non-DMSO CPA formulation was optimized in the work of this chapter for a fixed cooling rate of -1 ˚C/min, with such limitation to slow cooling. Future investigations may measure the post-thaw reattachment of hiPSC aggregates subjected to varying cooling rates (e.g., -0.5, -1, -3, -5, -7, -9 ˚C/min) to define our optimized non-DMSO solution's sensitivity to cooling rate deviations. They may also perform a new round of DE algorithm under a faster cooling rate (e.g., -7 ˚C/min) using a selection of non-DMSO CPAs as the variables of optimization to understand the molecular requirements and cryoprotective mechanisms of action that prevent intracellular ice during rapid freezing.

6.3.7 Mechanisms of action of albumin, P188 and other basal buffer components

Among the thermophysical properties of a CPA solution, melting temperature indicates the ability of the solution to depress ice crystallization, enthalpy of melting correlates to the amount of ice formed, and glass transition temperature indicates the extent of partial vitrification at low temperatures. A comparison of Solution A with and without two CPA components (isoleucine and albumin) showed no statistically significant difference in enthalpy of melting (Table 14), indicating that isoleucine and albumin did not affect the amount of ice that formed during freezing. However, significant differences in melting

temperature and enthalpy of melting were observed for Solution A with and without P188, indicating that the presence of P188 both depressed and suppressed ice formation during freezing.

Table 14. Melting temperatures, enthalpy of melting and glass transition temperatures for DMSO-free and DMSO CPA solutions measured by DSC[a]

CPA solution	T_{m1} (˚C)	T_{m2} (˚C)	ΔH_m (J/g)	T_g (˚C)
A (optimized non-DMSO)	-6.727 ± 0.712	-2.047 ± 0.0940	205.87 ± 21.49	-89.150 ± 1.631
A minus isoleucine	-7.027 ± 0.296	-1.913 ± 0.117	212.20 ± 4.390	-89.807 ± 2.414
A minus albumin	-6.770 ± 0.433	-1.830 ± 0.293	219.90 ± 13.12	-89.557 ± 5.594
A minus P188	-6.257 ± 0.0759*	-1.697 ± 0.2748*	230.47 ± 15.68*	-91.693 ± 0.737
C (optimized DMSO)	-8.013 ± 0.263*	-2.527 ± 0.123*	214.08 ± 9.392	-118.45 ± 0.723*

[a]T_{m1}: melting temperature defined as the onset of melting; T_{m2}: melting temperature defined as the peak of melting; ΔH_m: enthalpy of melting; T_g: glass transition temperature; A: Solution A; C: Solution C. Measurements shown as 95% confidence intervals. Asterisk (*) indicates statistical significance using a two-sample t-test (p<0.05) compared to Solution A.

The optimized non-DMSO CPA solution (or Solution A) developed from the work in this chapter and published on Frontiers[217] will be referred to as Li et al hereon. Different variant versions of the basal buffer and 2x CPA solution of the Li et al formulation were tested to dissect the effect and postulate the biological mechanism of action of individual CPAs and other basal buffer components in addition to the evidence provided by Raman

spectroscopy and DSC.

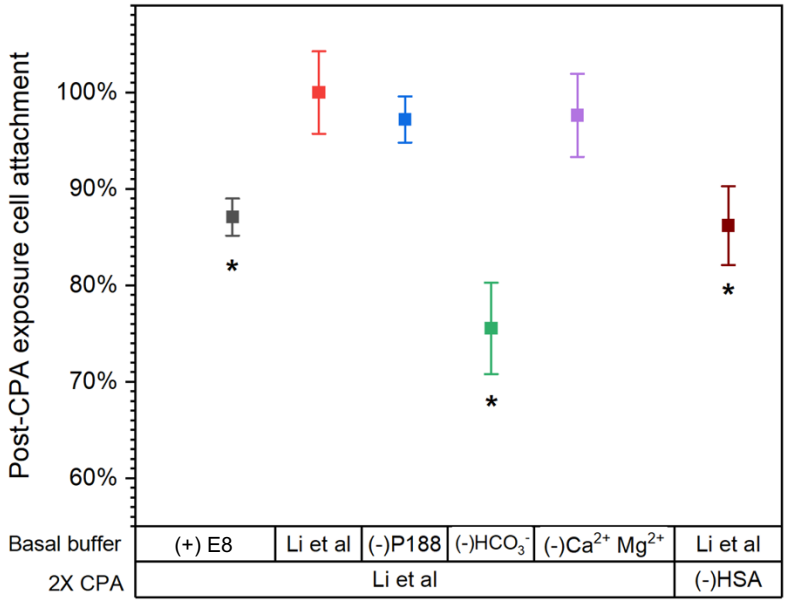

Figure 29. Reattachment of hiPSC aggregates upon collection in the respective variants of the basal buffer and 1 h exposure in the respective variants of the CPA solution, without freezing or thawing, normalized to the mean of the Li et al control group (red). *: $p < 0.05$ in comparison to the Li et al control.

By removing HSA, pre-freeze stability of hiPSCs in the CPA solution decreased significantly (Figure 29), supporting the protective effect of albumin for the non-cryopreserved step stabilizing the cells before freezing. In addition to its cryoprotective effect in concert with the other non-DMSO CPAs to alter ice formation, P188 was also found to increase the reattachment of dissociated hiPSC aggregates (Figure 30). The final working concentration of P188 in Li et al was closest to 4% w./v., which most significantly enhanced the cell reattachment compared to other concentrations tested, not only ensuring high post-thaw survival rate but also enabling wash-free thawing of the hiPSCs.

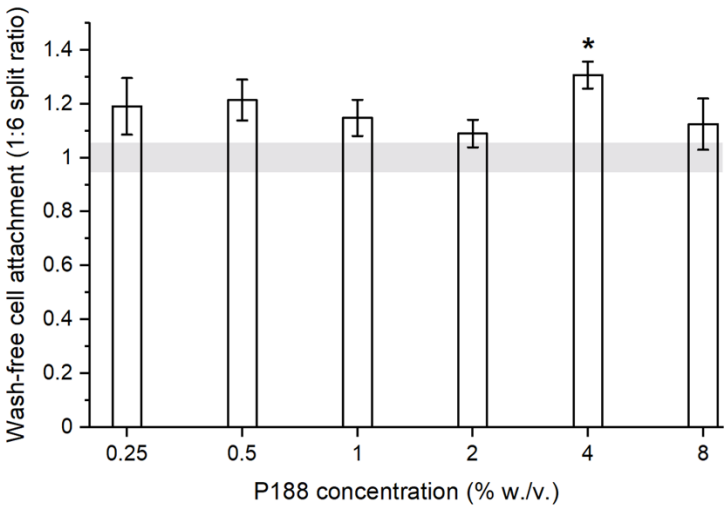

Figure 30. Reattachment of hiPSC aggregates suspended in varying concentrations of P188 and diluted in E8 medium, normalized to untreated fresh cell passaging. Data represented as mean +/- 95% confidence interval. Shaded region: 95% confidence interval of untreated fresh cell control. *: $p < 0.05$ in ANOVA comparison with the other sample groups and untreated fresh cell control.

Moreover, when the P188 content was removed from the basal buffer and added to the 2x CPA solution before introducing these components to the hiPSCs, nearly 90% cell loss was seen in the post-thaw culture (Figure 31) despite the equivalent final working concentration of P188. This finding may suggest that collecting hiPSC aggregates in a P188-based basal buffer played a critical role in ensuring proper partitioning internalization of other CPA molecules, balance of osmotic stresses, and consequently effective cryopreservation of the cells, which can be directly examined with further experimentation using low-temperature Raman spectroscopy.

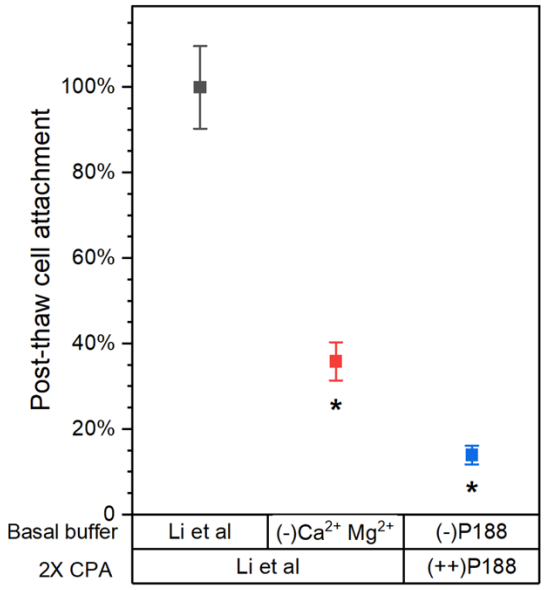

Figure 31. Post-thaw reattachment of hiPSC aggregates collected in the respective variants of the basal buffer, exposed to the respective variants of the 2x CPA solution, and cryopreserved with -1 ˚C/min cooling rate and -4 ˚C nucleation. Data represented as mean +/- 95% confidence interval, normalized to the Li et al control group. *: $p < 0.05$ in comparison to the Li et al control.

Besides P188, the basal buffer in Li et al was also composed of NEAA and HBSS with Ca^{2+}, Mg^{2+}, and HCO_3^-. When NEAA was removed from the formulation, post-thaw cell recovery dropped significantly by 48.3%, and no viable cells were detected in culture 24 hours post-thaw (data not shown), indicating its correlation with cell survival in general. Likely consistent with the purpose of NEAA in common growth media for a variety of cell types, the presence of NEAA in the CPA formulation conserved cell energy that would otherwise be spent towards their production and prevented cell death in the nutrient-deprived environment during non-cryopreserved steps before freezing. On the other hand, replacing HBSS with E8 medium in the CPA solution, as seen in Figure 29, would result in significant cell loss prior to freezing likely due to increased cell metabolic

activity and heightened response to osmotic stresses. Cell metabolic activity will be studied intensively by other students in our group to explore mechanisms of action as such.

Calcium (Ca^{2+}) and magnesium (Mg^{2+}) ions have been known as essential buffer components to support cell-cell and cell-ECM adhesion *in vitro*[131]. It is expected that the removal of these divalent cations to inhibit calcium-dependent cell-ECM adhesion and cause magnesium-dependent cell-cell dissociation-induced apoptosis. Interestingly, upon 1 h CPA exposure in Li et al without Ca^{2+} or Mg^{2+}, there was no significant change in the cell reattachment (Figure 29). However, it was after freezing and thawing in the divalent cation-depleted CPA solution that cells exhibited over 60% loss during the 24 hours of re-culture (Figure 31). As ice grows and propagates around cells, the presence of Mg^{2+} likely strengthens the cell-cell adhesion preventing ice formation in the intercellular space of a multicellular aggregate. While undergoing phase transitions in the freeze-thaw process can stress the cell membrane and membrane proteins, the presence of Ca^{2+} likely enables sufficient binding between cell adhesion molecules and ECM despite membrane impairment.

Lastly, the role of bicarbonate (HCO_3^-) involves the regulation of intracellular and extracellular pH. It is certain that without HCO_3^-, cell loss was significant upon the non-cryopreserved CPA exposure before freezing (Figure 29). However, it is unclear whether intracellular or extracellular pH fluctuation resulted in such cell loss, whether additional

HEPES would enhance pH regulation and further improve cell survival, and whether HSA also served as a pH buffer.

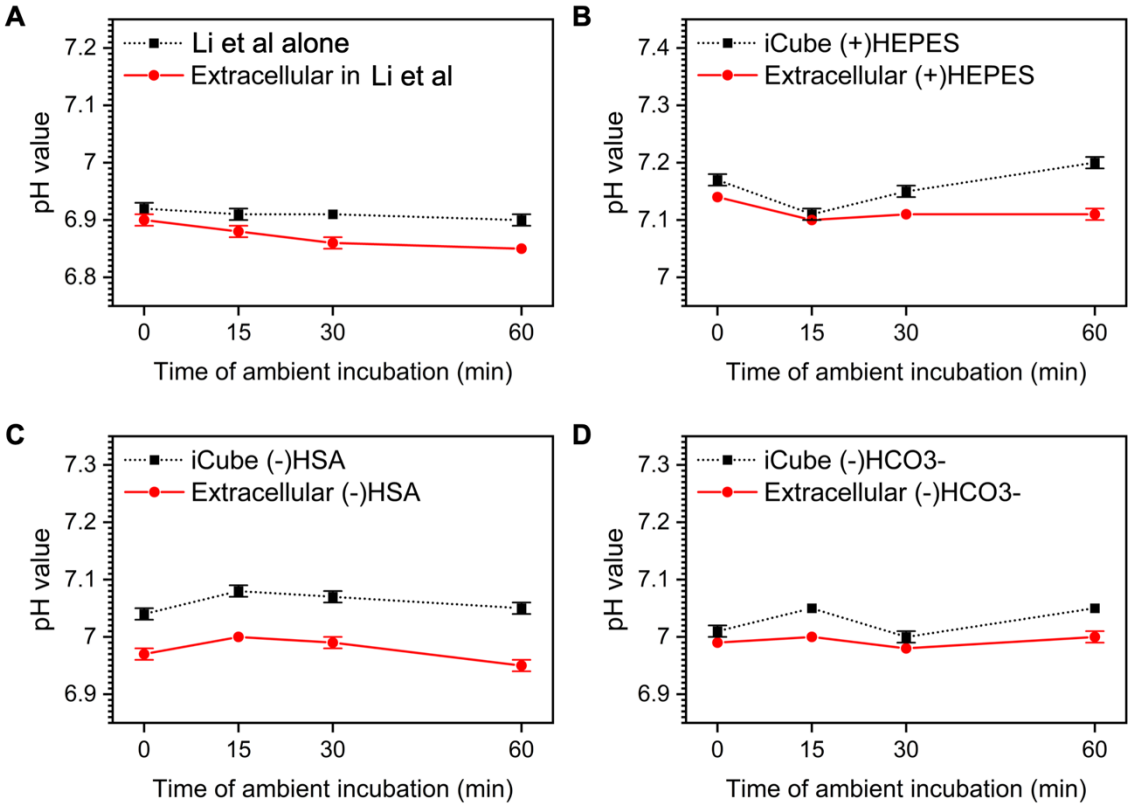

Figure 32. pH measurement in the (**A**) optimized non-DMSO solution developed earlier in this chapter and its variants (**B**) with HEPES added, (**C**) without HSA, and (**D**) without bicarbonate, respectively obtained without cells and in the respective extracellular supernatant over time corresponding to the length of pre-freeze incubation of cell-CPA mixture. Data represented as mean +/- 95% confidence interval. Subtle fluctuation of pH value +/- 0.1 over time was observed in the extracellular environment regardless of the CPA condition, with 0.05 to 0.1 points higher acidity than in the CPA solution alone.

Direct measurement of intracellular pH in the varying CPA solutions was attempted but deemed technically infeasible due to the fluorescent probe's high sensitivity to environmental temperature and predominant response to extracellular pH rather than isolated, robust measurement of intracellular pH (data not shown). However, based on

measurements as described in section 3.17 and shown in Figure 32, extracellular pH was maintained within a range of 0.1 over the course of pre-freeze CPA exposure regardless of the presence or absence of HCO_3^-, HEPES or HSA. Due to the subtilty of the extracellular pH fluctuation, it is more likely that intracellular pH fluctuation was the predominant source of cell stress in the non-cryopreserved condition before freezing as a result of cell metabolic activity.

6.4 Discussion

In this chapter, the DE algorithm produced an optimal non-DMSO formulation for the cryopreservation of hiPSC aggregates under a small number of experiments. Traditional approaches such as empirical trial-and-error and high-throughput screening would take up to 1296 experiments to locate an optimum in this multi-dimensional parameter space; this algorithm reduced the amount of experimentation to only 8 experiments. Alternative methods of optimization are design of experiment (DOE) and the Taguchi method, which is a variant of DOE. Both DOE and Taguchi methods assume that the topology of the parameter space that is being studied is unimodal and that there are no interactions between parameters. Both of these assumptions are not true, as this study has demonstrated that the topology is not unimodal, and our statistical model[85] has shown that there are synergistic effects between the CPA molecules tested, making these alternative approaches unsuitable. The emergent population staying constant for two generations was defined as the criterion of convergence for the DE algorithm. This has been validated in our recent study[106] to ensure ≥ 95% accuracy of predicting the global

optimum.

Compared to our previous DE algorithm studies[105,106], this study optimized 4 variable components instead of the former 3 variables, which resulted in 6 times as many possible vectors in the parameter space than before. However, the population size of each generation (i.e., 10) was smaller than what had been commonly used before (i.e., 13-27). Interestingly, the convergence speed (i.e., 7 iterations) was well-maintained in spite of the higher-dimensional parameter space and smaller experiments. It is also noteworthy that this study used the attachment of multicellular aggregates, a more complex biological system than previously reported and a functional metric. All of these further provide evidence for the stability of this DE algorithm and demonstrate its promising ability to achieve optimization with a small number of cells. With the capability of handling designs and data of greater complexity but no limit to the number of parameters or the type of application beyond cryopreservation, the DE algorithm could serve as a powerful tool to accelerate the otherwise resource-intensive process of optimization and encourage the beneficial practice of optimizing translational stem cell technologies in general.

A variety of methods for preserving hiPSCs have been developed (see review article[110]). These methods can be divided into two different categories: (1) vitrification and (2) slow freezing. DMSO has been a universal component in these cryopreservation solutions. ROCK inhibitor is commonly used as an additive to suppress post-thaw apoptosis[17,19,50,132]. In contrast, this investigation describes a non-DMSO method that

freezes hiPSCs in aggregates and avoids the use of apoptosis inhibitors.

The combination of previous studies[80,85] and new findings from this investigation provides insights into how the non-DMSO CPAs act to protect the hiPSCs from freezing damage. Mechanisms of cryoprotection for non-DMSO CPAs differ from that of DMSO, which is an organic solvent. Both sucrose and glycerol influence the hydrogen bonding with water[205,213,236] and interact with each other[86] to likely form natural deep eutectic systems (NADES)[184]. These molecular interactions can modify the freezing behavior of water around cells, specifically changing in ice crystal morphology to reduce cellular damage from ice.

The CPAs used also interact with the biological structures in cells. Low-temperature Raman spectroscopy has demonstrated that sucrose interacts with the plasma membrane[213]. While cellular dehydration plays a major role in preventing intracellular ice, glycerol also inhibits intracellular ice by forming strengthened hydrogen bonds with the remaining water content in the cytoplasm[205,237]. Isoleucine was found to be cryoprotective at a low concentration and higher concentrations resulting in lower post-thaw cell survival. While DSC results of the thermophysical properties of CPAs in this study showed that isoleucine did not significantly contribute to the ice inhibition effects of the CPA cocktail overall, DE algorithm results showed that post-thaw cell survival could be increased significantly (e.g., from 48.3% to 100%) by 7.5mM isoleucine. This is likely a “sweet spot” between the stabilizing[228,229] and destabilizing[230] effects of a

hydrophobic amino acid on protein molecules in the cells. While albumin may not have a significant effect on ice formation as shown by DSC, it can act as a scavenger of free radicals alleviating oxidative stress and a carrier of waste produced from any cell damage and stress in freezing and thawing[238].

Our earlier study found that hiPSC aggregates were more sensitive to undercooling than single cells frozen in DMSO[107]. The sensitivity to undercooling has been observed in a variety of biological systems. As described in a review article[239], controlled ice nucleation of samples or directional solidification, which eliminates undercooling, has been shown to improve post-thaw cell recovery. The outcome of this investigation expands our understanding of this issue. Specifically, cell aggregates frozen in a variety of DMSO-based solutions and a suboptimal formulation of a non-DMSO solution exhibited sensitivity to undercooling. This restricts the modalities of freezing suitable for hiPSCs in these solutions. However, hiPSC aggregates cryopreserved using an optimized non-DMSO solution exhibited far less sensitivity to undercooling, and ice nucleation temperatures of as low as -12 ˚C do not result in cell losses post-thaw. In contrast to DMSO, the optimal non-DMSO solution provides greater flexibility in freezing and can accommodate greater variability in execution of the freezing protocol. In design of a controlled rate freezing protocol, it is important that the ice nucleation (or seeding) temperature is lower than the peak temperature of melting for the CPA solution used to ensure that ice crystallization is feasible and that the frozen state can be maintained in the subsequent slow freezing steps. While ice nucleation at -4 ˚C optimized in our earlier

study[107] demonstrated effective cryopreservation using the optimized non-DMSO solution in this study, ice nucleation temperatures below -2.2 ˚C and above -4 ˚C may be alternative ice nucleation temperatures to be used with this method in future studies. In addition, the use of passive freezing devices as well as the rapid freezing in mechanical freezer resulted in significant drops in post-thaw cell survival when compared to controlled rate freezing. This observation is consistent with the sensitivity of hiPSCs to cooling rate variation.

In addition to the superior cryoprotection provided by the synergistic combination of sucrose, glycerol, L-isoleucine, human serum albumin and P188, components of the basal buffer protected the multicellular aggregates in non-cryopreserved conditions surrounding the freeze-thaw process. P188 was found to not only enhance reattachment of dissociated hiPSCs but also ensured proper osmotic balance upon CPA introduction. Calcium and magnesium ions in HBSS were found to enable post-thaw reattachment of hiPSCs that had been subjected to the stresses and possible impairment in their cell adhesion molecules. While extracellular pH may be very stable over the course of CPA exposure, bicarbonate played a significant role in regulating intracellular pH and ensuring cell stability in the non-physiological environment of cryopreservation. The outcome of this investigation enables not only improved cryopreservation of hiPSCs, but also insight into the sensitivity of multicellular systems to freezing, as well as to processes before freezing, and strategies to overcome those sensitivities.

6.5 Conclusion

Human induced pluripotent stem cells (hiPSCs) are an important cell source for regenerative medicine products. Effective methods of preservation are critical to their clinical and commercial applications. The use of a dimethyl sulfoxide (DMSO)-free solution containing all nontoxic molecules offers an effective alternative to the conventional DMSO and alleviates pain points associated with the use of DMSO in the cryopreservation of hiPSCs. Both hiPSCs and cells differentiated from them are commonly multicellular systems, which are more sensitive to stresses of freezing and thawing than single cells. In this investigation, low-temperature Raman spectroscopy visualized freezing behaviors of hiPSC aggregates in different solutions. These aggregates exhibited sensitivity to undercooling in DMSO-containing solutions. We demonstrated the ability to replace DMSO with nontoxic molecules, improve post-thaw cell survival, and reduce sensitivity to undercooling. An accelerated optimization process capitalized on the positive synergy among multiple non-DMSO molecules, which acted in concert to influence ice formation and protect cells before freezing, during freezing, and after thawing. A differential evolution algorithm was used to optimize the multivariable, non-DMSO preservation protocol in 8 experiments. hiPSC aggregates frozen in the optimized solution did not exhibit the same sensitivity to undercooling as those frozen in DMSO, indicating superior adaptability of the optimized solution to different freezing modalities and unplanned deviations. This investigation shows the importance of optimization, explains the mechanisms and advantages of a non-DMSO solution, and enables not only improved cryopreservation of hiPSCs but potentially other

cell types for translational regenerative medicine.

Chapter 7

Cell Cryobiology and Cryopreservation Challenge Change with Differentiation and Maturation from hiPSCs to Sensory Neurons

Much of the text and figures in this chapter will appear in the pending publication below, included here with copyright permission from potential publishers including Frontiers, Mary Ann Liebert, and Elsevier.

Li R, Walsh P, Truong V, Peterson A, Dutton JR and Hubel A. DMSO-free freezing of hiPSC-derived sensory neurons reveals stage-specific mechanisms for addressing cryopreservation challenges during cell manufacturing. (In preparation.)

7.1 Introduction

Human induced pluripotent stem cells (hiPSCs) can be manufactured from a range of somatic cell types and further differentiated into cells valuable for drug discovery[11], cell therapy[5], and tissue engineering[240] applications. However, the generation of hiPSC-derived cells involves complex, protracted and expensive manufacturing processes employing differentiation protocols that progress through increasingly mature cell stages. There is significant added value in derisking the manufacturing supply chain by being able to efficiently cryopreserve cells at multiple stages along the differentiation trajectory, from the originally isolated somatic tissue through the pluripotent stem cell stage, intermediate progenitor and differentiated phenotypes, to the terminal mature product. Effective cryopreservation of cells at different developmental stages may not

only simplify the multi-stage production of hiPSC-based technologies, but also enable off-the-shelf use of the end product.

The field of cryobiology has extensively studied the cell and tissue types at the front end of stem cell-based manufacturing process, from starting materials such as peripheral blood mononuclear cells (PBMCs)[12–14] and fibroblasts[15,16] to hiPSCs[241,242] and mesenchymal stromal cells (MSCs)[46,243]. While results of cryopreservation have been reported in some studies of hiPSC-derived cell types[22,23], we lack understanding of scientific principles on formulating cryopreservation media, freezing, thawing, cryoinjury mechanisms for many intermediate and mature cell product phenotypes, whether and how they change from one cell type to another, especially in relation to the expanding variety of cell types in this dynamic field of hiPSC-based manufacturing.

It has been commonly hypothesized among scientists that the more differentiated or the more mature the cells are, the more difficult they are to freeze and produce a viable post-thaw population. Cryopreservation practice in the stem cell biology field reflects a similar trend and suggests an imbalance of cryopreservation feasibility along hiPSC differentiation trajectories. Intermediate, progenitor-like cell types[18,244] predominate in the literature describing the cryopreservation of hiPSC-derived cells. The vast majority of academic and industrial use-case literature, in drug screening for example, completely foregoes cryopreservation of assay-ready cells in favor of months-long continuous cell production and maturation[245–253]. The limited use of cryopreservation is indicative of a

knowledge or capability gap that the cutting edge of cryobiological research can begin to address.

How do the mechanisms of cell loss in cryopreservation vary between different cell stages along a differentiation process? What will enable successful cryopreservation of challenging cells? Can an existing method for cryopreserving one cell type be effective for another cell type? These scientific questions will impact the future of hiPSC-based clinical translations. With the lack of answers to date, it is important to establish a new perspective by more thoroughly investigating cell cryobiology over the course of a defined hiPSC differentiation continuum.

To build understanding and discover a path toward practical solutions to these problems, we present the first systematic evaluation, to our knowledge, of discrete differentiation and maturation stages along a cell developmental trajectory, from undifferentiated hiPSC through neural crest cells, immature neurons to electrophysiologically active sensory neurons, in the context of several key process, molecular, and cellular parameters attributed to cryopreservation success. In this work, the process parameters are defined as cooling rate and ice nucleation temperature by the means of controlled rate freezing. Particularly, different ice nucleation temperatures represent different degrees of undercooling, a major cause of cryoinjury in cells[239]. In addition, the molecular factors here are a comparison between a non-DMSO CPA formulation previously optimized for hiPSC cryopreservation versus a DMSO-based formulation that is commercially

available and widely utilized for a variety of clinical cell cryopreservation scenarios. Low-temperature Raman spectroscopy is used during freezing to interrogate the response of these cell stages to differences in these parameters. An array of standard (e.g., intracellular ice formation) and novel (e.g., membrane partitioning of CPA solutes) Raman metrics are rendered from the label-free, high-resolution hyperspectral images of live cells and their surrounding microenvironment in a frozen state under the microspectroscopic lens, which would not be feasibly observed using conventional assays before or after controlled rate freezing. Corresponding to Raman studies, a progression of cell-based assays with increasing functional relevance are used after controlled rate freezing and thawing to reveal the cryopreservation outcome of these cell stages given the cooling rate and undercooling variations.

This investigation is intended to serve as an example of the novel perspective of conducting cryobiological research, tracing the cryobiological challenges inherent in a multi-stage progression of differentiation typical for hiPSC-derived cell manufacturing. The hiPSC-to-sensory neuron differentiation protocol used here was selected for its well-defined timeline and well-characterized cell stages. The investigational methodology may be subsequently adapted towards the cryopreservation and cryobiological research of alternative neural differentiations and tissue lineages. While the cryopreservation methods and outcomes specified by this study may not be directly applicable to other use-case scenarios, certain cryobiological trends can be translated to the broader understanding of cryopreservation challenge and design of cryopreservation strategy in a

manufacturing process of differentiating cells. As stem cell biology is translating from bench to bedside with rapidly emerging hiPSC technologies, it is timely to scrutinize this manufacturing science from the perspective of cryopreservation and cell cryobiology.

7.2 Methods

hiPSCs used in this chapter were of cell line UMN PCBC16iPS and maintained between passages 80 and 85 on a 4-day subculture cycle as described in section 3.2.1. Main subjects of the following investigation included three discrete cell stages of the hiPSC-derived sensory neuron lineage (Figure 33A), where neural crest cells (D5 crest), immature sensory neurons (D7 SN), and more mature sensory neurons (D14 mSN) were cultivated respectively as described in section 3.2.3. Their phenotypes were characterized as described in sections 3.3.3 through 3.3.5 and shown in Figure 33B-D. Suspended in a basal media (i.e., phenol red-free DMEM/F12), the membrane fluidity and diameter of D5 crest, D7 SN and D14 mSN were measured respectively as described in sections 3.18 and 3.19.

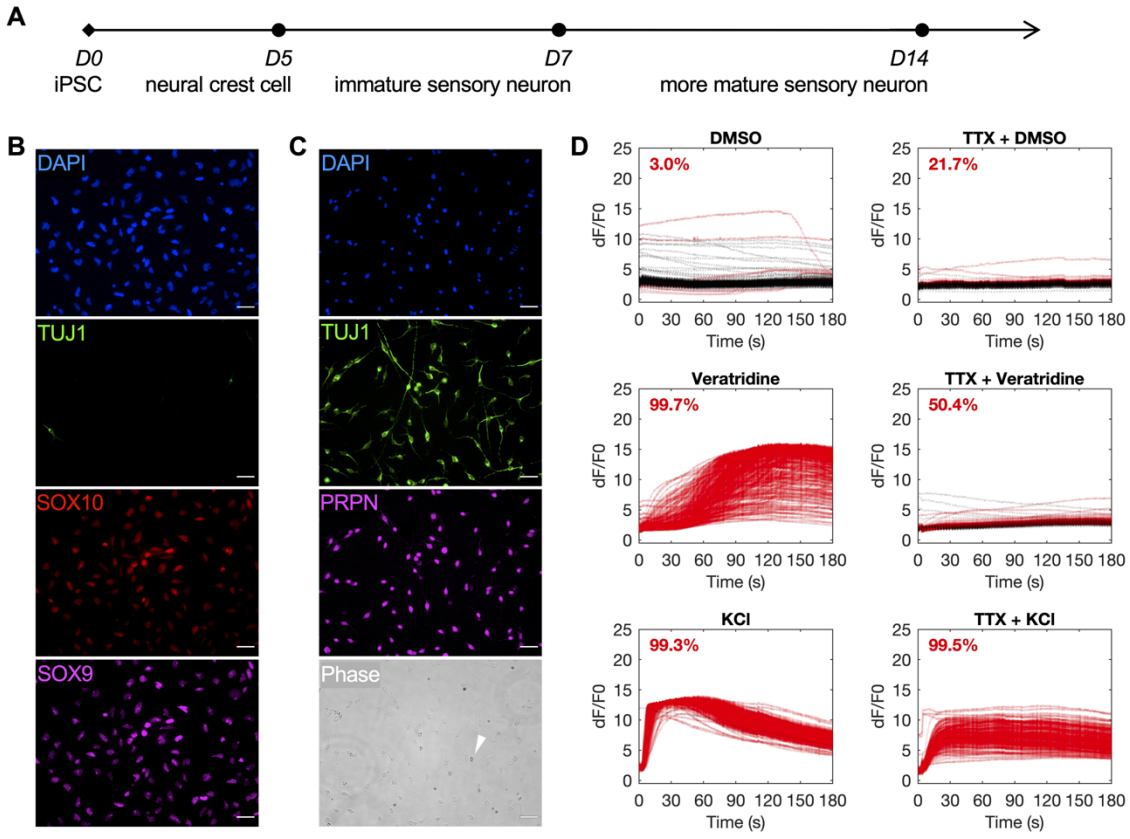

Figure 33. Characterization of three different cell stages along a hiPSC-to-sensory neuron trajectory. (**A**) A 14-day timeline for cultivating the three stages of neuronal cells of interest for this investigation. (**B**) Immunocytochemistry of day-5 neural crest cells (D5 crest) replated at 100,000 cells/cm^2, 98.4% TUJ1- SOX9+ SOX10+. Scale bar: 50 µm. (**C**) Phase contrast and immunocytochemistry of day-7 sensory neurons (D7 SN) replated at 50,000 cells/cm^2, 98.8% TUJ1+ PRPN+ excluding dead cells by morphology (example indicated by white arrow in phase). Scale bar: 50 µm. (**D**) Calcium imaging of day-14 sensory neurons (D14 mSN), seeded at 50,000 cells/cm^2 on day 7, showing minimal response to DMSO, strong and TTX-sensitive response to veratridine, and strong response to KCl. Lines color-coded red for responder cells and black for non-responder cells. Proportion of responder cell population indicated per graph. (**E**) Cell membrane fluidity at different stages of the sensory neuron differentiation and maturation process with all pairwise differences statistically significant. Data represented as mean +/- 95% confidence interval. n = 9. *: $p < 0.05$. (**F**) Diameter of D5 crest vs. D7 SN vs. D14 mSN dissociated from culture and suspended in growth medium. Data represented as mean +/- 95% confidence interval. Range of n: 60 – 98. *: $p < 0.05$. [Experiments for panels B and C were performed by Patrick Walsh.]

Cryobiology of these hiPSC-derived neuronal cells was examined as single cells

suspended in two different CPA formulations. One of the formulations was the non-DMSO solution optimized for hiPSCs in chapter 6 so as to assess the translation of a cryopreservation method from one cell stage (i.e., pluripotent) to another (i.e., progenitor, terminally differentiated, mature). The other formulation of interest was CS10, a commercially available, DMSO-based CPA solution commonly used in cell cryopreservation towards clinical applications, to serve as a benchmark in comparison with the non-DMSO solution and a basis for understanding the current challenge of cryopreserving hiPSC-derived neuronal cells. The solutions were prepared as described in section 3.4. Suspension of D5 crest, D7 SN and D14 mSN was respectively prepared in these solutions as described in section 3.5.3.

Prior to freezing, cell stability in the non-DMSO and DMSO-based solutions was respectively quantified over the course of CPA exposure. Upon 0, 30, 60 minutes of incubation at room temperature, viable cell count was measured based on membrane integrity per cell stage and CPA condition as described in section 3.7.2.

During freezing, the cryobiological response of each neuronal cell stage to different cooling profiles and CPA formulations was analyzed using low-temperature Raman spectroscopy following previously published methods described in section 3.13. Specifically, defined cooling rates of -1, -3 and -5 ˚C/min and ice nucleation temperatures of -4 and -8 ˚C were used as variables of the cooling profile. Data acquisition was performed at -50 ˚C when sample temperature had stabilized for a minimum of 5

minutes. Raman heat maps of different substances of interest were respectively rendered pixel-wise by integrating the Raman spectra under the peak at their characteristic wavenumbers (Table 15). Intracellular ice formation, membrane partitioning of CPA, cytochrome C release, cellular integrity, and cell size reduction were respectively quantified as described in section 3.14.

Table 15. Raman spectral peak assignments

Substance	**Wavenumber (cm^{-1})**	**Assignments**[232–235,254–257]
Cell	77 - 154	Hydrogen bond vibration
Protein	1622 - 1699	Amide I
Cytochrome C	1117 - 1137	Heme vibration
Ice	195 - 235	Hydrogen bond vibration
Ice	3087 - 3162	OH stretching
Non-DMSO CPAs (i.e., sucrose, glycerol, isoleucine, P188, HSA)*	815 - 865	CC stretching
DMSO	648 - 726	Symmetric CS stretching

*abbreviated and labeled in Raman images as “CPA”

After controlled rate freezing in vials as described in section 3.6.1 and thawing as described in section 3.6.3, sensitivity of D5 crest, D7 SN and D14 mSN to variations in cooling rate and undercooling was respectively quantified in terms of their post-thaw survival and function. Similar to Raman experiments, a cooling rate, B, of -1, -3 or -5 ˚C/min and ice nucleation temperature, T_{NUC}, of -4 or -8 ˚C were used (see Figure 34 for

the sample cooling profiles).

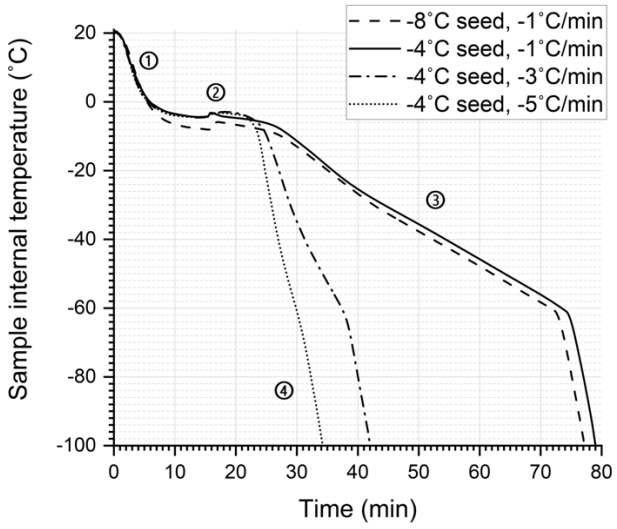

Figure 34. Sample temperature profiles during controlled rate freezing varied by three different cooling rates and two different ice nucleation temperatures. Step 1 represented gradual cooling to the intended ice nucleation temperature. Step 2 represented a subtle increase in sample temperature as the result of latent heat of fusion upon induced ice nucleation. Step 3 represented slow cooling at the intended cooling rate and ice growth phase. Step 4 represented fast cooling to the final sample temperature of -100˚C before samples were transferred to cryogenic storage.

Cell recovery based on membrane integrity was measured immediately post-thaw as described in section 3.7.3. Cell reattachment based on esterase activity and cell adhesion was measured 24 hours post-thaw as described in section 3.8.2. Post-thaw function of D5 crest, D7 SN and D14 mSN was measured respectively as described in sections 3.11.2 and 3.11.3. Fresh cells of each cell stage were used as a positive control.

In this chapter, data was represented as the mean plus/minus 95% confidence interval. Independent biological replicates were used with sample size specified in the Results per dataset. Power analysis was performed to ensure sufficient sample size to achieve a

power of 0.95. Two-tailed Student's *t*-tests were performed for two-sample comparisons. ANOVA with Bonferroni correction was performed for comparisons of multiple samples, with the exception of Kruskal-Wallis ANOVA performed for sample populations with non-normal distribution. The null hypothesis was defined as no statistical difference between the parameters (e.g., means) for any pair of groups or between the experimental group and control group. The null hypothesis was rejected, and differences were considered statistically significant for a *p*-value less than 0.05.

7.3 Results

7.3.1 Non-DMSO solution superior in maintaining viability of all cell stages before freezing

Cells are cryopreserved in specialized solutions containing cryoprotective agents (CPAs). These solutions are not physiological and cell losses can result from exposure to these solutions. Different cell types can have different responses to being exposed to the same CPA formulation, and different CPA formulations can have different levels of cytotoxicity for a given cell type. In order to quantify the toxicity of the cryoprotective solutions, viable cell count was tracked, via membrane exclusion fluorescent assay, for 1 hour from the introduction of non-DMSO CPA and DMSO solutions before freezing for D5 crest, D7 SN, and D14 mSN respectively (Figure 35).

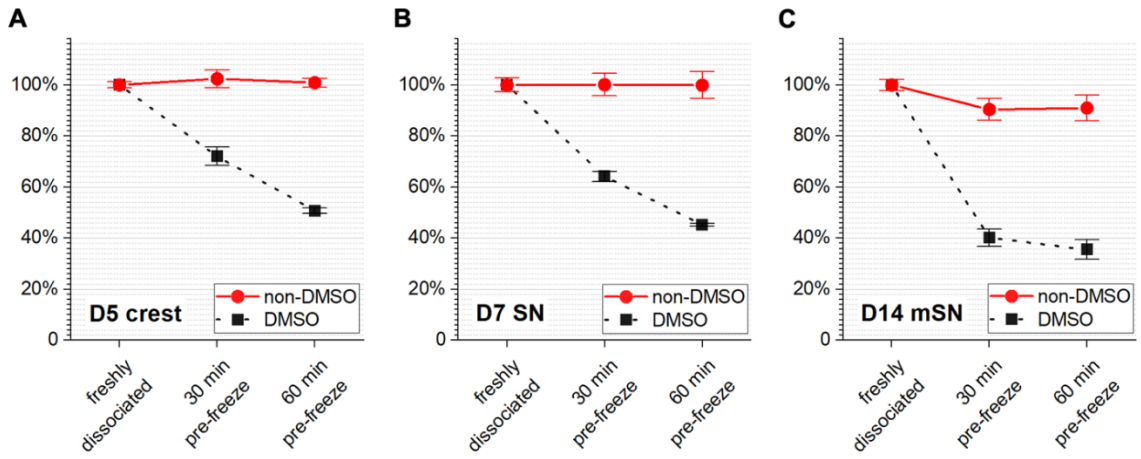

Figure 35. Cell survival rate before freezing monitored over time of exposure to non-DMSO CPA or DMSO for (**A**) D5 crest, (**B**) D7 SN, and (**C**) D14 mSN, respectively. Data represented as mean +/- 95% confidence interval. $n = 4$.

Compared to the non-DMSO CPA, the DMSO solution resulted in significant cell loss by both loss of membrane integrity and lysis (high cell count with compromised membrane and low total cell count, raw data not shown) for all cell stages within 30 minutes of exposure. After 1 hour of pre-freeze incubation in DMSO, all cell stages experienced close to (D5 crest, $p > 0.05$) or greater than (D7 SN and D14 mSN, $p < 0.05$) 50% cell loss. Notably, the cell loss increased over time regardless of cell stage. At both the 30 and 60-minute timepoints, it was found with statistical significance ($p < 0.05$) that the farther the cell stage in differentiation and maturation, the lower the cell stability in DMSO.

In contrast, no significant change in viable cell count ($p > 0.05$) was seen in either D5 crest or D7 SN throughout the 1-hour incubation in the non-DMSO solution. While the cell survival rate of D14 mSN decreased from 100% to approximately 90% within the first 30 minutes of non-DMSO CPA exposure, their viability remained statistically

unchanged ($p > 0.05$) for the next 30 minutes until freezing. Notably, regardless of cell stage, the non-DMSO CPA formulation was significantly superior ($p < 0.05$) to the DMSO-based formulation in stabilizing these neuronal cells and maintaining their viability in the time period prior to the start of freezing.

7.3.2 Membrane fluidity, cell size fluctuate as neuronal cells differentiate and mature

As one possible intrinsic factor influencing cells' sensitivity to freezing[258,259], membrane fluidity was measured for each cell stage, upon dissociation and in suspension, along the 14-day differentiation trajectory (Figure 36A). This included hiPSCs in the forms of single cells and multicellular aggregates, D5 crest, D7 SN, and D14 mSN in the form of single cells. Based on PDA excimer-to-monomer ratios, membrane fluidity of the cells underwent significant changes as they became more differentiated and mature. Interestingly, within the 5 days of differentiation from hiPSCs to neural crest cells, the relative membrane fluidity increased by more than 50%. In the next 48 hours from neural crest cells to fully differentiated sensory neurons, the change in membrane fluidity inverted direction by decreasing approximately 20%. This decrease continued, at an overall slower rate than earlier, for another week as the neurons matured. PDA assay also showed that hiPSC aggregates had significantly lower membrane fluidity than their single cell counterparts, inversely correlated with the significantly greater undercooling sensitivity that was found by previous studies[107,241]. Notably, the fluctuation in membrane fluidity along this differentiation trajectory was not unidirectional, increasing during the initial pluripotent-to-progenitor step but decreasing from progenitor through maturation

based on the selected discrete cell stages.

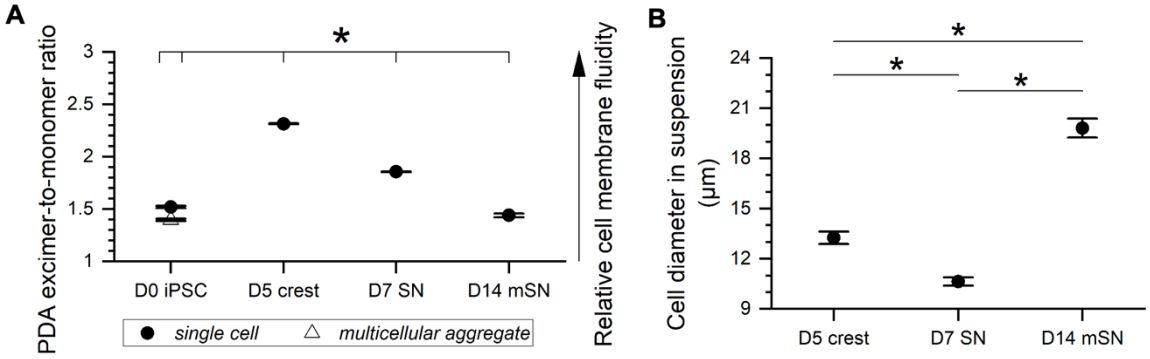

Figure 36. Membrane fluidity and cell size fluctuation along hiPSC derivation to sensory neurons. (**A**) Cell membrane fluidity at different stages of the sensory neuron differentiation and maturation process with all pairwise differences statistically significant. Data represented as mean +/- 95% confidence interval. $n = 9$. *: $p < 0.05$. (**B**) Diameter of D5 crest vs. D7 SN vs. D14 mSN dissociated from culture and suspended in growth medium. Data represented as mean +/- 95% confidence interval. Range of n: 60 – 98. *: $p < 0.05$.

In addition to membrane fluidity, cell size was considered another potential intrinsic factor influencing cell sensitivity to freezing[54,57]. Diameter of the cells in suspension was observed to fluctuate significantly from one cell stage to the next along this differentiation trajectory (Figure 36B). D7 SN was found with the smallest cell diameter in suspension at 10.6 µm, followed by D5 crest at 13.3 µm, and D14 mSN with the largest cell diameter at 19.8 µm. Changes in soma size have been known in literature to occur during neuronal development[260,261]. Notably, the fluctuation in cell size was not unidirectional from neuronal differentiation to maturation. However, somata (or cell body) enlargement over the course of neuronal maturation observed in this study was also consistently observed in stem cell biology practices. In subsequent experiments, freezing sensitivity of these different stages of neuronal cells were dissected using low-temperature Raman spectroscopy and post-thaw cell-based assays, where correlation

between freezing results and these membrane fluidity and cell size measurements was examined.

7.3.3 Undercooling sensitivity and mechanisms of damage varied by cell stage

The three stages of neuronal cells were frozen in the non-DMSO or DMSO-based solution under a confocal Raman microscope. The cells were subjected to different degrees of undercooling, where the freezing process was initiated with ice nucleation induced at different temperatures, -4 versus -8 ˚C, and subsequently cooled at a constant rate of -1 ˚C/min. In each frozen cell, intracellular ice formation, membrane partitioning of solutes, cellular protein distribution, and cytochrome C distribution were quantified (see Figure 37 for definition and illustrative examples of different values of the corresponding metrics). Cryobiological analysis of the frozen cells revealed mechanisms of damage, or the absence thereof, at each cell stage in response to the varied CPA solutions and varied undercooling conditions.

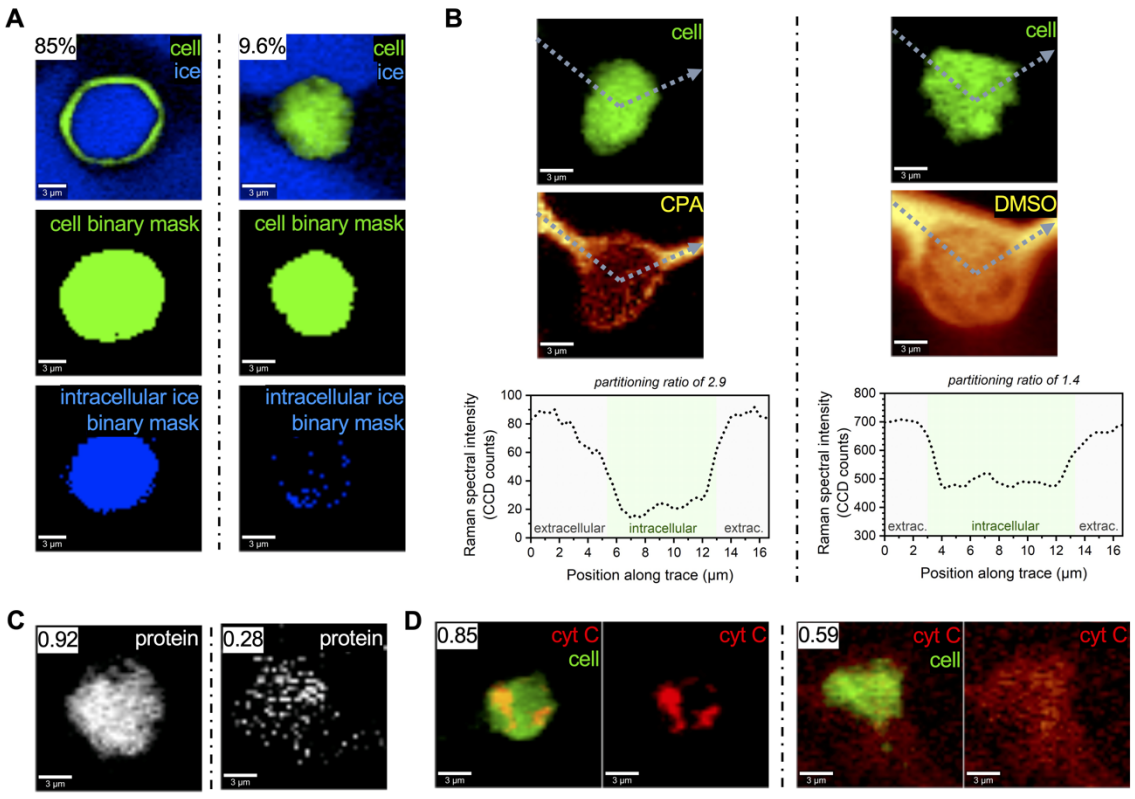

Figure 37. Illustrative examples of quantitative Raman metrics used in this investigation. Scale bar: 3 μm. (**A**) Contrast of two samples with high (left) versus low (right) intracellular ice formation. Overlay and binary mask of Raman heat maps of cell and ice with area proportion of ice inside cell (AIC) values displayed per sample. (**B**) Contrast of two samples with high (left) versus low (right) membrane partitioning of non-DMSO CPA molecules versus DMSO. Raman heat maps and CPA (or DMSO) concentration profile along the dotted segmented arrow with partitioning ratio values displayed per sample. (**C**) Contrast of two samples with normal versus disintegrated cellular proteins. Raman heat map of protein by amide I signal with spatial autocorrelation value displayed per sample. (**D**) Contrast of two samples with cytochrome C (cyt C) contained in (left) versus released from (right) mitochondrial region. Overlay of Raman heat maps of cyt C and cell, as well as a heat map of cyt C alone that was used for Moran's I analysis, with spatial autocorrelation value of cyt C displayed per sample.

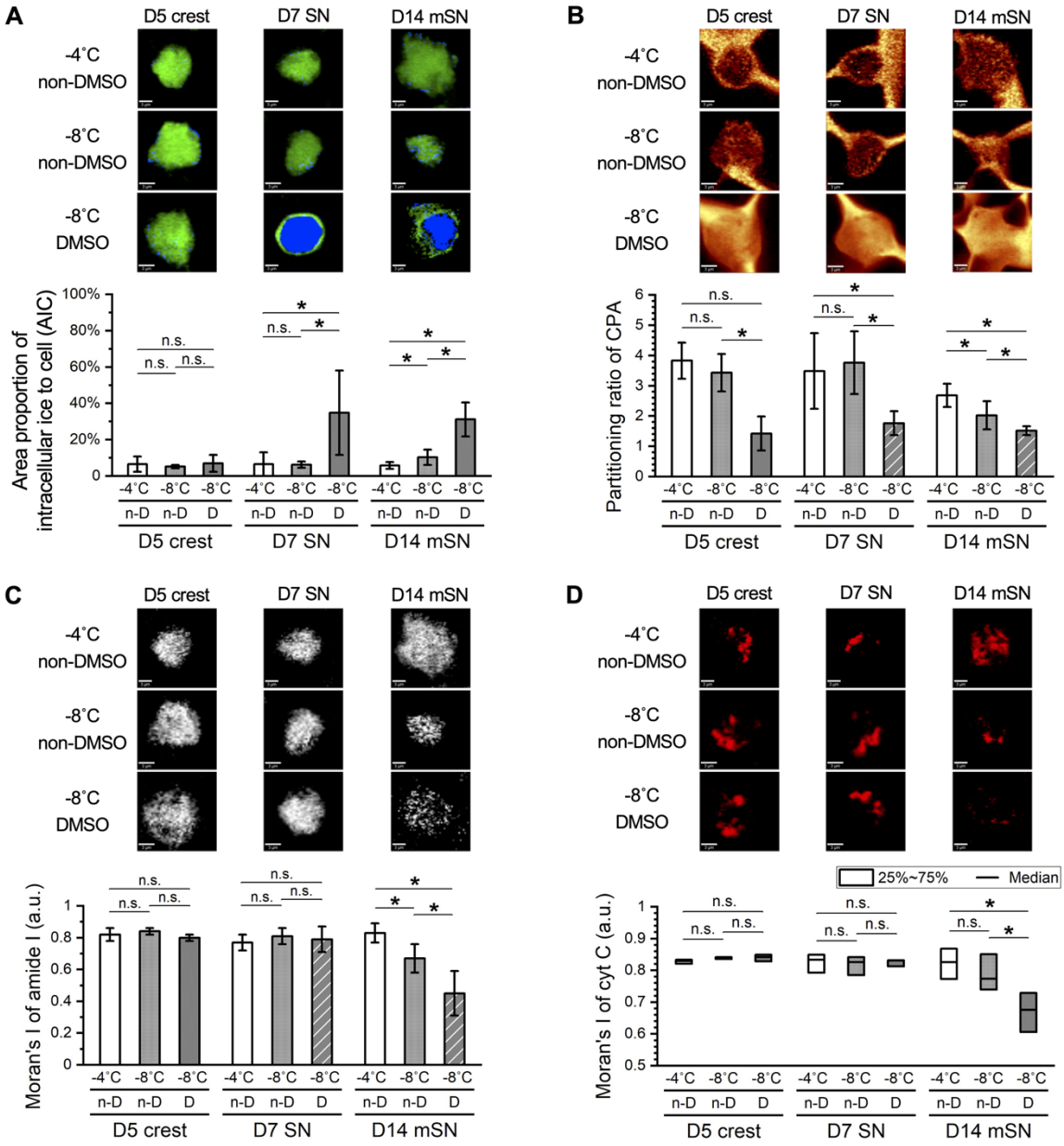

Figure 38. Effects of undercooling on freezing behaviors of D5 crest, D7 SN, and D14 mSN, respectively as observed by low-temperature Raman spectroscopy, comparing different ice nucleation temperatures between -4 and -8˚C. Data represented as mean +/- 95% confidence interval. n = 10, except for striped columns representing measurements of subset population n = 5 for D7 SN and n = 7 for D14 mSN due to interference of intracellular ice. n-D: non-DMSO; D: DMSO. n.s.: $p > 0.05$; *: $p < 0.05$. (See Figure 37 for method illustration of each metric.) (**A**) Intracellular ice formation significantly increased with greater undercooling only in the case of D7 SN in the DMSO solution and D14 mSN in both non-DMSO and DMSO solutions, no significant change otherwise. (**B**) Membrane partitioning of non-DMSO CPA

significantly decreased in D14 mSN subject to greater undercooling, partitioning of DMSO lower than that of non-DMSO CPA across all three cell stages. (**C**) Cellular integrity in terms of spatial autocorrelation of protein's amide I signal decreased significantly for D14 mSN with greater undercooling and decreased further in the DMSO solution, no significant loss of integrity in D5 crest or D7 SN. (**D**) Significant cytochrome C (cyt C) release was observed for D14 mSN in the DMSO solution but not for any cell stage in the non-DMSO CPA. Kruskal-Wallis ANOVA performed for non-normal distribution of cyt C Moran's I values.

While extracellular ice crystal formation is an essential and inevitable element of slow freezing, intracellular ice crystals of large quantity or size can cause lasting damage in the cryopreserved cells impacting their survival and function. In terms of intracellular ice formation (Figure 38A), D5 crest showed no statistically significant response between different ice nucleation temperatures or different CPA formulations. When the non-DMSO CPA was used, D7 SN also showed minimal intracellular ice that was consistent between different ice nucleation temperatures. However, a significantly greater amount of intracellular ice crystals was found in the D7 SN frozen in DMSO, where intracellular ice took up nearly the entirety of cytoplasmic space for approximately 30% of the cell population. Moving further along the cell developmental trajectory, D14 mSN had significantly more though sparsely distributed small intracellular ice crystals upon greater degree of undercooling when it was frozen in the non-DMSO solution. However, when D14 mSN was frozen in the DMSO solution, intracellular ice took a different form, where large chunks of ice crystals took up nearly entirety of the intracellular space (abbreviated as chunky intracellular ice from here on). As intracellular ice formation has been found to be indicative of cellular sensitivity to undercooling by our earlier studies[107,241], these new results from D5 crest, D7 SN and D14 mSN suggested not only

that undercooling sensitivity varied between the different cell stages but also that the sensitivity of a given cell stage was different in the two CPA formulations.

The following analyses (Figure 38B-D) represent cell populations without chunky intracellular ice crystals and reveal mechanisms of damage in certain cells despite relatively well-inhibited intracellular ice formation. Membrane partitioning of solutes (i.e., non-DMSO CPA or DMSO) describes the steady state of mass transport across the plasma membrane and is mathematically represented as the ratio of the extracellular concentration to the intracellular concentration. While a non-penetrating CPA (e.g., sucrose) is expected to remain out of the cytoplasm, a healthy cell membrane should also be able to partition a penetrating CPA (e.g., glycerol, DMSO), despite its name, into forming an extracellular-to-intracellular concentration ratio greater than 1. In terms of partitioning ratio of the non-DMSO CPA (Figure 38B), D5 crest and D7 SN both showed no significant change upon greater undercooling, whereas D14 mSN exhibited significantly weaker membrane partitioning when subjected to lower ice nucleation temperature. One possible explanation for the decrease in partitioning is impaired barrier function of the D14 mSN's plasma membrane upon undercooling, corresponding to its higher intracellular ice formation. Comparing non-DMSO CPA and DMSO, membrane partitioning of DMSO was found to be significantly (up to 2.4-fold) weaker than that of the non-DMSO CPA for the neuronal cell stages investigated. While it cannot indicate or rule out the possibility of membrane impairment by DMSO, the consistent trend across different cell stages clearly showed that cell membrane has a lower barrier effect to

DMSO than glycerol and other non-DMSO CPA molecules. As extracellular ice forms and grows with cooling, cells dehydrate, and intracellular solutes become more concentrated. When DMSO was used, the neuronal cells were more likely subjected to stresses of high intracellular CPA concentration than when non-DMSO CPA was used.

Moran's I of amide I signal in cells measured cellular material integrity on a protein level. As shown in Figure 38C, D14 mSN was the only cell stage among those tested to be affected by the stresses of undercooling and DMSO exposure on a protein level. When chunky intracellular ice was successfully inhibited, D5 crest and D7 SN exhibited consistently high cellular material integrity during freezing regardless of ice nucleation temperature or CPA formulation, whereas D14 mSN disintegrated upon greater undercooling and further disintegrated with visually apparent dispersion of cellular proteins when frozen in the DMSO-based solution. Moran's I of cytochrome C signal in cells measured the potential of post-thaw mitochondrial apoptosis. As shown in Figure 38D, D14 mSN was again the only cell stage to be affected by the use of DMSO, although the cytochrome C distribution of D14 mSN did not respond significantly to undercooling.

Summarizing these four cryobiological metrics, intracellular ice was the only observed mechanism of freezing damage in the earlier cell stages (i.e., D5 crest, D7 SN), which was only prominent in D7 SN frozen in the DMSO solution. Further downstream of this differentiation trajectory, greater undercooling sensitivity manifested in the more mature

cell stage (i.e., D14 mSN). For D14 mSN frozen in non-DMSO CPA and without chunky intracellular ice crystals, significantly higher quantity of small intracellular ice was found and likely resulted in impaired membrane barrier function, higher intracellular CPA concentration, and consequently partially disintegrated cellular structure. For D14 mSN frozen in DMSO, besides the damage of chunky intracellular ice, they suffered from cellular disintegration and likely consequential cytochrome C release. Similar to previously reported observations in hiPSCs[107,241], the non-DMSO CPA formulation utilized here was shown here to ease the level of cell damage upon lower ice nucleation temperature in comparison with a DMSO-based formulation, extrinsically mitigating the cells' sensitivity to undercooling. The overall increase in cell sensitivity to undercooling from a multitude of mechanisms along this sensory neuron differentiation trajectory correlated with the decrease in cell membrane fluidity from D5 crest through D14 mSN (Figure 36A), confirming membrane fluidity as a likely factor contributing to the cells' intrinsic sensitivity to undercooling.

7.3.4 Sensitivity to cooling rate varied among cell stages and correlated with cell size

Parallel to the examination of the effect of undercooling on cell behavior during freezing, potential mechanisms of damage, or the absence thereof, was also investigated using low-temperature Raman spectroscopy, subjecting the three developmental stages of neuronal cells to cooling rate varied between -1, -3 and -5 ˚C/min (Figure 39). The non-DMSO CPA formulation previously optimized for hiPSCs was used throughout these experiments, where the non-DMSO CPA solution previously optimized for hiPSCs was

used. Interestingly, D5 crest and D14 mSN both experienced freezing damages that varied by cooling rate, whereas D7 SN consistently exhibited no statistically significant change across the selection of Raman-based cryobiological analyses regardless of the cooling rate.

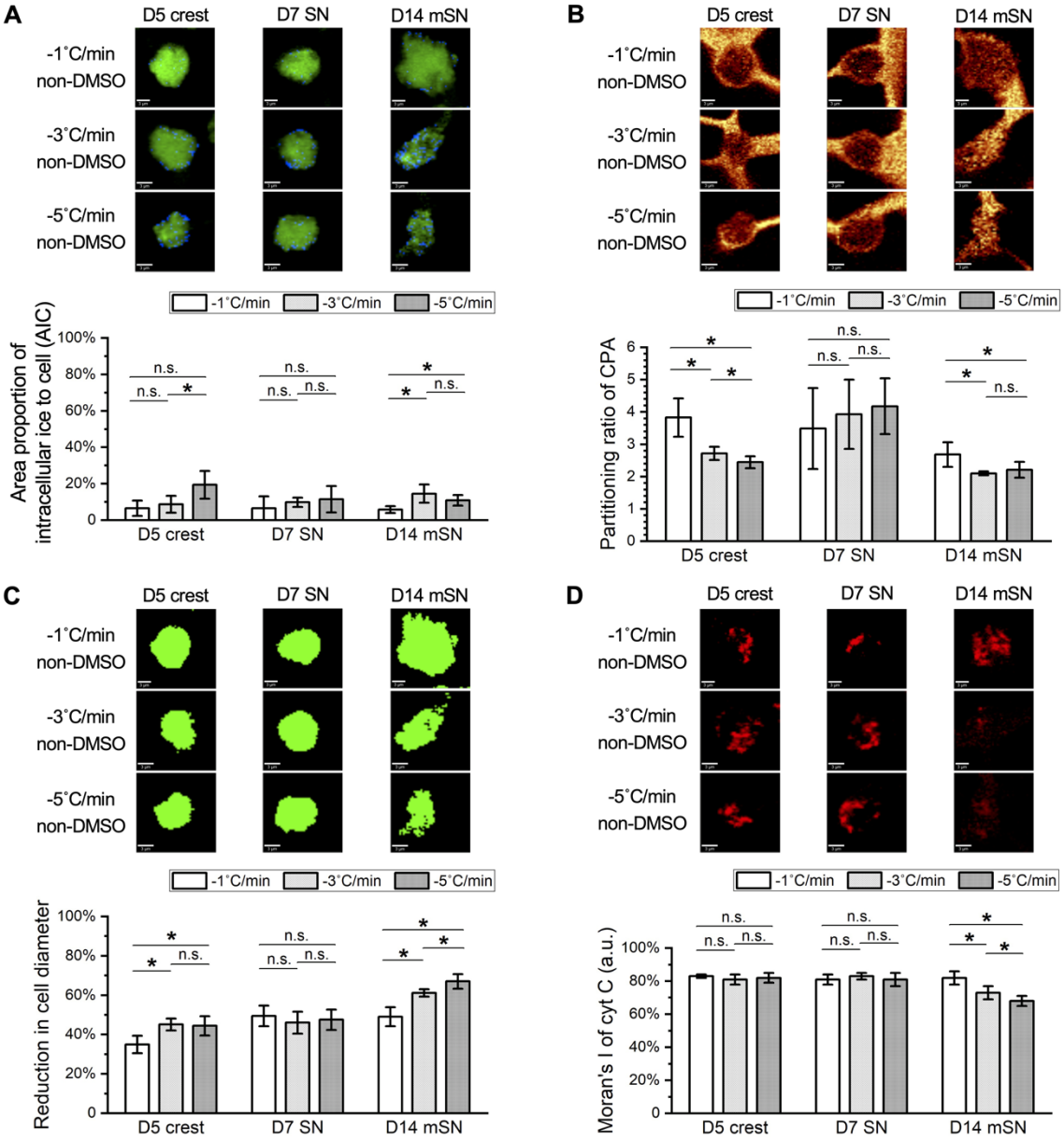

Figure 39. Effects of cooling rate on freezing behaviors of D5 crest, D7 SN, and D14 mSN, respectively as observed by low-temperature Raman spectroscopy, comparing different cooling rates between -1, -3, and -

5˚C/min. Data represented as mean +/- 95% confidence interval. $n = 10$. n.s.: $p > 0.05$; *: $p < 0.05$. (See Figure 37 for method illustration of each metric.) (**A**) Intracellular ice formation increased with the faster cooling rates in D5 crest and D14 mSN, no significant difference across cooling rates in D7 SN. (**B**) Membrane partitioning of non-DMSO CPA significantly decreased in D5 crest and D14 mSN with the faster cooling rates, no significant difference across cooling rates in D7 SN. (**C**) Cell shrinkage as a result of freezing intensified with the faster cooling rates for D5 crest and D14 mSN, no significant difference across cooling rates in D7 SN. (**D**) Significant cytochrome C release was observed for D14 mSN with the faster cooling rates but not for D5 crest or D7 SN at any of the cooling rates.

In terms of intracellular ice formation (Figure 39A), with ice nucleation temperature held constant at -4 ˚C, only small rather than chunky intracellular ice was observed. D5 crest maintained minimal levels of intracellular ice with the slower cooling rates (i.e., -1 and -3 ˚C/min) and contained a significantly greater quantity of ice with the fastest cooling rate tested (i.e., -5 ˚C/min). D14 mSN maintained a minimal level of intracellular ice with the slowest cooling rate (i.e., -1 ˚C/min) but had a significant increase in intracellular ice with the faster cooling rates starting at -3 ˚C/min. In terms of membrane partitioning of the non-DMSO CPA (Figure 39B), the faster cooling rates (i.e., -3 and -5 ˚C/min) resulted in significantly weaker partitioning in both D5 crest and D14 mSN than the slower cooling rate (i.e., -1 ˚C/min), subjecting the cells to higher concentrations of intracellular CPA and likely indicating impairment of the membrane's barrier function.

As extracellular ice grows during cooling, cells are expected to dehydrate and reduce in size. While greater dehydration is commonly expected with slower cooling rates and longer time for water to leave the cell via osmosis and balance the concentration gradient of solutes across the plasma membrane, this trend was not observed with the change in

cell size upon the varying cooling rates regardless of the neuronal cell stage. For D5 crest and D14 mSN (Figure 39C), the faster cooling rates (i.e., -3 and -5 ˚C/min) resulted in significantly greater cell size loss than the slower cooling rate (i.e., -1 ˚C/min). Comparing the ratio in spectral intensity of the C-H stretching peak to that of the broad O-H stretching band between the cells frozen at different cooling rates, no distinct difference in the cells' hydration level was observed (data not shown). Combined with the intracellular ice and membrane partitioning data, the greater cell size reduction in D5 crest and D14 mSN likely indicated both faster exosmosis and more leakage of subcellular content via more impaired plasma membrane, which potentially resulted from osmotic stresses of the more rapid increase in extracellular solute concentration as the samples cooled at a faster rate.

In addition, cytochrome C release was observed in D14 mSN at the faster cooling rates but not in D5 crest (Figure 39D). Summarizing the number of mechanisms of freezing damages observed per cell stage and the extent of its response to cooling rate variation, D14 mSN was found to be the most susceptible to fast cooling rates, followed by D5 crest, followed by D7 SN. This trend was consistent with the original cell sizes measured upon dissociation from fresh culture and suspension in the cell growth media (Figure 36B). The larger cells (i.e., D14 mSN at ~20 μm in diameter > D5 crest at ~13 μm in diameter) with lower surface to volume ratio required slower cooling rate (i.e., -1 ˚C/min) to prevent damages from both intracellular ice formation and dynamic osmotic stresses, whereas the smaller cell (i.e., D7 SN at ~11 μm in diameter) minimized intracellular ice

formation, maintained membrane integrity, and prevented disruption to subcellular materials across the range of cooling rates investigated (i.e., from -1 to -5 ˚C/min). While this correlation between cell size and cooling rate sensitivity in general was consistent with what has been demonstrated in literature, the absence of chunky intracellular ice and the analysis of membrane partitioning and cell volumetric loss in the present investigation presented an alternative mechanism of damage in large cells during fast cooling, in contrast with and supplementing to the commonly hypothesized, generalized mechanism that has been based solely on the formation of optically visible (i.e., chunky) intracellular ice crystals.

7.3.5 Successful cryopreservation relied on good cryoprotection and compatible process

Having understood the cryobiology of D5 crest, D7 SN and D14 mSN in the frozen state, we proceeded to test the performance of these cryopreserved cells respectively upon vial-based controlled rate freezing in the non-DMSO CPA formulation, with ice nucleation varied between -4 and -8 ˚C and cooling rate varied between -1, -3 and -5 ˚C/min. Post-thaw cell recovery was measured by membrane exclusion fluorescent assay to assess membrane integrity. Post-thaw cell reattachment was measured by esterase activity of adherent cells to assess the basic cell function to sustain a viable culture. Post-thaw differentiation to sensory neurons was examined for cryopreserved D5 crest to assess their differentiation potential; post-thaw maturation to electrophysiologically active neurons was examined for cryopreserved D7 SN to assess its ability to reach a more mature state; post-thaw electrophysiological response was intended for cryopreserved

D14 mSN to assess its ability to retain the level of maturity. The different forms of post-thaw assay progressed in the aforementioned order towards representing the ability of a given cryopreservation method to fulfill the cells' intended utility.

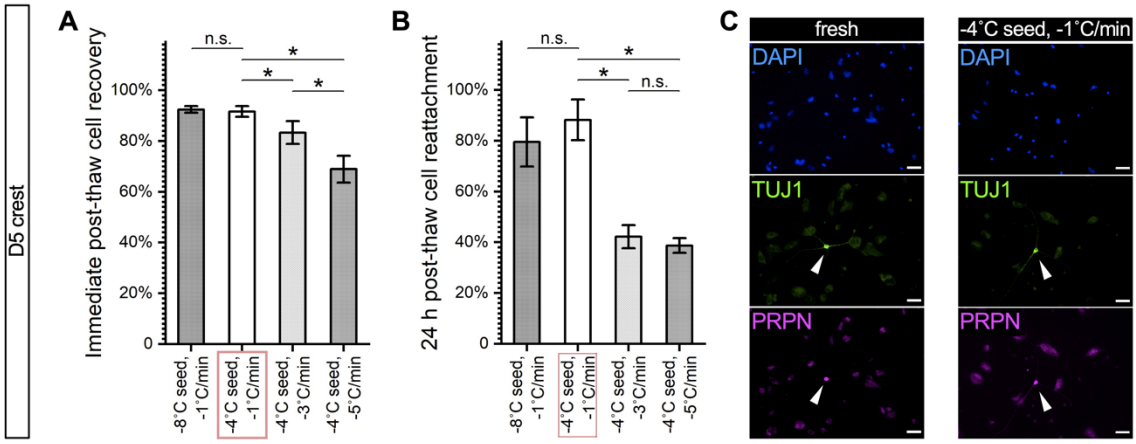

Figure 40. Post-thaw survival and function of cryopreserved D5 crest under varying nucleation temperatures and cooling rates. *: $p < 0.05$; n.s.: $p > 0.05$. Red box: best-case parameters tested the best-case scenario with the highest recovery and reattachment. (**A**) Post-thaw recovery of D5 crest showing no significant change with greater undercooling but trending significantly lower with faster cooling rate. $n = 4$. (**B**) Post-thaw reattachment of D5 crest showing similar trends as recovery but more distinct cell damage with cooling rates of -3 and -5˚C/min. $n = 4$. (**C**) Immunocytochemistry 48 h after re-culture of dissociated (fresh) or cryopreserved (best-case) D5 crest showing <1% TUJ1+, PRPN+ (white arrowheads) neuron differentiation and a vast majority of resulted cell population with crest-like morphology and low-level, cytoplasmic TUJ1 and PRPN staining. Scale bar: 100 µm. [Experiment for panel C was performed by Patrick Walsh.]

For D5 crest, both post-thaw recovery (Figure 40A) and post-thaw reattachment (Figure 40B) demonstrated a lack of cell sensitivity to undercooling and significant cell loss to faster cooling rates. This trend was consistent with the Raman results described earlier, indicating that a cooling rate of -1 ˚C/min or slower was required for D5 crest to prevent loss in membrane integrity or cell adhesion due to substantial intracellular ice formation and rapid intensification of a hypertonic environment. Despite the successful

cryoprotection demonstrated in the combination of -1 ˚C/min cooling and -4 ˚C ice nucleation by post-thaw recovery greater than 90% and post-thaw reattachment of 88%, the cryopreserved D5 crest failed to produce sensory neurons after resuming the subsequent days of neuronal induction (Figure 40C). However, notably, the fresh control group of D5 crest that was dissociated and replated into culture also lost its ability to differentiate into TUJ1-positive, PRPH-positive neurons. Such interruption to the differentiation process with cell dissociation at day 5 was a deviation from the continuous culture originally designed for this 7-day differentiation protocol, which proved to be detrimental despite an otherwise optimal cryopreservation process.

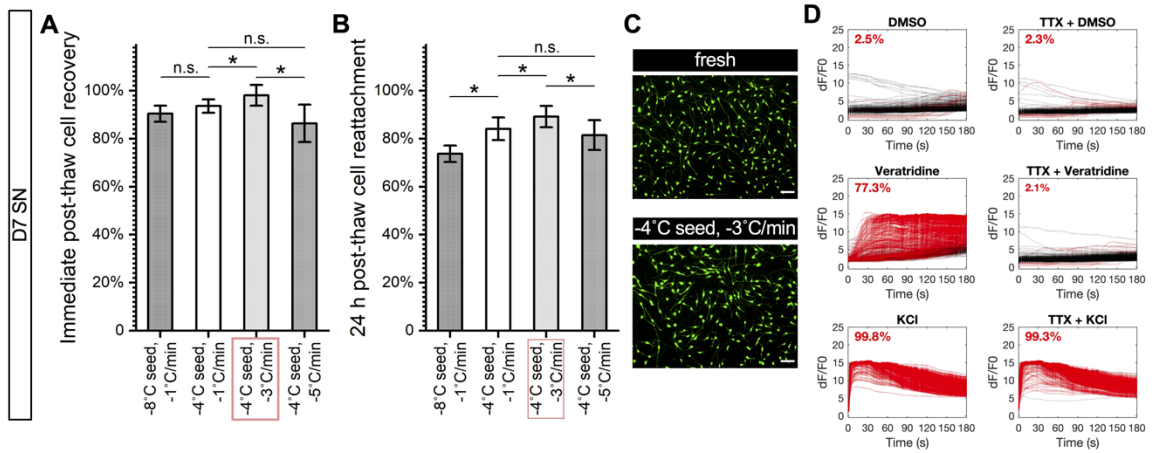

Figure 41. Post-thaw survival and function of cryopreserved D7 SN under varying nucleation temperatures and cooling rates. Data represented as mean +/- 95% confidence interval. *: $p < 0.05$; n.s.: $p > 0.05$. Red box: best-case parameters tested with the highest recovery and reattachment. (**A**) Post-thaw recovery of D7 SN showing no significant change with greater undercooling and the best cooling rate at -3˚C/min with statistical significance. $n = 4$. (**B**) Post-thaw reattachment of D7 SN showing similar trends as recovery but more distinct cell damage with lower nucleation temperature (-8˚C). $n = 4$. (**C**) Calcein AM-stained culture 24 h after replating dissociated (fresh) or cryopreserved (best-case) D7 SN showing high confluence and normal morphology of immature neurons. Scale bar: 100 µm. (**D**) Calcium imaging of post-thaw culture after 7-day maturation of D7 SN cryopreserved with -4˚C nucleation and -3˚C/min cooling rate, showing little to no response to 0.1% DMSO (negative control), positive response to 1 µM veratridine that was inhibited by TTX, and positive response to 30 mM KCl that was unaffected by TTX. Red line: responder

cell; black line: non-responder cell. Proportion of responder cell population indicated per graph. Range of *n* = 417– 662.

For D7 SN, post-thaw recovery (Figure 41A) demonstrated a lack of cell sensitivity to undercooling that was consistent with the Raman results described earlier. However, post-thaw recovery showed a statistically significant difference between different cooling rates that was not revealed by the Raman measurements of intracellular ice, membrane partitioning, volumetric change or cytochrome C release. In addition, post-thaw reattachment of D7 SN (Figure 41B) demonstrated not only cell sensitivity to cooling rate but also to undercooling that was not reflected by the Raman measurements of intracellular ice, membrane partitioning, cellular material integrity or cytochrome C release. -4 ˚C ice nucleation and -3 ˚C/min cooling were shown as the best combination of controlled rate freezing parameters for D7 SN. Post-thaw functional assay of cryopreserved D7 SN demonstrated a high-confluence viable post-thaw culture upon seeding (Figure 41C) that successfully produced more mature neurons with normal electrophysiological responses to the panel of drug molecules (Figure 41D and Figure 42).

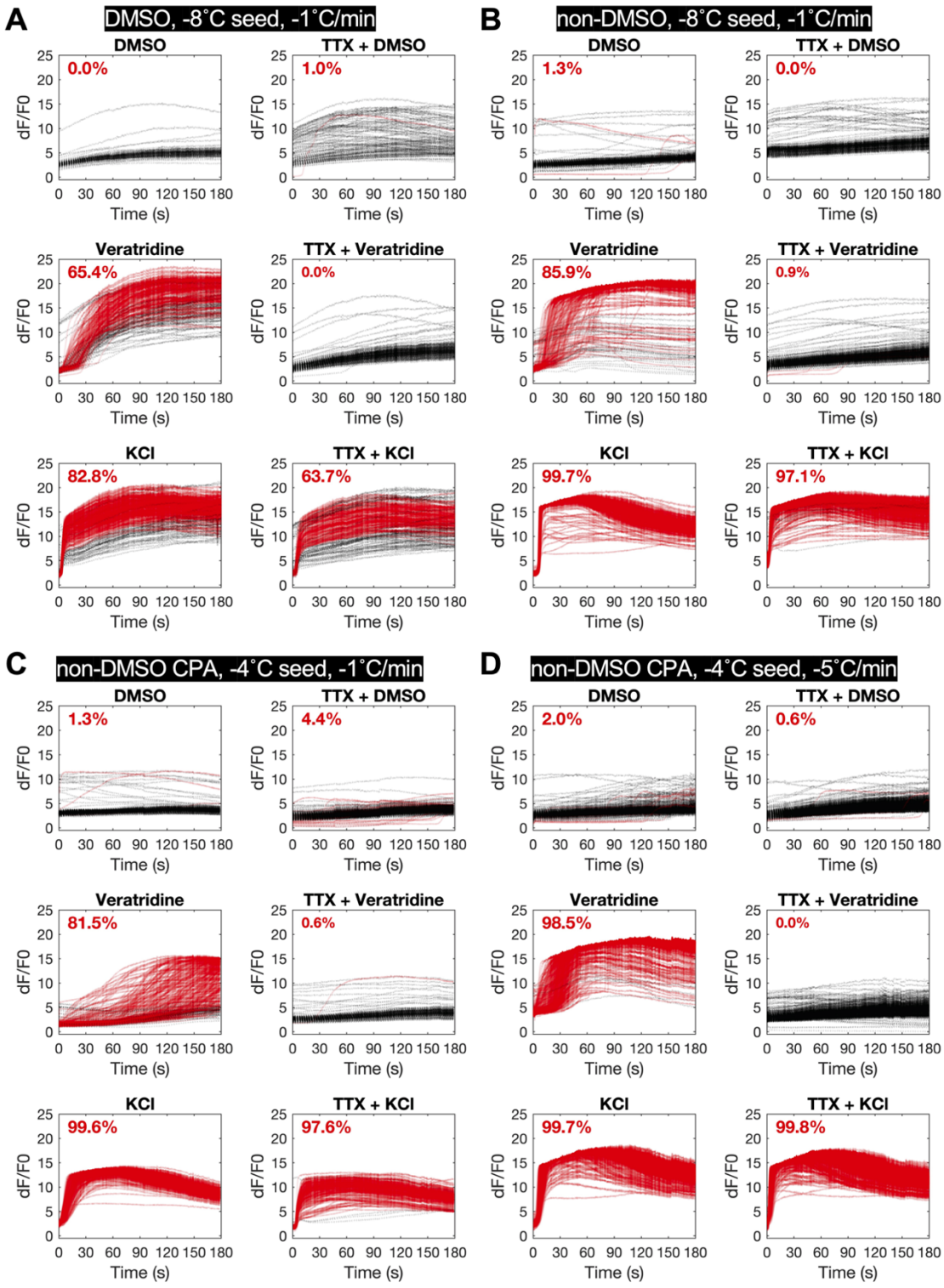

Figure 42. Calcium imaging of post-thaw culture after 7-day maturation of D7 SN cryopreserved in DMSO versus non-DMSO solutions, under varying nucleation temperatures and cooling rates, in addition to

Figures 1D and 6D. All non-DMSO conditions showed little to no response to 0.1% DMSO (negative control), positive response to 1 µM veratridine that was inhibited by TTX, and positive response to 30 mM KCl that was largely unaffected by TTX, whereas the DMSO condition showed fractionally lower proportion responding to KCl that was also fractionally reduced upon TTX treatment. Red line: responder cell; black line: non-responder cell. Proportion of responder cell population indicated per graph. Range of *n* = 204 – 544.

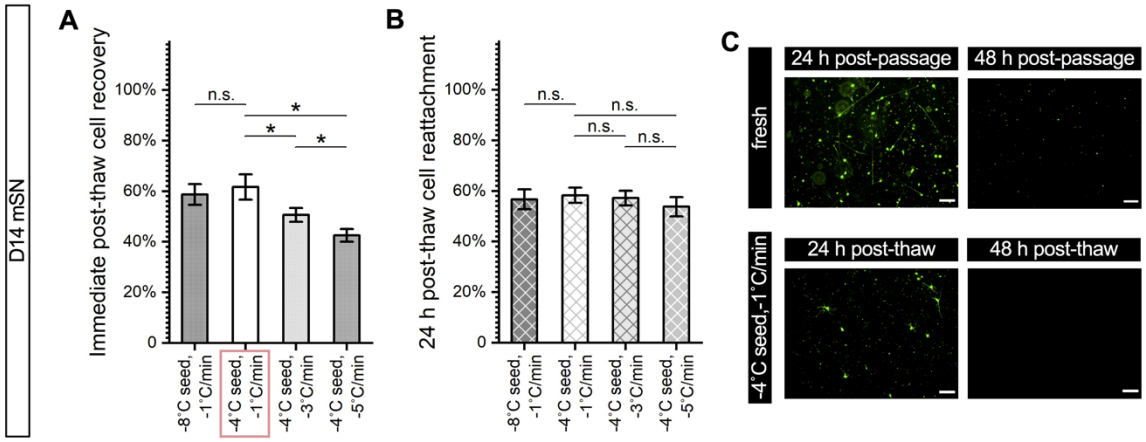

Figure 43. Post-thaw survival and function of cryopreserved D14 mSN under varying nucleation temperatures and cooling rates. Data represented as mean +/- 95% confidence interval. *: $p < 0.05$; n.s.: $p > 0.05$. (**A**) Post-thaw recovery of D14 mSN showing no significant change with greater undercooling but trending significantly lower with faster cooling rate. $n = 4$. Red box: best-case parameters tested with the highest recovery. (**B**) Post-thaw reattachment of D14 mSN, normalized to reattachment of dissociated fresh cell control, showing no significant difference between any of the test conditions. $n = 4$. Crossed-out columns denoting insensitive post-thaw assay due to poor outcome of control cells. (**C**) Calcein AM-stained culture 24 and 48 h after replating dissociated (fresh) or cryopreserved (best-case) D14 mSN, showing a vast majority of live (calcein AM-positive) cell population non-adherent or with rounded morphology in the first 24 h that was more sparsely distributed in the post-thaw culture, as well as subsequent nearly complete cell loss in both conditions at 48 h. Scale bar: 100 µm.

For cryopreserved D14 mSN, measurement of immediate post-thaw recovery (Figure 43A) appeared to demonstrate a lack of sensitivity to undercooling that was otherwise shown in the earlier Raman results, but it showed a trend of more cell death with faster

cooling rate that was consistent with the trend in intracellular ice, membrane impairment, volumetric loss, and cytochrome C release observed by Raman. 24-hour post-thaw reattachment of D14 mSN (Figure 43B) also appeared to show a lack of sensitivity to both undercooling and cooling rate variations. However, upon a closer examination D14 mSN post-thaw using the optimal freezing parameters (i.e., -1 ˚C/min cooling and -4 ˚C ice nucleation) as well as post-passage (Figure 43C), we found that both fresh and cryopreserved cells failed to produce viable culture upon prolonged enzymatic dissociation, rendering the metric of post-thaw reattachment invalid in this specific case to assess the cryopreservation performance and its variation by cooling rate or undercooling.

7.4 Discussion

7.4.1 Cell loss before freezing and after thawing challenges in vitro neuronal cell production

A commonly recognized process bottleneck in the developing supply chain of hiPSC-derived cryopreserved cell therapies has been the temporal restriction on the fill-and-finish step immediately preceding the freezing of cells to minimize cell loss due to DMSO cytotoxicity[46,71–73]. As demonstrated in Figure 35, the non-DMSO CPA molecules used in this study (i.e., sucrose, glycerol, isoleucine, P188, HSA) provided a superior alternative to the widely used DMSO in preserving cell viability before freezing. This result supports the transition from DMSO to non-DMSO in order to enable scale-up of the fill-and-finish process in a manufacturing setting while adhering to a high batch

consistency. Compared to DMSO whose cytotoxicity arises from molecular disintegration, epigenetic and genomic alteration, these non-DMSO CPAs, typically with larger molecular weight than DMSO, can cause pre-freeze cell loss predominantly due to osmotic stress upon CPA introduction[262–264]. Compared to D5 crest and D7 SN, whose exhibited no significant cell loss over the course of pre-freeze exposure to the non-DMSO CPA solution ($p > 0.05$), D14 mSN experienced minor (10%) yet significantly decrease in viable cell count during the first 30 minutes of this process, suggesting that sensitivity to the osmotic stress varied by cell stage with the most mature cells being most sensitive. Pre-freeze CPA exposure testing in this study of the neuronal cells in the non-DMSO solution may be expanded in a future study to include longer times of exposure and determine the time limit for a given quality control (QC) range of cell viability.

Evident in the scarce utilization of cryopreservation, primary and stem cell-derived neuronal cell production have been broadly challenged by cryopreservation. Mirroring the example of neuronal cells for drug screening purposes mentioned previously, few reports can be found to cryopreserve their neuronal cells of interest. One of the few studies reported the cryopreservation of primary mouse cortical and dopaminergic neurons in DMSO-containing formulations and subsequent phenotypic characterization of the cryopreserved cells at 2 and 4 weeks post-thaw[265], without survival data obtained in shorter terms post-thaw, which was not directly comparable with results in the present study. Another study reported the cryopreservation of primary mouse motor neurons in DMSO and post-thaw cell recovery rate of 68.8%[266]. There were two accounts of

cryopreserved dopaminergic progenitors and neurons derived from hiPSCs and human embryonic stem cells (hESCs), with highest reported post-thaw recovery approaching 50% upon 24-hour treatment in apoptosis inhibitors[267,268]. In comparison, this study demonstrated DMSO-free cryopreservation of neuronal cells, with post-thaw survival of D5 crest measured at 91.6% immediately post-thaw, 88.2% 24 hours post-thaw, and of D7 SN measured at 93.6% immediately post-thaw, 84.1% 24 hours post-thaw, all of which significantly higher than 50% even without the use of apoptosis inhibitor. As stem cell technologies translate from scientific discovery to commercial and clinical manufacturing, cell loss experienced in the process of cryopreservation can play a pivotal role against cost efficiency and accessibility of the therapeutic product. Understanding how to improve the efficiency of cryopreservation with better post-thaw cell survival and function will be key to enabling the future of hiPSC-based regenerative medicine.

Besides the financial impact of poor cryopreservation in cell manufacturing, the presence of dead cells in cryopreserved patient-ready cell products would likely negatively impact therapeutic safety and efficacy. When a poorly cryopreserved neural cell therapy is transplanted, the significant proportion of dead and dying cells are not expected to be neutral or inert, as they release substances such as ATP that binds to purinergic receptors and consequently activate surrounding cells such as endogenous neurons, astrocytes, oligodendrocytes, or microglia that may express these receptors. Washing by centrifugation and returning to culture after thawing and before administration of the cryopreserved cells may be used to mitigate this risk as well as safety concerns[74–77]

related to the direct injection of DMSO as an ancillary material into the neural system. However, post-thaw cell manipulation at clinical sites remains poorly standardized[269]. Minimizing cell loss from the cryopreservation process and toxicity of the CPA formulation is important to advance the clinical translation of these sensitive cell populations like neurons for transplantation in sensitive anatomic domains like the brain.

Cryobiological research is both founded upon and a critical element supporting the engineering of novel cellular technologies. For cell cryobiology to broadly benefit the vast and increasingly diverse space of hiPSC-derived cell phenotypes, beyond improving cryopreservation on a case-by-case basis, it is valuable to create systematic knowledge that not only identifies critical quality attributes advocating for best practices, but also summarizes predictable trends of cryobiologically relevant characteristics between different cell stages related by a given developmental timeline and correlations between such observable characteristics and cryopreservation design criteria. In-depth analysis of the cryobiological characteristics of neuronal cells does not exist in literature, regardless of tissue-specific lineages. The following discussion may provide fundamental insights to such technical advancement in future cryopreservation of hiPSC-derived neuronal and other cell types.

7.4.2 Membrane fluidity informs undercooling sensitivity and cryopreservation design

Literature in the field of gamete cryobiology has explored and demonstrated the inverse correlation between membrane fluidity and desirable cryopreservation outcome such as

motility of recovered spermatozoa[258,259]. In addition, Noutsi et al.[270] showed the varying extent of fluctuation in membrane fluidity among a selection of cell lines over the course of 4-day static cultures and spontaneous differentiation. These previous studies have required highly specialized spectrofluorometer or two-photon fluorescent microscopy to quantify membrane fluidity for their measurement, both of which are limited by low throughput and adaptability.

In comparison, this study utilized the excimer-to-monomer ratio of a pyrene-decanoic acid fluorescent probe measured by a fluorescent microplate reader to quantify membrane fluidity of different cell stages along a defined 14-day sensory neuron differentiation and maturation process. Fraction of the excimer depicts not only the rotational but also the lateral motility of the lipophilic molecule in the plasma membrane. Its measurement is not limited to one modality of fluorescence instrumentation. The low technical requirement of this method enhances the relevance of our reported results to future applications in cryobiological research and cryopreservation design of hiPSC-derived cell manufacturing.

We found that membrane fluidity trended lower as differentiation and maturation progressed. The decrease in membrane fluidity was consistent with the cells' increase in undercooling sensitivity. This result supports the correlation between membrane fluidity and cell freezing damage previously postulated in literature[258,259] and provides more in-depth evidence specifying the nature of freezing damages as intracellular ice and cell

disintegration consequent of extensive undercooling. On one hand, cells like D5 crest with very high membrane fluidity may exhibit little to no sensitivity to changes in ice nucleation temperature, relaxing the QC range of sample temperature profile in controlled rate freezing and accommodating deviations in the CRF performance from batch to batch. On the other hand, cells like D14 mSN with low membrane fluidity would require a tight QC range of ice nucleation temperature (e.g., -3 to -7 ˚C) in order to ensure the same level of consistency in their post-thaw cell survival and function.

One may note that despite having relatively higher membrane fluidity than hiPSC aggregates and utilizing the same non-DMSO CPA formulation, D14 mSN responded significantly more poorly to undercooling (Figures 38 and 43) than hiPSC aggregates[241]. Membrane fluidity is likely not the only factors influencing cell response to undercooling. Mechanistically, kinetic energy and molecular motion are lower in case of undercooling, and upon ice nucleation in the extracellular space, a more rigid plasma membrane may not allow water molecules to transport quickly enough from the intracellular space following the sudden increase in the transmembrane concentration differential and avoid intracellular ice formation. In addition, other factors such as perfectly synergistic molecular interaction between CPA molecules inside the hiPSCs and water may decrease the probability of water leaving the intermolecular hydrogen bond network and forming intracellular ice crystals, therefore countering the effect of the cells' low membrane fluidity. Optimization of a multicomponent non-DMSO CPA formulation on a cell type-to-cell type basis may achieve such molecular balance and effectively

mitigate the sensitivity to undercooling for cells like the mature sensory neurons. As the same non-DMSO solution effectively mitigated the undercooling damages for the earlier cell stages from hiPSC, D5 crest to D7 SN but to a lesser extent for the later cell stage of D14 mSN, it may be more critical to re-optimize a CPA formulation for a new cell phenotype of interest that is further removed from the original phenotype.

It is also important to note that the non-DMSO solution was found to eliminate lethal intracellular ice formation regardless of the cell stage, whereas the DMSO-based solution was observed to result in significant amounts of such ice crystals when subjected to the same degree of undercooling. As membrane fluidity may drop as cells differentiate and mature, it becomes increasingly important to transition from DMSO, or a single-CPA non-DMSO alternative formulation, to a non-DMSO CPA cocktail like the one used in this study, in order to counter the intrinsic cell vulnerability to undercooling with proper cryoprotection and consequently improve the consistency of cryopreservation outcome and flexibility of CRF in hiPSC-based cell manufacturing.

7.4.3 Cell size measurement informs cooling rate sensitivity and cooling rate selection

It has been hypothesized and demonstrated in cryobiological literature[54,57] that the relationship between cooling rate and cryopreservation outcome for a given cell type should resemble an inverted "U", and that the optimal cooling rate of different cell types correlate with their difference in cell size. Within the cooling rate range (-1 to -5 ˚C/min) tested in this study, the optimal cooling rate for D5 crest lay near or below -1 ˚C/min, that

for D7 SN around -3 ˚C/min, and that for D14 mSN also near or below -1 ˚C/min but skewed to a likely slower optimal cooling rate than that of D5 crest. This relativity in optimal cooling rate was consistent with their different cell sizes, where the larger cells (i.e., D14 mSN > D5 crest) require a slower cooling rate (i.e., -1 ˚C/min and potentially lower) to avoid lethal intracellular ice formation.

Interestingly, compared to the nearly 50% drop in post-thaw reattachment of larger cell (D5 crest) along with the increase in cooling rate from -1 to -3 ˚C/min, the decrease in cooling rate from -3 to -1 ˚C/min resulted in less cell loss (i.e., 5% drop in post-thaw reattachment) in the smaller cell (D7 SN). Consistent with what was previously proposed[57], cooling rate sensitivity is most critical towards large cells with higher than optimal cooling rates. Insulative passive freezing devices and liquid nitrogen-free controlled rate freezers are limited by the typical maximum momentary cooling rate of -2 ˚C/min, where freezing damage by fast cooling may not be a primary concern in their applications. In liquid nitrogen-based controlled rate freezing applications, measuring cell diameter in suspension by light microscopy may be useful to determine whether the cell form of interest requires the slower cooling rate to decrease the probability of freezing damages or relaxes the acceptable range to accommodate deviations towards faster cooling rates or intentional use of accelerated programs.

7.4.5 Dissociation of adherent culture remains a challenge to cell cryopreservation

Selection of a fit-for-purpose post-thaw metric is critical to inform both development of a

cryopreservation formulation or process and quality control of an established cryopreservation-based manufacturing protocol. This investigation advances the panel of post-thaw metrics utilized in cryobiological research to include not only post-thaw recovery[271,272] to account for cell lysis, post-thaw reattachment[105,273] to capture cytoskeletal freezing damages in adherent cells, but also cell stage-specific functional assays in line with the particular objective of driving the cell phenotypic changes along the defined sensory neuron trajectory from each discrete cell stage. Such scrutinization of the cryopreserved D7 SN presented a reliable database supporting the use of controlled-rate freezing, our non-DMSO CPA formulation, and proper cryopreservation of sensory neurons and other differentiated cells in general for cell production towards research and clinical applications.

In addition to providing an adoptable method of cryopreserving post-mitotic sensory neurons, the extensive post-thaw examination revealed a critical challenge to realizing successful cryopreservation of hiPSC-derived cells. For D5 crest and D14 mSN, the observed failure to produce functionally viable cells after cryopreservation did not originate from the CPA formulation or the freeze-thaw process, but from harvesting these cells from adherent culture by dissociation. The method of dissociating fresh D14 mSN was preliminary and has been under development. It is only with cultivation processes established successfully on fresh cells that one may achieve successful cryopreservation and derive a feasible post-thaw metric to evaluate the cryopreserved cells. The dissociation of D5 crest was not intended in the middle of the continuous 7-day

differentiation culture and created a barrier to neuronal induction that could not be resolved by effective cryobiological protection of the dissociated cells. For intermediate cell stages of a differentiation process designed to require continuous culture, the feasibility of cryopreservation strongly will be determined by the outcome of the disruption of culture regardless of the cellular response to CPA molecules, freezing and thawing. It is therefore important to test the effect of necessary dissociation and resumption at the intended time point of cryopreservation in either the original design of a differentiation protocol or its adaptation into a cryopreserved supply chain. Process and formulation parameters may need to be further optimized to allow the particular cell stage to be cryopreserved.

A recent study demonstrated vitrification of adherent hiPSC-derived neural progenitor cells using the TWIST method with 80% post-thaw recovery. While the methodology of vitrification is limited in scalability, advances as such in improving its sterility and future studies in validating the method for more differentiated, mature cell stages may present practical value towards *in situ* cryopreservation of hiPSC-derived 2D adherent culture at laboratory scale. Furthermore, while slow freezing has been predominantly used for cryopreserving single cell suspensions, its feasibility for *in situ* cryopreservation of adherent culture was recently demonstrated for readily implantable hiPSC-derived retinal pigment epithelium[274]. Suspension culture of hiPSCs and differentiated cells in the form of 3D spheroids has recently gained popularity due to its scalability demanded by preclinical and clinical cell production[31–33]. Cryopreservation of hiPSC-derived cell

spheroids may be studied in the future to examine how the effect of cryopreservation on continuity of differentiation varies between different modalities.

7.4.6 Limitation of study

While the generalized correlation between different variables informed our investigation of cell sensitivity to undercooling and cooling rate, testing more than two ice nucleation temperatures and three cooling rates would support a stronger argument and establish a statistical correlation. As much as the present study contributed to a novel cryobiological perspective of different cell stages along a hiPSC differentiation trajectory, there are many alternative perspectives valuable to the advance of cryopreservation in hiPSC-based cell manufacturing. Future studies may explore the perspective of how biologically similar cells may have different cryobiological characteristics and require different cryopreservation strategies, as well as how the interactive effects of a defined mixture of different cells may play a role in the bankability of the entire population, especially in the advent of hiPSC or hESC-derived cell therapies that rely upon the production of highly dynamic and potentially heterogeneous populations.

7.5 Conclusion

During differentiation from human induced pluripotent stem cells (hiPSCs), cells undergo phenotypic changes presenting a diversity of functional values towards cell therapy and personalized medicine. Successful translation of these hiPSC-derived therapeutic products will rely upon effective cryopreservation at multiple stages of the manufacturing

cycle. From the perspective of cryobiology, we attempted to understand how the challenge of cryopreservation evolves between cell phenotypes along a hiPSC-to-sensory neuron differentiation trajectory. Cells were cultivated at three different stages along a 14-day process to represent the intermediate, differentiated, and matured cell products. All cell stages remained ≥90% viable in a non-DMSO formulation but suffered ≥50% loss in DMSO before freezing. Raman spectroscopy revealed higher sensitivity to undercooling in cells with lower membrane fluidity and higher sensitivity to suboptimal cooling rates in stages with larger cell bodies. Highly viable and functional sensory neurons were produced following DMSO-free cryopreservation. Our study also signified a critical influence of interrupting dissociating cultures on the feasibility of cryopreserving adherent cells.

Chapter 8

Conclusions and Future Directions

8.1 Conclusions

In line with the clinical translation of hiPSCs and hiPSC-derived cell manufacturing, understanding the challenges of banking these cells builds a necessary foundation for designing effective formulation and protocol for their cryopreservation. This research proposed to dissect the mechanisms of damages in hiPSC aggregates and differentiated cells during cryopreservation as well as the mechanisms of action of different CPAs. To fulfill this goal, we hypothesized that:

(1) cell sensitivity to cooling rate and undercooling will differ by cell form and cell developmental stage;

(2) a synergistic combination of multiple non-DMSO CPAs will provide superior cryoprotection against freezing damages in cells compared to DMSO.

We confirmed these hypotheses by fulfilling the following aims in Chapters 4-7.

Aim 1 – Mechanisms of freezing damage in hiPSCs and hiPSC-derived neuronal cells as elucidated by Raman spectroscopy and supported by cell-based fluorescence assays.

Aim 1.1 – Characterize damage in hiPSC single cells versus multicellular aggregates given different cooling rates.

In Chapter 4, three different forms of hiPSCs (i.e., large aggregate, small aggregate, and single cell) were frozen in DMSO under varied cooling rate (i.e., -1, -3 or -10 ˚C/min) to determine the relative sensitivity of each cell form to the cooling rate variation in terms of intracellular ice formation and post-thaw cell survival. This sub-aim directly tested a part of the first hypothesis that *cooling rate* sensitivity varies between different *forms* of the same cell type. Findings included that in the context of intracellular ice formation, response of small aggregates to the cooling rates resembled that of single cells. The post-thaw survival of hiPSC aggregates and that of single cells, whether in terms of post-thaw recovery or reattachment, were not a comparable pair due to the masking effect of cell-cell dissociation-induced apoptosis in single hiPSCs. However, the post-thaw survival of large hiPSC aggregates favored the medium cooling rate of -3 ˚C/min significantly over -1 or -10 ˚C/min, whereas that of small aggregates favored the slowest cooling rate of -1 ˚C/min and suffered drastic loss upon faster cooling.

Aim 1.2 – Characterize damage in hiPSC single cells versus multicellular aggregates given different ice nucleation temperatures (undercooling).

Also in Chapter 4, two different forms of hiPSCs (i.e., small aggregate and single cell) were frozen in DMSO upon varied temperatures of ice nucleation (i.e., -4 or -8 ˚C) to determine the relative sensitivity of each form of hiPSCs to the undercooling variation in terms of intracellular ice formation and post-thaw cell survival. This sub-aim directly tested another part of the first hypothesis that *undercooling* sensitivity varies between different *forms* of hiPSCs. Findings included that small aggregates experienced significantly greater intracellular ice formation in response to undercooling than single cells. Additionally, compared to single cells, aggregates had more rigid plasma membrane and thus lower permeability to water and other solutes at low temperatures, which likely resulted from their complex membrane-cytoskeletal network and

contributed to their greater sensitivity to undercooling.

Aim 1.3 – Compare damage by suboptimal cooling rate in hiPSC-derived neuronal cells of different development stages.

In Chapter 7, three different developmental stages of hiPSC-derived neuronal cells (i.e., D5 crest, D7 SN, and D14 mSN) were frozen in the optimized solution from Aim 3.1 under varied cooling rates (i.e., -1, -3 or -5 ˚C/min) to determine the relative sensitivity of each cell stage to the cooling rate variation in terms of intracellular ice formation, membrane partitioning, cell shrinkage, and cytochrome C release. This sub-aim directly tested another part of the first hypothesis that *cooling rate* sensitivity varies between different *cell stages*. Findings included that D7 SN was not sensitive to cooling rate variations, where its freezing behavior as elucidated by Raman did not vary significantly with different cooling rates, and that only subtle difference in post-thaw reattachment was observed favoring -3 ˚C/min. In comparison, D5 crest and D14 mSN strongly favored the slowest cooling rate of -1 ˚C/min and suffered significantly greater intracellular ice, impaired membrane partitioning, and volumetric loss upon faster cooling at -5 ˚C/min, with D14 mSN manifesting all of these freezing damages at a lower cooling rate threshold at -3 ˚C/min than D5 crest. This relativity in cooling rate sensitivity (i.e., D14 mSN > D5 crest > D7 SN) correlated with their differences in cell size.

Aim 1.4 – Compare damage by undercooling in hiPSC-derived neuronal cells of different development stages.

Also in Chapter 7, three different developmental stages of hiPSC-derived neuronal cells (i.e., D5 crest, D7 SN, and D14 mSN) were frozen in the optimized solution from Aim 3.1 upon varied temperatures of ice nucleation (i.e., -4 or -8 ˚C) to determine the relative sensitivity of each cell

stage to undercooling in terms of intracellular ice formation, membrane partitioning, cellular protein integrity, and cytochrome C release. This sub-aim directly tested the last part of the first hypothesis that *undercooling* sensitivity varies between different *cell stages*. Findings included that D5 crest was not sensitive to undercooling within the nucleation temperature range between -4 and -8 ˚C. In comparison, D7 SN did not exhibit any of the freezing damage observable by Raman and subtle impairment in cell adhesion that manifested post-thaw upon greater undercooling, whereas D14 mSN suffered significantly greater intracellular ice damage, impaired membrane partitioning, and cellular protein disintegration during freezing. This relativity in undercooling sensitivity (i.e., D5 crest < D7 SN < D14 mSN) inversely correlated with their differences in membrane fluidity (i.e., D5 crest > D7 SN > D14 mSN).

Summarizing the experiments above, cooling rate sensitivity varies by aggregate size of multicellular aggregates and by cell size of single cells, and undercooling sensitivity varies between aggregates and single cells as well between cell development stages with different membrane fluidity. Aim 1 fulfills Hypothesis 1.

Aim 2 – Mechanisms of cryoprotection by CPA-CPA, CPA-water and CPA-cell interactions as unveiled by Raman and assisted by other analytical chemistry techniques.

Aim 2.1 – Analyze interfacial interactions of sucrose during freezing.

In Chapter 5, based on Jurkat cells as a simplified cell model, under constant cooling rate and nucleation temperature (CRF parameters), the molecular concentration of sucrose in the nonfrozen solution, the spatial distribution of sucrose at its interface with extracellular ice and with cell, and the correlation between intracellular ice formation and extracellular sucrose

distribution were analyzed during freezing using low-temperature Raman spectroscopy. This sub-aim elucidates the mechanism of action of sucrose, an essential non-DMSO CPA used by this dissertation work for hiPSC cryopreservation and by previous work for T cells and MSCs. Findings included that upon freezing to -50 ˚C, sucrose had concentrated in the nonfrozen region between ice crystals far beyond its ambient solubility limit and strengthened its hydrogen bond with water inhibiting dynamic motions of water molecules towards crystallization as well as that of sucrose molecules towards precipitation. It separated each cell from surrounding extracellular ice phase, reducing the likelihood of intracellular ice, and directly interacted with the plasma membrane, replacing water and stabilizing the cell upon dehydration. Additionally, cells in the nonfrozen region were subjected to a spatially heterogeneous microenvironment of sucrose concentration (i.e., higher in wider regions of cell-extracellular ice interface).

Aim 2.2 – Examine interactions of NADES with water and NADES with cells.

Also in Chapter 5, based on Jurkat cells, under constant CRF parameters, the mechanism of action of a sugar-sugar alcohol NADES was analyzed. Dilute trehalose-glycerol NADES was found to have a neutral effect on producing ice crystals with cryoprotective morphology, compared to trehalose or glycerol alone, but strengthen the intermolecular hydrogen bond network with water. As a result, it both suppressed the overall amount of ice formation and the dehydration of nonfrozen regions protecting cells from both mechanisms of damage. While higher concentration of NADES exhibited superior thermophysical properties, it also resulted in more post-thaw apoptosis, lower recovery and proliferation in the cryopreserved cell population likely by subjecting the cells to greater osmotic stress. Thermophysical properties of CPA solutions alone could not predict optimal cell survival, suggesting that biological interaction between CPA and cells may play a role in successful cryopreservation. Additionally, the

optimized non-DMSO solution from Aim 3.1 displayed a Raman spectral waveform in its intermolecular hydrogen bond and intramolecular OH bond vibrations upon freezing that was distinctly different from that of a dilute NADES, despite strengthening the overall hydrogen bond network with water as well.

Aim 2.3 – Investigate the nature of cryoprotection by isoleucine and albumin.

In Chapters 5 and 6, based on Jurkat cells representing simpler cell forms and hiPSC aggregates representing multicellular systems, under constant CRF parameters, mechanisms of action of isoleucine and albumin were analyzed based on a combination of low-temperature Raman spectroscopy, DSC, membrane exclusion and reattachment assays. Findings included that supplementing isoleucine to dilute NADES from Aim 2.2 or the non-NADES solution from Aim 3.1 did not suppress or depress ice formation but significantly improved post-thaw cell survival, suggesting a mechanism of cryoprotection founded upon its biological interaction with cells rather than its thermophysical properties. Similarly, removal of albumin from the optimized non-DMSO solution from Aim 3.1 did not suppress or depress ice formation but helped to stabilize hiPSCs during prolonged CPA exposure before freezing, suggesting a rather biological than thermophysical protection of cells from non-cryopreservation stresses. The “sweet spot” of isoleucine concentration was never found at the higher end of the parametric range in either the T-cell or the hiPSC optimization experiment, likely requiring a balance of the stabilizing and destabilizing effect of a hydrophobic amino acid on cellular proteins.

Aim 2.4 – Explore the effect of poloxamer 188 on water crystallization and cell adhesion.

Also in Chapters 5 and 6, based on hiPSC aggregates representing multicellular systems, the mechanism of action of P188 was analyzed via low-temperature Raman spectroscopy and post-

thaw reattachment assay. Findings included that the addition of P188 not only both suppressed and depressed ice formation overall but also strengthened the hydrogen bond network in extracellular water lattice inhibiting ice inside and outside the cells. Moreover, in concert with sucrose, glycerol, isoleucine and albumin, P188 softened the solid-liquid interface of ice and nonfrozen regions and increased the distance between adjacent ice crystals, a unique, synergistic effect on water crystallization that did not allow minor deviation of the multicomponent CPA composition. Additionally, P188 was found to enhance cell-cell, cell-ECM adhesion enabling wash-free thawing of cryopreserved hiPSCs.

In summary, Aim 2 builds a fundamental understanding of the mechanisms of action of the non-DMSO CPAs that support the efficacy observed in Aim 3 of their synergistic formulation.

Aim 3 – Translational development of a new DMSO-free method to cryopreserve hiPSC aggregates.

Aim 3.1 – Optimize a multicomponent non-DMSO CPA solution using the DE algorithm.

In Chapter 6, a CPA formulation composed of sucrose, glycerol, L-isoleucine, human serum albumin and P188 was optimized for the highest post-thaw reattachment of hiPSC aggregates using DE algorithm in a 1296-point parameter space under 8 experiments. Despite a parameter space 6 times as populated than previous studies, much smaller population size per generation, the convergence speed of this study was well-maintained at 7 iterations. Post-thaw survival, growth, phenotype and karyotype of the optimally cryopreserved hiPSCs were found to be comparable to fresh cells and stable upon three freeze-thaw stress amplification cycles. The resulting post-thaw cell reattachment was 40% higher than that in DMSO given the same freezing conditions. Additionally, upon suboptimal, passive freezing, the optimized non-DMSO CPA

formulation also allowed significantly higher post-thaw cell survival. This sub-aim directly tested the second hypothesis of this dissertation by producing the superior non-DMSO CPA solution.

Aim 3.2 – Benchmark against standard DMSO solutions on undercooling sensitivity.

In Chapter 6, under a constant cooling rate but varied degrees of undercooling by ice nucleation induced at -4 or -12 ˚C, hiPSC aggregates cryopreserved in the optimized non-DMSO formulation were benchmarked against a basic 7.5% DMSO solution as well as DMSO-based commercial solutions, CS10, mFreSR, and BAMBanker hRM. This sub-aim directly tested the second hypothesis by validating the superior performance of the non-DMSO CPAs in the context of undercooling sensitivity – a key challenge of hiPSC cryopreservation. Post-thaw cell reattachment showed that the non-DMSO solution reduced the hiPSC aggregates' sensitivity to undercooling below detectable level, whereas all of the DMSO-based solutions suffered significantly more cell loss upon the 8 ˚C greater undercooling.

Aim 3.3 – Establish requirements for basal buffer components.

In Chapter 6, under ambient environment, hiPSC aggregates were collected in a basal buffer upon the presence, exclusion or replacement of Ca^{2+}, Mg^{2+}, NEAA, HCO_3^-, and P188. After introducing the optimized non-DMSO CPAs from Aim 3.1 and incubating for 1 hour, cell reattachment was measured with or without freeze-thaw and compared between the basal buffer variants. Findings included that Ca^{2+} and $Mg^{2+}$are essential to preventing cell dissociation-induced apoptosis throughout the cryopreservation process and ensuring successful reestablishment of hiPSC culture post-thaw. NEAA is essential to preserving cell energy and maintaining cell viability over time during cell preparation before freezing. HCO_3^- is essential to stabilizing intracellular pH. P188 is essential not only in the 2x CPA solution but in the basal

buffer to stabilize cell-cell adhesion upon dissociation from adherent culture and mitigate potential osmotic stress upon introduction of sucrose, glycerol and isoleucine. Replacing HBSS with E8 in the basal buffer is detrimental to the stability of hiPSCs upon initial exposure to CPA molecules, likely due to enhanced nutrient supply and cell stresses in response to the non-physiological temperature and hypertonic environment.

Aim 3.4 – Test the cryopreservation method optimized for hiPSCs on hiPSC-derived neuronal cells.

In Chapter 7, D5 crest, D7 SN and D14 mSN were frozen in the optimized non-DMSO CPA solution from Aim 3.1 using the best-case cooling rate and nucleation temperature from Aim 1.4. The main difference between the non-DMSO solution and the DMSO-based gold standard solution (i.e., CS10) existed before freezing upon prolonged cell exposure to the CPAs. The non-DMSO CPAs maintained cell viability of over 90% of the population for each stage of the neuronal cells for 1 hour, whereas DMSO resulted in 30% to 60% cell loss in 30 minutes. The non-DMSO formulation optimized for hiPSC cryopreservation was found effective in inhibiting a variety of freezing damages and mitigating undercooling sensitivity for all three stages from hiPSC-derived progenitors through mature cells. Passaging of fresh D5 crest revealed that cryopreservation of dissociated cells at this intermediate stage was incompatible with the differentiation protocol, where interrupting the otherwise continuous adherent culture on day 5 disabled the downstream differentiation into sensory neurons. Passaging of fresh D14 mSN revealed that the dissociation method required further optimization to enable successful re-culture of cryopreserved, likely stressed cells at this advanced developmental stage.

Summarizing the experiments above, the synergistic formulation of non-DMSO CPAs was superior to DMSO-based solutions in terms of pre-freeze cell stability upon CPA exposure,

intracellular ice inhibition during freezing, and post-thaw cell reattachment withstanding the stresses of undercooling. Aims 2 and 3 fulfill Hypothesis 2.

In addressing these specific aims, we have found that undercooling sensitivity is a main reason why hiPSC aggregates are more difficult to freeze than single cells, that membrane fluidity and cell size influence the bankability of differentiating cells, that non-DMSO CPAs like sucrose, glycerol, L-isoleucine and poloxamer 188 act in concert to protect cells against cryopreservation stresses by their interaction with water, with each other, and with the cell membrane, and that our DMSO-free method does improve post-thaw cell survival and function from DMSO-based standards. The outcome of this dissertation has brought empirical perspectives into subsequent designs of the cells' cryopreservation strategy and presented a potentially imitable approach for future cryobiological studies of other hiPSC-derived cellular technologies.

8.2 Future Directions

Beyond the potential follow-up experiments suggested throughout Chapters 4 – 7 that may provide additional information complementary to the mechanism of cryoinjury and cryoprotection discussed thus far, there are two major directions of future work that may build upon this dissertation and advance the utilization of cryopreservation to support the translational needs of hiPSC-derived and other cell-based technologies as described below.

8.2.1 Scale up mechanistic investigation and cryopreservation design from 2D to 3D

multicellular aggregates and from dissociated cells to adherent 2D monolayers

The work in Chapters 4 – 6 surrounded the cryopreservation of hiPSC multicellular aggregates dissociated from 2D adherent cultures. As introduced in Chapter 2, the clinical translation of hiPSC-based cell manufacturing often requires scale-up of the hiPSC cultivation modality from 2D adherent culture to 3D suspension (or bioreactor) culture. Our understanding of the cells' cryobiology and our design of the cryopreservation strategy should follow this transition as well. In addition to hiPSCs, there are numerous differentiated cell types cultivated as either 2D adherent monolayers or 3D spheroids, such as hiPSC-derived cardiomyocytes and cerebral organoids that may also benefit from this transition in our cryobiological research. As discussed in Chapters 4 and 7, dissociation of cell-cell, cell-ECM adhesion and interruption of continuous adherent culture are prone to apoptosis and cell functional loss, therefore challenging the utility of suspended single cells or 2D aggregates as a cryopreservation modality. To avoid such cell culture disruption, future studies may choose to cryopreserve adherent 2D monolayers *in situ* or suspended 3D aggregates dependent on the use-case scenario.

As mentioned in Chapter 2, Heiko Zimmermann group has reported a vitrification method to cryopreserve adherent 2D hiPSC culture in a specialized TWIST culture vessel[17]. Additionally, Ido Braslavsky's group has developed a motion-controlled directional freezing device proposed for *in situ* cryopreservation of adherent 2D cultures[275]. Published by Dennis Clegg group in March 2021 and showing high post-thaw survival of phenotypically stable cells *in vitro* and their efficacy *in vivo*, slow freezing of

hiPSC-derived retinal pigment epithelium (RPE) on its implantable substrate was one of the most recent and advanced examples of successful cryopreservation of adherent 2D monolayer, demonstrating optimization of harvest time, CPA formulation, cooling rate, and post-thaw wash buffer[274]. This literature shows an existing interest in the development and translational utilization of adherent 2D culture as a cryopreservation modality. However, there is a lack of systematic, scientific understanding in regard to the mechanisms of cryoinjury and cryoprotection. In order to support and enable the design and improvement of future cryopreservation strategies, confocal Raman microspectroscopy may be capitalized. Distribution and uptake of CPA molecules by the cell sheet in a liquid or frozen state, intracellular ice formation in relation to position within the cell sheet, and structural, molecular integrity of the cell-cell, cell-ECM junctions are a few examples of such Raman metrics.

Methods and results of 3D spheroid cryopreservation can be found in literature since 2020, showing newly gained interest in this area. One study demonstrated the vitrification of large MSC spheroids (10,000- to 30,000-cell) using 2.8 M DMSO among other highly concentrated CPAs, which showed high post-thaw organoid structural integrity, little cell membrane impairment but low metabolic activity except for the thin peripheral layer in 50,000-cell or larger spheroids[276]. Another study demonstrated the passive slow freezing of small MSC spheroids (<100 μm in diameter) using 5% DMSO in FBS, which showed low post-thaw apoptosis, normal proliferation and osteogenic potential[277]. A third study demonstrated the passive slow freezing of large fibroblast spheroids (25,000-cell) using

StemSure, which showed high post-thaw structural integrity but significant apoptosis and impaired collagen deposition[278]. With over 1000 federally funded projects in organoid research and numerous hiPSC-derived organoid technologies entering IND application, translational research of 3D spheroid cryopreservation will be timely. Similar to 2D monolayers, Raman spectroscopy may be capitalized to investigate the diffusion and partitioning of different CPA molecules within spheroids of varying sizes in a liquid or frozen state, the intracellular ice formation under different cooling rates and nucleation temperatures, and the integrity of subcellular materials such as cytochrome C, in order to shine light on the challenges and potential solutions for the cryopreservation of 3D spheroids.

8.2.2 Investigate molecular interventions to mitigate cell undercooling sensitivity

The work in Chapters 4 – 7 focused on developing a synergistic multi-component osmolyte formulation to mitigate cells' undercooling sensitivity by altering the crystallization pattern of water and improving the cells' tolerability for lower nucleation temperatures. However, there are alternative strategies that may be explored in place of or complementary with the present method. Molecular interventions like nucleating agents may be used to control ice nucleation temperature and minimize undercooling, and cholesterol may be used to enrich the plasma membrane, increase its membrane fluidity and, therefore, reduce cell sensitivity to undercooling. Nucleating agents including silver iodide, gold nanoparticles, Snowmax, IceStart, and crystalline cholesterol of varying concentrations may be tested as variables of optimization and rapidly screened using

dual-objective DE algorithm[81] for highest mean spontaneous ice nucleation temperature measured by DSC and lowest cytotoxicity based on post-treatment cell viability. Methyl-β-cyclodextrin/cholesterol complex[279] of different concentrations and varying incubation time may be tested for incorporation of cholesterol into the plasma membrane, resulted membrane fluidity may be measured using Laurdan and two-photon microscopy, and cell undercooling sensitivity may be re-evaluated upon induced ice nucleation at -12 ˚C and freezing to -50 ˚C in terms of intracellular ice formation using low-temperature Raman spectroscopy. Both methods of molecular intervention should also be assessed for their impact on the cells' intended use-case function, where inert molecules causing no significant change in cell function would be desirable. In addition, their removal or clearance from the treated cells should be assessed to determine whether washing by centrifugation and resuspension would be sufficient to eliminate trace materials or *in vivo* toxicity of the molecule should be considered and evaluated.

The experiments performed in the dissertation work and in the future will ultimately improve the cryoprotective effectiveness, workflow efficiency, reproducibility and flexibility of cryopreserved cell-based products in the translational research and clinical supply chain of therapeutic applications.

Bibliography

1. Yu, J. *et al.* Induced pluripotent stem cell lines derived from human somatic cells. *Science (80-.).* **318**, 1917–1920 (2007).
2. Yu, J. *et al.* Human induced pluripotent stem cells free of vector and transgene sequences. *Science (80-.).* **324**, 797–801 (2009).
3. Madonna, R. Human-induced pluripotent stem cells: in quest of clinical applications. *Mol Biotechnol* **52**, 193–203 (2012).
4. Singh, V. K., Kalsan, M., Kumar, N., Saini, A. & Chandra, R. Induced pluripotent stem cells: applications in regenerative medicine, disease modeling, and drug discovery. *Front. cell Dev. Biol.* **3**, 2 (2015).
5. Yamanaka, S. Pluripotent Stem Cell-Based Cell Therapy-Promise and Challenges. *Stem Cell* **27**, 523–531 (2020).
6. Bastami, F. *et al.* Induced pluripotent stem cells as a new getaway for bone tissue engineering: A systematic review. *Cell Prolif* **50**, (2017).
7. Gao, L. *et al.* Myocardial Tissue Engineering With Cells Derived From Human-Induced Pluripotent Stem Cells and a Native-Like, High-Resolution, 3-Dimensionally Printed Scaffold. *Circ Res* **120**, 1318–1325 (2017).
8. Mihara, Y. *et al.* Production of pancreatic progenitor cells from human induced pluripotent stem cells using a three-dimensional suspension bioreactor system. *J. Tissue Eng. Regen. Med.* **11**, 3193–3201 (2017).
9. Chun, Y. S., Byun, K. & Lee, B. Induced pluripotent stem cells and personalized medicine: current progress and future perspectives. *Anat Cell Biol* **44**, 245–255 (2011).
10. Matsa, E., Ahrens, J. H. & Wu, J. C. Human Induced Pluripotent Stem Cells as a Platform for Personalized and Precision Cardiovascular Medicine. *Physiol Rev* **96**, 1093–1126 (2016).
11. Ko, H. C. & Gelb, B. D. Concise review: drug discovery in the age of the induced pluripotent stem cell. *Stem Cells Transl. Med.* **3**, 500–9 (2014).
12. Pi, C. H., Hornberger, K., Dosa, P. & Hubel, A. Understanding the freezing

responses of T cells and other subsets of human peripheral blood mononuclear cells using DSMO-free cryoprotectants. *Cytotherapy* **In Press:**, (2020).

13. Germann, A. *et al.* Temperature fluctuations during deep temperature cryopreservation reduce PBMC recovery, viability and T-cell function. *Cryobiology* **67**, 193–200 (2013).
14. Nazarpour, R. *et al.* Optimization of Human Peripheral Blood Mononuclear Cells (PBMCs) Cryopreservation. *Int. J. Mol. Cell. Med.* **1**, 88–93 (2012).
15. Ragoonanan, V., Hubel, A. & Aksan, A. Response of the cell membrane–cytoskeleton complex to osmotic and freeze/thaw stresses. *Cryobiology* **61**, 335–344 (2010).
16. Naaldijk, Y., Johnson, A. A., Friedrich-Stöckigt, A. & Stolzing, A. Cryopreservation of dermal fibroblasts and keratinocytes in hydroxyethyl starch–based cryoprotectants. *BMC Biotechnol.* **16**, 85 (2016).
17. Beier, A. F., Schulz, J. C. & Zimmermann, H. Cryopreservation with a twist – Towards a sterile, serum-free surface-based vitrification of hESCs. *Cryobiology* **66**, 8–16 (2013).
18. Nishiyama, Y. *et al.* Safe and efficient method for cryopreservation of human induced pluripotent stem cell-derived neural stem and progenitor cells by a programmed freezer with a magnetic field. *Neurosci. Res.* **107**, 20–29 (2016).
19. Hunt, C. J. Cryopreservation of Human Stem Cells for Clinical Application: A Review. *Transfus. Med. Hemother.* **38**, 107–123 (2011).
20. Martín-Ibáñez, R., Hovatta, O. & Canals, J. M. Cryopreservation of Human Pluripotent Stem Cells: Are We Going in the Right Direction? in *Current Frontiers in Cryobiology* (ed. Katkov, I. I.) 139–166 (IntechOpen, 2012). doi:10.5772/34853
21. Crook, J. M., Tomaskovic-Crook, E. & Ludwig, T. E. Cryobanking Pluripotent Stem Cells. *Methods Mol Biol* **1590**, 151–164 (2017).
22. van den Brink, L. *et al.* Cryopreservation of human pluripotent stem cell-derived cardiomyocytes is not detrimental to their molecular and functional properties. *Stem Cell Res.* **43**, 101698 (2020).

23. Linville, R. M. *et al.* Long-Term Cryopreservation Preserves Blood–Brain Barrier Phenotype of iPSC-Derived Brain Microvascular Endothelial Cells and Three-Dimensional Microvessels. *Mol. Pharm.* **17**, 3425–3434 (2020).
24. Takahashi, K. & Yamanaka, S. Induction of pluripotent stem cells from mouse embryonic and adult fibroblast cultures by defined factors. *Cell* **126**, 663–76 (2006).
25. Puri, M. C. & Nagy, A. Concise Review: Embryonic Stem Cells Versus Induced Pluripotent Stem Cells: The Game Is On. *Stem Cells* **30**, 10–14 (2012).
26. Costigan, M., Scholz, J. & Woolf, C. J. Neuropathic Pain: A Maladaptive Response of the Nervous System to Damage. *Annu. Rev. Neurosci.* **32**, 1–32 (2009).
27. Sugita, S. *et al.* HLA-Matched Allogeneic iPS Cells-Derived RPE Transplantation for Macular Degeneration. *J. Clin. Med.* **9**, (2020).
28. Li, Y., Hermanson, D. L., Moriarity, B. S. & Kaufman, D. S. Human iPSC-Derived Natural Killer Cells Engineered with Chimeric Antigen Receptors Enhance Anti-tumor Activity. *Cell Stem Cell* **23**, 181-192.e5 (2018).
29. Chen, G. *et al.* Chemically defined conditions for human iPSC derivation and culture. *Nat. Methods* **8**, 424–429 (2011).
30. Nie, Y., Walsh, P., Clarke, D. L., Rowley, J. A. & Fellner, T. Scalable Passaging of Adherent Human Pluripotent Stem Cells. *PLoS One* **9**, e88012 (2014).
31. Kwok, C. K. *et al.* Scalable stirred suspension culture for the generation of billions of human induced pluripotent stem cells using single-use bioreactors. *J. Tissue Eng. Regen. Med.* **12**, e1076–e1087 (2018).
32. Takahashi, Y. *et al.* A Refined Culture System for Human Induced Pluripotent Stem Cell-Derived Intestinal Epithelial Organoids. *Stem Cell Reports* **10**, 314–328 (2018).
33. Chen, V. C. *et al.* Development of a scalable suspension culture for cardiac differentiation from human pluripotent stem cells. *Stem Cell Res.* **15**, 365–375 (2015).
34. Lee, B. *et al.* Challenges and Solutions for Commercial Scale Manufacturing of

Allogeneic Pluripotent Stem Cell Products. *Bioengineering* **7**, 31 (2020).

35. Chen, K. G., Mallon, B. S., McKay, R. D. G. & Robey, P. G. Human pluripotent stem cell culture: considerations for maintenance, expansion, and therapeutics. *Cell Stem Cell* **14**, 13–26 (2014).
36. Ezashi, T., Das, P. & Roberts, R. M. Low O2 tensions and the prevention of differentiation of hES cells. *Proc. Natl. Acad. Sci.* **102**, 4783–4788 (2005).
37. Belinsky, G. S. & Antic, S. D. Mild Hypothermia Inhibits Differentiation of Human Embryonic and Induced Pluripotent Stem Cells. *Biotechniques* **55**, (2013).
38. Yoshihara, M., Hayashizaki, Y. & Murakawa, Y. Genomic Instability of iPSCs: Challenges Towards Their Clinical Applications. *Stem Cell Rev. Reports* **13**, 7–16 (2017).
39. Li, L., Bennett, S. A. L. & Wang, L. Role of E-cadherin and other cell adhesion molecules in survival and differentiation of human pluripotent stem cells. *Cell Adh. Migr.* **6**, 59–70 (2012).
40. Ohgushi, M. *et al.* Molecular Pathway and Cell State Responsible for Dissociation-Induced Apoptosis in Human Pluripotent Stem Cells. *Stem Cell* **7**, 225–239 (2010).
41. John G. Baust, J. M. B. *Advances in Biopreservation*. (CRC Press, 2006).
42. Holzapfel, H. *et al.* Post-thaw cellular therapy products trypan blue viability assay standardization by dextran40 sample dilution and time-lapse digital microphotography. *Cytotherapy* **17**, S26 (2015).
43. Pollock, K., Sumstad, D., Kadidlo, D., McKenna, D. H. & Hubel, A. Clinical mesenchymal stromal cell products undergo functional changes in response to freezing. *Cytotherapy* **17**, 38–45 (2015).
44. Pegg, D. E. Viability assays for preserved cells, tissues, and organs. *Cryobiology* **26**, 212–231 (1989).
45. Curtsinger, J. M. *et al.* Postthaw characterization of umbilical cord blood: markers of storage lesion. *Transfusion* **55**, 1033–1039 (2014).
46. Pollock, K. *et al.* Improved Post-Thaw Function and Epigenetic Changes in Mesenchymal Stromal Cells Cryopreserved Using Multicomponent Osmolyte Solutions. *Stem Cells Dev.* **26**, 828–842 (2017).

47. Fahy, G. M. *et al.* Cryopreservation of organs by vitrification: perspectives and recent advances. *Cryobiology* **48**, 157–178 (2004).
48. Practice Committees of the American Society for Reproductive Medicine and Society of Reproductive Biologists and Technologists. A review of best practices of rapid-cooling vitrification for oocytes and embryos: a committee opinion. *Fertil. Steril.* **115**, 305–310 (2021).
49. Porcu, E. *et al.* High-security closed devices are efficient and safe to protect human oocytes from potential risk of viral contamination during vitrification and storage especially in the COVID-19 pandemic. *J. Assist. Reprod. Genet.* **38**, 681–688 (2021).
50. Imaizumi, K. *et al.* A Simple and Highly Effective Method for Slow-Freezing Human Pluripotent Stem Cells Using Dimethyl Sulfoxide, Hydroxyethyl Starch and Ethylene Glycol. *PLoS One* **9**, e88696 (2014).
51. Yuan, Y. *et al.* Efficient long-term cryopreservation of pluripotent stem cells at −80 °C. *Sci. Rep.* **6**, 34476 (2016).
52. Baharvand, H., Salekdeh, G. H., Taei, A. & Mollamohammadi, S. An efficient and easy-to-use cryopreservation protocol for human ES and iPS cells. *Nat. Protoc.* **5**, 588–594 (2010).
53. Mollamohammadi, S. *et al.* A simple and efficient cryopreservation method for feeder-free dissociated human induced pluripotent stem cells and human embryonic stem cells. *Hum Reprod* **24**, 2468–2476 (2009).
54. Hubel, A. *Preservation of Cells: a practical manual*. (John Wiley & Sons, Inc., 2018). doi:10.1002/9781118989883
55. Steponkus, P. L., Dowgert, M. F. & Gordon-Kamm, W. J. Destabilization of the plasma membrane of isolated plant protoplasts during a freeze-thaw cycle: The influence of cold acclimation. *Cryobiology* **20**, 448–465 (1983).
56. Lovelock, J. E. E. The haemolysis of human red blood-cells by freezing and thawing. *Biochim. Biophys. Acta* **10**, 414–426 (1953).
57. Gao, D. & Critser, J. K. Mechanisms of Cryoinjury in Living Cells. *ILAR J.* **41**, 187–196 (2000).

58. Dalvi-Isfahan, M., Hamdami, N., Xanthakis, E. & Le-Bail, A. Review on the control of ice nucleation by ultrasound waves, electric and magnetic fields. *J. Food Eng.* **195**, 222–234 (2017).
59. Vali, G. Exploratory experiments on pre-activated freezing nucleation on mercuric iodide. *Atmos. Chem. Phys.* **21**, 2551–2568 (2021).
60. Edwards, G. R. & Evans, L. F. Ice Nucleation by Silver Iodide: III. The Nature of the Nucleating Site. *J. Atmos. Sci.* **25**, 249–256 (1968).
61. Han, X., Ma, H. B., Wilson, C. & Critser, J. K. Effects of nanoparticles on the nucleation and devitrification temperatures of polyol cryoprotectant solutions. *Microfluid. Nanofluidics* **4**, 357–361 (2008).
62. Margaritis, A. & Bassi, A. S. Principles and Biotechnological Applications of Bacterial Ice Nucleation. *Crit. Rev. Biotechnol.* **11**, 277–295 (1991).
63. Campbell, L. H. & Brockbank, K. G. M. Cryopreservation of Adherent Cells on a Fixed Substrate. in *Recent Advances in Cryopreservation* (InTech, 2014). doi:10.5772/58618
64. Wragg, N. M., Tampakis, D. & Stolzing, A. Cryopreservation of Mesenchymal Stem Cells Using Medical Grade Ice Nucleation Inducer. *Int. J. Mol. Sci.* **21**, (2020).
65. Massie, I., Selden, C., Hodgson, H. & Fuller, B. Cryopreservation of Encapsulated Liver Spheroids for a Bioartificial Liver: Reducing Latent Cryoinjury Using an Ice Nucleating Agent. *Tissue Eng. Part C Methods* **17**, 765–774 (2011).
66. Massie, I. *et al.* GMP Cryopreservation of Large Volumes of Cells for Regenerative Medicine: Active Control of the Freezing Process. doi:10.1089/ten.tec.2013.0571
67. Sosso, G. C. *et al.* Unravelling the origins of ice nucleation on organic crystals. *Chem. Sci.* **9**, 8077–8088 (2018).
68. Lovelock, J. E. & Bishop, M. W. Prevention of freezing damage to living cells by dimethyl sulphoxide. *Nature* **183**, 1394–1395 (1959).
69. Hornberger, K., Yu, G., McKenna, D. & Hubel, A. Cryopreservation of Hematopoietic Stem Cells: Emerging Assays, Cryoprotectant Agents, and

Technology to Improve Outcomes. *Transfus. Med. Hemotherapy* **46**, 188–196 (2019).

70. Solocinski, J. *et al.* Effect of trehalose as an additive to dimethyl sulfoxide solutions on ice formation, cellular viability, and metabolism. *Cryobiology* **75**, 134–143 (2017).
71. de Abreu Costa, L. *et al.* Dimethyl Sulfoxide (DMSO) Decreases Cell Proliferation and TNF-α, IFN-γ, and IL-2 Cytokines Production in Cultures of Peripheral Blood Lymphocytes. *Molecules* **22**, 1789 (2017).
72. Yuan, C. *et al.* Dimethyl Sulfoxide Damages Mitochondrial Integrity and Membrane Potential in Cultured Astrocytes. *PLoS One* **9**, e107447 (2014).
73. Verheijen, M. *et al.* DMSO induces drastic changes in human cellular processes and epigenetic landscape in vitro. *Sci. Rep.* **9**, 4641 (2019).
74. Galvao, J. *et al.* Unexpected low-dose toxicity of the universal solvent DMSO. *FASEB J.* **28**, 1317–1330 (2014).
75. Kollerup Madsen, B., Hilscher, M., Zetner, D. & Rosenberg, J. Adverse reactions of dimethyl sulfoxide in humans: a systematic review. *F1000Research* **7**, 1746 (2018).
76. Awan, M. *et al.* Dimethyl sulfoxide: a central player since the dawn of cryobiology, is efficacy balanced by toxicity? *Regen. Med.* **15**, 1463–1491 (2020).
77. Júnior, A. M. *et al.* Neurotoxicity associated with dimethylsulfoxide-preserved hematopoietic progenitor cell infusion. *Bone Marrow Transplant.* **41**, 95–96 (2008).
78. Knight, C. A., De Vries, A. L. & Oolman, L. D. Fish antifreeze protein and the freezing and recrystallization of ice. *Nature* **308**, 295–296 (1984).
79. Eskandari, A., Leow, T. C., Rahman, M. B. A. & Oslan, S. N. Antifreeze Proteins and Their Practical Utilization in Industry, Medicine, and Agriculture. *Biomolecules* **10**, 1649 (2020).
80. Pollock, K. *et al.* Combinations of Osmolytes, Including Monosaccharides, Disaccharides, and Sugar Alcohols Act in Concert During Cryopreservation to Improve Mesenchymal Stromal Cell Survival. *Tissue Eng. Part C Methods* **22**,

999–1008 (2016).

81. Pi, C.-H., Hornberger, K., Dosa, P. & Hubel, A. Understanding the freezing responses of T cells and other subsets of human peripheral blood mononuclear cells using DSMO-free cryoprotectants. *Cytotherapy* **22**, 291–300 (2020).
82. Deller, R. C., Vatish, M., Mitchell, D. A. & Gibson, M. I. Synthetic polymers enable non-vitreous cellular cryopreservation by reducing ice crystal growth during thawing. *Nat. Commun.* **5**, 3244 (2014).
83. López, M., Bollag, R. J., Yu, J. C., Isales, C. M. & Eroglu, A. Chemically Defined and Xeno-Free Cryopreservation of Human Adipose-Derived Stem Cells. *PLoS One* **11**, e0152161 (2016).
84. Schrader, A. M., Cheng, C.-Y., Israelachvili, J. N. & Han, S. Communication: Contrasting effects of glycerol and DMSO on lipid membrane surface hydration dynamics and forces. *J. Chem. Phys.* **145**, 041101 (2016).
85. Pi, C.-H., Yu, G., Dosa, P. I. & Hubel, A. Characterizing modes of action and interaction for multicomponent osmolyte solutions on Jurkat cells. *Biotechnol. Bioeng.* **116**, 631–643 (2019).
86. Pi, C.-H., Yu, G., Petersen, A. & Hubel, A. Characterizing the “sweet spot” for the preservation of a T-cell line using osmolytes. *Sci. Rep.* **8**, 16223 (2018).
87. Pollock, K. Algorithm optimization of cryopreservation protocols to improve mesenchymal stem cell functionality. (University of Minnesota, 2016).
88. Pi, C.-H. Using Computational Tools to Understand Interactions between Osmolytes and Optimize the Preservation of Heterogeneous Populations of Primary Cells. (University of Minnesota, 2019).
89. Diller, K. R. & Cravalho, E. G. A cryomicroscope for the study of freezing and thawing processes in biological cells. *Cryobiology* **7**, 191–199 (1971).
90. Dong, J., Malsam, J., Bischof, J. C., Hubel, A. & Aksan, A. Spatial distribution of the state of water in frozen mammalian cells. *Biophys. J.* **99**, 2453–2459 (2010).
91. Yu, G., Yap, Y. R., Pollock, K. & Hubel, A. Characterizing Intracellular Ice Formation of Lymphoblasts Using Low-Temperature Raman Spectroscopy. *Biophys. J.* **112**, 2653–2663 (2017).

92. Raman, C. V. & Krishnan, K. S. A New Type of Secondary Radiation. *Nature* **121**, 501–502 (1928).
93. Das, R. S. & Agrawal, Y. K. Raman spectroscopy: Recent advancements, techniques and applications. *Vib. Spectrosc.* **57**, 163–176 (2011).
94. Butler, H. J. *et al.* Using Raman spectroscopy to characterize biological materials. *Nat. Protoc.* **11**, 664–687 (2016).
95. Baena, J. R. & Lendl, B. Raman spectroscopy in chemical bioanalysis. *Curr. Opin. Chem. Biol.* **8**, 534–539 (2004).
96. Schie, I. W. & Huser, T. Methods and applications of Raman microspectroscopy to single-cell analysis. *Appl. Spectrosc.* **67**, 813–828 (2013).
97. Swain, R., Kemp, S., Goldstraw, P., Journal, T. T.-B. & 2010, U. Assessment of cell line models of primary human cells by Raman spectral phenotyping. *Biophys. J.* **98**, 1703–1711 (2010).
98. Nawaz, H. *et al.* Evaluation of the potential of Raman microspectroscopy for prediction of chemotherapeutic response to cisplatin in lung adenocarcinoma. *Analyst* **135**, 3070–3076 (2010).
99. Harkness, L., Novikov, S. M., Beermann, J., Bozhevolnyi, S. I. & Kassem, M. Identification of abnormal stem cells using Raman spectroscopy. *Stem Cells Dev.* **21**, 2152–9 (2012).
100. Bailey, T. L. *et al.* Protective effects of osmolytes in cryopreserving adherent neuroblastoma (Neuro-2a) cells. *Cryobiology* **71**, 472–480 (2015).
101. Kreiner-Møller, A., Stracke, F. & Zimmermann, H. Hydrohalite spatial distribution in frozen cell cultures measured using confocal Raman microscopy. *Cryobiology* **69**, 41–7 (2014).
102. Kreiner-Møller, A., Stracke, F. & Zimmermann, H. Confocal raman microscopy as a non-invasive tool to investigate the phase composition of frozen complex cryopreservation media. *Cryo Letters* **34**, 248–54 (2013).
103. Ye, L. *et al.* Effective Cardiac Myocyte Differentiation of Human Induced Pluripotent Stem Cells Requires VEGF. *PLoS One* **8**, e53764 (2013).
104. Storn, R. & Price, K. Differential Evolution – A Simple and Efficient Heuristic for

Global Optimization over Continuous Spaces. *J. Glob. Optim.* **11**, 341–359 (1997).

105. Pollock, K., Budenske, J. W., McKenna, D. H., Dosa, P. I. & Hubel, A. Algorithm-driven optimization of cryopreservation protocols for transfusion model cell types including Jurkat cells and mesenchymal stem cells. *J. Tissue Eng. Regen. Med.* **11**, 2806–2815 (2017).
106. Pi, C.-H., Dosa, P. & Hubel, A. Differential evolution for the optimization of DMSO-free cryoprotectants: influence of control parameters. *J. Biomech. Eng.* BIO-19-1207
107. Li, R., Yu, G., Azarin, S. M. & Hubel, A. Freezing Responses in DMSO-Based Cryopreservation of Human iPS Cells: Aggregates Versus Single Cells. *Tissue Eng. Part C Methods* **24**, 289–299 (2018).
108. Yu, G., Li, R. & Hubel, A. Raman Cryomicroscopic Imaging and Sample Holder for Spectroscopic Subzero Temperature Measurements. in *Cryopreservation and Freeze-Drying Protocols* (eds. Wolkers, W. F. & Oldenhof, H.) 351–361 (Springer Nature, 2021). doi:10.1007/978-1-0716-0783-1_14
109. Baboo, J. *et al.* The Impact of Varying Cooling and Thawing Rates on the Quality of Cryopreserved Human Peripheral Blood T Cells. *Sci. Rep.* **9**, 3417 (2019).
110. Li, Y. & Ma, T. Bioprocessing of Cryopreservation for Large-Scale Banking of Human Pluripotent Stem Cells. *Biores. Open Access* **1**, 205–214 (2012).
111. Ware, C. B., Nelson, A. M. & Blau, C. A. Controlled-rate freezing of human ES cells. *Biotechniques* **38**, 879-880,882-883 (2005).
112. Yang, P. F. *et al.* Cryopreservation of human embryonic stem cells: a protocol by programmed cooling. *Cryo Letters* **27**, 361–368 (2006).
113. Valbuena, D. *et al.* Efficient method for slow cryopreservation of human embryonic stem cells in xeno-free conditions. *Reprod Biomed Online* **17**, 127–135 (2008).
114. Lee, J. Y. *et al.* High concentration of synthetic serum, stepwise equilibration and slow cooling as an efficient technique for large-scale cryopreservation of human embryonic stem cells. *Fertil Steril* **93**, 976–985 (2010).
115. Li, X., Meng, G., Krawetz, R., Liu, S. & Rancourt, D. E. The ROCK inhibitor Y-

27632 enhances the survival rate of human embryonic stem cells following cryopreservation. *Stem Cells Dev* **17**, 1079–1085 (2008).

116. Claassen, D. A., Desler, M. M. & Rizzino, A. ROCK inhibition enhances the recovery and growth of cryopreserved human embryonic stem cells and human induced pluripotent stem cells. *Mol. Reprod. Dev.* **76**, 722–732 (2009).
117. Walker, A. *et al.* Non-muscle myosin II regulates survival threshold of pluripotent stem cells. *Nat. Commun.* **1**, 71 (2010).
118. Chen, G., Hou, Z., Gulbranson, D. R. & Thomson, J. A. Actin-myosin contractility is responsible for the reduced viability of dissociated human embryonic stem cells. *Cell Stem Cell* **7**, 240–248 (2010).
119. Vicente-Manzanares, M., Ma, X., Adelstein, R. S. & Horwitz, A. R. Non-muscle myosin II takes centre stage in cell adhesion and migration. *Nat Rev Mol Cell Biol* **10**, 778–790 (2009).
120. Li, D. *et al.* Integrated biochemical and mechanical signals regulate multifaceted human embryonic stem cell functions. *J Cell Biol* **191**, 631–644 (2010).
121. Fuller, B. J. *Life in the Frozen State*. *Life in the Frozen State* (CRC Press, 2004). doi:10.1201/9780203647073
122. Berger W.K. & Uhrik B. Freeze-induced shrinkage of individual cells and cell-to-cell propagation of intracellular ice in cell chains from salivary glands. *Cell. Mol. Life Sci.* **52**, 843–850 (1996).
123. Acker, J. P., Elliott, J. A. & McGann, L. E. Intercellular ice propagation: experimental evidence for ice growth through membrane pores. *Biophys J* **81**, 1389–1397 (2001).
124. Irimia, D. & Karlsson, J. O. M. Kinetics and Mechanism of Intercellular Ice Propagation in a Micropatterned Tissue Construct. *Biophys. J.* **82**, 1858–1868 (2002).
125. Okotrub, K. A. & Surovtsev, N. V. Raman scattering evidence of hydrohalite formation on frozen yeast cells. *Cryobiology* **66**, 47–51 (2013).
126. Kreiner-Moller, A., Stracke, F. & Zimmermann, H. Hydrohalite spatial distribution in frozen cell cultures measured using confocal Raman microscopy. *Cryobiology*

69, 41–47 (2014).

127. Yu, G., Yap, Y. R., Pollock, K. & Hubel, A. Characterizing Intracellular Ice Formation of Lymphoblasts Using Low-Temperature Raman Spectroscopy. *Biophys. J.* **112**, 2653–2663 (2017).
128. Dong, J., Hubel, A., Bischof, J. C. & Aksan, A. Freezing-Induced Phase Separation and Spatial Microheterogeneity in Protein Solutions. *J. Phys. Chem. B* **113**, 10081–10087 (2009).
129. Mazur, P. Principles of Cryobiology. in *Life in the Frozen State* (eds. Fuller, B., Lane, N. & Benson, E.) 3–66 (CRC Press, 2004).
130. Watanabe, K. *et al.* A ROCK inhibitor permits survival of dissociated human embryonic stem cells. *Nat Biotechnol* **25**, 681–686 (2007).
131. Ohgushi, M. *et al.* Molecular pathway and cell state responsible for dissociation-induced apoptosis in human pluripotent stem cells. *Cell Stem Cell* **7**, 225–239 (2010).
132. Katkov, I. I. *et al.* DMSO-Free Programmed Cryopreservation of Fully Dissociated and Adherent Human Induced Pluripotent Stem Cells. *Stem Cells Int.* **2011**, 981606 (2011).
133. Baust, J. M., Van Buskirk, R. & Baust, J. G. Cell viability improves following inhibition of cryopreservation-induced apoptosis. *Vitr. Cell. Dev. Biol. - Anim.* **36**, 262–270 (2000).
134. Sasnoor, L. M., Kale, V. P. & Limaye, L. S. Prevention of Apoptosis as a Possible Mechanism behind Improved Cryoprotection of Hematopoietic Cells by Catalase and Trehalose. *Transplantation* **80**, 1251–1260 (2005).
135. Mazur, P. Freezing of living cells: mechanisms and implications. *Am J Physiol* **247**, C125-42 (1984).
136. Foreman, J. & Pegg, D. E. Cell preservation in a programmed cooling machine: The effect of variations in supercooling. *Cryobiology* **16**, 315–321 (1979).
137. Harris, C. L. *et al.* Cryopreservation of isolated hepatocytes: intracellular ice formation under various chemical and physical conditions. *Cryobiology* **28**, 436–444 (1991).

138. Diller, K. R. Intracellular freezing: Effect of extracellular supercooling. *Cryobiology* **12**, 480–485 (1975).
139. Toner, M. Nucleation of ice crystals inside biological cells. *Adv. low-temperature Biol.* **2**, 1–51 (1993).
140. Narva, E. *et al.* A Strong Contractile Actin Fence and Large Adhesions Direct Human Pluripotent Colony Morphology and Adhesion. *Stem Cell Reports* **9**, 67–76 (2017).
141. Noiles, E. E., Thompson, K. A. & Storey, B. T. Water permeability, Lp, of the mouse sperm plasma membrane and its activation energy are strongly dependent on interaction of the plasma membrane with the sperm cytoskeleton. *Cryobiology* **35**, 79–92 (1997).
142. Lande, M. B., Donovan, J. M. & Zeidel, M. L. *The Relationship between Membrane Fluidity and Permeabilities to Water, Solutes, Ammonia, and Protons*.
143. Acker, J. P., Larese, A., Yang, H., Petrenko, A. & Mcgann, L. E. Intracellular Ice Formation Is Affected by Cell Interactions. **371**, 363–371 (1999).
144. Acker, J. P., Elliott, J. A. W. & Mcgann, L. E. Intercellular Ice Propagation : Experimental Evidence for Ice Growth through Membrane Pores. *Biophys. J.* **81**, 1389–1397 (2001).
145. Bidault, N. P., Hammer, B. E. & Hubel, A. Water content in an engineered dermal replacement during permeation of Me2SO solutions using rapid MR imaging. *Biotechnol Prog* **17**, 530–536 (2001).
146. Fahy, G. M., Lilley, T. H., Linsdell, H., Douglas, M. S. & Meryman, H. T. Cryoprotectant toxicity and cryoprotectant toxicity reduction: in search of molecular mechanisms. *Cryobiology* **27**, 247–268 (1990).
147. Heng, B. C. *et al.* Loss of viability during freeze-thaw of intact and adherent human embryonic stem cells with conventional slow-cooling protocols is predominantly due to apoptosis rather than cellular necrosis. *J Biomed Sci* **13**, 433–445 (2006).
148. de Boer, F. *et al.* Early apoptosis largely accounts for functional impairment of CD34+ cells in frozen-thawed stem cell grafts. *J Hematother Stem Cell Res* **11**,

951–963 (2002).

149. Stroh, C. *et al.* The role of caspases in cryoinjury: caspase inhibition strongly improves the recovery of cryopreserved hematopoietic and other cells. *FASEB J.* **16**, 1651–1653 (2002).

150. Fowke, K. R., Behnke, J., Hanson, C., Shea, K. & Cosentino, L. M. Apoptosis: a method for evaluating the cryopreservation of whole blood and peripheral blood mononuclear cells. *J Immunol Methods* **244**, 139–144 (2000).

151. Boraas, L. C., Guidry, J. B., Pineda, E. T. & Ahsan, T. Cytoskeletal Expression and Remodeling in Pluripotent Stem Cells. *PLoS One* **11**, e0145084 (2016).

152. Sart, S., Ma, T. & Li, Y. Cryopreservation of pluripotent stem cell aggregates in defined protein-free formulation. *Biotechnol Prog* **29**, 143–153 (2013).

153. Iwatani, M. *et al.* Dimethyl Sulfoxide Has an Impact on Epigenetic Profile in Mouse Embryoid Body. *Stem Cells* **24**, 2549–2556 (2006).

154. Moll, G. *et al.* Do cryopreserved mesenchymal stromal cells display impaired immunomodulatory and therapeutic properties? *Stem Cells* **32**, 2430–2442 (2014).

155. Windrum, P., Morris, T. C. M., Drake, M. B., Niederwieser, D. & Ruutu, T. Variation in dimethyl sulfoxide use in stem cell transplantation: a survey of EBMT centres. *Bone Marrow Transplant.* **36**, 601–603 (2005).

156. Petrenko, Y. a, Jones, D. R. E. & Petrenko, a Y. Cryopreservation of human fetal liver hematopoietic stem/progenitor cells using sucrose as an additive to the cryoprotective medium. *Cryobiology* **57**, 195–200 (2008).

157. Cardoso, L. M. da F., Pinto, M. A., Henriques Pons, A. & Alves, L. A. Cryopreservation of rat hepatocytes with disaccharides for cell therapy. *Cryobiology* **78**, 15–21 (2017).

158. Rodrigues, J. P. *et al.* Evaluation of trehalose and sucrose as cryoprotectants for hematopoietic stem cells of umbilical cord blood. *Cryobiology* **56**, 144–151 (2008).

159. Shiraga, K., Adachi, A. & Ogawa, Y. Characterization of the hydrogen-bond network of water around sucrose and trehalose: H-O-H bending analysis. *Chem. Phys. Lett.* **678**, 59–64 (2017).

160. Lerbret, A. *et al.* Influence of homologous disaccharides on the hydrogen-bond network of water: Complementary Raman scattering experiments and molecular dynamics simulations. *Carbohydr. Res.* **340**, 881–887 (2005).
161. Roozen, M. J. G. W. & Hemminga, M. A. Molecular motion in sucrose-water mixtures in the liquid and glassy state as studied by spin probe ESR. *J. Phys. Chem.* **94**, 7326–7329 (1990).
162. Lerbret, A. *et al.* Slowing down of water dynamics in disaccharide aqueous solutions. in *Journal of Non-Crystalline Solids* **357**, 695–699 (2011).
163. Anchordoguy, T. J., Rudolph, A. S., Carpenter, J. F. & Crowe, J. H. Modes of interaction of cryoprotectants with membrane phospholipids during freezing. *Cryobiology* **24**, 324–331 (1987).
164. Crowe, J. H., Leslie, S. B. & Crowe, L. M. Is vitrification sufficient to preserve liposomes during freeze-drying? *Cryobiology* **31**, 355–366 (1994).
165. Crowe, J. H. *et al. Interactions of sugars with membranes*. *BBA - Reviews on Biomembranes* **947**, 367–384 (1988).
166. Crowe, H. & Crowe, L. M. Infrared Spectroscopic Carbohydrates Studies on Interactions of Water and with a Biological Membrane. **232**, 400–407 (1994).
167. Leslie, S. B., Israeli, E., Lighthart, B., Crowe, J. H. & Crowe, L. M. Trehalose and sucrose protect both membranes and proteins in intact bacteria during drying. *Appl. Environ. Microbiol.* **61**, 3592–3597 (1995).
168. Green, J. L. & Angell, C. A. Phase relations and vitrification in saccharide-water solutions and the trehalose anomaly. *J. Phys. Chem.* **93**, 2880–2882 (1989).
169. Crowe, J. H., Hoekstra, F. A., Nguyen, K. H. N. & Crowe, L. M. Is vitrification involved in depression of the phase transition temperature in dry phospholipids? *Biochim. Biophys. Acta - Biomembr.* **1280**, 187–196 (1996).
170. Lee, C. W. *et al.* Characterization of the L_lambda phase in trehalose-stabilized dry membranes by solid-state NMR and X-ray diffraction. *Biochemistry* **28**, 5000–5009 (1989).
171. Rudolph, B. R., Chandrasekhar, I., Gaber, B. P. & Nagumo, M. Molecular modelling of saccharide-lipid interactions. *Chem. Phys. Lipids* **53**, 243–261

(1990).

172. Hubel, A., Darr, T. B., Chang, A. & Dantzig, J. Cell partitioning during the directional solidification of trehalose solutions. *Cryobiology* **55**, 182–188 (2007).
173. Beckmann, J., Körber, C., Rau, G., Hubel, A. & Cravalho, E. G. Redefining cooling rate in terms of ice front velocity and thermal gradient: First evidence of relevance to freezing injury of lymphocytes. *Cryobiology* **27**, 279–287 (1990).
174. Hubel, A., Cravalho, E. G., Nunner, B. & Körber, C. Survival of directionally solidified B-lymphoblasts under various crystal growth conditions. *Cryobiology* **29**, 183–198 (1992).
175. Lipp, G., Galow, S., KÖrber, C. & Rau, G. Encapsulation of human erythrocytes by growing ice crystals. *Cryobiology* **31**, 305–312 (1994).
176. Ishiguro, H. & Rubinsky, B. Mechanical interactions between ice crystals and red blood cells during directional solidification. *Cryobiology* **31**, 483–500 (1994).
177. Chang, A., Dantzig, J. A., Darr, B. T. & Hubel, A. Modeling the interaction of biological cells with a solidifying interface. *J. Comput. Phys.* **226**, 1808–1829 (2007).
178. Carin, M. & Jaeger, M. Numerical simulation of the interaction of biological cells with an ice front during freezing. *Eur. Phys. J. Appl. Phys.* **16**, 231–238 (2001).
179. Abazari, A., Chakraborty, N., Hand, S., Aksan, A. & Toner, M. A Raman Microspectroscopy Study of Water and Trehalose in Spin-Dried Cells. *Biophys. J.* **107**, 2253–2262 (2014).
180. Craveiro, R. *et al.* Properties and thermal behavior of natural deep eutectic solvents. *J. Mol. Liq.* **215**, 534–540 (2016).
181. Hubálek, Z. Protectants used in the cryopreservation of microorganisms. *Cryobiology* **46**, 205–229 (2003).
182. Gertrudes, A. *et al.* How Do Animals Survive Extreme Temperature Amplitudes? the Role of Natural Deep Eutectic Solvents. *ACS Sustain. Chem. Eng.* **5**, 9542–9553 (2017).
183. Liu, Y. *et al.* Natural Deep Eutectic Solvents: Properties, Applications, and Perspectives. *J Nat Prod* **81**, 679–690 (2019).

184. Castro, V. I. B. *et al.* Natural deep eutectic systems as alternative nontoxic cryoprotective agents. *Cryobiology* **83**, 15–26 (2018).
185. Qiao, Y., Cai, H. L., Yang, X., Zang, Y. Y. & Chen, Z. G. Effects of natural deep eutectic solvents on lactic acid bacteria viability during cryopreservation. *Appl. Microbiol. Biotechnol.* **102**, 5695–5705 (2018).
186. Luzar, A. & Chandler, D. Structure and hydrogen bond dynamics of water-dimethyl sulfoxide mixtures by computer simulations. *J. Chem. Phys.* **98**, 8160–8173 (1993).
187. Cox, M. A., Kastrup, J. & Hrubiško, M. Historical perspectives and the future of adverse reactions associated with haemopoietic stem cells cryopreserved with dimethyl sulfoxide. *Cell Tissue Bank.* **13**, 203–215 (2012).
188. Dai, Y., Witkamp, G. J., Verpoorte, R. & Choi, Y. H. Tailoring properties of natural deep eutectic solvents with water to facilitate their applications. *Food Chem.* **187**, 14–19 (2015).
189. Dai, Y., van Spronsen, J., Witkamp, G. J., Verpoorte, R. & Choi, Y. H. Natural deep eutectic solvents as new potential media for green technology. *Anal. Chim. Acta* **766**, 61–68 (2013).
190. Esquembre, R. *et al.* Thermal unfolding and refolding of lysozyme in deep eutectic solvents and their aqueous dilutions. *Phys. Chem. Chem. Phys.* **15**, 11248–11256 (2013).
191. Hayyan, M. *et al.* Natural deep eutectic solvents: cytotoxic profile. *Springerplus* **5**, (2016).
192. Brizuela, A. B. *et al.* A complete characterization of the vibrational spectra of sucrose. *Carbohydr. Res.* **361**, 212–218 (2012).
193. Branca, C., Magazu, S., Maisano, G. & Migliardo, P. Anomalous cryoprotective effectiveness of trehalose: Raman scattering evidences. *J. fo Chem. Phys.* **111**, 281–287 (1999).
194. Körber, C. Phenomena at the advancing ice—liquid interface: Solutes particles and biological cells. *Q. Rev. Biophys.* **21**, 229–298 (1988).
195. Sitaula, R., Elmoazzen, H., Toner, M. & Bhowmick, S. Desiccation tolerance in

bovine sperm: A study of the effect of intracellular sugars and the supplemental roles of an antioxidant and a chelator. *Cryobiology* **58**, 322–330 (2009).

196. Lynch, A. L. *et al.* Biopolymer mediated trehalose uptake for enhanced erythrocyte cryosurvival. *Biomaterials* **31**, 6096–6103 (2010).
197. Zhang, M., Oldenhof, H., Sieme, H. & Wolkers, W. F. Freezing-induced uptake of trehalose into mammalian cells facilitates cryopreservation. *Biochim. Biophys. Acta - Biomembr.* **1858**, 1400–1409 (2016).
198. Pegg, D. E. & Diaper, M. P. On the mechanism of injury to slowly frozen erythrocytes. *Biophys. J.* **54**, 471–488 (1988).
199. MAZUR, P. Kinetics of Water Loss from Cells at Subzero Temperatures and the Likelihood of Intracellular Freezing. *J. Gen. Physiol.* **47**, 347–369 (1963).
200. Angell, A. C. A. & Angell, C. A. Formation of Glasses from Liquids and Biopolymers. *Science (80-.).* **267**, 1924–1935 (1995).
201. Angell, C. A. Liquid Fragility and the Glass Transition in Water and Aqueous Solutions. (2002). doi:10.1021/cr000689q
202. Richardson, S. J., Baianu, I. C. & Steinberg, M. P. Mobility of water in sucrose solutions determined by deuterium and oxygen-17 nuclear magnetic resonance measurements. *J. Food Sci.* **52,** 806–809 (1987).
203. Shiraga, K. *et al.* Characterization of the hydrogen-bond network of water around sucrose and trehalose: Microwave and terahertz spectroscopic study. *J. Chem. Phys.* **146**, 105102 (2017).
204. Douglas Goff, H. Low-temperature stability and the glassy state in frozen foods. *Food Res. Int.* **25**, 317–325 (1992).
205. Dashnau, J. L., Nucci, N. V., Sharp, K. A. & Vanderkooi, J. M. Hydrogen Bonding and the Cryoprotective Properties of Glycerol/Water Mixtures. *J. Phys. Chem. B* **110**, 13670–13677 (2006).
206. Galkina, Y. A., Kryuchkova, N. A., Vershinin, M. A. & Kolesov, B. A. Features of strong O–H···O and N–H···O hydrogen bond manifestation in vibrational spectra. *J. Struct. Chem.* **58**, 911–918 (2017).
207. Harmison, H. R., Diller, K. R., Walsh, J. R., Neils, C. M. & Brand, J. J.

Measurement of cell volume loss in the liquid region preceding an advancing phase change interface. in *Annals of the New York Academy of Sciences* **858**, 276–283 (1998).

208. Mao, L., Udaykumar, H. S. & Karlsson, J. O. M. Simulation of micro-scale interaction between ice and biological cells. *Int. J. Heat Mass Transf.* **46**, 5123–5136 (2003).
209. Jaeger, M., Carin, M., Medale, M. & Tryggvason, G. The osmotic migration of cells in a solute gradient. *Biophys. J.* **77**, 1257–1267 (1999).
210. Dantzig, J. & Rappaz, M. Thermodynamics. in *Solidification* 55–59 (EPFL Press, 2017).
211. Kao, J. C. T., Golovin, A. A. & Davis, S. H. Particle capture in binary solidification. *J. Fluid Mech.* **625**, 299–320 (2009).
212. Carin, M. & Jaeger, M. Numerical simulation of the interaction of biological cells with an ice front during freezing. *EPJ Appl. Phys.* **16**, 231–238 (2001).
213. Yu, G., Li, R. & Hubel, A. Interfacial Interactions of Sucrose during Cryopreservation Detected by Raman Spectroscopy. *Langmuir* **35**, 7388–7395 (2019).
214. Zhang, X., Chen, S. & Li, J. Hydrogen-bond potential for ice VIII-X phase transition. *Sci. Rep.* **6**, 37161 (2016).
215. Li, J. & Ross, D. K. Evidence for two kinds of hydrogen bond in ice. *Nature* **365**, 327–329 (1993).
216. Ignatov, I. & Mosin, O. *Nature of Hydrogen Bonds in Liquids and Crystals. Ice Crystal Modifications and Their Physical Characteristics*. *An Open Access Journal* **4**, (2014).
217. Li, R., Hornberger, K., Dutton, J. R. & Hubel, A. Cryopreservation of Human iPS Cell Aggregates in a DMSO-Free Solution—An Optimization and Comparative Study. *Frontiers in Bioengineering and Biotechnology* **8**, 1 (2020).
218. Rahman, A. T. *et al.* Ice recrystallization is strongly inhibited when antifreeze proteins bind to multiple ice planes. *Sci. Rep.* **9**, 2212 (2019).
219. Haque, E.; Kikuchi, T.; Kanemitsu, K.; Tsuda, Y. Effect of Cryoprotectants on the

Eutectic Crystallization of NaCl in Frozen Solutions Studied by Differential Scanning Calorimetry (DSC) and Broad-Line Pulsed NMR. *Chem. Pharm. Bull.* **34**, 430–433 (1986).

220. Haussinger, D., Roth, E., Lang, F. & Gerok, W. Cellular hydration state: an important determinant of protein catabolism in health and disease. *Lancet (London, England)* **341**, 1330–1332 (1993).
221. Fahy, G. M. & Wowk, B. Principles of cryopreservation by vitrification. *Methods Mol. Biol. (Methods Protoc.* **1257**, (2015).
222. Arakawa, T., Kita, Y. & Carpenter, J. F. Protein-solvent interactions in pharmaceutical formulations. *Pharm. Res.* **8**, (1991).
223. Wen, X. *et al.* Antifreeze proteins govern the precipitation of trehalose in a freezing-avoiding insect at low temperature. *Proc. Natl. Acad. Sci. U. S. A.* **113**, 6683–6688 (2016).
224. Sarkar, S., Kalia, V. & Montelaro, R. C. Caspase-mediated apoptosis and cell death of rhesus macaque CD4 + T-cells due to cryopreservation of peripheral blood mononuclear cells can be rescued by cytokine treatment after thawing. *Cryobiology* **47**, 44–58 (2003).
225. Chong, E. A. *et al.* CD19-Directed CAR T-Cell (CTL019) Product Viability and Clinical Outcomes in Non-Hodgkin Lymphomas and B-Cell Acute Lymphoblastic Leukemia. *Blood* **132**, (2018).
226. Pollock, K. *et al.* Combinations of Osmolytes, Including Monosaccharides, Disaccharides, and Sugar Alcohols Act in Concert During Cryopreservation to Improve Mesenchymal Stromal Cell Survival. *Tissue Eng. Part C Methods* **22**, 999–1008 (2016).
227. Pi, C., Yu, G., Petersen, A. & Hubel, A. Characterizing the " sweet spot " for the preservation of a T-cell line using osmolytes. *Sci. Rep.* 1–13 (2018). doi:10.1038/s41598-018-34638-7
228. Bozorgmehr, M. R. & Monhemi, H. How can a free amino acid stabilize a protein? insights from molecular dynamics simulation. *J. Solution Chem.* **44**, 45–53 (2015).
229. Brennan, J. D., Benjamin, D., DiBattista, E. & Gulcev, M. D. Using Sugar and

Amino Acid Additives to Stabilize Enzymes within Sol−Gel Derived Silica. *Chem. Mater.* **15**, 737–745 (2003).

230. Taneja, S. & Ahmad, F. Increased thermal stability of proteins in the presence of amino acids. *Biochem. J.* **303**, 147–53 (1994).
231. Jiang, Z., Han, Y. & Cao, X. Induced pluripotent stem cell (iPSCs) and their application in immunotherapy. *Cell. Mol. Immunol.* **11**, 17–24 (2014).
232. Stone, N., Kendall, C., Smith, J., Crow, P. & Barr, H. Raman spectroscopy for identification of epithelial cancers. *Faraday Discuss.* **126**, 141–157 (2004).
233. Mathlouthi, M. & Vinh Luu, D. Laser-raman spectra of d-glucose and sucrose in aqueous solution. *Carbohydr. Res.* **81**, 203–212 (1980).
234. Mendelovici, E., Frost, R. L. & Kloprogge, T. Cryogenic Raman spectroscopy of glycerol. *J. Raman Spectrosc.* **31**, 1121–1126 (2000).
235. Salzmann, C. G., Hallbrucker, A., Finney, J. L. & Mayer, E. Raman spectroscopic study of hydrogen ordered ice XIII and of its reversible phase transition to disordered ice V. *Phys. Chem. Chem. Phys.* **8**, 3088 (2006).
236. Dashnau, J. L., Sharp, K. A. & Vanderkooi, J. M. Carbohydrate Intramolecular Hydrogen Bonding Cooperativity and Its Effect on Water Structure. *J. Phys. Chem. B* **109**, 24152–24159 (2005).
237. Towey, J. J. & Dougan, L. Structural Examination of the Impact of Glycerol on Water Structure. *J. Phys. Chem. B* **116**, 1633–1641 (2012).
238. Boldt, J. Use of albumin: an update. *Br. J. Anaesth.* **104**, 276–284 (2010).
239. John Morris, G. & Acton, E. Controlled ice nucleation in cryopreservation – A review. *Cryobiology* **66**, 85–92 (2013).
240. Mazzola, M. & Di Pasquale, E. Toward Cardiac Regeneration: Combination of Pluripotent Stem Cell-Based Therapies and Bioengineering Strategies. *Front. Bioeng. Biotechnol.* **8**, 455 (2020).
241. Li, R., Hornberger, K., Dutton, J. R. & Hubel, A. Cryopreservation of Human iPS Cell Aggregates in a DMSO-Free Solution—An Optimization and Comparative Study. *Front. Bioeng. Biotechnol.* **8**, 1 (2020).
242. Beier, A. F., Schulz, J. C. & Zimmermann, H. Cryopreservation with a twist –

Towards a sterile, serum-free surface-based vitrification of hESCs. *Cryobiology* **66**, 8–16 (2013).

243. Hunt, C. J. Cryopreservation of Human Stem Cells for Clinical Application: A Review. *Transfus Med Hemother* **38**, 107–123 (2011).
244. McNeish, J. *et al.* High-throughput Screening in Embryonic Stem Cell-derived Neurons Identifies Potentiators of α-Amino-3-hydroxyl-5-methyl-4-isoxazolepropionate-type Glutamate Receptors. *J. Biol. Chem.* **285**, 17209–17217 (2010).
245. Engle, S. J., Blaha, L. & Kleiman, R. J. Best Practices for Translational Disease Modeling Using Human iPSC-Derived Neurons. *Neuron* **100**, 783–797 (2018).
246. Fujimori, K. *et al.* Modeling sporadic ALS in iPSC-derived motor neurons identifies a potential therapeutic agent. *Nat. Med.* **24**, 1579–1589 (2018).
247. Egawa, N. *et al.* Drug screening for ALS using patient-specific induced pluripotent stem cells. *Sci. Transl. Med.* **4**, 145ra104 (2012).
248. Yang, Y. M. *et al.* A Small Molecule Screen in Stem-Cell-Derived Motor Neurons Identifies a Kinase Inhibitor as a Candidate Therapeutic for ALS. *Cell Stem Cell* **12**, 713–726 (2013).
249. Ryan, S. D. *et al.* Isogenic Human iPSC Parkinson's Model Shows Nitrosative Stress-Induced Dysfunction in MEF2-PGC1α Transcription. *Cell* **155**, 1351–1364 (2013).
250. Burkhardt, M. F. *et al.* A cellular model for sporadic ALS using patient-derived induced pluripotent stem cells. *Mol. Cell. Neurosci.* **56**, 355–364 (2013).
251. Höing, S. *et al.* Discovery of Inhibitors of Microglial Neurotoxicity Acting Through Multiple Mechanisms Using a Stem-Cell-Based Phenotypic Assay. *Cell Stem Cell* **11**, 620–632 (2012).
252. Brownjohn, P. W. *et al.* Phenotypic Screening Identifies Modulators of Amyloid Precursor Protein Processing in Human Stem Cell Models of Alzheimer's Disease. *Stem Cell Reports* **8**, 870–882 (2017).
253. Kondo, T. *et al.* iPSC-Based Compound Screening and In Vitro Trials Identify a Synergistic Anti-amyloid β Combination for Alzheimer's Disease. *Cell Rep.* **21**,

2304–2312 (2017).

254. Zhan, T. *et al.* Interaction of solute and water molecules in cryoprotectant mixture during vitrification and crystallization. *J. Mol. Liq.* **325**, 114658 (2021).

255. Okotrub, K. A. & Surovtsev, N. V. Raman scattering evidence of hydrohalite formation on frozen yeast cells. *Cryobiology* **66**, 47–51 (2013).

256. Adar, F., Erecinska, M. & University of Pennsylvania, U. of. Resonance Raman spectra of whole mitochondria. *Biochemistry* **17**, 5484–5488 (1978).

257. Selvarajan, A. Raman spectrum of dimethyl sulfoxide (DMSO) and the influence of solvents. *Proc. Indian Acad. Sci. - Sect. A* **64**, 44–50 (1966).

258. Giraud, M. N., Motta, C., Boucher, D. & Grizard, G. Membrane fluidity predicts the outcome of cryopreservation of human spermatozoa. *Hum. Reprod.* **15**, 2160–2164 (2000).

259. Blesbois, E., Grasseau, I. & Seigneurin, F. Membrane fluidity and the ability of domestic bird spermatozoa to survive cryopreservation. *Reproduction* **129**, 371–378 (2005).

260. Deshpande, A. *et al.* Cellular Phenotypes in Human iPSC-Derived Neurons from a Genetic Model of Autism Spectrum Disorder. *Cell Rep.* **21**, 2678–2687 (2017).

261. Nixdorf-Bergweiler, B. E. Enlargement of Neuronal Somata in the LMAN Coincides with the Onset of Sensorimotor Learning for Song. *Neurobiol. Learn. Mem.* **69**, 258–273 (1998).

262. Matsumura, K., Hayashi, F., Nagashima, T., Rajan, R. & Hyon, S.-H. Molecular mechanisms of cell cryopreservation with polyampholytes studied by solid-state NMR. *Commun. Mater.* **2**, 15 (2021).

263. Best, B. P. Cryoprotectant Toxicity: Facts, Issues, and Questions. *Rejuvenation Res.* **18**, 422–36 (2015).

264. Hornberger, K., Li, R., Duarte, A. R. C. & Hubel, A. Natural deep eutectic systems for nature-inspired cryopreservation of cells. *AIChE J.* **67**, e17085 (2021).

265. Pischedda, F. *et al.* Cryopreservation of Primary Mouse Neurons: The Benefit of Neurostore Cryoprotective Medium. *Front. Cell. Neurosci.* **12**, 81 (2018).

266. Parker, S. S. *et al.* High Fidelity Cryopreservation and Recovery of Primary

Rodent Cortical Neurons. *eNeuro* **5**, (2018).

267. Drummond, N. J. *et al.* Cryopreservation of midbrain dopaminergic neural cells differentiated from human embryonic stem cells. *bioRxiv* 2020.02.11.944272 (2020). doi:10.1101/2020.02.11.944272
268. Wakeman, D. R. *et al.* Cryopreservation Maintains Functionality of Human iPSC Dopamine Neurons and Rescues Parkinsonian Phenotypes In Vivo. *Stem cell reports* **9**, 149–161 (2017).
269. Joules, A. *et al.* Comparative analysis of cell therapy infusion workflows at clinical sites. *Cytotherapy* **23**, 285–292 (2021).
270. Noutsi, P., Gratton, E. & Chaieb, S. Assessment of Membrane Fluidity Fluctuations during Cellular Development Reveals Time and Cell Type Specificity. *PLoS One* **11**, e0158313 (2016).
271. Murray, K. A. & Gibson, M. I. Post-Thaw Culture and Measurement of Total Cell Recovery Is Crucial in the Evaluation of New Macromolecular Cryoprotectants. *Biomacromolecules* **21**, 2864–2873 (2020).
272. Kilbride, P. *et al.* Recovery and Post-Thaw Assessment of Human Umbilical Cord Blood Cryopreserved as Quality Control Segments and Bulk Samples. *Biol. Blood Marrow Transplant.* **25**, 2447–2453 (2019).
273. Bahsoun, S., Coopman, K. & Akam, E. C. The impact of cryopreservation on bone marrow-derived mesenchymal stem cells: a systematic review. *J. Transl. Med.* **17**, 397 (2019).
274. Pennington, B. O. *et al.* Xeno-free cryopreservation of adherent retinal pigmented epithelium yields viable and functional cells in vitro and in vivo. *Sci. Rep.* **11**, 6286 (2021).
275. Bahari, L., Bein, A., Yashunsky, V. & Braslavsky, I. Directional freezing for the cryopreservation of adherent mammalian cells on a substrate. *PLoS One* **13**, e0192265 (2018).
276. Jeong, Y.-H. *et al.* Vitrification for cryopreservation of 2D and 3D stem cells culture using high concentration of cryoprotective agents. *BMC Biotechnol.* **20**, 45 (2020).

277. Dong, H., Li, X., Chen, K., Li, N. & Kagami, H. Cryopreserved Spontaneous Spheroids from Compact Bone-Derived Mesenchymal Stromal Cells for Bone Tissue Engineering. *Tissue Eng. Part C Methods* **27**, 253–263 (2021).
278. Arai, K., Murata, D., Takao, S., Verissiomo, A. R. & Nakayama, K. Cryopreservation method for spheroids and fabrication of scaffold-free tubular constructs. *PLoS One* **15**, e0230428 (2020).
279. Fernández-Pérez, E. J. *et al.* Effect of Cholesterol on Membrane Fluidity and Association of Aβ Oligomers and Subsequent Neuronal Damage: A Double-Edged Sword. *Front. Aging Neurosci.* **10**, 226 (2018).

Appendix 1

FIJI macro for calcium imaging data processing

```
run("Set Measurements...", "mean redirect=None decimal=3");
rename("raw stack");
run("Duplicate...", "title=pre-ROI duplicate range=1-1");
//change duplicate range to your desired frame number best for ROI extraction
run("Duplicate...", "title=pre-ROI_threshold");
selectWindow("pre-ROI_threshold");
setAutoThreshold("Default dark");
//run("Threshold...");
setAutoThreshold("Default dark");
setOption("BlackBackground", false);
run("Convert to Mask");
run("Calculator Plus", "i1=pre-ROI i2=pre-ROI_threshold operation=[Multiply: i2
    = (i1*i2) x k1 + k2] k1=0.004 k2=0 create");
run("Green");
run("Find Maxima...", "prominence=20 output=[Segmented Particles]");
run("Invert");
selectWindow("pre-ROI_threshold");
run("Invert");
run("Calculator Plus", "i1=pre-ROI_threshold i2=[Result Segmented]
    operation=[Add: i2 = (i1+i2) x k1 + k2] k1=1 k2=0 create");
run("Invert");
run("Watershed");
run("Analyze Particles...", "size=100-2500 show=Masks add");
selectWindow("raw stack");
roiManager("Multi Measure");
```

APPENDIX 2

MATLAB script for calcium imaging data analysis

```
% DEFINE BASELINE
f0raw=table2array(readtable('.csv'));
f0raw(:,1)=[];
f0=mean(f0raw,2);
Trim=1:20; % Trim off first 20 frames ~ 5 seconds
f0(Trim,:)=[];
space=100;
baseraw=table2array(readtable('.csv'));
t0=baseraw(:,1);
base=mean(baseraw,2);
color1=[1,0,0,0.1]; % last value is transparency
color2=[0,0,0,0.1]; % last value is transparency
ytitle={'dF/F0'};
ylim=[-0.5 25];
fontsize=10;

der0=ones(size(baseraw,1)-space,size(baseraw,2));
for i = 1:size(der0,2)
   for j = 1:size(der0,1)
      dy=baseraw(j+space,i)-baseraw(j,i);
      dx=t0(j+space)-t0(j);
      der0(j,i)=dy/dx;
   end
end
threshold=prctile(der0,97,'all');

% GRAPH PANEL PER DRUG MOLECULE
```

```
T1raw=table2array(readtable('.csv')); % Filename
T1raw(Trim,:)=[];
x1=T1raw(:,1);
t1=x1.*0.245-size(Trim,2)*0.245;
y1raw=T1raw(1:end,2:size(T1raw,2));
y1=y1raw;
for i = 1:size(y1raw,2)
   y1(:,i)=(y1raw(:,i)-f0)./f0;
end
der1=ones(size(y1,1)-space,size(y1,2)); % 1st derivative of graph
hits1=0;
nexttile
for i = 1:size(der1,2)
   for j = 1:size(der1,1)
      dy=y1(j+space,i)-y1(j,i);
      dx=t1(j+space)-t1(j);
      der1(j,i)=dy/dx;
   end
   if max(der1(:,i))>threshold % Set threshold to a responder
      hits1=hits1+1; % Count responders
      plot(t1,y1(:,i),'-','LineWidth',1,'color',color1)% Responders
      hold on
   else
      plot(t1,y1(:,i),':','LineWidth',1,'color',color2)% Not responders
      hold on
      grid off
   end
end
pctresp_DMSO=hits1/size(T1raw,2); % Calculate percent responders
prop1=prop_ci(hits1,size(y1,2),0.05);
```

```
CI1=(prop1(3)-prop1(2))/2;
title('drug name','FontSize',fontsize)
xlabel('Time (s)','FontSize',fontsize)
ylabel(ytitle,'FontSize',fontsize)
set(gca, 'xlim', [0 180],'ylim', ylim)
xticks(linspace(0,180,7))
text(10,22.5,string([sprintf('%.1f',pctresp_DMSO*100) '%']),...
   'FontWeight','bold','FontSize',fontsize,'Color','r')
```